Present and future probability of meteorological and hydrological hazards in Europe

Groenemeijer, P; Vajda, A; Lehtonen, I; Kämäräinen, M; Venäläinen, A; Gregow, H; Becker, N; Nissen, K; Ulbrich, U; Paprotny, Dominik

Important note
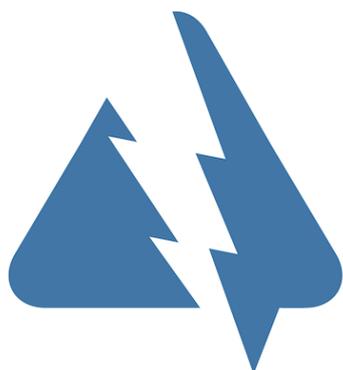To cite this publication, please use the final published version (if applicable).
Please check the document version above.

Security Sensitivity Committee Deliverable Evaluation

Deliverable Reference	D 2.5
Deliverable Name	**Present and future probability of meteorological and hydrological hazards in Europe**
Contributing Partners	**ESSL/FMI/FU-Berlin/TU-Delft**
Date of Submission	**May 2016**

The evaluation is:
• **The content is not related to general project management**
• **The content is not related to general outcomes as dissemination and communication**
• **The content is not related to critical infrastructure vulnerability or sensitivity**
Diagram path 1-2-3. Therefor the evaluation is Public.

Decision of Evaluation	Public	~~Confidential~~
	~~Restricted~~	

Evaluator Name	**P.L. Prak, MSSM**
Evaluator Signature	**Signed 27 May 2016**
Date of Evaluation	**2016-05-19**

Present and future probability of meteorological and hydrological hazards in Europe

Authors

Pieter Groenemeijer (ESSL)

Andrea Vajda (FMI)

Ilari Lehtonen (FMI)

Matti Kämäräinen (FMI)

Ari Venäläinen (FMI)

Hilppa Gregow (FMI)

Nico Becker (FU-Berlin)

Katrin Nissen (FU-Berlin)

Uwe Ulbrich (FU Berlin)

Oswaldo Morales Nápoles (TU-Delft)

Dominik Paprotny (TU-Delft)

Tomáš Púčik (ESSL)

*Correspondence author:

Pieter Groenemeijer, European Severe Storms Laboratory e.V.

c/o DLR Institute for Atmospheric Physics, Münchner Str. 20, 82234 Wessling, Germany,

pieter.groenemeijer@essl.org, +49 151 59031839

DOCUMENT HISTORY

Index	Date	Author(s)	Main modifications
0.0	28 April 2016	Pieter Groenemeijer (ESSL), Andrea Vajda (FMI), Ilari Lehtonen (FMI), Matti Kämäräinen (FMI), Ari Venäläinen (FMI), Hilppa Gregow (FMI), Nico Becker (FU-Berlin), Katrin Nissen (FU-Berlin), Uwe Ulbrich (FU Berlin), Oswaldo Morales Nápoles (TU-Delft), Dominik Paprotny (TU-Delft), Tomáš Púčik (ESSL)	First draft for review by co-authors
1.0	18 May 2016	"	Second draft for project-internal review
2.0	07 June 2016	"	Version after the project internal review, to be submitted to the Commission

Document Name: Report on the present severe weather probability distribution

Work Package: 2

Task: 2.3 and 2.4

Deliverable: 2.5

Deliverable scheduled date :   30 April 2016

Responsible Partner: ESSL

Table of Contents

1. Executive Summary

This report presents analyses of the probability of hydro-meteorological hazard occurrence, which were carried out within the RAIN project. Those probabilities and their projected changes[1] during the 21st century are an input to subsequent risk analyses which assist the identification of optimal adaptation measures. These data are available at the location specified in Appendix B. The spatial distributions of the probabilities in the present climate were mapped and projections of changes according to the RCP 4.5 and RCP 8.5 climate scenarios were developed. The investigations by the European Severe Storms Laboratory, the Freie Universität Berlin, the Finnish Meteorological Institute and Delft University of Technology focused on thunderstorm-related phenomena, windstorms and heavy precipitation, winter weather and forest fires, and coastal and river floods, respectively.

The analyses are primarily based on datasets of observations, atmospheric reanalyses and regional climate models, although several other datasets were used for analyses of floods. The Modelled climate model data covered the European domain in the World Climate Research Program Coordinated Regional Downscaling Experiment (EURO-CORDEX). Information to infer hazard probability of occurrence was extracted from those datasets in several novel ways, for example by using Bayesian networks to infer the flood hazard risk.

Besides establishing the present spatial distribution of probability, projections for the 21st century indicate that a number of changes are to be expected across Europe. First, the windstorm hazard may become more relevant across continental Europe, while a slight decrease is expected across the Mediterranean region and the North Atlantic Ocean. Extreme precipitation, of both short (3 hour) and medium (24 hours) time ranges are forecast to increase across most of Europe. The increase will be most pronounced in North-Western Europe, especially over Scandinavia and across the British Isles. The numbers of sub-daily, high-intensity events are predicted to increase at a higher rate than the number of long-duration events characterised by high accumulated rain amounts.

In part resulting from the increased frequency of heavy rainfall, river floods will become more likely over large areas, especially the case of central Europe and the UK, unless mitigation efforts are taken. Throughout Europe, the regions at risk from 10-year, 30-year and 100-year return period floods will expand greatly. Germany, Hungary, Poland and France are expected to have the largest absolute increases in flood-prone areas. On the other hand, northern Europe will encounter a decrease in flood-prone areas. Lightning will become more common, in particular across northern and central Europe. Conditions supportive of severe thunderstorms with large hail, tornadoes and severe wind gusts become more likely as well, especially in south-central Europe.

---

[1] These data, which constitute RAIN Deliverable 2.4, can be downloaded from http://data.3tu.nl/repository/collection:ab70dbf9-ac4f-40a7-9859-9552d38fdccd
See Appendix B for more information.

Longer dry spells will cause conditions supportive of forest fires and wildfires to become much more frequent across Europe, in particular in the south and especially in the RCP 8.5 scenario. Heavy snowfall, blizzards and snow load should become less likely across much of Europe, with the exception of central and northern Fennoscandinavia and northern Russia, where increases are predicted for heavy snowfall and snow load. The occurrence of freezing rain is expected to undergo a northward shift, with slight decrease in probability in central Europe but intensification in Fennoscandinavia and Northern Russia.

2. Introduction

2.1   Hazard Identification in the RAIN project

This report presents the results of the analyses of hazard probability that were carried out within the RAIN project, more precisely its Work Package 2 on "Hazard Identification". These results are an essential input to the risk analysis framework developed within RAIN, in particular because it will take into account the changing risk as a result of climate change. The risk analysis framework developed in RAIN Work Package 5 will use the probabilities as input variables, jointly with information on Critical Infrastructure vulnerability developed Work Packages 3 and 4. This framework is subsequently applied in RAIN Work Packages 6 and 7, that study "Costs and Benefits" and develop "Mitigation Strategies", respectively. Further details can be found in the reports from the respective Work packages.

The quantitative results that are presented, discussed and interpreted in this report are available as gridded datasets as [RAIN deliverable D2.4](#).

The four research groups that have contributed to this report are the European Severe Storms Laboratory (ESSL), the Finnish Meteorological Institute (FMI), the Meteorological Institute of the Freie Universität Berlin (FU-Berlin), and Delft Technical University (TU-Delft). ESSL analysed the occurrence of thunderstorm-related hazards, FMI of winter weather phenomena and wildfires, FU-Berlin of wind storms and heavy precipitation and TU-Delft of river and coastal flooding.

The analyses of the present and future probability have been carried out for all twelve hazards defined to be within the scope of the RAIN project in its project report D2.1 "List of Past Cases". These include various meteorological hazards as well as the hydrological hazards (river and coastal floods). The analyses have been performed by applying newly developed methods to new data sets. For most hazards, pan-European probability maps such as those presented in this report have not been available before in any form (e.g. based on older underlying data). For others, maps available before were of a different nature and were developed using different methods.

2.2   Climate scenarios

2.2.1   Present climate

The following common approach was followed. In order to evaluate the present climate, observations and reanalysis data from the period 1981-2010 were used, wherever this was possible and useful. For some phenomena, a different reference period was necessary due to a lack of data. For thunderstorm-related hazards such as hail and tornadoes, observational datasets are not sufficiently homogeneous to allow direct interpretation. For flood- and flood-protection related data, direct observations are scarcely available, if at all. The authors of this report have formulated recommendations regarding increasing data availability in RAIN report D2.3 "Report on national and regional state-of-the-art risk monitoring and early-to-medium-range warning systems".

2.2.2 Future Scenarios and reference period

In order to assess trends during the 21st century, three time periods and the two emission scenarios RCP 4.5 and RCP 8.5 were considered. These two scenarios correspond to those adopted by the Intergovernmental Panel on Climate Change in its 5th fifth Assessment Report (AR5). They describe four possible climate futures, that differ only on how much greenhouse gases are emitted in the years to come. The four RCPs, RCP2.6, RCP 4.5, RCP6, and RCP 8.5, are named after a possible range of radiative forcing values in the year 2100 relative to pre-industrial values (+2.6, +4.5, +6.0, and +8.5 W/m^2, respectively) (Weyant et al. 2009). The two selected RCPs are those for which regional climate model data was made available the RAIN researchers: The RCP 2.6 and RCP 6.0 scenarios were modelled too rarely for consideration in the RAIN work.

2.2.3 Models and time period

The analysis of the hazards involved the use of regional climate model simulations from the EURO-CORDEX consortium (Jacob et al. 2014). These are described in more detail in Chapter 3. Using these models and several other sources, which are described in Chapter 3, methods have been developed to extract information on hazard occurrence and probability.

For all but the hydrological hazards, it was feasible to address the uncertainty of the expected changes caused by differences between climate models, by using an ensemble. In order to compare future changes to the present or past climate, two future time periods, namely 2021 - 2050 and 2071 – 2100 were contrasted to simulations of the past period 1971-2000. Because of the different nature of the hazards and methods, the significance of the climate change signal was determined in a number different ways for different hazards.

2.3   Structure of this report

This report is structured as follows: In Chapter 3, the Data Sets used in the analyses are described. In Chapters 4 - 7 and 9 - 17, the results of the analyses of the individual hazards are presented. Each of these Chapters is divided into four sub-sections. First, a brief introduction to the hazard is provided. Second, a description of the analysis method is given. Last, the obtained hazards probability distributions across Europe are presented for the present climate and in future climate scenario's respectively. The Chapters on river floods and coastal floods additionally contain a brief summary. Chapter 8 presents the assessment of the severity thresholds developed for winter weather phenomena. The report's last Chapter 18, finally provides a summary of all the hazards.

2.4   Acknowledgements

We, the authors of the report, would like to thank the project-internal reviewers Milenko Halat and Chiara Bianchizza for their comments.

We also would like to express our thanks for the support provided by several modelling groups in the EURO-CORDEX experiment. The following individuals have supported the RAIN work by post-processing data of their simulations and providing it to the RAIN consortium: Grigory Nikulin (Rossby Centre, University of Norrköping), Claas Teichmann (MPI-CSC, now Helmholtz-Zentrum Geesthacht),

3. Data sets

3.1 Meteorological observations

3.1.1 E-OBS

The E-OBS dataset (Haylock et al. 2008) has been developed within the EU-funded ENSEMBLES project. It is a European land-only gridded data set of surface data, which has been produced through spatial interpolation of daily station data by a three-stage process using the Kriging interpolation method. The data set contains daily mean, maximum and minimum temperature, as well as precipitation sums and sea level pressure at a horizontal resolution of 0.25°. The station data used for the data set has been described by Klok and Klein (2009). The full period of records used for the interpolation is 1950–2014, but the period 1961–1990 has the highest station density (Hofstra et al. 2009). The data set is regularly updated. For this study, version 11.0 has been used.

3.1.2 European Severe Weather Database (ESWD)

Version 3 of the ESWD has been described by Dotzek et al. (2009). The database was initially developed as an implementation of a standardized, flexible data format for severe weather reports used for the verification of weather forecasts. Upon the founding of ESSL, ESWD development and management became a statutory purpose of the European Severe Storms Laboratory. The database contains information on the phenomena large hail, tornadoes (including waterspouts), heavy rain, and severe wind gusts, among others. The ESWD covers the World Meteorological Organization's region VI, including Europe and the Middle East, as well as a few countries that are not part of region VI (almost) bordering the Mediterranean Sea. The dataset is relatively inhomogeneous in both space and time, so that its use in hazard modelling is by the finding of covariates in other, more homogeneous data sets (Groenemeijer and Kühne 2014).

3.2 Reanalysis datasets

3.2.1 ERA-Interim

ERA-Interim reanalysis dataset (Dee et al. 2011, Simmons et al. 2006) uses 4D-variational analysis on a spectral grid with a triangular truncation of 255 waves (corresponding to approximately 80 km) and a hybrid vertical coordinate system with 60 levels; it produces four analyses per day (00, 06, 12 and 18 UTC) and two 10-day forecasts per day, initialized from analyses at 00 and 12 UTC. The wind gust parameterization implemented in ERA-Interim incorporates friction, horizontal wind speed and its estimated standard deviation at the 10 m level as well as universal turbulence spectra to finally calculate the three-second wind gust values (ECMWF 2007). Fields from the atmospheric model are archived on the N128 reduced Gaussian grid with a spacing of about 0.7° (Berrisford et al. 2009).

3.2.2 NCEP/NCAR reanalysis

The NCEP/NCAR re-analysis dataset uses a data assimilation and model system identical to the global system implemented operationally at the NCEP on 11 January 1995, except that the horizontal resolution is T62, about 210 km (Kalnay et al. 1996). The analysis scheme is a three-dimensional

variational (3DVAR) scheme cast in spectral space denoted spatial spectral statistical interpolation (Kistler et al. 2001). The dataset covers a time period from 1948 until today. The data is available four times daily, daily and monthly. The data is provided by the NOAA/OAR/ESRL PSD, Boulder, Colorado, USA, from their Web site at http://www.esrl.noaa.gov/psd/. The data used for the analysis in this work is on a 1.875° Gaussian grid.

3.2.3   JRA-55

The Japan Meteorological Agency (JMA) provides their second global atmospheric reanalysis product named the Japanese 55-year Reanalysis (JRA-55), which starts in 1958, when the global radiosonde observing system was established, and continues until today (Ebita et al. 2011). The resolution of the atmospheric model is T319 (60km) and a 4DVAR data assimilation system was used. The data used for this analysis is on a 0.5625° Gaussian grid.

3.3   EURO-CORDEX Regional climate model simulations

Simulations from the international Coordinated Downscaling Experiment (CORDEX) on a standardized domain covering Europe (Fig. 3.1) are called EURO-CORDEX (Jacob et al. 2014). The CORDEX initiative is sponsored by the World Climate Research Program (WRCP) of the World Meteorological Organization. The aim of CORDEX is to develop regional climate change projections for all land regions world-wide. EURO-CORDEX simulations are carried out on two different spatial resolutions with grid spacing of 0.44° (~50 km) and 0.11° (~12.5 km), respectively, covering Europe, the Mediterranean Sea and adjacent regions.
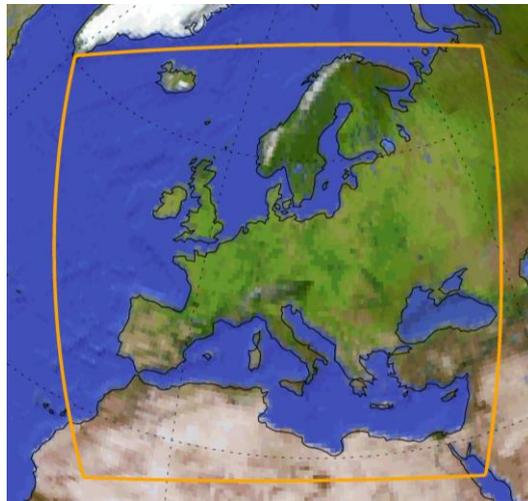
Fig. 3.1. EURO-CORDEX domain. From CORDEX web site: http://www.cordex.org.

Many of the simulations carried out by several groups of researchers across Europe have been made available to support the RAIN work. Each of these groups used one particular regional climate model (RCM), forced by one or more global climate models (GCMs), which were in turn each forced by different emission pathways (Representative Concentration Pathways; RCP's) or by a reanalysis data set. The model runs that were used in this report are given in Table 3-1 and Table 3-2.

Table 3-1. EUR-44 (0.44°) EuroCORDEX simulations used in RAIN analyses. For abbreviations, see Appendix A.

Centre	RCM	GCM	Member	RCP	Simulation used for:
CCCma	CanRCM4_r2	CanESM2	r1i1p1	4.5 8.5	**W**
KNMI	RACMO22E	EC-EARTH	r1i1p1	4.5 8.5	**W T S FF**
		HadGEM2-ES	r1i1p1	4.5 8.5	**W T S FF**
	HIRHAM5	EC-EARTH	r3i1p1	4.5 8.5	**W**
SMHI	RCA4	CanESM2	r1i1p1	4.5 8.5	**W T S FF**
		CNRM-CM5	r1i1p1	4.5 8.5	**W T**
		NorESM1-M	r1i1p1	4.5 8.5	**W T S FF**
		EC-EARTH	r12i1p1	4.5 8.5	**W T**
		HadGEM2-ES	r1i1p1	4.5 8.5	**W T**
		MIROC5	r1i1p1	4.5 8.5	**W T**
		IPSL-CM5A-MR	r1i1p1	4.5 8.5	**W T S FF**
		GFDL-ESM2M	r1i1p1	4.5 8.5	**W T**
		MPI-ESM-LR	r1i1p1	4.5 8.5	**W T**
		CSIRO-Mk-3-6-0	r1i1p1	4.5 8.5	**W T**
MPI-CSC	REMO2009	MPI-ESM-LR	r1i1p1	4.5 8.5	**W T S FF**
		MPI-ESM-LR	r2i1p1	4.5 8.5	**W**
	CCLM4-8-17	MPI-ESM-LR	r1i1p1	4.5 8.5	**W**
NUIM	WRF341	EC-EARTH	r1i1p1	8.5	**T**
WEGC	CCLM4	HadGEM2-ES	r1i1p1	4.5	**T**

Table 3-2. EUR-11 (0.11°) EuroCORDEX simulations used in RAIN analyses. For abbreviations, see Appendix A.

Centre	RCM	GCM	member	RCP	
KNMI	HIRHAM5	EC-EARTH	r3i1p1	4.5 8.5	**W Rd**
	RACMO22E	EC-EARTH	r1i1p1	4.5 8.5	**W Rd R3**
MPI-CSC	CCLM4-8-17	CNRM-CM5	r1i1p1	4.5 8.5	**W Rd**
		EC-EARTH	r12i1p1	4.5 8.5	**W Rd RF**
		HadGEM2-ES	r1i1p1	4.5 8.5	**W**
		MPI-ESM-LR	r1i1p1	4.5 8.5	**W Rd**
	REMO2009	MPI-ESM-LR	r1i1p1	4.5 8.5	**W**
SMHI	RCA4	CNRM-CM5	r1i1p1	4.5 8.5	**W Rd R3**
		EC-EARTH	r12i1p1	4.5 8.5	**W Rd R3 CF**
		IPSL-CM5A-MR	r1i1p1	4.5 8.5	**W Rd R3**
		HadGEM2-ES	r1i1p1	4.5 8.5	**W Rd R3**
		MPI-ESM-LR	r1i1p1	4.5 8.5	**W Rd R3**

Abbreviations of hazard analyses:

W   Windstorm hazard

S   Heavy snowfall, blizzards, crown snow load, and freezing rain

FF   Forest fires

T   Thunderstorms, hail, convective windgusts and tornadoes

Rd   Daily to multi-day precipitation

R3   3-hourly precipitation

CF, RF Coastal floods, River floods

3.4 Hydrological and geophysical datasets for river flood analyses

3.4.1 River discharge observations

Several datasets were compiled into a database of annual maxima and mean river discharges for use in the river flood hazard analysis (Chapter 7). Those sources are:

- 1186 stations from the Global Runoff Data Centre (2015);
- 82 stations from the Norwegian Water Resources and Energy Directorate (2015);
- 284 stations from the Swedish Meteorological and Hydrological Institute (2015);
- 239 Spanish stations from Centro de Estudios Hidrográficos (2012);
- 50 Polish stations from Fal (2000).

In total, 1841 stations from 37 countries containing 74,757 years of data (1950–2005) were used. Most station-years are from France, Spain, Sweden (14% each), United Kingdom (12%), Germany (9%) and Norway (7%).

3.4.2 River and Catchment Database

Data on the river network and drainage basin for the river flood hazard analysis (Chapter 7) was derived from the Catchment Characterisation and Modelling (CCM) River and Catchment Database v2.1 (Vogt et al. 2007, de Jager and Vogt 2010). It covers the entire European continent and its vicinity (about 12m km^2) and consists of vector layers with a 100 m horizontal resolution. The total number of primary catchments in this dataset is about 2,150,000. The source material were digital elevation models (used to calculate flow direction and accumulation) supplemented by land cover data and satellite imagery.

3.4.3 Digital elevation models

Elevation was obtained mostly from EU-DEM digital surface model. This dataset was produced for the European Environment Agency from satellite altimetry data – Shuttle Radar Topography Mission (SRTM) and ASTER GDEM. It has a 25 m resolution and covers 39 countries (DHI GRAS 2014). The model uses vertical datum EVRS2000, geoid EGG08, and reference epoch 2000.0. For Eastern Europe and some other locations not covered by EU-DEM, SRTM data where used instead (Farr et al. 2007). This model has a 3 arc second resolution and has several versions available. The one used here was downloaded from Viewfinder Panoramas (2014).

3.4.4 Land cover datasets

The primary source for land cover was CORINE Land Cover (CLC), a pan-European dataset. It is produced by the European Environment Agency. CLC 2000 edition, version 17 (12/2013) in raster format was used here (European Environment Agency 2014). It has a resolution of 100 m and includes 44 land cover classes with a minimum mapping unit of 25 ha for 39 countries. The main source material of classification were Landsat 7 satellite images from years 1999-2001 (European Environment Agency 2007). The dataset does not cover some catchments in Eastern Europe, therefore the information had to be supplement by Global Land Cover 2000 dataset. This product has a 30 arc second resolution and includes 22 land cover classes. It was produced by the Joint

Research Centre using algorithmic processing of SPOT 4 satellite images (Joint Research Centre 2015).

3.4.5 Reference flood hazard maps

For calibration and validation of river flood hazard maps, one pan-European and three local maps where used. A European map was prepared by Alfieri et al. (2014). It covers a slightly smaller domain than the one used here and includes only rivers with catchments bigger than 500 km². Only one scenario – 100-year return period – was used based on a rainfall-runoff model (using 1990–2010 meteorological data) and a two-dimensional hydraulic model for the flood zone. Local, high-resolution maps used for validation are:

- Flood map of Lower Austria state, prepared by the regional government and including 30-, 100- and 300-year flood scenarios (Land Niederösterreich 2015);
- Flood map of Saxony Länder, Germany, prepared by the regional government and including a 100-year flood scenario (Sächsisches Landesamt für Umwelt, Landwirtschaft und Geologie 2015);
- Flood map of England, prepared by the Environment Agency and including 30-, 100- and 1000-year flood scenarios (Environment Agency 2015).

3.4.6 FLOPROS

FLOPROS is a global flood protection standards database created at Vrije Universiteit Amsterdam (Scussolini et al. 2015). It currently consists of three "layers". First is the design layer, where information on protection standards of existing flood defences is collected. Then, the policy layer contains information on standards that should be in place in accordance with existing legislation. This information is then aggregated into subnational territorial units, with the design layer given priority over the policy layer, if both information is available. Missing information is supplemented by the modelled layer. A simple linear relationship between flood protection standards and flood risk, in four groups of countries divided by wealth, is used as a proxy for the actual protection. The FLOPROS map (Fig. 3.1) was adjusted to fit the study area, with some small gaps in the data filled using nearest neighbour interpolation. FLOPROS was used for both river and coastal analysis, though the database is generally based river flood protection data. For the purpose of creating maps in the flood protection scenario, it is assumed that the return periods defined in the protection standards correspond to river discharges and storm surge heights calculated for the historical scenario (1971–2000).
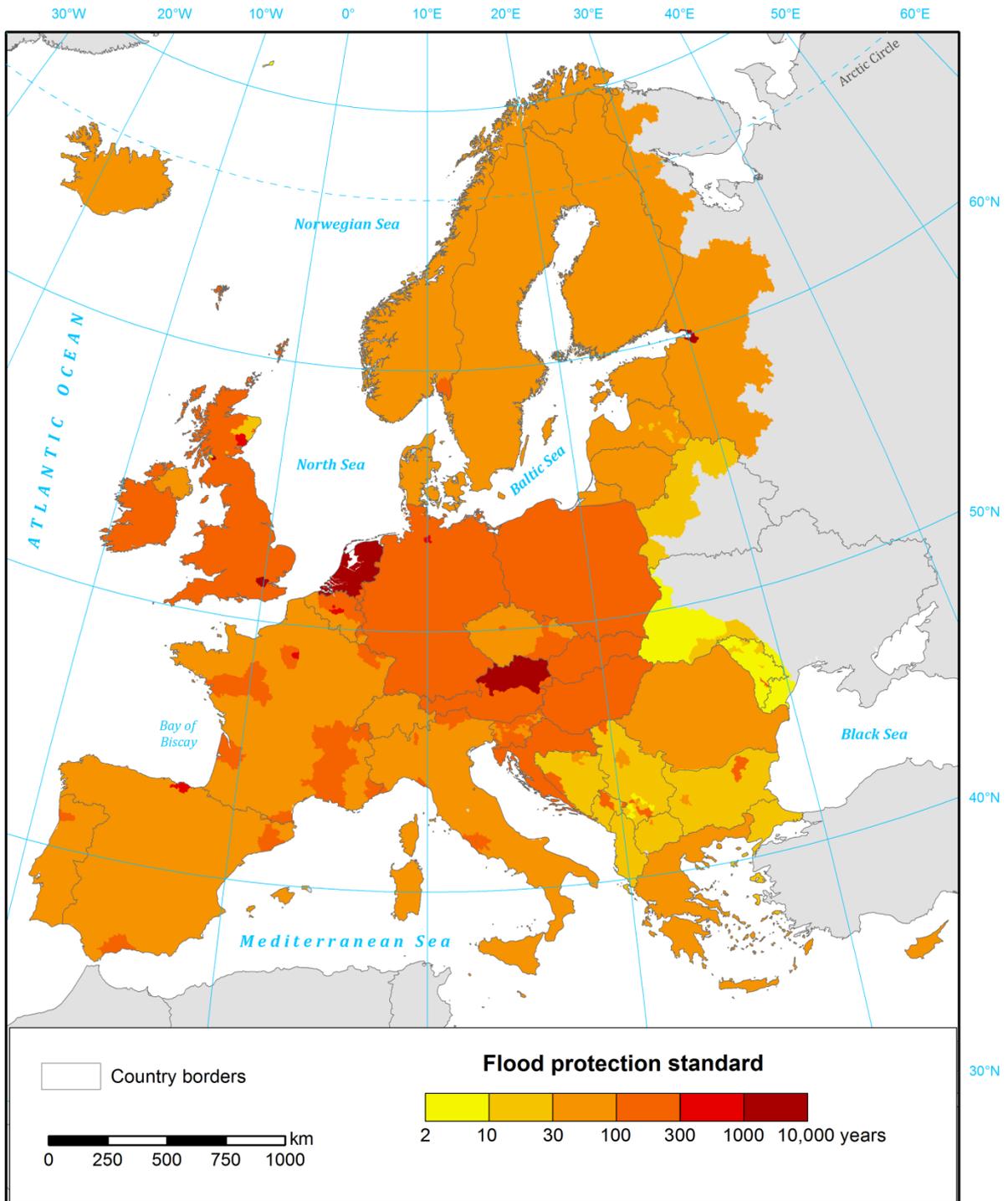
Fig. 3.2. Flood protection standards used in river and coastal flood maps (flood protection scenario). Based on FLOPROS database by Scussolini et al. (2015).

3.5   Hydrological and geophysical datasets for coastal flood analyses

3.5.1   Bathymetry

Bathymetry of basins around Europe was obtained from the European Marine Observation and Data Network (EMODnet 2016). This digital terrain model (DTM) has a very fine resolution of 1/8 arc minute (approx. 200 m). Its source material were bathymetric survey datasets, composite DTMs, with voids filled with a global GEBCO Digital Bathymetry dataset.

3.5.2   Tide gauge observations

Several sources of tide gauge records were used for calibration and validation. High-frequency quality-checked data include:

- 21 stations from 12 countries from University of Hawaii Sea Level Center (UHSLC 2015);
- 42 (mostly British) stations from the British Oceanographic Data Centre (BODC 2015);
- 19 Swedish stations from SMHI (2016);
- 8 Dutch stations from Rijkswaterstaat (2016).

Most of the stations have long series of data covering the entire period of interest (1970–2014). Additionally, high-frequency raw data from 66 Mediterranean stations (2008–2014) obtained from the Joint Research Centre (JRC) through personal communication with Michalis Vousdoukas. Finally, 5 Polish stations containing only information on annual maxima (1970–2007) were used for validation (Wiśniewski and Wolski 2009).

3.5.3   Tidal constituents

Tidal constituents for the entire European coast were derived from TPXO8 model. This is the latest version of a global model originally developed by Egbert et al. (1994), which shown to be the most accurate available out of several existing tide models (Stammer et al. 2014). It provides nine tidal constituents in 1/30° resolution (K1, K2, M2, M4, N2, O1, P1, Q1, S2) and four in 1/6° resolution (MS4, MN4, MF, MM). The tidal solutions were derived using satellite altimetry data and hydraulic modelling, including local refinements in coastal and shallow areas (Egbert and Erofeeva 2002, 2014).

3.5.4   Mean sea level

Baseline mean sea level was obtained from MDT_CNES-CLS13 dataset. It contains mean sea surface height above geoid during 1993–2012. The dataset was obtained by combining several sources. Primarily, it shows the difference between sea level from satellite altimetry and the reference geoid EGM-DIR-R4 (based on GOCE and GRACE satellite gravimetry data). The results were corrected with *in situ* measurements and sea surface velocity data. The dataset has a global coverage and its spatial resolution is 0.25°. Methodology behind it was described by Rio et al. (2014) and is available from Aviso (2015).

3.5.5 Sea level rise

Sea level rise caused by climate change and human activity has several constituents. They are:

- Ocean circulation ("dynamic" topography);
- Ocean water volume ("steric" component, reacting to changes in ocean temperature and salinity);
- Atmospheric loading (atmospheric circulation and moisture content);
- Glacier and ice sheet mass balance;
- Ice sheet dynamics (affecting e.g. ocean circulation);
- Groundwater depletion (caused by withdrawal of water from underground storage).

Steric and dynamic changes in sea level were obtained from CNRM-CM5 model (Voldoire et al. 2013). It is one of the general circulation models under CMIP5 framework. This particular one was chosen because it includes European inner seas (unlike many other models) and has better accuracy for representing the dynamic topography compared to other models (Slangen et al. 2014). The horizontal resolution of the model is variable, but mostly ca. 0.5° over Europe. Atmospheric loading was omitted as it has negligible impact. The other factors (glacier, ice sheet and groundwater contributions) were obtained from estimates by Slangen et al. (2014) and Carson et al. (2016), provided for 1986–2100 at 1° resolution. 1986–2005 trend was extrapolated to 1971 in order to provide data for the historical scenario. It should be noted that dynamic, steric, glacier and ice sheet mass balance are available for both climate change scenarios used in the project (RCP 4.5 and RCP 8.5). Meanwhile, contributions of ice sheet dynamics and groundwater depletion to sea level rise are assumed to be the same for both scenarios.

3.5.6 Glacial isostatic adjustment

The Glacial Isostatic Adjustment (GIA) rate is available from ICE-6G_C (VM5a) model by Peltier et al. (2015). This global dataset is provided in a 1° resolution and includes both the rate (mm/year) of vertical movement of the ground (radial displacement) and GIA effect on sea level. The dataset was produced by combining satellite altimetry and gravimetry data with GPS measurements of vertical motion of the crust.

3.5.7 Digital elevation models

Digital Elevation Models (DEM) used to delimitate coastal flood hazard zone is the same as for river hazards, but with corrections applied. In several countries there are large biases in the EU-DEM, even exceeding the range of extreme water levels. Using publicly available national DEMs from Poland, the Netherlands (REF) and the United Kingdom we found that in coastal floodplains (up to 3 m water level) the bias is almost identical to country averages presented in the validation report (DHI GRAS 2014). For example, in the Polish coast the bias is -2.31 m (country average: -2.38 m). In the Netherlands the values are -0.96 and -0.85 m, respectively, and for the UK +0.70 in the floodplain and +0.72 m for the whole territory. Therefore, the elevation in the European DEM was increased or decreased by a country-specific value taken from the validation report.

4. Windstorms

Nico Becker (Freie Universität Berlin)

4.1 Introduction

Extra-tropical cyclones are day to day phenomena in the European region. These low pressure systems develop within the mid-latitudes and draw their energy from the temperature gradient between the equator and the pole. Extra-tropical cyclones are generally associated with increased wind speeds, precipitation and cloudiness (Fig. 4.1). Certain conditions, like increased temperature gradients, humidity or upper level divergence, can lead to an intensification of extra-tropical cyclones. Such intense cyclones can cause windstorms with hurricane force wind speeds. Often these extreme wind speeds cause fatalities and damages. In fact, extreme windstorms are among the most destructive and costly extreme weather phenomena in the European region. In terms of insured losses, the damages caused by windstorms in Europe are among the largest compared to other natural disasters (MunichRe 2000, SwissRe 2000). This is also due to the large areas which can be affected by individual storms.

In many cases critical infrastructure is affected by windstorms. The energy system and the rail and road network is affected, both by direct and indirect damages. Extreme wind speeds can directly damage or destroy structures like power pylons. Indirect damages are caused by falling trees, which can break power lines or block roads and railways.

In general, insured losses caused by extreme wind speeds occur if the 98th percentile of the local wind speed distribution is exceeded (Klawa and Ulbrich 2003). However, building regulations of critical infrastructure are usually based on the 50-year return level of the local wind climate, which is higher than the 98th percentile. Thus, critical infrastructure is built to withstand wind speeds that occur on average once within 50 years, which is equal to an annual occurrence probability of 2%. In this work return levels of wind speeds are estimated for the recent climate and changes of occurrence probabilities are derived for future climate projections.

Fig. 4.1. Satellite image of an extra-tropical cyclone. (from earthobservatory.nasa.gov)

4.2 Method

In general, one can distinguish two basic approaches to study a meteorological phenomenon like windstorms. One way is to focus on a certain point in space and analyze the local windstorm climate based on the wind speed distribution. The other way is to identify and track individual windstorm events and follow their development in space and time. The aim of this work is to combine those two approaches in order to study windstorms and their occurrence frequencies, which are relevant for critical infrastructure. First, extreme value statistics are used to estimate the local occurrence probabilities and return levels of wind speeds relevant for critical infrastructure. Second, a tracking algorithm is used to associate exceedances of return levels to individual windstorm events.

4.2.1 Extreme value statistics

The estimation of return level is based on the Fisher-Tipper theorem, which states that the distribution of maxima of samples of random variables can only converge to one of three possible distributions, namely the Gumbel distribution, the Fréchet distribution, or the Weibull distribution (Coles et al. 2001). Those three distribution families can be combined to the generalized extreme value (GEV) distribution

$$F(x) = exp\left\{-\left[1 + \xi\left(\frac{x-\mu}{\sigma}\right)\right]^{-1/\xi}\right\}, \quad \text{Eq. 4-1}$$

where μ is called the location, σ the shape and ξ the scale parameter.

In practice, the maxima of the analyzed variables are often calculated for consecutive time periods of one year length. Estimates of extreme quantiles of the annual maximum distribution are then obtained by inverting the equation of $F(x)$:

$$x_p = \begin{cases} \mu - \frac{\sigma}{\xi}\left[1 - \{-\log(1-p)\}^{-\xi}\right], & \text{for } \xi \neq 0 \\ \mu - \sigma \log\{\log(1-p)\}, & \text{for } \xi = 0 \end{cases} \quad \text{Eq. 4-2}$$

where $F(x_p) = 1 - p$. x_p is usually called the "return level", which is associated with the "return period" $1/p$. x_p is expected to be exceeded on average every $1/p$ years.

In this work, x is equal to the maximum wind speeds that occurred in each individual winter half-year (October-March) of the analyzed time periods. Thus, for example, the 50-year return level is expected to be exceeded on average once every 50 years. In other words, the probability that the maximum wind speed exceeds the 50-year return level in a particular winter is $p = 1/50 = 0.02$.

The parameters μ, σ and ξ of the GEV distribution are estimated by using a log-likelihood approach. In the stationary case, μ, σ and ξ are assumed to be constant within the analyzed time period. The stationary approach is used to estimate GEV distributions for the present day climate from reanalysis data in section 4.3.

In Section 4.4, present-day GEV distributions of wind speed maxima are compared to those in different future scenarios. Thus, we compare 30-years periods, one period in the present day climate

(P_1), and one period in the future climate (P_2). In a simple approach, one would estimate the GEV distributions for P_1 and P_2 separately, by using the stationary approach. However, the log-likelihood method allows to estimate the GEV distribution in a non-stationary setting, where one or more of the parameters can depend on time. In our case, we allow the form parameter μ to depend on time:

$$x_t \sim GEV(\mu(t), \sigma, \xi),$$
Eq. 4-3

where

$$\mu(t) = \begin{cases} \mu_1, & \text{for } t \in P_1, \\ \mu_2, & \text{for } t \in P_2. \end{cases}$$
Eq. 4-4

In other words, μ is assumed to be constant in the present day period and in the future period, however, the value of μ may be different in the two periods. The benefit of estimating the return period for both periods at the same time in a non-stationary approach is that twice the amount of data is available and the uncertainty of the estimation is reduced. Here, we only allow the form parameter to depend on the time period, because the shape and scale parameters are more difficult to estimate.

Fig. 4.2 shows an example of such a non-stationary fit, derived from the daily maxima of the 10m wind speeds in the CORDEX model HIRHAM5 for a grid box close to Berlin. The blue line corresponds to the estimated GEV distribution in P_1, based on the parameters μ_1, σ and ξ, the red line corresponds to the estimated GEV distribution in P_2, based on the parameters μ_2, σ and ξ. The vertical blue line indicates a return period of 50 years. Thus, the corresponding return level of 18.1 m/s (black line) has an occurrence probability of $p_1 = 0.020$ in the recent climate. The vertical red line indicated the return period of these 18.1 m/s in in the future period P_2, which is 32.1 years. Thus, the occurrence probability of the recent climate 50-year return level in the future climate is
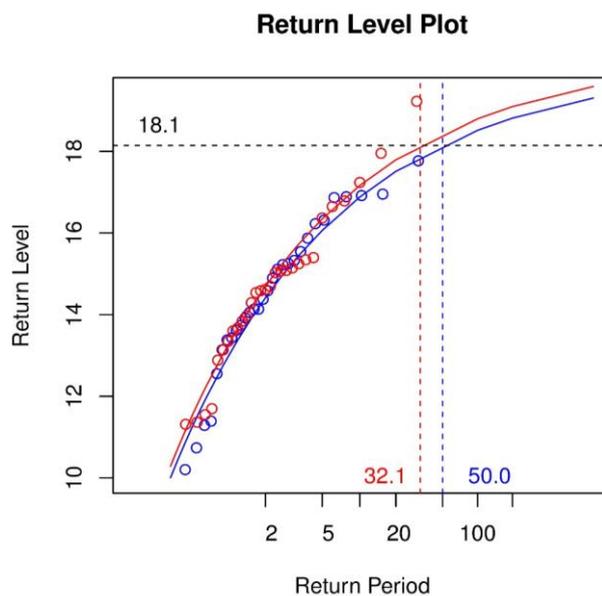

Fig. 4.2. Return level plot for 10m daily maximum 10m wind speeds for a grid point in the HIRHAM5 CORDEX simulations for the years 1970-2000 of the historical experiment (blue) and the year 2070-2100 in the RCP 8.5 scenario (red). Return periods are in in years and return level in m/s.

$p_2 = 0.031$. We can conclude that the occurrence probability of the present day 50-year return level has increased by $\Delta p = p_2 - p_1 = 0{,}011$.

By following this approach, we can compute the change in occurrence probability for different present day return levels for each grid point of each CORDEX model using different future periods and different RCP scenarios.

4.2.2   Tracking of windstorms

Leckebusch et al (2008) introduced a windstorm tracking algorithm based on exceedances of the local 98th percentile. Areas of exceedance are identified usually in the 6-houly wind fields and tracked in time by using a nearest neighbor approach. Here we modify this approach in order to account only for extreme windstorm relevant for critical infrastructure. The windstorms are still identified and tracked based on exceedances of the 98th percentile, but only those windstorms are selected, which also exceed the 50-year return level at some point during their lifetime. Finally, we can compare the number of extreme windstorms in certain regions of interest in the different future scenarios. By following this approach, exceedances of the 50-year return levels can be assigned to certain events. Furthermore, simultaneous exceedances at neighboring grid points can be assigned to an individual windstorm, which would not be possible in a pure grid point based approach.

4.3   Present climate

In general, two different data sources exist to estimate the present day wind climate for the land area in the European region: wind observations from weather stations and reanalysis datasets. However, the availability of quality checked station data of wind measurements is not sufficient to produce two-dimensional fields covering the European region.
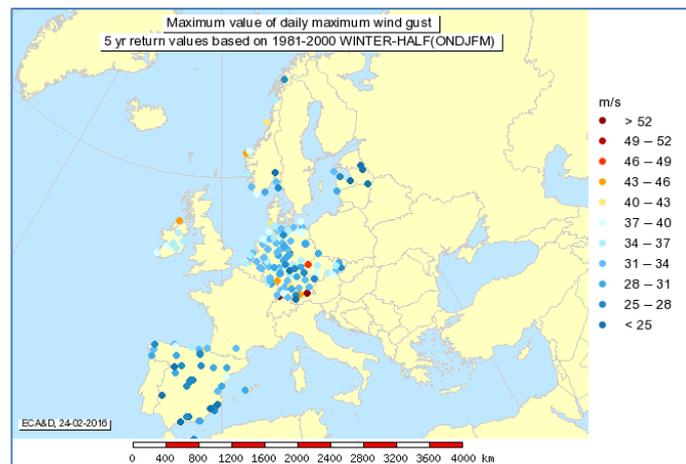

Fig. 4.3. 5-year return level of the highest maximum wind gust in the winter half year for the period 1980-2000, derived from the stations available in the European Climate Assessment Dataset (http://www.ecad.eu/returnvalues/index.php)

Fig. 4.3 shows, for example, the 5-year return level of the highest maximum wind gust in the winter half year for the period 1980-2000, derived from the stations available in the European Climate Assessment Dataset (http://www.ecad.eu/returnvalues/index.php). Most return levels lie between 25 and 35 m/s. However, only a few of the European countries are covered by the measurements.

In contrast to direct measurements, a reanalysis is a gridded dataset which is produced by combining models and observation data using data assimilation techniques in order to create a best estimate of the atmospheric state. Since wind speed measurements are usually not assimilated into the reanalysis system, however, wind speeds in reanalyses depend on the model and the parameterizations used to derive the wind speeds. One has to distinguish between different types of wind speeds produced by the model. First, there are the wind speeds on the original model grid at certain horizontal grid boxes on a certain model level. These wind speeds can be interpreted as values representing the average conditions within the area of the grid box. Wind speeds are usually analyzed in 10m height, which generally does not correspond to a certain model level. Thus, the instantaneous wind speeds are interpolated from the model levels to 10m height and written into output files at certain time intervals (usually every 3 or 6 hours). Also daily maximum wind speeds may be available. However, this is not the case for all reanalysis datasets. Additionally, daily maximum wind gusts may be provided, which are computed by gust parameterization schemes, which can take into account other parameter like the surface roughness or the stability of the atmospheric stratification. The use of these different types of wind speed information in different data sources makes it difficult to compare the different datasets.

Here, we used the 6-hourly wind speeds, which were available for three different reanalyses for the time period 1980-2010. Data from ERA-Interim, NCEP1 and JRA-55 went into the analysis. We estimated the 50-year return level for each reanalysis and calculated the mean and standard deviation of the three reanalyses (Fig. 4.4). The mean return level field shows large differences between land and ocean, with high values of up to 35 m/s in the North Atlantic and values of less than 22 m/s on land. The standard deviation between the different reanalyses gives indications about the uncertainty of the wind speeds in the reanalyses. The spatial structure of the standard deviations is very heterogeneous and no clear structure is evident. High values of 20% and more occur in for example in Italy and in Norway. Reasons for these differences between the reanalyses could be different measurements which went into the data assimilation process, or differences between the models used for the creation of the reanalyses. For example, if a different surface type of land cover was used in a certain area, this could also affect the 10m wind speeds.
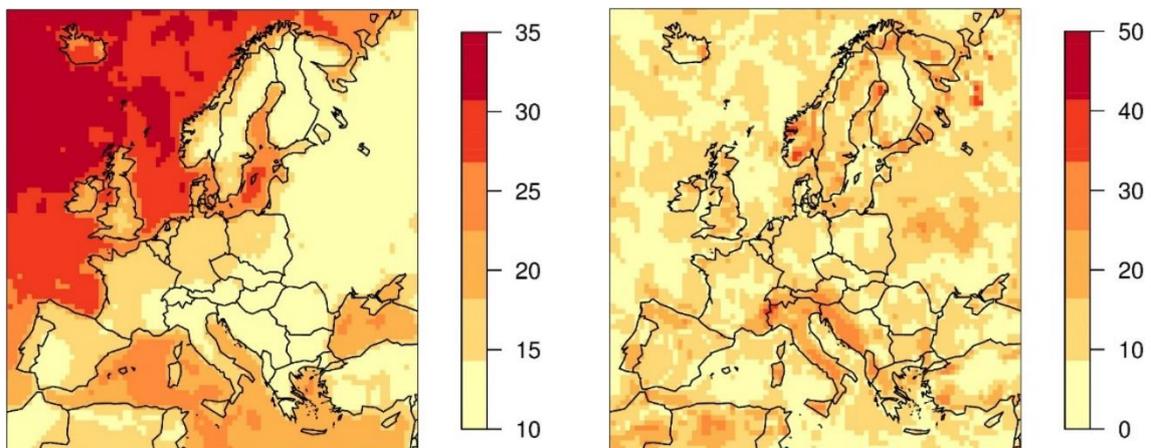
Fig. 4.4. (left) Mean and (right) standard deviation of the 50-year return levels derived from the instantaneous 6-hourly 10m wind speeds from the ERA-Interim, NCEP1 and JRA-55 reanalysis. The mean return level is in m/s and the standard deviation is in %, relative to the mean.

4.4   Climate predictions

To estimate the change of the occurrence probability of extreme wind speeds, we analysed a multi-model ensemble of different EURO-CORDEX simulations (See Section 3.3 for details). The multi-model ensemble consists of 29 different sets of simulations, each set containing an historical, an RCP 4.5 and an RCP 8.5 experiment. The 29 sets of simulations contain simulations with different regional climate models using different global models as lateral boundary forcing, as well as different model resolutions. 17 ensemble members cover the EUR-44 domain with a horizontal resolution of 0.44°. 12 ensemble members cover the EUR-11 domain, which is the same as EUR-44, but with a resolution of 0.11°. For each of the ensemble members, three different periods are analyzed: one in the historical run (1970-2000) and two in the future scenarios (2020-2050 and 2070-2100). While for the reanalysis data in the previous section only 6-hourly wind speeds were available, for the CORDEX simulations the variable with the best availability were daily maximum 10m wind speeds, which are subsequently used for the analysis.

The non-stationary block maxima approach described in 4.2.1 is used to estimate the GEV distribution of the maximum wind speeds that occurred in each winter half year (Oct.-Mar.) of the historical and future periods in each of the ensemble members separately. For the historical period the 50-year return levels are derived from the GEV distributions for each ensemble member and the ensemble means and standard deviations are calculated for each grid box. Before calculating the ensemble statistics, the return levels of the EUR-11 simulations are interpolated to the EUR-44 grid to allow a direct comparison.

The spatial structure of the ensemble mean 50-year return level in 1970-2000 agrees well with the 50-year return level fields derived from the reanalysis datasets (Fig. 4.5 top left). The pattern correlation between the CORDEX and reanalysis ensemble mean fields amounts to 0.94 using the Spearman method. Maximum values of 35 m/s are reached over the North Atlantic, while the values on land vary between 10 and 20 m/s. The return levels in CORDEX are on average 1.5 m/s higher than in the reanalysis. The EURO-CORDEX return levels are higher, because here daily maximum winds are used, while in the reanalysis case only instantaneous 6-hourly wind speeds were available. The latter underestimate the extreme winds because of sampling errors.

Windstorms

50-year return interval (0.02 exceedance probability) of wind speed 10 m above ground (m/s)
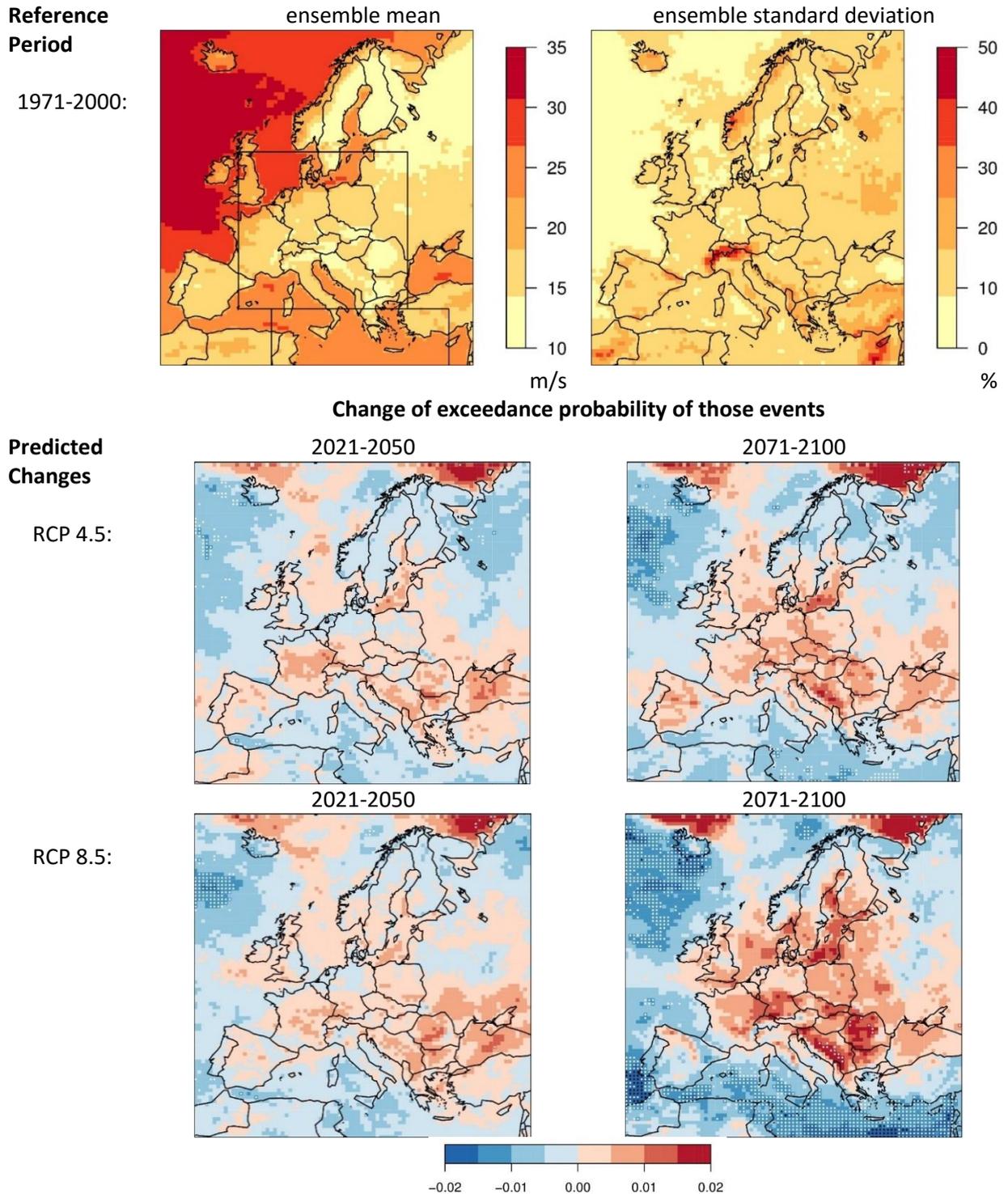

Fig. 4.5. 50-year return level of 10m wind speeds in present climate and the change of annual exceedance probability of the return level in different future scenarios and time periods. White (black) dots mark grid points, where the ensemble mean of the changes of probability is larger than one (two) ensemble standard deviations. Boxes mak regions for evaluation of tracking results (upper left).

The standard deviation between the 50-year return levels of the different EURO-CORDEX ensemble members (as a percentage relative to the ensemble mean) is lowest above the North Atlantic with less than 10% (Fig. 4.5, top right). Here the different models agree comparably well. On land the relative standard deviation is higher, mostly between 10 and 20%. Only in regions with complex topography like the Alps it increases up to 50%. Here the uncertainty of the models is highest.

Per definition, the probability that the 50-year return levels calculated for the historical period (1970-2000) is exceeded in a particular year is 0.02. Fig. 4.5 shows how the probability that the present day 50-year return level is exceeded changes in the early period 2020-2050 (left) and the late period 2070-2100 (right) in the two scenarios RCP 4.5 (middle) and RCP 8.5 (bottom). The change in probability is calculated for each ensemble member separately by using the non-stationary approach described in section 4.2.1. Afterwards, ensemble mean and standard deviation of the probability change is calculated for each grid box. A black dot is drawn in a grid box, if the ensemble mean of the change in probability is significantly different from 0 on the 0.95 level, according to a t-test.

The amplitude of the changes in probability is smallest in the early period of RCP 4.5 and largest in the late period of RCP 8.5. This is in agreement with the prescribed greenhouse gas concentrations in the different scenarios, which are lowest in the beginning of RCP 4.5 and highest at the end of RCP 8.5. In general, increasing probabilities are evident in the center of the domain, in particular Central and Eastern Europe. In the late period of RCP 8.5 the probability increases by 0.02 in southern Germany and parts of the Balkan region. That represents a doubling of the present day occurrence probability.

Negative changes in probability occur mainly over the oceans, in particular in the North Atlantic and the Mediterranean region. In the Mediterranean, these changes are in large areas not significant in the early periods of the two RCP scenarios, but become significant in the late periods.

The spatial pattern of the probability changes, which are observed for the 50-year return level, are found in a similar way also for other return level, e.g. the 5-year return level (not shown). Areas of positive changes are found within Europe and negative changes are found over the ocean.

The multi-model ensemble which is analyzed here consists of simulations with two different horizontal resolutions (0.11° and 0.44°). Furthermore, the ensemble is dominated by simulations with the model RCA4. To find out if the specific combination of the ensemble members has a large effect on the results, sub-ensembles have been evaluated (not shown). If only EUR-11 simulations are compared to only EUR-44, the 50-year return level in the historical period is on average 1.2 m/s higher in the EUR-11 ensemble, which is due to the higher resolution. However, the spatial structure of the future changes remains similar to the full ensemble, with positive changes on the European continent and negative changes over the oceans. The amplitude of the changes is not as pronounced in the EUR-11 ensemble as in the EUR-44 ensemble. If all RCA4 simulations are removed from the full ensemble, the characteristics of spatial patterns do not change significantly.

The results found in this study are in line with previously published work. Rockel and Woth (2007) find a positive change of the number of gusts of more than 8 Bft on the European continent in the

future climate in two RCMs. A similar but more heterogeneous pattern was found in the 95th percentile of the daily maximum wind speeds in another RCM by Leckebusch and Ulbrich (2004). Positive wind speed changes are explained by a southward shift of cyclone paths. Positive changes of the 90th percentile in Central Europe were also reported by Beniston et al. (2007). They could confirm findings from Zwiers and Kharin (1998), who suggested that these increases in wind speeds in Europe are related to a negative pressure anomaly over Northern Europe, which develops under higher CO_2 concentrations. This pressure anomaly then leads to an increased pressure gradient and increasing wind speeds in Central Europe.

In this study we could confirm previous findings. However, in previous studies only single simulations or small ensembles were analyzed, which made it difficult to test the robustness of the climate change signals. In this study, the analysis of the extensive set of ensemble members was able to show that a large uncertainty lies in the climate change signals in most of continental Europe,
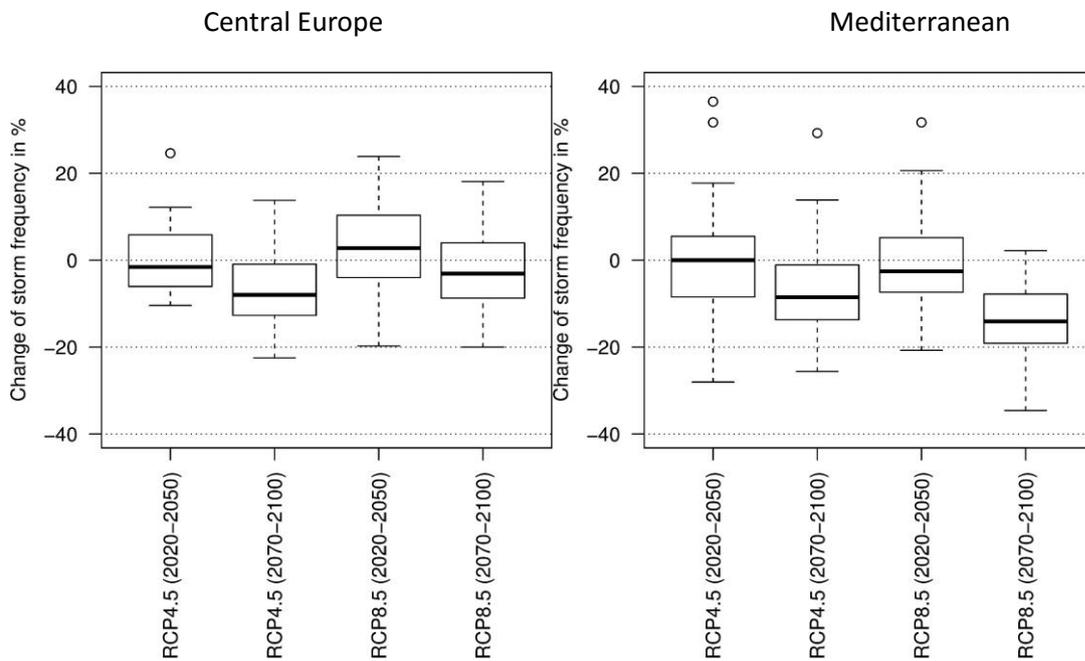
Fig. 4.6. Relative changes of numbers of windstorms that exceed the local 50-year return level in the Central European box (left) and the Mediterranean box (right) in different scenarios and different time periods compared to the historical runs (1970-2000). The boxplots show the distribution of all 29 CORDEX ensemble members. The boxes are defined in Fig. 4.5 (upper left).

since the standard deviation between the ensemble members are high compared to the signal. However, it should be noted that the applied method to test the significance by exceedance of the standard deviation is a rather restrictive criterion. If, for example, a one sample t-test is used to test for significant deviation of the ensemble mean from zero, also the increasing probabilities found on the European land areas are regarded as statistically significant.

The tracking algorithm described in Section 4.2.2 is applied to the different EURO-CORDEX experiments and tracks of windstorms are identified in the historical and future scenarios, which exceed the 50-year return level of the historical time period. The number of windstorms that pass

through two different regions is counted. The regions are marked in Fig. 4.5 (upper left). One region covers large parts of the European land area, where positive changes in occurrence frequency were detected. The other region covers the Mediterranean area, where negative changes were found.

In the Central European box, the climate change signals do not point in a clear direction (Fig. 4.6 left). In the early periods of both RCP scenarios the medians of the distributions are close to zero. The largest signal is evident in the late period of RCP 4.5. Here, the number of windstorms decreases by about 8 %. The signal in RCP 8.5 is only half as large.

In the Mediterranean box, the percentual change of windstorm numbers is small in the early periods of both RCP scenarios (Fig. 4.6 right). The largest signal of -13 % is found in the late period of RCP 8.5. This is in line with the results from the return level occurrence probabilities, which decrease in this area. However, the negative windstorm changes in the Central Europe box are contradictory to the positive changes of return level occurrence probabilities in this area. The changes could be explained if there are many smaller windstorms in the historical period, which exceed the 50-year return level only at single grid points, but a lower number of windstorms in the later scenarios, which exceed the return level at many grid points. Thus, in the future periods, fewer storms would lead to a larger number of threshold exceedances. However, to study this effect, a more detailed analysis of the tracking results is required.

5. Heavy precipitation

Katrin Nissen (Freie Universität Berlin)

5.1 Introduction

Heavy precipitation poses a major threat to critical infrastructure. Land-based transportation and emergency services are especially vulnerable to such events, as they can lead to the flooding of tunnels and can damage streets, railway lines and bridges (see e.g. Fig. 5.1). This makes it in turn difficult for emergency rescue services to reach people in need for help. The electricity and telecommunication networks are less often affected by heavy precipitation. At times, however, flooding of electric transformer stations causes power outages. The nature of the precipitation events that can be of risk covers a wide range of scales both in space and time. Apart from the direct effect of local flooding, heavy precipitation can trigger secondary effects such as river floods, landslides and mudslides.

Fig. 5.1. Online news report on a heavy precipitation event affecting the island of Sardinia in Novemver 2013 (BBC 2013).

5.2 Method

Rainfall is highly variable in terms of spatial extent, duration and intensity. Both small-scale and large-scale events can impact infrastructure. In addition, both short-duration rain spells of high intensity and long lasting rainfall of moderate intensity, which can accumulate to damaging amounts of water, have to be considered. To take these characteristics of rainfall into account, an

identification tool for heavy precipitation which detects events of various duration and spatial extent is developed here. All events exceeding a predetermined critical threshold are identified.

5.2.1   Critical threshold

Two surveys have been performed for the project, aimed at determining the threshold at which damage to infrastructure elements may occur. 28 infrastructure providers from the fields of energy, telecommunication, land transport (streets and rail) and emergency rescue services have been interviewed as well as 18 national and private weather services (RAIN report D2.3). As expected, there is no universal critical value relevant for all types of infrastructure and all areas within Europe. For some providers, the amount of precipitation is more important and for others the intensity. The rainfall intensity of extreme precipitation events occurring at a given return interval increases with decreasing   duration   (
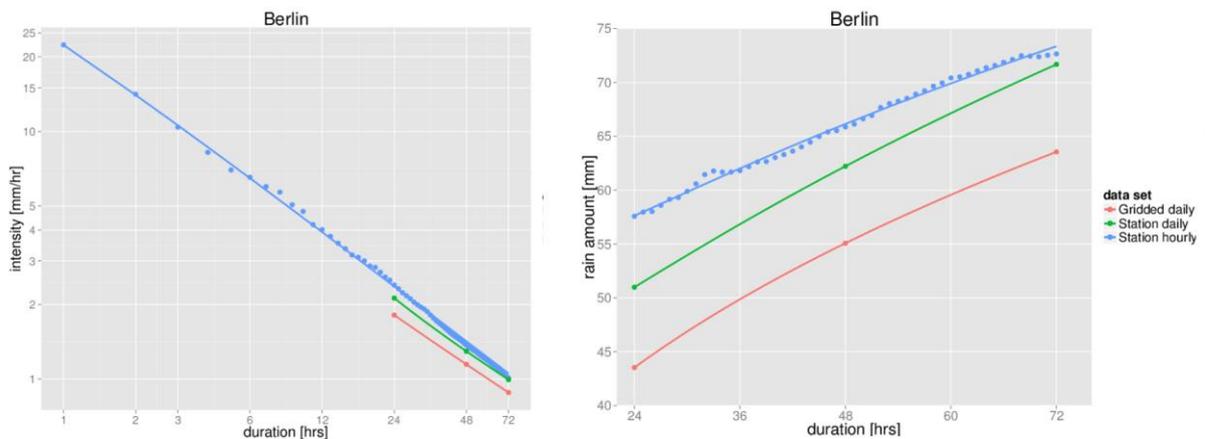
Fig. 5.2), while the accumulated amount increases with increasing duration. The thresholds mentioned in the questionnaires range between 20 mm/hour and 30 mm/hour for high intensity events and between 50 mm/day and 100 mm/day for events with high water accumulation.
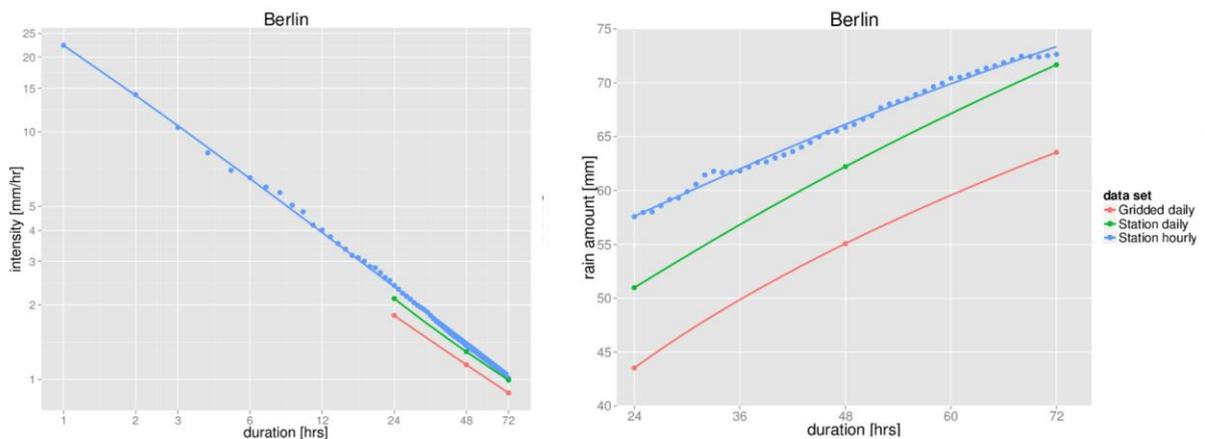
Fig. 5.2. Intensity (left) and amount (right) exceeded on average once every 10-years. Blue: Values determined from station data at Berlin with an hourly temporal resolution, Green: Values determined from station data at Berlin with a daily temporal resolution, Red: Values determined from the grid point in the observational E-OBS data set, that is closest to Berlin.

It is important to note that the area mean values from gridded data sets, such as the ones analysed in the RAIN project, differ from the point values that affect an infrastructure element. Göber et al.

(2008), for example, show that the maximum precipitation value in mm/day at a point within a 40 km x 40 km grid box can be almost twice as high as the grid-box mean value. An additional factor that reduces the recorded extreme precipitation amounts in the data sets is the temporal resolution of the data (usually daily resolution): The rainfall amount associated with a strong 24-hour event will probably not all fall within the same data aggregation period, but will contribute to the rain amount accumulated on two consecutive days. This effect is illustrated in
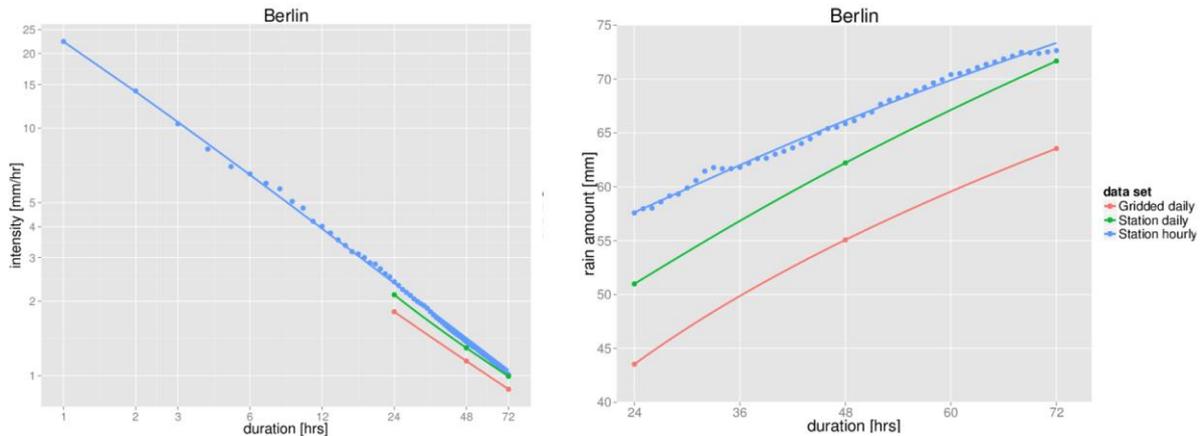
Fig. 5.2. The difference between the blue and the green curve is due the data set's different temporal resolutions, while the difference between the green and the red curve can be attributed to the gridding process. As a consequence, using the absolute thresholds suggested by the infrastructure providers for a gridded data set would lead to a severe underestimation of the number of detected events. Therefore, it was decided not to use a fixed value threshold for this study. Instead, this study will use local return values for a given return period as thresholds for extreme events (i.e. the amount of rain per time unit on average exceeded every n years). This approach is consistent with engineering practice and legislation. Drainage systems for components of critical infrastructure networks are usually designed to be able to cope with a certain amount of water per time unit. This amount, which is also called the "design rainfall", is specified in terms of local return values. The International Union for Railways, for example, recommends to use 10-year return values. Using the "design rainfall" as a threshold for the detection of relevant precipitation events seems reasonable, as one can assume that only precipitation which exceeds the drainage capacity can be harmful for the infrastructure component. The resulting thresholds are relative values which depend on the spatial resolution and on the climatology of the data set and are thus calculated separately for each data set.

For this study, the 10-year return values have been used as a threshold for the detection of infrastructure threatening events as this threshold is consistent with legislation. In addition, for flat terrain stations over continental Europe, these values fit well to the thresholds the interviewed infrastructure providers found relevant (
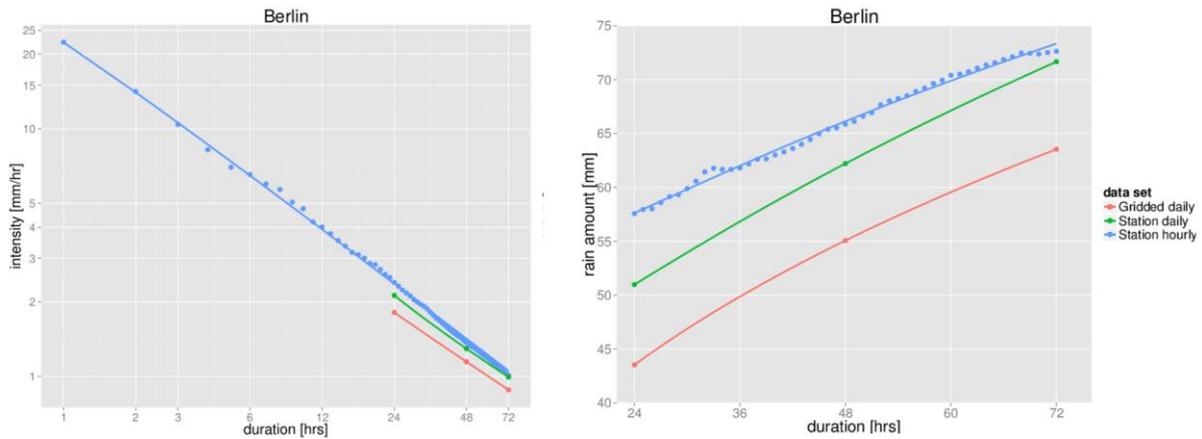
Fig. 5.2).

The return values are estimated using the Peak Over Threshold (POT) method (e.g. Coles et al. 2001). To ensure consistency of the return values for events of different durations, intensity-duration-frequency (IDF) curves are fitted to the resulting return values following the recommendations of the World Meteorological Organization (WMO, 2009).
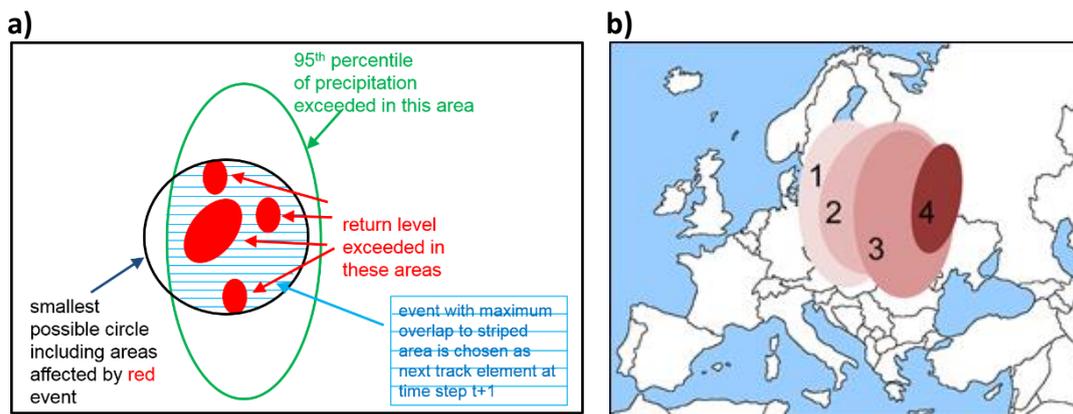

Fig. 5.3. Schematic illustration of the detection scheme; a) illustration of the areas used for event detection described in the text, b) illustration of event tracking, where the numbers denote consecutive time steps and the shaded areas correspond to the striped area in panel a.

5.2.2   Detection of heavy precipitation events

The detection algorithm developed for this study identifies heavy precipitation events of various durations and spatial extents in gridded data sets. The approach is based on a method that has originally been developed for the detection of windstorms (Leckebusch et al. 2008). The method was extended for the RAIN project to account for the special characteristics of heavy precipitation, in particular for the fact that rain accumulates over time.
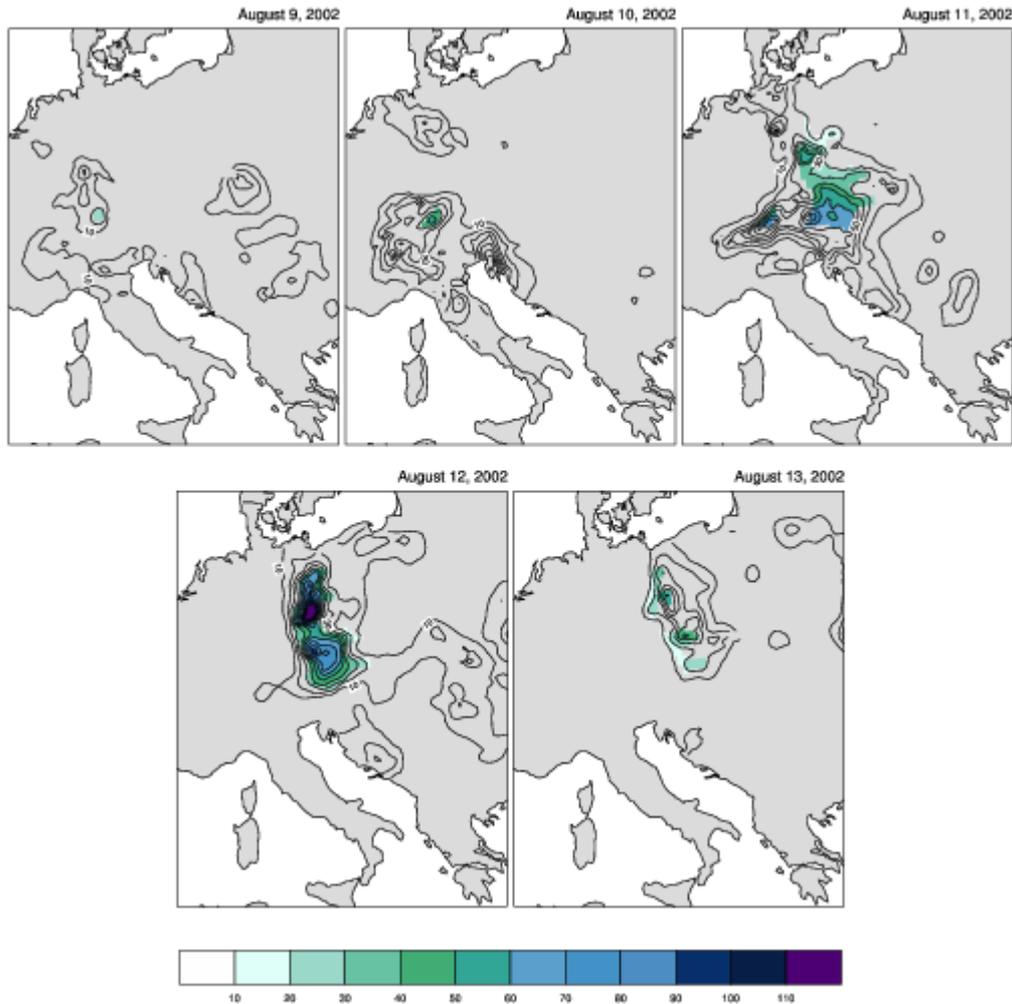
Fig. 5.4. Precipitation per day for the period August 9 2002 to August 13 2002 based on the E-OBS data set. Contour lines show precipitation amounts on that day. Color denotes grid boxes attributed to the detected event (exceedance of the local 10-year return levels). Units mm.

In a first step the algorithm identifies all grid boxes in which the rainfall exceeds the critical threshold (i.e. 10-year return value). All identified grid boxes which are located within the same continuous area with considerable precipitation (>95th percentile) are considered as belonging to the same event and form a cluster. This is illustrated in Fig. 5.3a, where areas with precipitation exceeding the threshold are shown in red. As all red areas are located within the same area of substantial rain, outlined by the green ellipse, they are considered to belong to the same cluster. For each identified cluster an envelope is defined. The envelope (hatched area) is determined by the overlap of the area of the smallest possible circle including all exceedance areas (black outline) and the area where the rainfall amounts exceed the 95th percentile (green outline). The clusters are then tracked in time. The cluster at time step t+1 is considered as the next track element which exhibits the largest overlap to the area within the envelope (Fig. 5.3b). Each detected event can consist of several grid boxes and can last for several time steps.

A precipitation severity index (PSI) is assigned to all events. It is calculated only from grid boxes and time steps where the threshold was exceeded and is defined as follows:

$$PSI = \sum_{t}^{T} \sum_{k}^{K} \frac{precip_{k,t}}{annualprecip_{k}} * A_k ,$$

where T is the duration of the event, K is the number of affected grid boxes and A_k is the area of grid box k. Thus, the severity index takes the affected area and the amount of precipitation accumulated over the duration of the event into account. It is normalized by the long-term mean annual precipitation sum expected for the grid box. The severity index can be used to compare the strength of the identified events. The detection algorithm also stores additional information for each event, such as the date, location, affected area, duration and maximum precipitation.

In order to distinguish between the two types of relevant events (high intensity events and events with high accumulated rain amounts), the detection algorithm is applied twice. For the detection of events with high accumulated rain amounts, thresholds for 3 different aggregation periods are considered (1, 2 and 3 days). Here, daily data is used, which is available for all model simulations. Events with high intensities are detected using 3-hourly values, which is the highest temporal resolution for which data for at least some of the model simulations is available.

An example for a detected event is shown is Fig. 5.4. In August 2002 record-breaking rainfall amounts and intensities occurred in Central Europe. They resulted in a large-scale flooding event (e.g. Ulbrich et al. 2003). The heavy-precipitation event detection algorithm identifies the event as shown in Fig. 5.4. Displayed is the 5-day sequence between the 9th and the 13th of August 2002. Shading denotes areas were the 10-year return levels were exceeded. These areas and time steps are attributed to the event. The severity index PSI for this event is 50, which corresponds to the 99th percentile of the PSI for all detected events.

5.3 Present climate

From the choice of the thresholds used for detecting precipitation events in this study (see Section 5.2), it follows that the annual probability of occurrence of an event with a specific duration is 0.1 (i.e. once every 10 years) at each grid box. In this section, the spatial distribution of the return values associated with this probability threshold is shown. For precipitation accumulated over 1-3 days, which is relevant for events with high precipitation amounts, the return values for the present day climate were calculated from the E-OBS data set (see Section 3.1, Meteorological observations). As there is no purely observational data set available with sub-daily precipitation data, 3-hourly 10-year return values had to be calculated from reanalysis data (ERA-Interim) downscaled with the two regional models RACMO22E and RCA4.
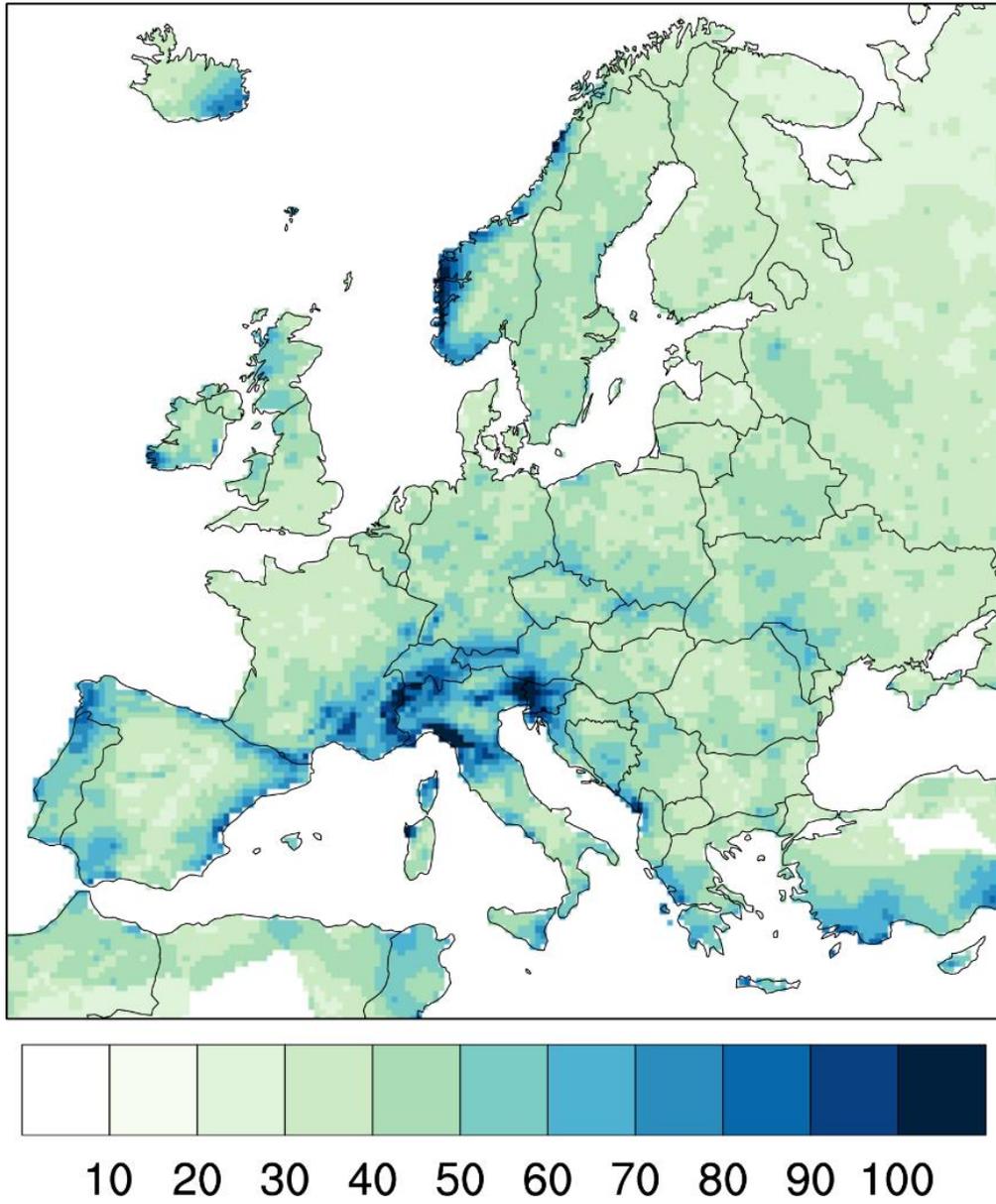
Fig. 5.5. 10-year return level of daily precipitation (mm). Data from E-OBS data set for the period 1981-2010.
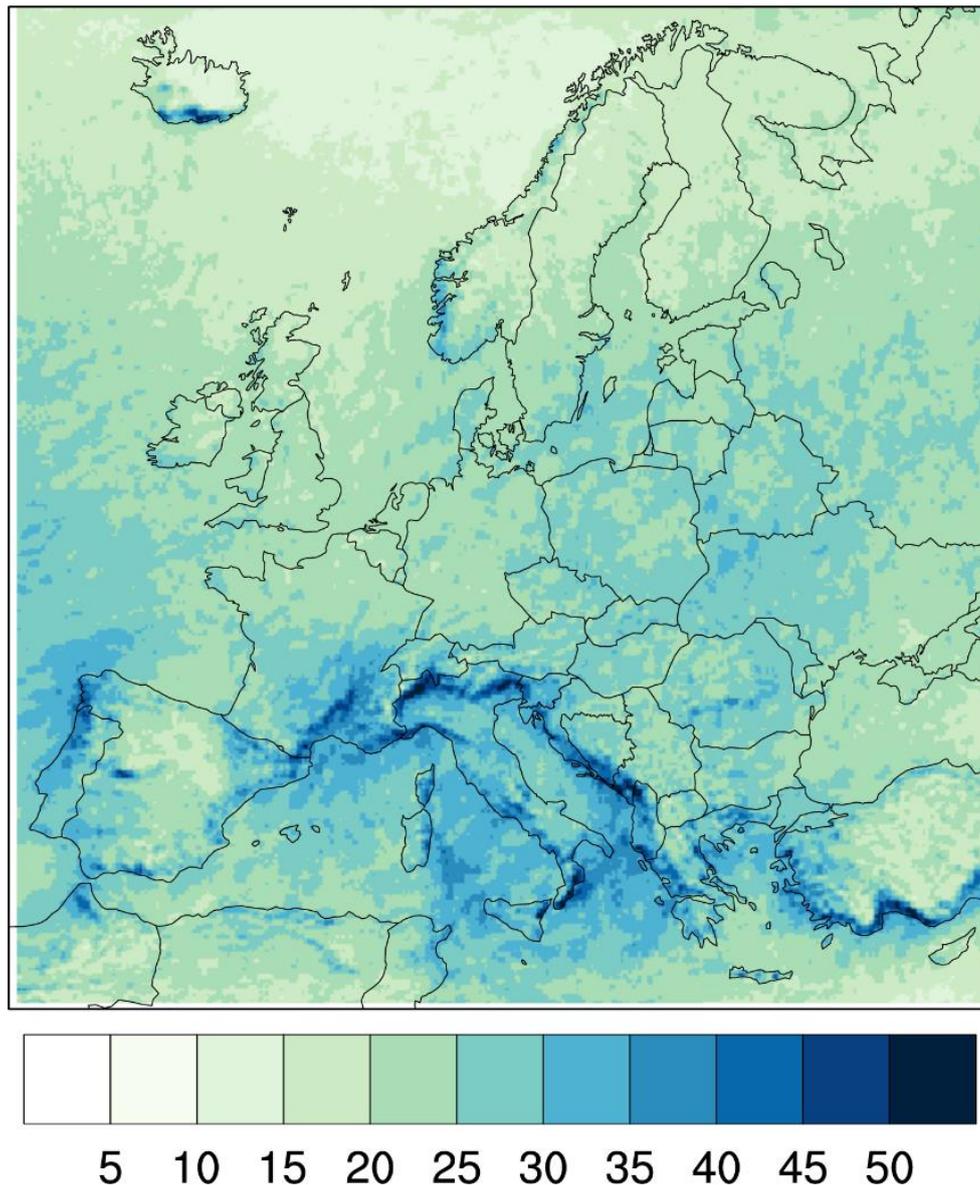
Fig. 5.6. 10-year return level of 3-hourly precipitation. Data from ERA-Interim for the period 1981-2010 downscaled by the two regional models RCA4 and RACMO22E. Shown is the ensemble mean of the two simulations. Units mm/3 hours.

5.3.1 High accumulated precipitation amounts

A map of the 10-year return level for 24-hour rainfall over Europe based on the gridded observational E-OBS data set is shown in Fig. 5.5. In general, return levels are higher over elevated regions, such as the Alps, as precipitation is often triggered by orographic lifting. Especially high return levels are also present at the western Norwegian coast. The general flow as well as the passage of mid-latitude cyclones are mostly directed from west to east. The western coasts of the continents and the western flanks of mountainous regions are therefore especially prone to precipitation, which is reflected in the return levels. In the Mediterranean region, cyclones coming from the sea can transport humid air masses. Here, the regions bordering on the coast show the highest return levels. As stated before, the values in this gridded data set are lower than the extremes actually occurring at a site (e.g. 25% for Berlin,
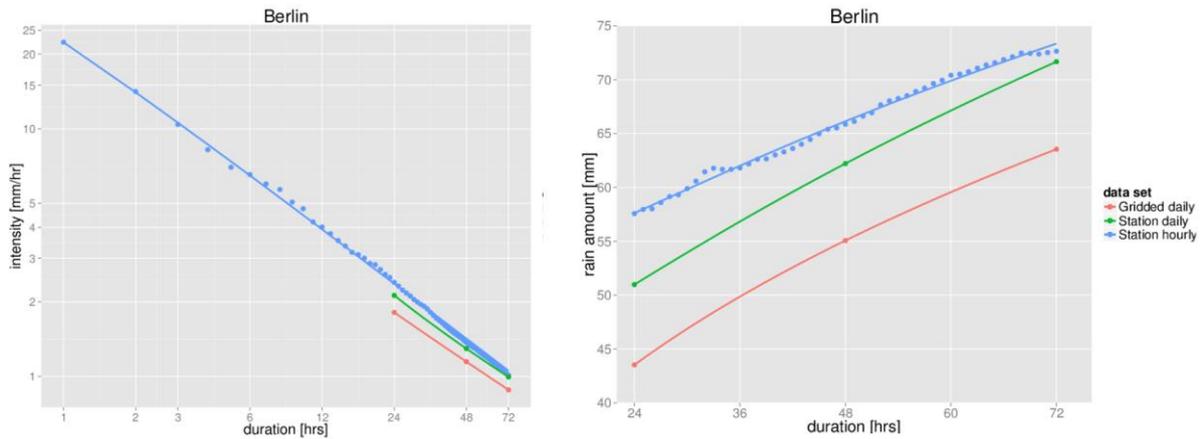
Fig. 5.2). 10-year return values for precipitation accumulated over 48 and 72 hours are not shown here as they exhibit a similar spatial distribution only with somewhat higher return values. High precipitation intensities

The distribution for sub-daily events with high intensities, which are often of convective nature, slightly differs from that for high precipitation amounts. The North-South gradient is more pronounced with higher values occurring at more southerly latitudes (Fig. 5.6). This is caused by the fact that convective precipitation is often thermodynamically induced, a process requiring relatively high surface temperatures. The highest return values are found in the vicinity of the Mediterranean Sea. Orographic effects again play a role. Mountains and coastlines can induce orographic lifting and exhibit higher return values.

5.4   Climate predictions

The climate change signal was calculated from a multi-model ensemble of EURO-CORDEX simulations with a horizontal resolution of approximately 12 km (0.11°), so called EUR-11 simulations. 0.11° is the highest horizontal resolution available within the EURO-CORDEX framework and was chosen to minimize the effects the resolution has on the strength of the precipitation events (cf. Section 5.2). The ensemble includes a total number of 10 model combinations for which data at a daily temporal resolution were available (Rd in Table 3-2). These simulations were analysed to evaluate long-lasting precipitation events with high accumulated rain amounts. For the analysis of high-intensity, sub-daily events, 6 model combination were available, dominated by RCA4 as the regional component (R3 in Table 3-2.

To investigate the climate change signal, the detection algorithm for heavy precipitation events was applied to all available climate change simulations. The number of events exceeding the thresholds was determined for each simulation at each grid box. Please note that the number of events may be different than the number of affected days, as an event may last for several days.

The difference between the number of detected events occurring in the historical period and the number of events in an equally-long period of a scenario simulation was determined for the multi-model ensemble. The result was tested both for statistical significance and for consistency between the model simulations. This was done in two steps. In the first step, each model was tested independently using a Monte-Carlo technique. The detected events were randomly redistributed

between the two periods (historical and scenario) and the difference between the two periods was determined. This process was repeated 1000 times. If the observed difference between the two periods exceeded the randomly obtained difference in 90% of the cases, the change is significant at the 90%-level.

According to IPCC recommendations (Mastrandrea et al. 2010) a hypothesis can be considered as "very likely" at a statistical significance level of 90%. The test was applied to neighbouring groups of 9 grid boxes and the result was assigned to the central box. Including neighbouring boxes increases the sample size and rewards regions which show a consistent signal. The second step of the testing process is meant to ensure consistency between the model simulations. Only those grid boxes at which 90% of the simulations show a statistically significant signal of the same sign pass the test. Grid boxes passing both tests are marked by black dots in the following figures.

Multi-day precipitation

10-year return value for 24 hours
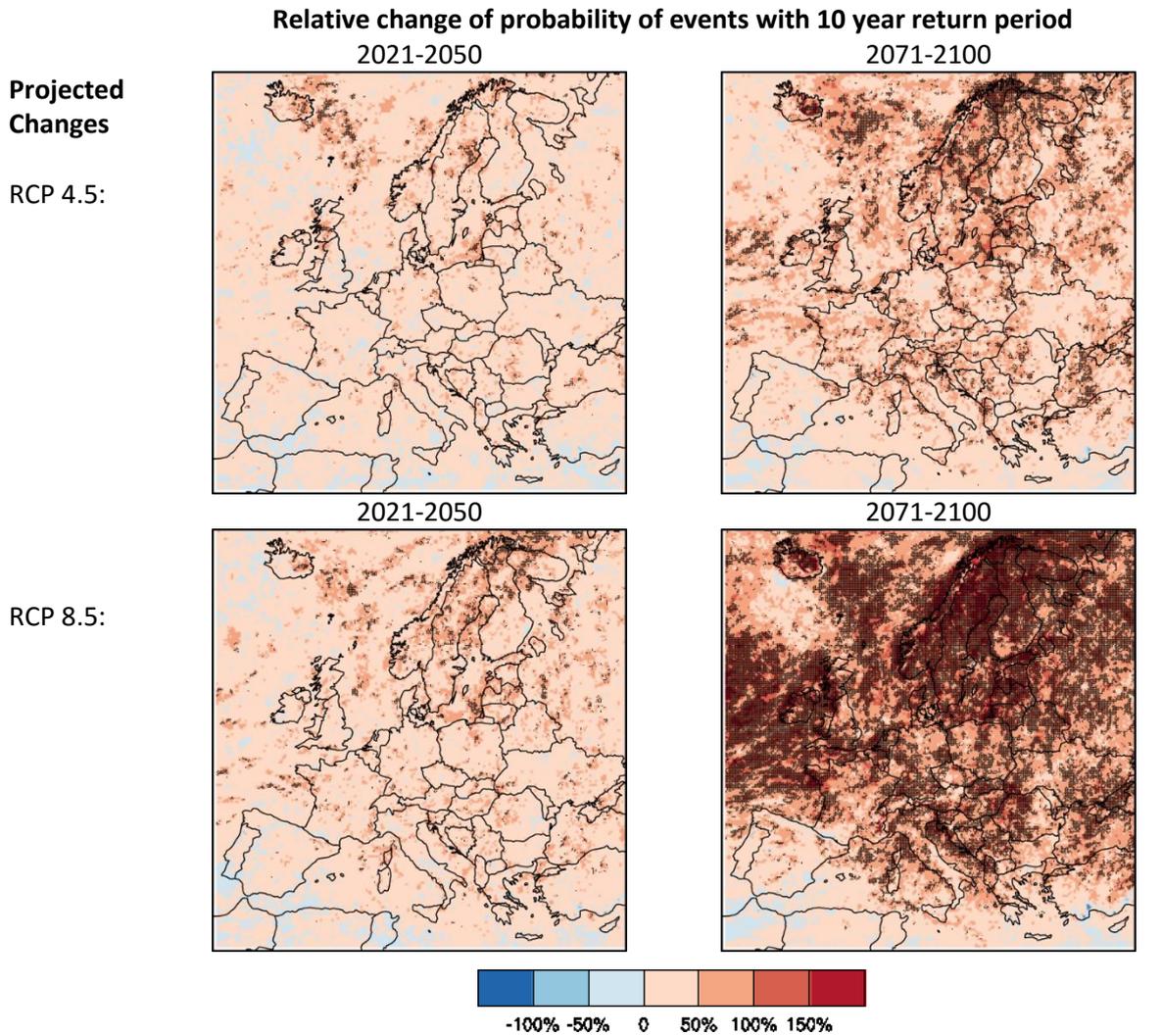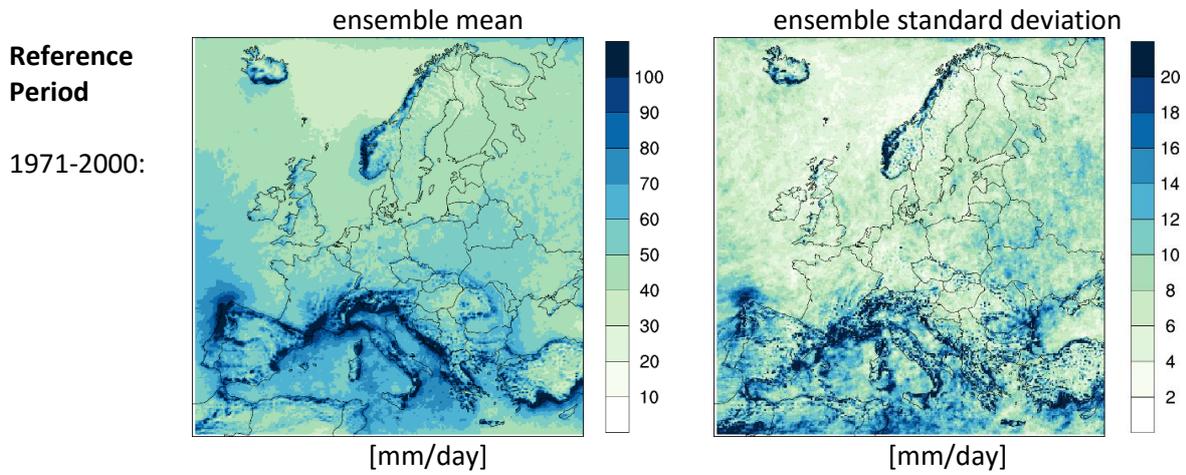
Fig. 5.7. Top row: 10-year return value for daily precipitation in the historical simulation (1971-2000). 48-hours and 72 hours are not shown. Other panels: Change in the occurence probability for heavy precipitation events between the historical period and the scenario simulations. Ensemble mean detected using daily data.

5.4.1 Changes in high accumulated precipitation amounts

Comparing the present-day 10-year 1-3 day return values of the observations (here only shown for 24-hour accumulation; Fig. 5.5) with the modelled ones (Fig. 5.7, top row) reveals that the multi-model ensemble captures the main features of the observed spatial distribution. As expected, the return values are higher for the data set with the higher horizontal resolution (i. e. the simulations). Some additional differences can be noted especially at the Mediterranean coastline, which exhibits proportionally too high return values in the simulations.

The climate change simulations suggest that the number of heavy precipitation events with high accumulated rain amounts increases with increasing greenhouse gas concentrations (Fig. 5.7 middle and lower row). The highest increases can be found for Northern Scandinavia, Western Ireland and Western Scotland. By the end of the century and under RCP 8.5 conditions infrastructure elements in these regions may be affected by potentially damaging long-lasting precipitation events once every 4-5 years, where they were affected only once every 10-years during the recent past. In Central Europe the frequency may increase to once every 5-7 years. The lowest increase was simulated for the Western Mediterranean region.
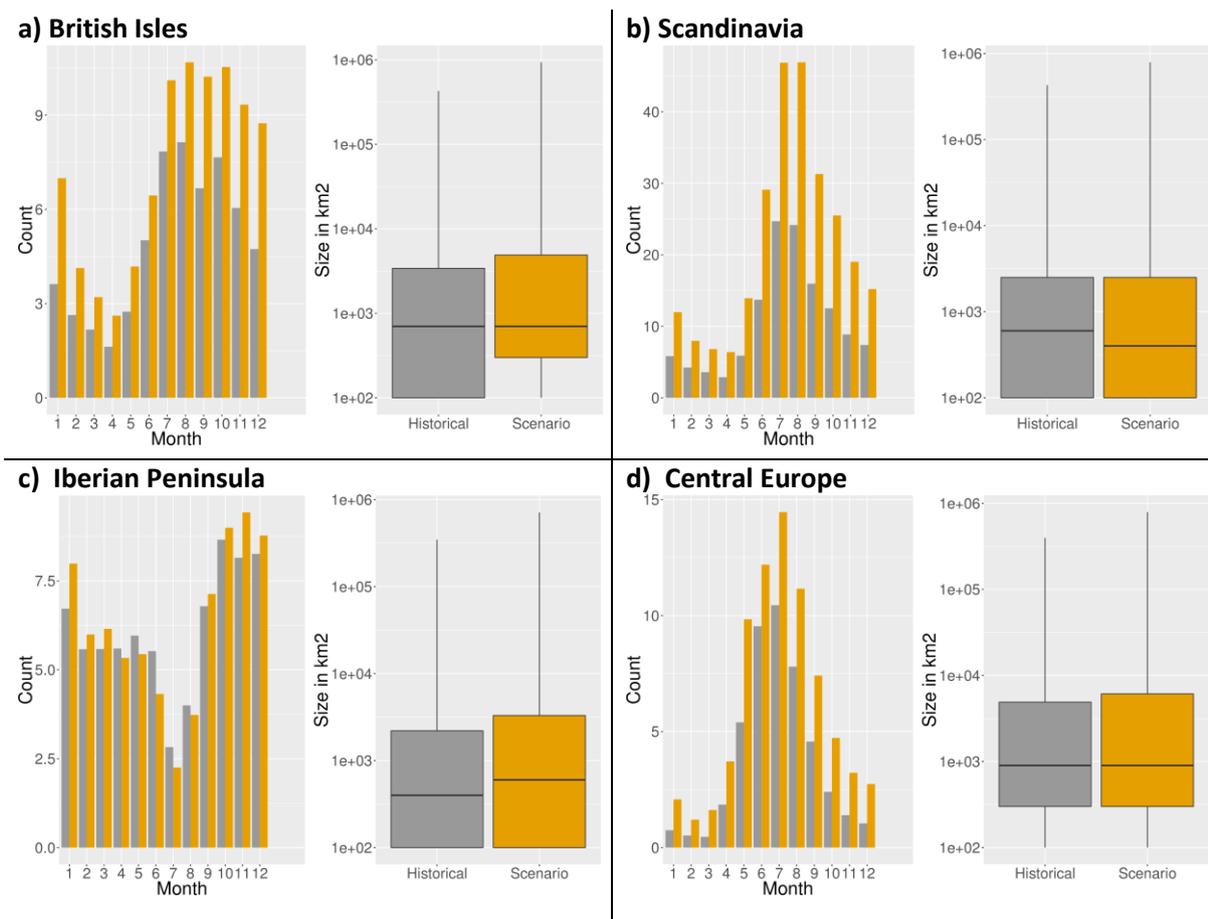
Fig. 5.8. Seasonal cycle and size distribution of detected heavy precipitation events in 4 different regions. The ensemble mean for the historical simulation (grey) and the RCP 8.5 scenario simulation for the period 2071-2100 (yellow) are shown. Included are only events detected using daily rainfall data (with high precipitation amounts). The box plots show the median, 25th and 75th percentile and the whiskers span the range from the smallest to the largest event.

For the first half of the century the simulations predict a modest uniform increase for both emission scenarios, mostly staying below 1 event in 20 years (probability change of 50%).

During the first half of the 21st century, only a few grid-boxes pass the strict 2-step test for statistical significance and consistency. The ensemble mean shows a steady increase in event numbers throughout Europe over time and with increasing emissions, suggesting a robust relationship between greenhouse gas concentrations and heavy precipitation events. This is reflected in the size of the area where the signal is statistical significant, which also increases with time and emission levels.

The characteristics of heavy precipitation events, such as the seasonal cycle and the area affected by individual events, differ considerably for different European regions (Fig. 5.8). Over the Iberian Peninsula, the heaviest precipitation events occur during autumn. The climate change simulations suggest a slight increase in the number of heavy precipitation events during this season for increasing greenhouse gas concentrations, while the number of events during summer decreases.

The area affected by events detected over the Iberian Peninsula is rather small compared to other European regions. Scandinavia, the British Isles and Central Europe exhibit a different seasonal cycle with the highest number of heavy precipitation events occurring during summer.

The number of detected events increases under climate change conditions during all seasons. Over Britain and Ireland, the climate change signal indicates that in future periods the summer season maximum may start to extend well into autumn. For this region, the lowest increase is found for spring.

The annual cycle of the climate change signal suggests that an increase of the sea surface temperatures (SSTs) in the North Atlantic may be responsible for the increase in the number of heavy precipitation events in this region. The ocean remains comparably warm well into the winter season leading to enhanced evaporation. This in turn increases the water supply available for precipitation. The effect decreases when the ocean is at its coldest at the end of the winter season. In addition, the simulations in this region suggest that the area affected by individual events may increase in the future.

Central Europe shows an increase for the number of events for all seasons, which in terms of percentage change is highest during winter. This suggests an increase in winter temperatures under climate change conditions. The highest and most homogeneous percentage increase can be found for Scandinavia. The number of events almost doubles in all seasons.

In terms of severity, the strongest events occur in the climate change simulations, even though the median of the PSI remains unchanged or even decreases in some regions (not shown). No pronounced changes in event duration could be detected anywhere within Europe (not shown).
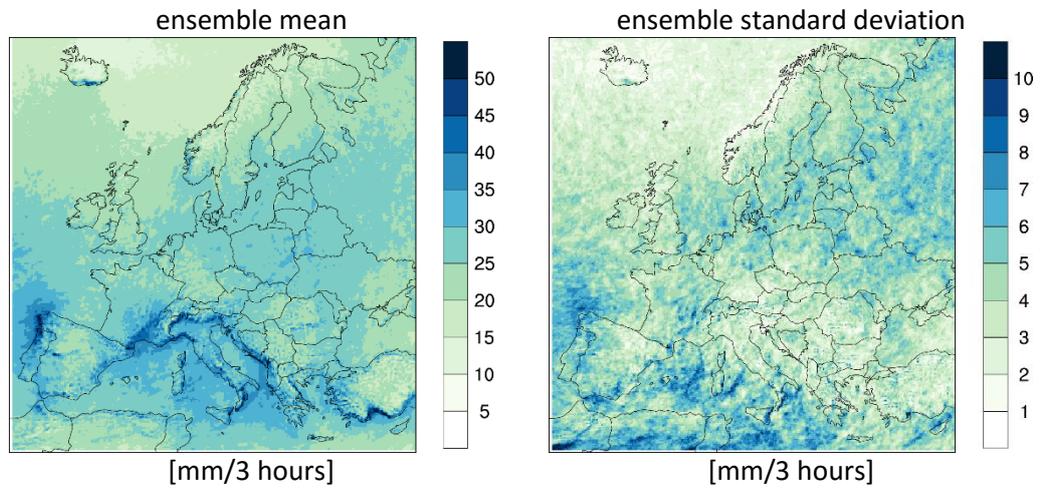
5.4.2 Changes in high (3 hourly) precipitation intensity

The 3-hourly 10-day return values downscaled from reanalysis data (Fig. 5.6) and the present-day simulations (Fig. 5.9, top row) agree well with each other. It should, however, be noted that no

3-hourly precipitation

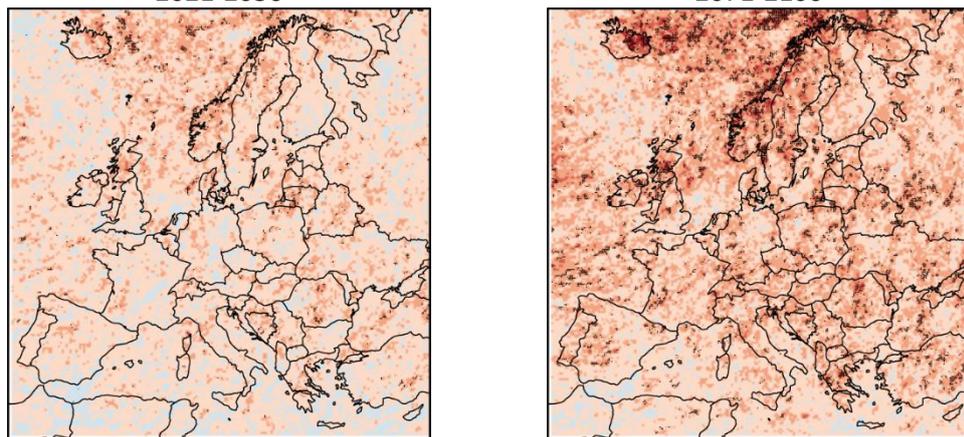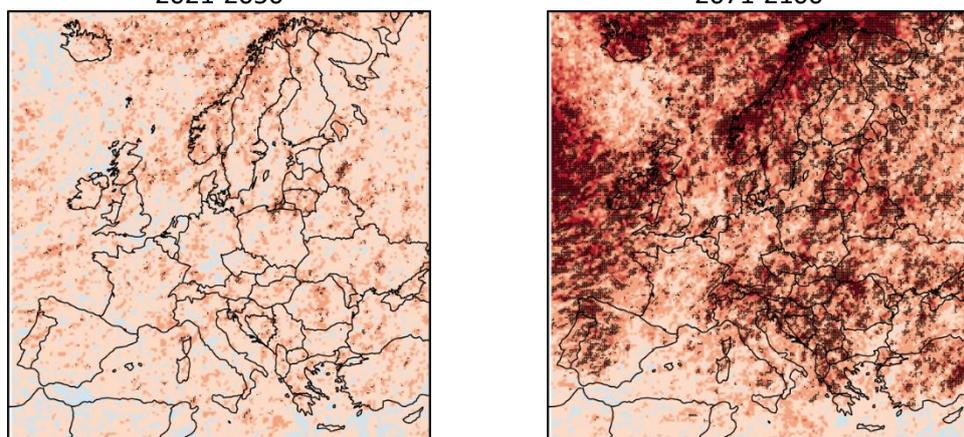**10-year return value of 3-hourly precipitation**

Fig. 5.9: As Fig. 5.7, but for events detected using 3-hourly data. Please note the different colour scale.
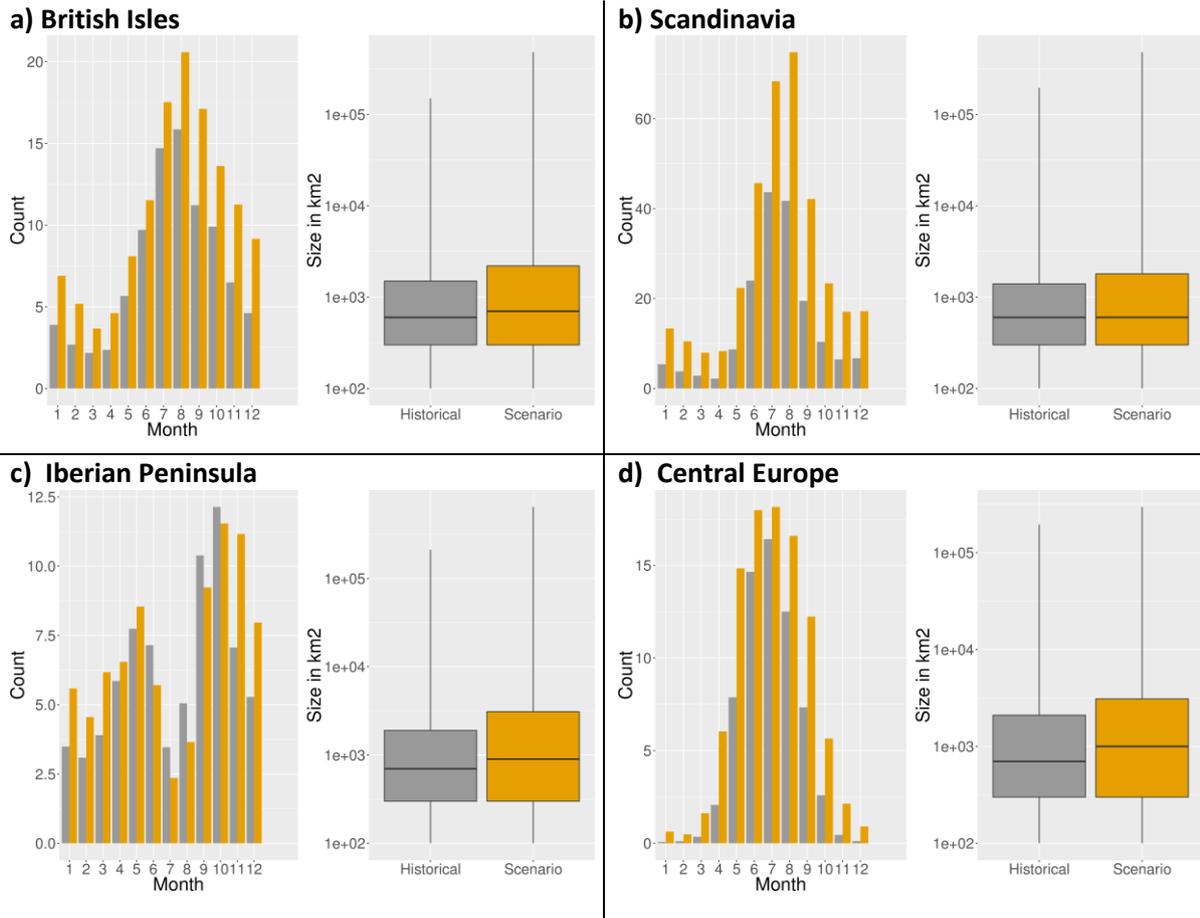
Fig. 5.10: As Fig. 5.8, but for sub-daily high intensity events detected using the 3-hourly data .

independent observational data set was available at this time resolution and the calculations were based on the output of the same two regional models.

The increase in the number of detected events under climate change conditions is approximately two times larger for sub-daily events than for long-lasting events (Fig. 5.9). Please note that the colour scales are different to those in Fig. 5.7. The regions showing the highest increase in high-intensity events are similar to those detected for long-lasting events: Northern Scandinavia and the western coasts of the British Isles. Here, the occurrence probability for a high-intensity precipitation event increases in some grid boxes from once every 10 years by more than 300% to once every 2-3 years. In the Western Mediterranean the increase is similar to the increase simulated for France and Germany (approximately 100%).

The increase in the number of sub-daily convective events is pronounced for all regions and seasons, with the exception of the Western Mediterranean region during summer (Fig. 5.10). The simulations suggest that Central Europe will start to see high-intensity precipitation events during winter, which were almost non-existent during the historical period. This result is probably related to an increase in simulated winter surface temperatures. The results found in this study are in good agreement with other studies reported in the literature, which also suggest that increasing greenhouse gas concentrations will probably lead to an increase in extreme precipitation, which is associated with an

increase in air temperatures (e.g. IPCC 2007). Proportionately more precipitation is expected per precipitation event over most regions for future climate periods. This can be explained by the fact that with increasing surface temperatures, the moisture-holding capacity of the atmosphere increases. When sufficient moisture is available, precipitation extremes are expected to increase by 6%–7% °C^{-1} according to the Clausius–Clapeyron relation.

6. Coastal floods

Dominik Paprotny and Oswaldo Morales Nápoles (TU Delft)

6.1   Introduction

The main weather-related hazard in seaside areas is an increase of water levels caused by windstorms, which may result in breaching of coastal defences and flooding. Though storm surges rarely cause such an outcome, the consequences are often disastrous when they occur. Indeed, Barredo's (2007) list of large floods in Europe for 1950–2005 includes only three coastal floods compared to 44 river and flash floods; yet, ranked by number of casualties, storm surges come first, third and sixth. The biggest was the 1953 North Sea flood, which caused over 2,000 casualties in the Netherlands and Belgium. That storm surge also resulted in 546 deaths in the United Kingdom, while the 1962 Hamburg flood killed 347 persons. The most recent large coastal flood occurred in 2010 in western France, with a death toll of 41 (Lumbroso and Vinet 2011).

Changes in coastal flood hazard over time are due to many factors. Storm surges are influenced by air pressure as well as wind speeds and direction. Rising mean sea levels also increase storm surge heights. Vertical motion of the ground is another modifier, as is the erosion/accretion of the coast.

Several studies have analyzed storm surges on European scale, but only two used hydrodynamic modelling to extract storm surge heights. Muis et al. (2015) presented a global hindcast of extreme water levels (including tides). Vousdoukas et al. (2016   ) made a comprehensive study for Europe, concentrating on climate change influence on extreme water levels. We are the first to present pan-European flood hazard maps based on storm surge heights from a hydrodynamic study.


Fig. 6.1. Coastal flood in Hamburg, Germany, December 2013. Source: Wikimedia Commons.

6.2 Method

6.2.1 Storm surge model

Assessing coastal flood hazards in Europe involved several steps. Firstly, storm surge heights under present and future climate were calculated using a two-dimensional (2D) hydrodynamic model. The results were analyzed using extreme value statistics in order to obtain return periods. Then, data on other factors influencing extreme water levels were collected (e. g. tides, sea level rise and glacial isostatic adjustment). Finally, flood hazards maps were generated using a "bathtub fill" method. The data sets used for the analyses in this chapter are described more in detail in Section 3.5, *Hydrological and geophysical datasets for coastal flood analyses*.
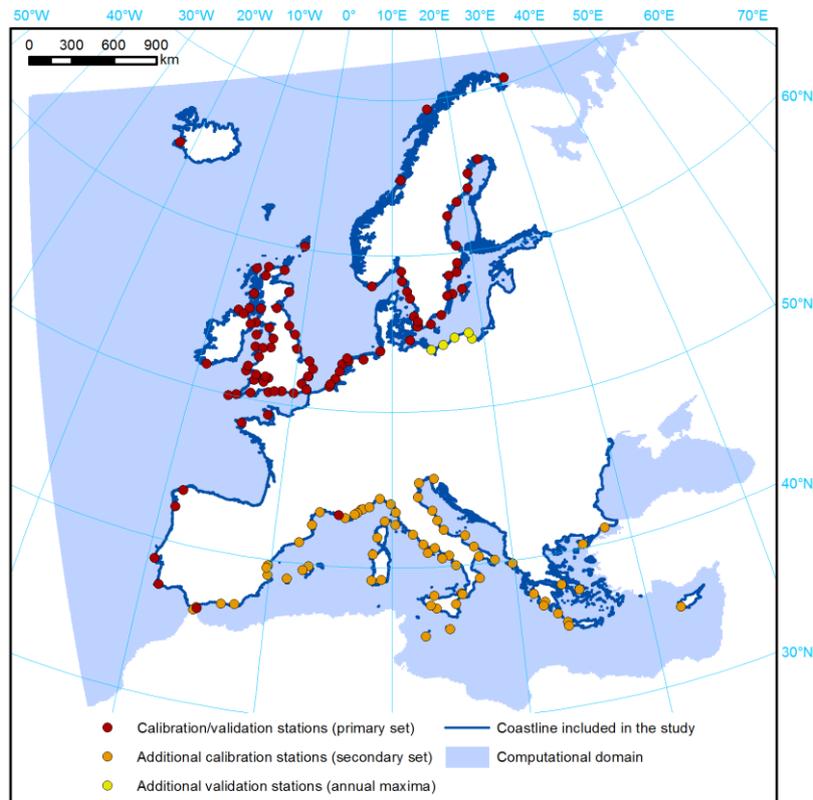
Fig. 6.2. Computational domain and tide gauge stations used for calibration and validation of the model.

Simulations of storm surges were performed using Delft3D software by Deltares (2014a). The mathematical core is comprised of a 2D derivative of de Saint-Venant equations (variant known as 'shallow water equations'), which provide depth-averaged flows of water. The model was forced by EURO-CORDEX data provided by the Rossby Centre of the Swedish Meteorological and Hydrological Institute, i.e. meteorological variables were the driving force of the water levels in the hydrodynamic simulation. It is a simulation of the SMHI-RCA4 regional circulation model (realization t12i1p1), forced by the EC-EARTH general circulation model (see Section Data for details). The input consists of 6-hour series of air pressure and wind speed (u- and v-component). The resolution of the climate data is 0.11° (about 12 km) and the same grid will be used for Delft3D, but the domain was made

slightly smaller for computational efficiency. Bathymetry representing the basins around Europe was interpolated from EMODnet (2016) high-resolution digital terrain model.

Tides were not calculated in the Delft3D model, due to the relatively low accuracy of Delft3D for that purpose. The purpose of including tides in a storm surge simulation, as done in some studies (e.g. Muis et al. 2015) is modelling the influence of this factor on surge heights. However, we performed a statistical analysis modelling the dependency between tide amplitude and extreme surge heights with copulas. The tide-surge interaction was found to be negligible (no correlation) at almost all tide gauges. Therefore, tides were obtained from an external dataset, similarly to an approach chosen by Vousdoukas et al. (2016).

6.2.2 Calibration of storm surge model

The model was first calibrated to tide gauge data for short time periods using ERA-Interim reanalysis data instead of EURO-CORDEX. Focus was put on an accurate representation of monthly maxima, though daily maxima and whole timeseries were also analyzed. The calibration runs encompassed years 1997–2000 and 2011–2014. A comparison was made with a total of 156 tide gauge stations (with different availability, see Fig. 6.2). Surge levels are modelled as values relative to long-term mean sea level (MSL). Therefore, sea level observations for each station were detrended and the long-term MSL was subtracted. Then, the skew surge was calculated, i.e. the difference between the predicted astronomical high tide and nearest observed high water (Batstone et al. 2013). The tidal predictions required for such a calculation were derived through harmonic analysis (using a script by Aslak Grinsted), or–if it led to better performance–IHO predictions[2], or finally JRC's calculation for the stations they provided. Finally, the Delft3D model was validated with a full run using ERA-Interim (1979–2014) and EURO-CORDEX (1970–2005) data.

The calibration results are presented in Table 6-1. "Primary stations" are all stations except the 66 Mediterranean stations provided by the JRC ("Secondary stations"), which have much shorter data series. "Timeseries" refers to the full 6-hour water levels from the model and corresponding skew surges from observations. According to Moriasi et al. (2007), satisfactory values of R^2 and Nash-Sutcliffe efficiency (NSE) are above 0.5, while RMSE-observations standard deviation ratio (RSR) should be lower than 0.7 (methodology of those measures is described in the aforementioned source). In this context, the results for the whole timeseries and daily maxima are all less than satisfying. However, monthly maxima which is the closest indicator to annual maxima we are interested in, show good correlation and little bias, except for the Mediterranean stations, where surge heights are very low; it is noticeable, the absolute error (RSME) is lower than in primary stations, but the relative error is higher (RSR).

For full model runs (36 years), the results were transformed into return period by first extracting annual maxima of skew surge heights, and then fitted to a Gumbel distribution. This particular

---

[2] Modelled tidal predictions from IHO (International Hydrographic Organization) were downloaded using Delft Dashboard modeling-support software (Deltares 2014b).

distribution was chosen because it indicated the highest performance in the Akaike Information Criterion goodness-of-fit test (Mutua 1994). The same calculation was done for available observations from tide gauges. Results of the comparison are presented in Table 6-2.

Table 6-1. Calibration results for the storm surge model. The measures are: Pearson's coefficient of determination (R²) [-1,1], Nash-Sutcliffe efficiency (NSE) [-∞,1], root mean square error (RMSE) in meters and RMSE-observations standard deviation ratio (RSR) [0,∞].

Run	Series	R^2	NSE	RMSE (m)	RSR
2011-2014 primary stations	Timeseries	0.53	0.42	0.15	0.78
	Daily maxima	0.60	0.50	0.15	0.74
	Monthly maxima	0.75	0.72	0.15	0.53
2011-2014 secondary stations	Timeseries	0.23	-0.15	0.10	1.07
	Daily maxima	0.29	0.03	0.10	0.98
	Monthly maxima	0.43	0.29	0.10	0.86
2011-2014 all stations	Timeseries	0.48	0.36	0.13	0.81
	Daily maxima	0.55	0.48	0.13	0.74
	Monthly maxima	0.77	0.77	0.13	0.48
1979-2014 all stations	Timeseries	0.55	0.42	0.15	0.79
	Daily maxima	0.62	0.50	0.15	0.74
	Monthly maxima	0.77	0.73	0.15	0.53

Table 6-2. Validation results for the storm surge model.

Return period (years)	ERA-Interim (1979–2014) vs 86 tide gauges				EURO-CORDEX (1970–2005) vs 65 tide gauges			
	R^2	NSE	RMSE (m)	RSR	R^2	NSE	RMSE (m)	RSR
1000	0.87	0.76	0.33	0.52	0.86	0.83	0.26	0.40
500	0.87	0.77	0.30	0.50	0.87	0.84	0.25	0.40
300	0.87	0.78	0.27	0.48	0.87	0.84	0.23	0.40
100	0.86	0.81	0.23	0.45	0.87	0.84	0.21	0.40
50	0.86	0.82	0.20	0.43	0.87	0.83	0.20	0.41
30	0.85	0.83	0.18	0.42	0.87	0.83	0.19	0.41
10	0.84	0.83	0.15	0.41	0.86	0.81	0.18	0.44
2	0.76	0.71	0.15	0.55	0.80	0.69	0.17	0.58

Overall, the calculations gave very good results. The correlation is high, while the bias and relative errors are small. The performance changes little between return periods for the EURO-CORDEX simulation. It is also better than results reported by Muis et al. (2015). That study indicated $R^2 = 0.49$ for global simulation of annual maxima and $R^2 = 0.61$ for Europe, while indicating very large bias (no exact value given, but from the graphical presentation of the results, NSE was likely less than 0). Performance is also similar to one reported for our river flood analysis.
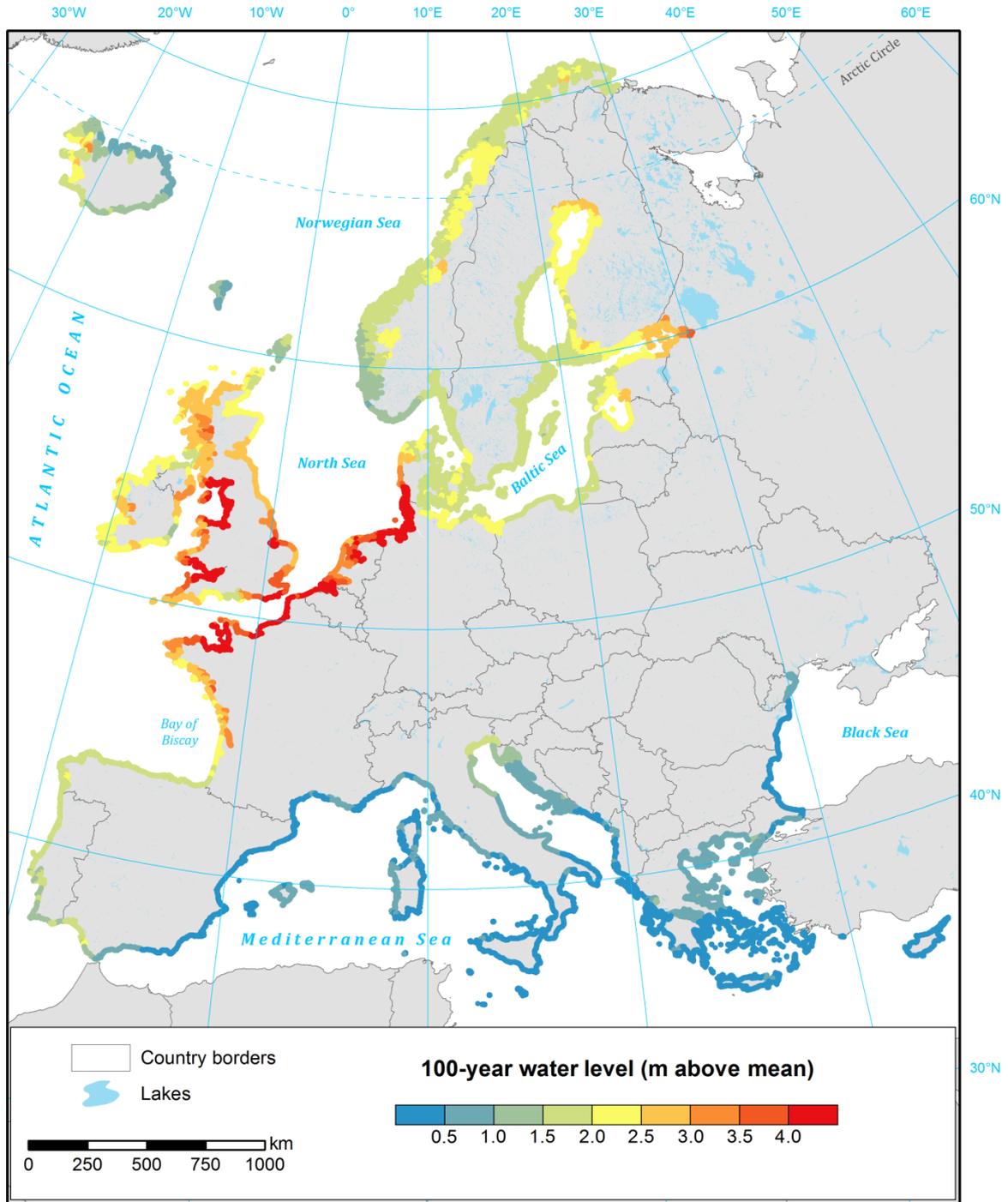
Fig. 6.3. Extreme water levels along European coast, 100-year return period, historical scenario (1971-2000).

6.2.3 Computation of Extreme Water Levels (EWL) with particular return periods

The next step was to derive for each scenario the extreme water levels (*EWL*) corresponding to different return periods. For each coastal segment the following formula was used:

$$EWL_{p,T,S} = SURGE_{p,T,S} + TIDE + MSL + SLR_{T,S} + GIA_T \qquad \text{Eq. 6-1}$$

where:

- *p* is the probability of occurrence (or, conversely, return period).
- *T* is the time period (1971–2000, 2021–2050, 2071–2100).
- *S* is the climate model run scenario (historical for 1971–2000, RCP 4.5 and RCP 8.5 for other periods).
- $SURGE_{p,T,S}$ is the storm surge height at given probability of occurrence *p*, time period *T* and scenario *S*, as described above**.**
- *TIDE* is the mean high tide, derived through calculating tide heights from 13 tidal constituents obtained from TPXO8 model.
- *MSL* is the baseline mean sea level from MDT_CNES-CLS13 dataset. It is the difference between the actual mean topography of the ocean (1993–2012) and the geoid. This factor is included because in elevation models the geoid is the "zero" level.
- $SLR_{T,S}$ is the difference between mean sea level in time period *T* and scenario *S* compared to the baseline MSL. This factor includes several components and sources, as described in the "Data sets" section.
- GIA_T is the accumulated effect of glacial isostatic adjustment between time period *T* and year 2000 (the elevation model's epoch).

Coastal segments were derived from the CCM2 dataset. The total number of segments is 70,297 (225,800 km). The coverage is almost identical to the river flood maps, with only a few sections left out–those on Jan Mayen Island and along the White Sea. It should be noted that, since all datasets used in Eq. 6-1 are grids of different resolutions, information was assigned to each coastal segment from the nearest grid point of each dataset. The water levels for the historical scenario are visualised in Fig. 6.3. The highest extreme water levels are observed in the north-western part of Europe, due to both very high surges and large tide amplitude, while in the Mediterranean and Black seas they are many times smaller.

6.2.4 Generation of flood maps using 'bathtub fill' method

The final step was calculating the flood maps. The 'bathtub fill' method was applied here. It is a simple cut-off of a DEM at a certain elevation (as calculated from Eq. 6-1). However, only those areas hydrologically connected with the sea are considered flooded (Poulter and Halpin 2008). It is assumed that the water can move and flood neighbouring cells only in four directions (no movement in diagonal direction allowed). The DEM used here was corrected for bias in elevation, as described in the "Data sets" section. Maps were created for five return periods – 1000, 300, 100, 30 and 10 years.

6.3   Present climate

Coastal flood hazards zones in the historical scenario are presented in two variants: without flood protection (Fig. 6.4) and with flood protection estimated from the FLOPROS database (Fig. 6.5). The area of the flood zones, broken down by country, is presented in Fig. 6.6.

Commonly perceived as the country with the highest flood hazard, the Netherlands are indeed at top of the list when no flood protection is considered. However, almost no flood zones were identified once flood protection standards are taken into account. In this country, the coastal zone is mostly protected against surges with a 4000 or 10,000-year return period. In other countries, the difference between the two scenarios is very small for a 1000-year return period. In any case, inclusion of flood defences has large influence on the results. Without them, hazard zones in the domain equal to about 62,200 km^2 already at 10-year return period. It increases to 68,000 km^2 for 100-year flood and 73,200 km^2 for 1000-year flood.

With flood defences, a 10-year flood is a hazard to only 700 km^2 of surface area (mostly in Ukraine), increasing to 1,100 km^2 for a 30-year flood. A further 24,800 km^2 is located within the 100-year zone, mainly in Italy, France, Spain and Scandinavian countries. An additional 27,300 km^2 is threatened by floods with a return period of 100–300 years, mainly in the United Kingdom and Germany.

As a proportion of country area, the Netherlands comes first, with 46.6% laying below 1000-year water level, followed by Belgium (6.5%) and Denmark (6.3%). 15 regions (NUTS 3 level) have more than 90% of their area in the flood zone, of which 12 are located in the Netherlands, and the other 3 in Germany. In general, the flood zones concentrate around the North Sea, where the amplitude of extreme water levels is among the highest, while many low-lying areas occur. Other pockets of flood hazard mostly are river deltas, often featuring depressions: Po in Italy, Guadalquivir and Ebro in Spain, Vistula in Poland, Nemunas in Lithuania, as well as the Danube in Romania and Ukraine, to name a few. 26% of the 1000-year flood zone is within 1 km of the coastline and 35% within 2 km. The median distance from the coastline is slightly less than 5 km.

Note on map usage: Coastal and river flood risk maps presented in this report, as well as data available for download as a result of the project, were made using large-scale datasets and are intended for providing a European-wide overview of present and future probability of occurrence of floods. Therefore, extreme caution should be made when drawing local-scale conclusions from the maps. Local factors can have substantial influence on the actual level of hazard, especially the presence of hydraulic structures such as dams or flood defences. In case of the latter ("with flood protection" scenario) they represent either flood protection standard defined by law or design of the structure rather than its actual failure probability or, in most cases, only a rough estimate of the level of protection.
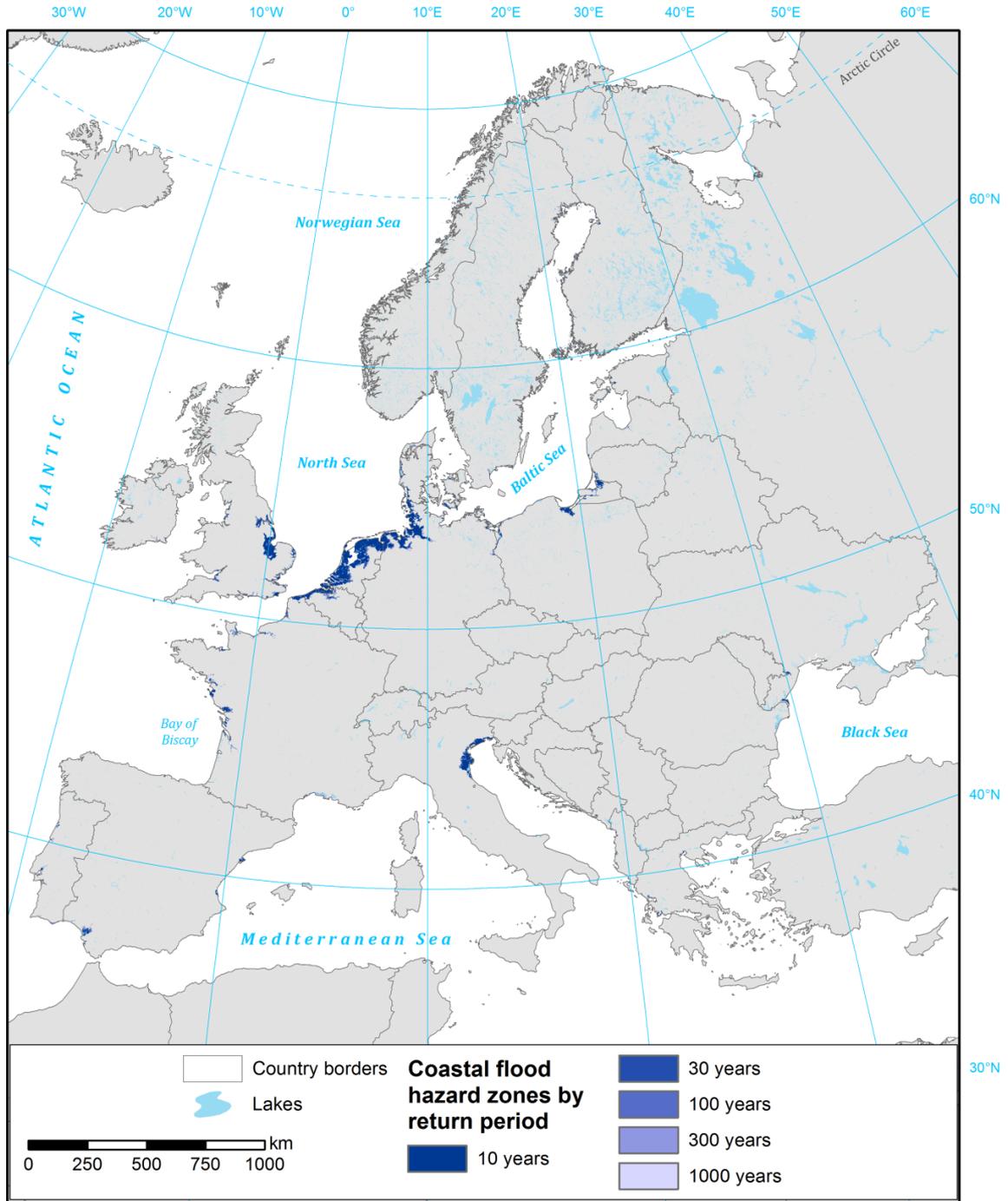

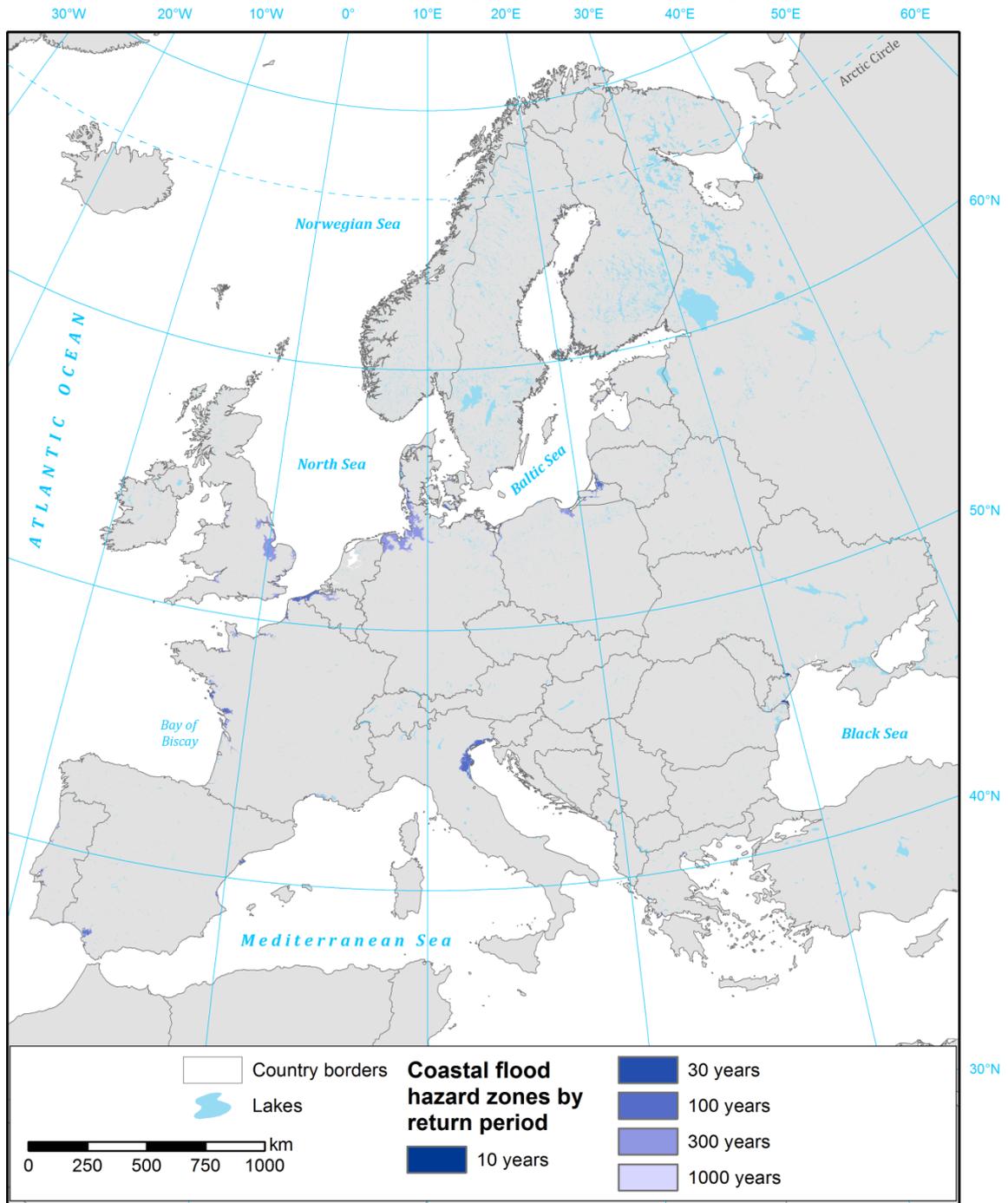**Fig. 6.4. Coastal flood hazard zones by return period, historical scenario (1971-2000), no flood protection.**

Fig. 6.5. Coastal flood hazard zones by return period, historical scenario (1971-2000), with flood protection.

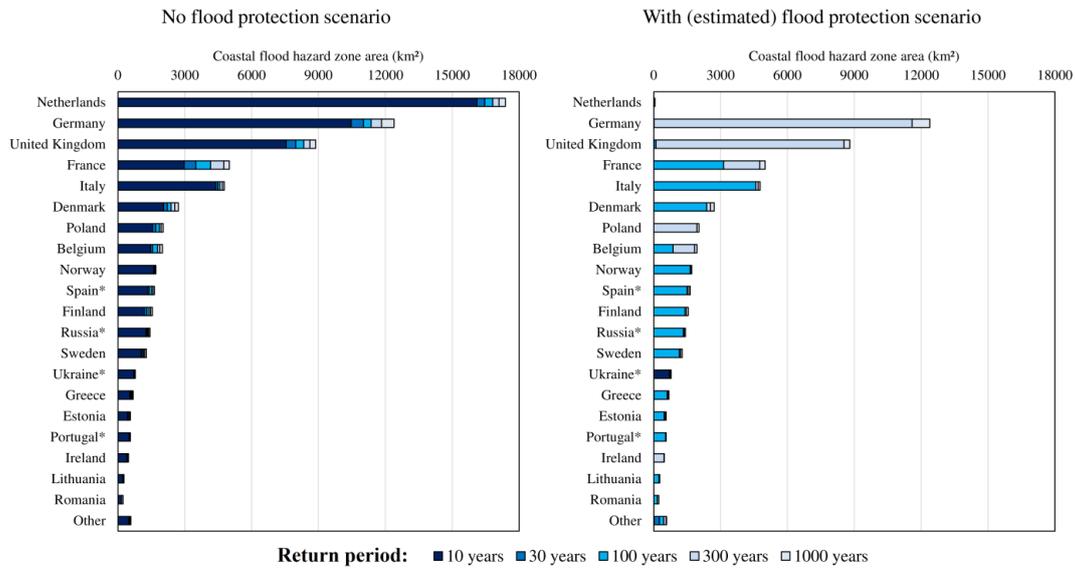No flood protection scenario   With (estimated) flood protection scenario

Fig. 6.6. Size of coastal flood hazard zones by country, without (left) and with (right) flood protection. Countries only partially located within the simulation domain are marked with an asterisk (*).

6.4 Climate predictions

6.4.1 General remarks

Future coastal flood hazard depends on several factors. Here, we consider three sources driving those trends:

- Changes in storm surge occurrence due to shifts in climate parameters: air pressure and wind speeds/directions
- Changes in mean sea level caused by several climate-related phenomena (see "Data sets" section);
- Effects of glacial isostatic adjustment (GIA), which are unrelated to current or future climate.

The hazard was analysed in five increments – 10-, 30-, 100-, 300- and 1000-year return periods. We also considered the change in flood hazard in the context of existing (estimated) flood protection standards. For the purpose of this analysis, the dikes were assumed to be as high as the water level for a given return period in the historical scenario (1971–2000). The return period was taken from the protection standards database FLOPROS (Scussolini et al. 2015). Therefore, if the water level with the same return period equalling the protection standard was higher in the future scenario compared to the historical scenario, the area currently protected by this theoretical dike was considered flooded.

Flood hazard zones cover only up to 1.3% of the domain, therefore for the sake of clarity the graphical representation in the maps (Fig. 6.7 and Fig. 6.8) was changed compared to the previous section (Fig. 6.4 and Fig. 6.5). Here, we calculated the area covered by flood hazard zones per 50x50 km cells, and the change in that area in the future. We only present the 100-year flood scenario in those graphs, but the presented trends are mostly representative for the other return periods as

Coastal floods

Area of hazard zones at risk from a 100-year flood, assuming <u>no flood protection</u>.
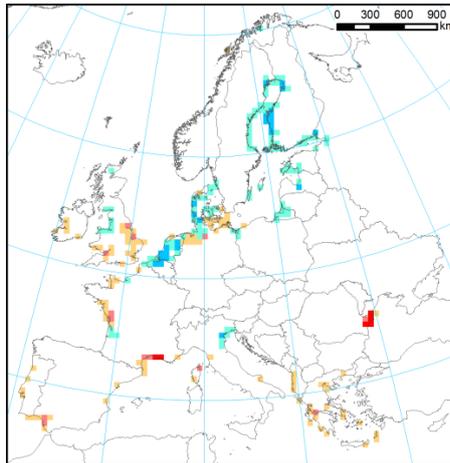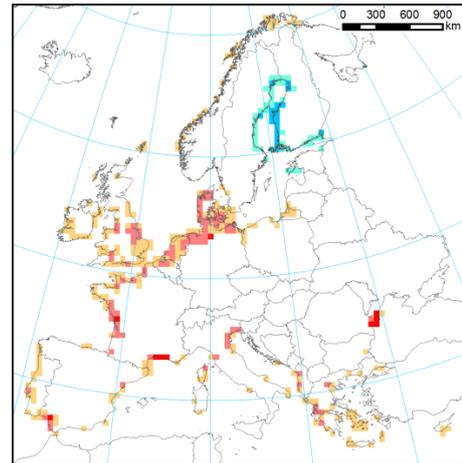
**Reference
Period**

1971 – 2000:

Total flooded area (km²): 0 1 10 100 1000
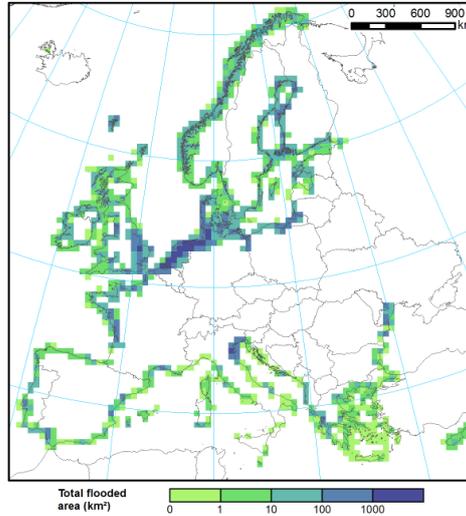
**Predicted
changes**

RCP 4.5:

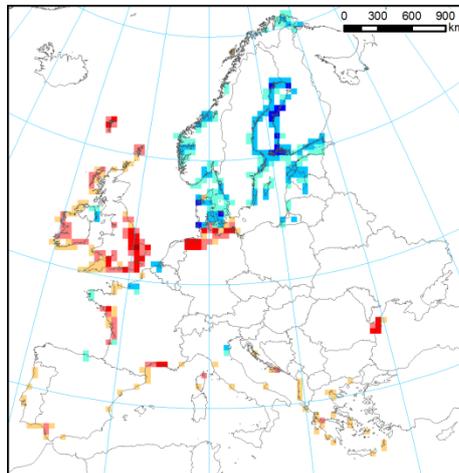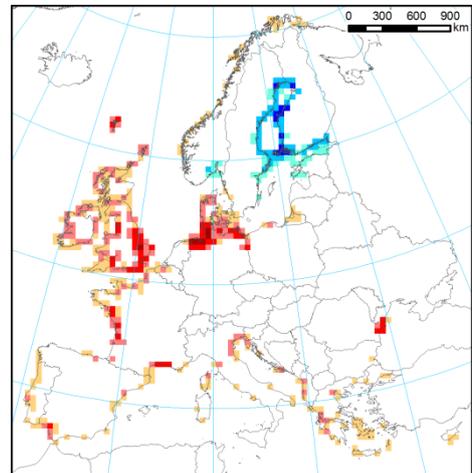2021-2050   2071-2100

RCP 8.5:
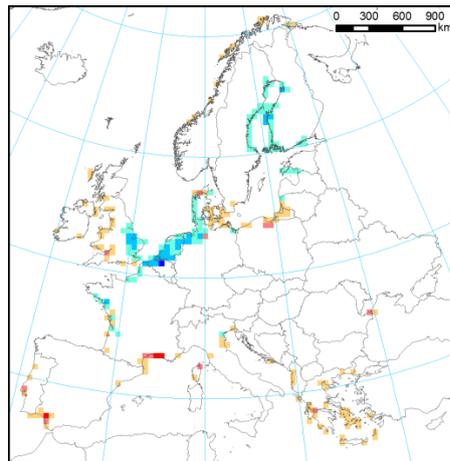
2021-2050   2071-2100

Change in flood zone area (km²): -100 -10 -1 +1 +10 +100 +1000

Fig. 6.7. Total area of 100-year coastal flood hazard zones (no flood protection), aggregated to 50x50 km grid, and changes under climate scenarios.Coastal floods

Area of hazard zones at risk from a 100-year flood, assuming <u>current flood protection</u>.

Reference Period

1971-2000

Predicted Changes

RCP 4.5:

2021-2050

2071-2100

RCP 8.5:

2021-2050

2071-2100

Fig. 6.8. Total area of 100-year coastal flood hazard zones (with estimated current flood protection), aggregated to 50x50 km grid, and changes under climate scenarios.

well. Only for some countries in the "with flood protection" scenario there are differences. Those cases are discussed in the text.

6.4.2   Trends in flood hazard

The size of the flood hazard zones increased for all four future scenarios. The changes are relatively modest when flood protection is not considered. In the 2021–2050 period the increase is very small, at around 400 km^2 (RCP 4.5) or 300 km^2 (RCP 8.5), or 0.2–0.4% of the 1971–2000 flood zone. By the end of the century, the increase amounts to 3900–5500 km^2 (4–8%). This can also be seen in the top left graph of Fig. 6.9. The general picture of flood hazard doesn't change much between scenarios. Interestingly, surge heights actually decrease on average, from 1.29 m in the historical scenario to 1.20-1.27 m in the climate change scenarios.

GIA presented, on average, a negative trend, i.e. a decrease by 8 cm by 2021–2050 and 15 cm by 2071–2100 compared to 1971–2000). By mid-century, sea level rise was only 6–9 cm, and therefore offset by the other two factors. By end-century, however, the increase is projected to be 30–45 cm on average, causing a general increase in extreme water levels. The reason why flood zones expanded in all climate change scenarios despite drops in extreme water levels by mid-century is the uneven distribution of flood zones.

More visible changes can be noted when flood protection is included. By mid-century, there is a substantial expansion of the flood zones with the highest probability of occurrence. A 30-year zone that had an area of 1,000 km^2 in 1971–2000 is projected to reach 6700–10,800 km^2, i.e. 7–11 times. Meanwhile, the 100-year zone increased only slightly, while 300-year and 1000-year flood hazard zones actually decreased. That illustrates the diversified trends along European coasts. Some flood defences will be overwhelmed by rising water, while others will become safer due to opposite trends. By the end of the century, however, there is an across-the-board increase in flood extents. In the RCP 8.5 scenario, 10-year flood zone is bigger than the present 100-year zone and the 30-year zone is bigger than the 300-year zone during 2021–2050. In both emission scenarios the 100-year zone doubles by the end of the century.

Netherlands

Trends in flood hazard are very diversified across European coasts. Changes in flood extents presented in Fig. 6.7 and Fig. 6.8 were aggregated to a 50x50 km grid, whereas Fig. 6.9 shows the size of the flood zones for selected countries, which between themselves contain almost 80% of all flood hazard in Europe. The country with the largest flood hazard, the Netherlands, is at the same time the most protected one. Almost no flooding is expected when flood protection is considered not only for the historical scenario, but also for both emission scenarios in the 2021–2050 time period. By the end of the century, however, more than 3000 km^2 is projected to become at risk in a 1000-year flood event, as the flood defences in "dike rings" with the lowest protection standards become insufficient.
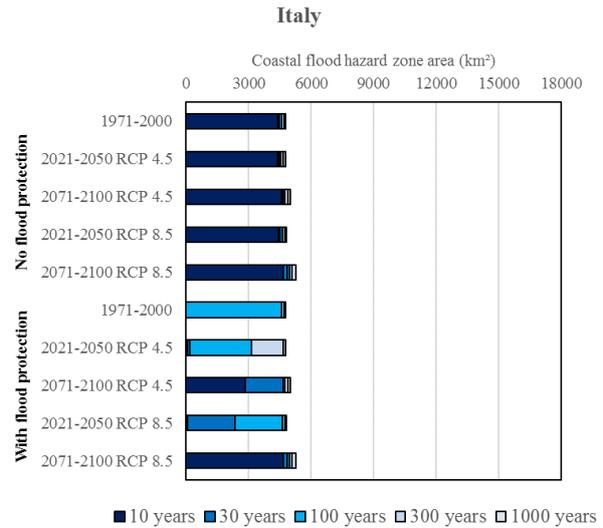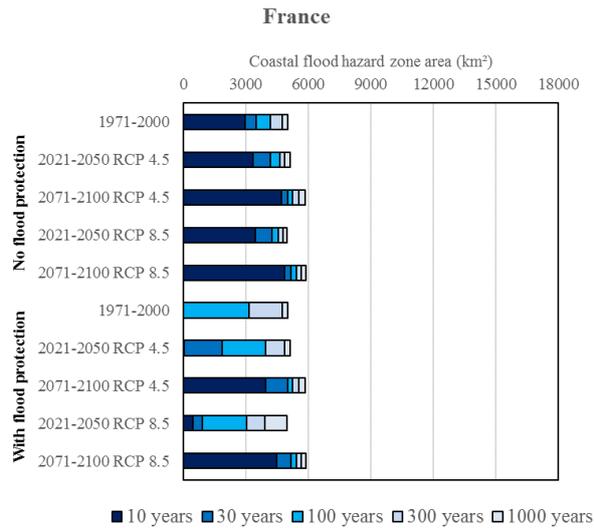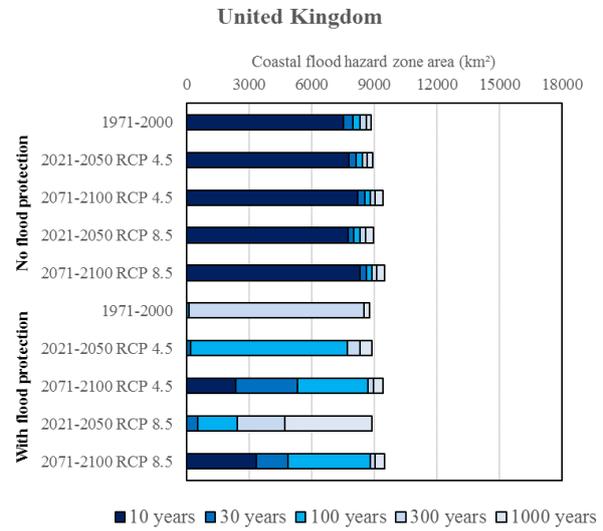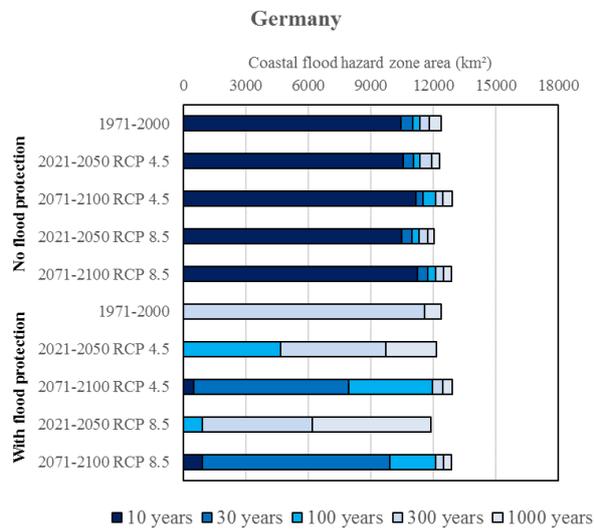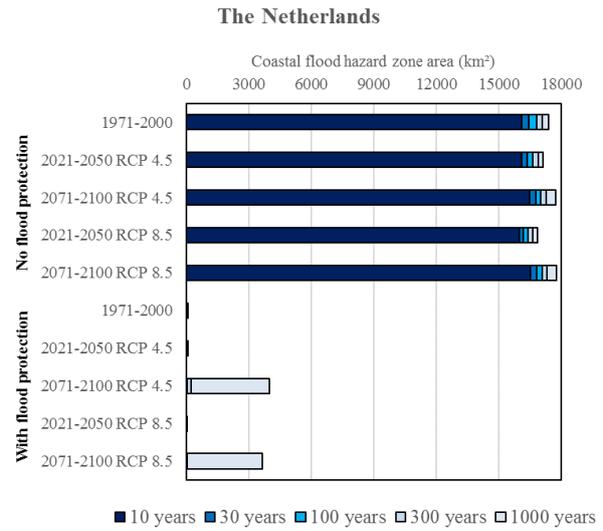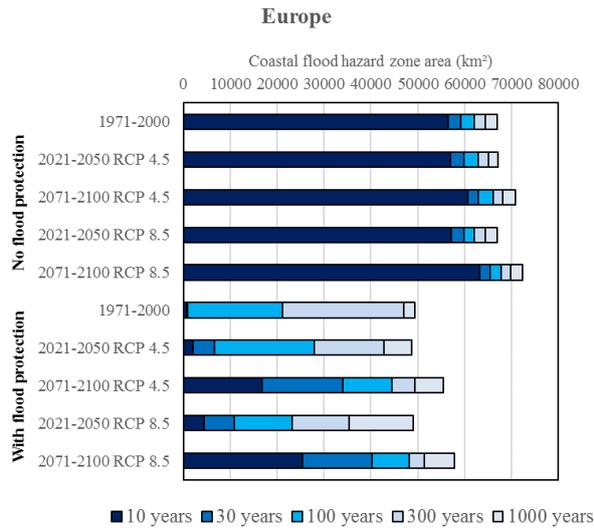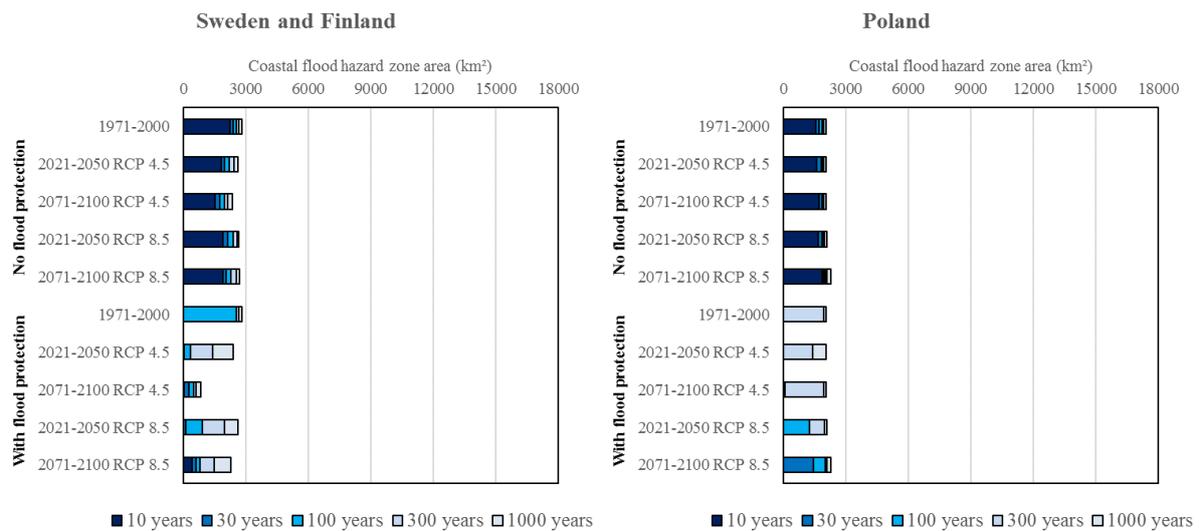
Fig. 6.9. Impact of climate change on coastal flood hazard zone area, with and without flood protection, for selected countries and Europe within the domain (note different scale for the graph for Europe).

Germany

In Germany, very little change is observed between scenarios when flood defences are not included in the analysis. Flood protection will be put under pressure in many locations. However, while the 100-year flood zone will expand by mid-century, the 300-year zone will decrease due to different trends in the North Sea and Baltic Sea coasts of Germany; in the former, lower water levels are expected, while in the Baltic higher levels are anticipated. Yet by 2071–2100 period, most of the area at risk of flooding from the sea will be already exposed to a 30-year event, especially in the North Sea coast.

United Kingdom

Along the United Kingdom's coasts, the trends are diversified, but the extent of flood zones (without flood protection) barely changes between scenarios. Almost all of the area in the historical scenario is flooded by a 300-year event. By mid-century the trends are very different between emission scenarios. In RCP 4.5, the 300-year flood zone becomes essentially a 100-year flood zone, while in RCP 8.5 the 30-year and 100-year zones increase, but the 300-year decreases significantly. This is mainly caused by changes in storminess in the eastern coast of England, which increases in RCP 4.5, but declines in RCP 8.5. By the end of the century, around half of the flood zone is already affected with a 30-year event, with a large part projected to be inundated already by a 10-year flood. The remainder of the flood zones corresponds to a 100-year event.

France

In France the difference in size of flood zones is more visible, with a 1000-year flood zone being double the size of a 10-year zone (without flood protection). There are also more noticeable changes in the future: the 10-year zone is projected to increase by more than half by the end of the century. More than half of the coastal flood hazard zone is estimated to be protected by flood defences with a standard of protection equal to a 30–100-years return period. By mid-century, some flood defences are projected to become inadequate for a 30-year event, and the 100-year flood zone will

58

expand, but only in the RCP 4.5 scenario. In RCP 8.5, some additional 10-year and 30-year flood zones appear, but the 100-year and 300-year zones decrease. This is caused mainly by large increase of flood extents in the Mediterranean coast of France, particularly in the Rodan delta, while surges in the English Channel (La Manche) are expected to decrease. In the 2071–2100 timeframe, the flood hazard becomes very large, with flood defences making little difference from the "no flood protection" scenarios. In both emission scenarios most of the floodplains are already exposed to a 10-year flood.

Mediterranean countries

Italy, like the whole Mediterranean region, is projected to have a relative increase in water levels bigger than other parts of the continent. Yet, except for the Po river delta, the flood hazard zones are small, and the increase in their extent will be relatively small as well. In the RCP 4.5 scenario, the aforementioned delta will encounter even a decrease in hazard, though in RCP 8.5 the flood zones are expected to expand. Large increases of hazard are expected when flood defences are considered. It is estimated that the flood protection standards in the Mediterranean region are lower than in northern Europe. In Italy, almost all areas with a coastal flood hazard could be inundated by a 100-year event in the historical scenario. By mid-century, some of the 100-year zone will become a 300-year zone in RCP 4.5, but the opposite would happen in RCP 8.5: half of the 100-year zone will become a 30-year zone. By 2071–2100, half of the flood hazard zone in Italy is expected to be endangered by only a 10-year surge in RCP 4.5, and almost all of it in RCP 8.5. A similar pattern (100-year flood zone displaced by 10-year zone by the end of century) can be observed in Spain or Greece.

Nordic countries

At the same time, Sweden and Finland will be in total contrast to the rest of Europe. In the RCP 4.5 scenario, glacial isostatic adjustment will cause a greater decrease of the water level than the increase that climate change will generate. In effect, by the end of the century the flood hazard zones in Finland will shrink by more than a quarter; they would decrease in Sweden too. Under RCP 8.5, the two forces are more in balance, and the flood hazard zones will only decrease slightly in the "no flood protection" scenario. The flood protection standards in Sweden and Finland are not too high and are estimated to be below a 100-year return period. Yet, by 2071–2100, the 1000-year flood zone decreases by two-thirds in RCP 4.5, while in the other emission scenario the 100-year zone becomes mostly a 300-year or 1000-year zone. Only in southern Sweden an increase of hazard could be noticed. In other Nordic countries, the trends are different than in Sweden and Finland. In Denmark the flood hazard will generally decrease by mid-century, only to rise substantially in subsequent decades. Along the coasts of Norway, the trends are very diversified, with decreases mostly in the southern part, and increases in the far north. In Iceland the coastal flood hazard is very low at present and that is not expected to change in the future.

Baltic states and Black Sea coast

In the southern coast of the Baltic Sea, the coastal flood hazard is projected to be rather stable under climate change, at least in the RCP 4.5 scenario. Considering the existing (estimated) flood protection standards, the 300-year flood zone will partially become a 1000-year zone by mid-century, but will revert to a 300-year return period in 2071–2100. In RCP 8.5, however, the 300-year zone is projected to mostly be endangered by a 100-year event by 2021–2050, and a 30-year event in 2071–2100. In

the Kaliningrad administrative region, the flood hazard will similarly increase, while in Lithuania and Latvia it is expected to remain roughly at current level, and decrease in Estonia. Finally, one additional location worth mentioning is the Danube river delta, located mostly in Romania. A large increase in flood extents (about fivefold) is projected in all scenarios, both with or without considering flood protection.

6.4.3   Uncertainties

The analysis includes several sources of uncertainties and on many levels. The first is related to input data. Storm surge heights are derived through a hydrodynamic model. Though it was shown that, as a whole, it has good accuracy, the performance for individual stations was very diverse. Also, some regions, especially the Black and Mediterranean seas or coast of France, had limited or no observational data for comparison. Moreover, because of the resolution of the model (~12 km) the complicated shape of the coast could often not be incorporated, especially shores of Norway, Finland, Greece or Croatia. Therefore, the error in deriving the surge height could be locally significant. Tides were obtained from a high-resolution model, but it still includes only 13 constituents which may compromise accuracy along complicated coasts. Datasets on GIA and sea-level rise have relatively coarse resolution, causing relatively steep changes between some coastal segments.

Another source of uncertainty is the methodology. Some factors such as tide-surge interaction or the impact of sea-level rise on tides have been omitted. These, however, have more local effects than over all the domain of interest. We also do not include the influence of ground motion other than GIA, as these are very local factors with a number of causes, and no large-scale datasets are available. There is also coastal dynamics, resulting in erosion and accumulation of the coast, which is also a very local factor; it is also of little relevance compared to the resolution of the DEM. We also only considered five increments of return periods of floods for clarity of presentation and alignment to the river flood analysis, where the same return periods were used.

Substantial uncertainty is related to the delimitation of flood hazard zones. Vertical accuracy and bias of the DEM could influence the results to some degree. More importantly, the static "bathtub fill" method typically overestimates the hazard. Additionally, the flood protection standards used here are only the nominal values that do not take into account the failure probability of the flood defence structure itself. A large part of those standards are only estimates in the first place, or merely relate to river flood hazard. Also, we assume that the protection levels equal the water levels from the historical scenario, whereas they are actually locally defined using various techniques, time periods and safety margins added on top of the "design" water levels. Additionally we assume that the flood defence structure remain unchanged in the future, even though they can deteriorate or be maintained to different levels over time.

Finally, there is uncertainty related to future projections, especially with climate data. GIA is a very slow process, and the rate of vertical motion of the crust changes very little over time. Meanwhile, sea level rise is a combination of several climate-related factors, which are only understood and quantified to a varying degree. Existing estimates have a low spatial resolution, and large uncertainty bounds. Accuracy of storm surge projections is dependent on the accuracy of air pressure and wind

speed/direction projections. As can be noticed from Fig. 6.7-Fig. 6.9 and the text, difference between RCP 4.5 and RCP 8.5 scenarios is sometimes very large, to the point that opposite trends are indicated. This alone illustrates the significant uncertainty related with climate change.

6.5 Summary

In this chapter we analysed coastal flood hazard in a domain covering the majority of European coasts. The storm surge probability of occurrence was calculated utilizing a hydrodynamic model driven by EURO-CORDEX climate simulations. The model was validated and presented good accuracy, and its output was combined with estimates of tidal amplitudes, present and future mean sea levels as well as glacial isostatic adjustment trends, all obtained from external sources. Water levels with five different return periods were obtained for the entire domain, for the historical scenario (1971–2000) and for two climate change scenarios (RCP 4.5 and 8.5) in two time periods (2021–2050 and 2071–2100). Water levels were used to calculate flood extents by intersecting them with a pan-European digital elevation model.

The main conclusions in the face of the uncertainties described in the previous section are presented next. It was found that the majority of the area of coastal flood hazard zones can be found in only a few regions. Low-lying river deltas and estuaries are most endangered, as well as countries located along the North Sea coast. The Netherlands had the highest flood hazard, though only when flood protection was not considered, as its defences protect almost all its territory from a 1000-year surge, the highest return period analysed here. Germany, United Kingdom, France and Italy are other countries with large coastal flood hazard. Future trends of hazard were found to be very diversified between regions and scenarios. Sweden, Finland and Estonia, lying in area with significant ground uplift rate with encounter a decrease in their flood hazard zones in all scenarios. In some territories, mainly along the North Sea and English Channel, the hazard will also decrease by mid-century. However, in the majority of Europe hazard is projected to increase in subsequent decades. Sea level rise (SLR) will be the main driver of this trend, more relevant than changes in storminess. Between emission scenarios, there is significant variation in SLR projections, while this aspect is most crucial for the future outlook of coastal flood hazard. The difference in hazard across Europe is also very large when flood protection is considered – 100-year and 300-year flood zones, which constitute the majority of total hazard, will mostly become 10-year and 30-year zones by 2071–2100. Many flood defences, therefore, will no longer fulfil their designed or intended protection standards.

7. River floods

Dominik Paprotny and Oswaldo Morales Nápoles (TU Delft)

7.1 Introduction

River floods are inundations of land caused by increased river discharges. In natural conditions, a river spills outside its banks every second year on average (natural river banks generally correspond to water level with a return period about 1.5 year). There are several causes for river floods. In winter and spring they are caused by melting snow, with the size of the flood being dependent on the amount of stored snow and rate of melting. They frequently occur together with melting of ice cover on the rivers, resulting in the flow being blocked. In northern Europe they are relatively frequent, with rivers like Rhine and Vistula particularly prone to those events. In summer, intense rain covering a large area, especially over several days, causes extensive floods. Saturation of the soil with water is an important factor controlling those events. Such floods caused many disasters particularly in central Europe (Danube, Elbe or Oder catchments). Finally, flash floods are the most dangerous kind for the population, due to their sudden and unpredictable nature. They are caused by very intense, but also very short rainfalls (in the range of hours, or even less). They are most frequent in mountain catchments, though it should be noted that no river is needed for such flood to happen. In effect, any area with insufficient drainage is prone to such events, especially urban areas where soil is mostly sealed by artificial surfaces. In general, the biggest flash floods were observed mostly in the southern parts of Europe. Additionally, river floods could be caused by increased water levels in the sea; the dependency between the two was not analysed here. Barredo's (2007) list of big flood in the EU between 1950 and 2005 includes 23 flash floods, 16 floods caused by extensive rainfall and 5 caused by snowmelt together with rainfall.

Fig. 7.1. River flood in Wrocław, Poland, May 2010. Source: Wikimedia Commons.

There are a few studies analysing storm surges on European or global scale (e.g. Feyen et al. 2012, Ward et al. 2013, Winsemius et al. 2013, Alfieri et al. 2014). However, only one had so far combined statistical methods for deriving flood scenarios with physical models for calculating flood extents (Sampson et al. 2015). The one presented here, however, is the first is to employ Bayesian Network for that task.

7.2 Method

The analysis of river floods is divided into two parts. Firstly, a database of extreme river discharges and their return periods in Europe is created using a new statistical model. Secondly, flood extents are calculated based on those scenarios utilizing one-dimensional (1D) hydrodynamic modelling.

The method applied here to calculate river discharges is an innovative approach, devised to reduce computational effort related with full physical models, while at the same time retaining accuracy and expanding coverage. We use Bayesian networks, a statistical method to analyse conditional probability distributions. In this model, various variables describing the characteristics of river catchments are used to estimate annual maxima of river discharges. A preliminary methodology and results were reported in Paprotny and Morales-Napoles (2015).

7.2.1 Bayesian network

Briefly, a Bayesian network (BN) is a probabilistic graphical model that represents a high-dimensional uncertainty distribution over a set of variables. In this study a non-parametric continuous Bayesian network is applied (Kurowicka and Cooke 2006, Hanea et al. 2006). All variables ("nodes" of the graph) are parametrized as empirical distributions of values at each node, in this case taken directly from a large sample of river gauge stations and their corresponding catchments. Dependencies between the variables ("arcs") are quantified by (conditional) rank correlations. The result is a directed acyclic graph, where joint probability distributions are represented by copulas. About 40 variables were analysed for inclusion in the model, with the final model including 7 variables, plus the river discharge. The variables are listed in Table 7-1. Variables used in the model. Details on the sources can be found the "Data sets" section. and the model is visualised in Fig. 7.2. By conditionalizing, i.e. replacing the probability distributions in variables with a single value, on 7 variables other than river discharge, an updated estimate of the distribution of the remaining variable (river discharge) can be obtained.

Table 7-1. Variables used in the model. Details on the sources can be found the "Data sets" section.

Variable	Unit	Description/source
Annual maximum of daily river discharge (*MaxDischarge*)	m³/s	74,757 station-years from 1841 river gauge stations from global/national data sources
Catchment area (*Area*)	km²	CCM2 dataset
Catchment steepness (*Steepness*)	m/km	The elevation difference in the catchment divided by its total area. From EU-DEM and SRTM DEM.
Annual maximum of daily precipitation and snowmelt (*MaxEvent*)	mm	EURO-CORDEX data
Extreme runoff coefficient (*RunoffCoef*)	-	Annual maximum of total runoff divided by *MaxEvent*. From EURO-CORDEX data
Catchment fraction covered by lakes (*Lakes*)	%	CORINE Land Cover 2000 and CCM2 dataset
Catchment fraction covered by marshes (*Marshes*)	%	
Catchment fraction covered by build-up areas (*Buildup*)	%	CORINE Land Cover 2000 and Global Land Cover 2000
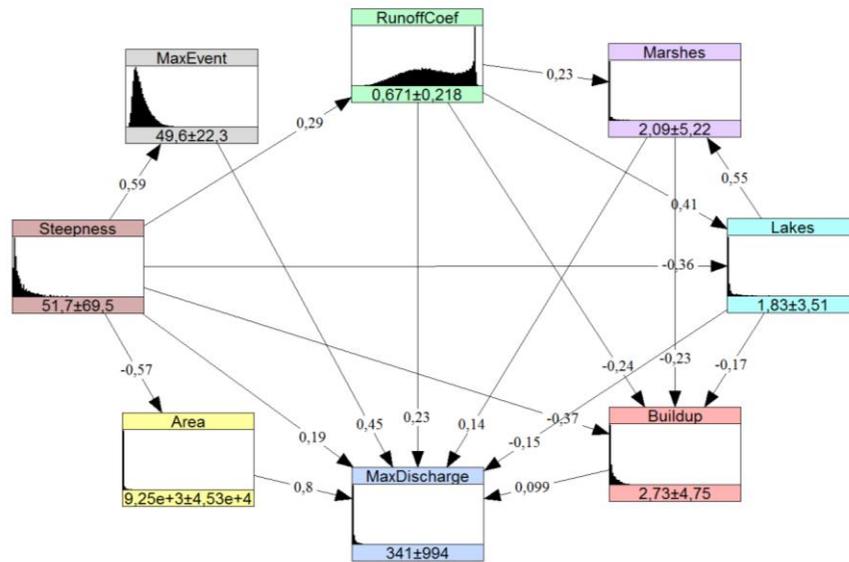
Fig. 7.2. Bayesian network for river discharges in Europe. See Table 7-1 for variable definitions. Values under histograms show the mean and standard deviation, while the values on the links between the variables are the (conditional) correlation coefficients.
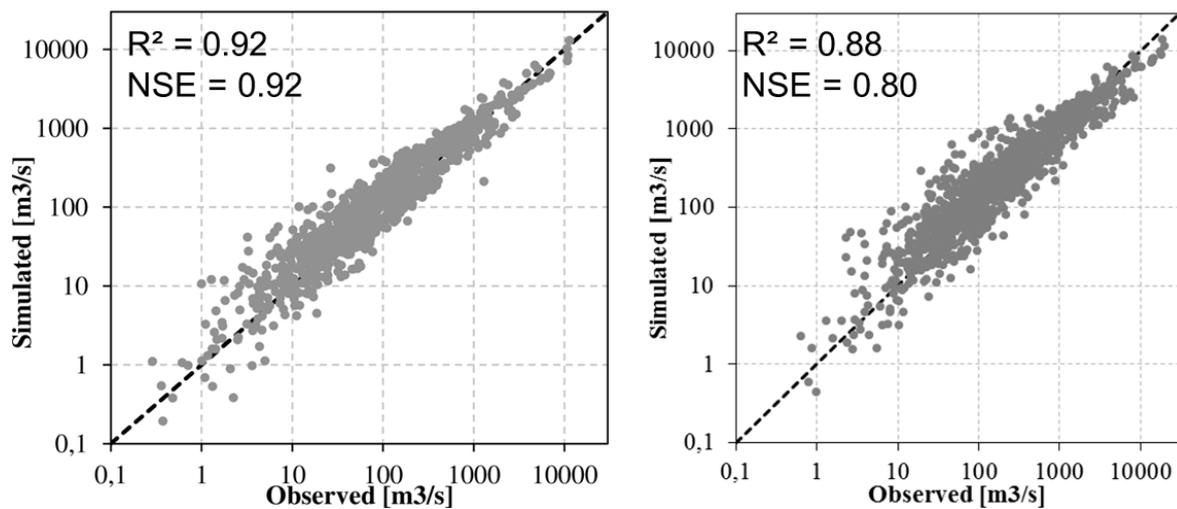
Fig. 7.3. Comparison of simulated and observed daily discharges: average annual maxima (left) and discharges with a 100-year return period (Gumbel distribution) (right). Data for 1125 stations for 30-year periods (1951–80, 1961–90 or 1971–2000, depending on data availability for a station).

7.2.2   Model quantification and validation

The model was quantified using data on 1841 gauged catchments with almost 75,000 yearly values of extreme river discharges as well as precipitation, snowmelt and runoff estimates from climate simulations covering the years 1950 to 2005. The EURO-CORDEX simulations used here were made by Climate Limited-area Modelling-Community utilizing ICHEC-EC-EARTH general circulation model with COSMO_4.8_clm17 regional climate model (realization r12i1p1). This model was chosen because of the relatively good performance of the CCLM model in estimating extreme precipitation (Kotlarski et al. 2014); differences between various models were also found to be rather small (Rojas et al. 2012). It is also important that only the meteorological variables change over time, while the land cover is assumed constant.

The BN was used to provide a 30-year series of annual data, which were then fitted to a Gumbel distribution in order to derive return periods of extreme discharges. The same distribution was used to calculate return periods from river gauge records (a total of 1125 stations had sufficient completeness of observations). The comparison between observed and simulated discharges is presented in Fig. 7.3. The method gives a good coefficient of determination (R^2) of 0.92 for average annual maxima and 0.88 for 100-year discharge. This is achieved by a rainfall-runoff model for Europe forced by bias-corrected meteorological data – Rojas et al. 2012 reported R^2 values of 0.90-0.94 and NSE of 0.89-0.93 for annual maxima. The accuracy of the method is somewhat lower for very small catchments (with extreme discharges below 10 m^3/s), but that is not unusual, since at that scale (up to a few dozens of square kilometres) very local factors play a major role. Several outliers can be observed, but that may be largely due to incorrect assignment of river gauges to catchments (as those are separate databases) and influence of reservoirs.

A full database for the entire domain was created, covering annual maxima for 831,125 catchments (1.94m km of rivers) and all scenarios. It is presented in Fig. 7.4. However, only river sections located in catchments larger than 100 km^2 were then included in the calculation of flood extents. This

selection was not only made to reduce computational load, but also because of the reduced accuracy of the scenarios for such small rivers (where mostly flash floods occur). This amounts to about 19% of the total number of catchments (155,663), but retains 26% of river length (498,000 km). It should be noted that this is still many times more than in other studies, which have e.g. thresholds of 500 km^2 catchment size (Alfieri et al. 2014) or of at least 6th river order (Sampson et al. 2015).

SOBEK v2.13 hydrodynamic model (Deltares 2015) was used for the calculations. The one-dimensional (1D) module was chosen, as it is computationally significantly less demanding than a two-dimensional (2D) model, even though it is theoretically less accurate. A "steady" calculation was performed, which means that the model tried to find an "equilibrium" state of the river at given discharge amount. This conserves time compared to an "unsteady" calculation, where water levels are calculated for each defined time step. As the validation will show, it also retained the similar level of accuracy. The SOBEK model requires the following inputs:

- River network: linear representation of the rivers, which was derived from the CCM2 dataset.
- Calculation points: in a 1D simulation hydraulic calculations of water flow are only performed at certain points along the river network. Those were defined, on average, every 2 km of rivers.
- Upstream boundary: this is a location where water enters the model. Because of the threshold of 100 km^2 catchment area, almost all are located somewhere along the rivers. At the boundaries, the discharge from our database is defined. In rare cases where the source river section already has a catchment bigger than the threshold, the value of discharge was taken from the estimate made for that catchment.
- Downstream boundary: this is a location where water is withdrawn from the model. Here, it is a body of water (typically the sea) to which the river drains. The boundary was defined as zero water level, representing the mean sea level, unless due to the bias in the DEM the mean sea level is below zero meters.
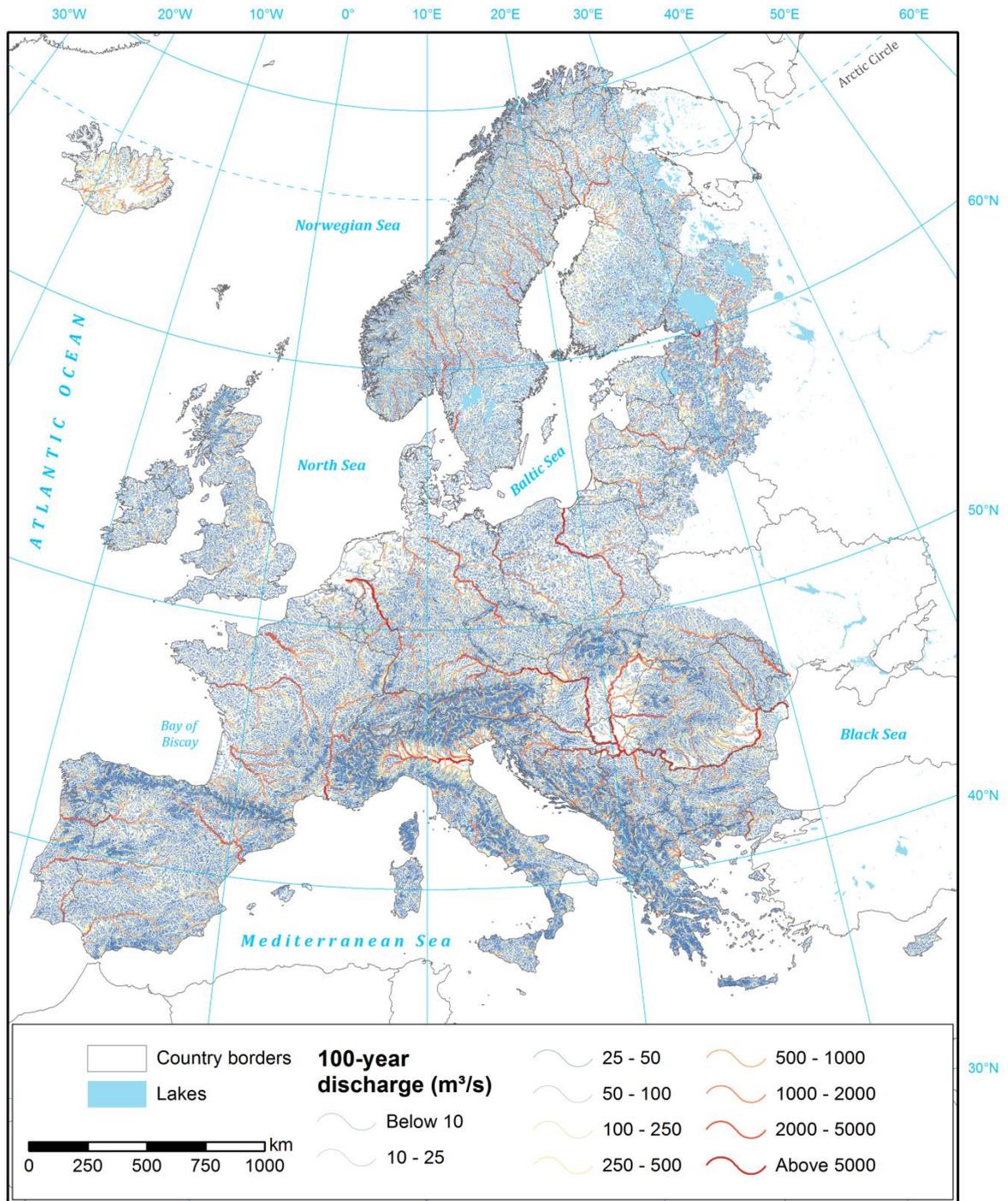
Fig. 7.4. Extreme daily river discharge with a 100-year return period, 1971–2000.

- Lateral discharge: an option to enter or withdraw water from the model at locations different than the boundaries. This is necessary to properly represent the discharge scenarios in the network. At an intersection of two rivers, the water flow in both rivers is summated and continues downstream. However, extreme discharges with an, e.g., 100-year return period do not necessarily happen at the same time. Hence, the 100-year discharge in the river below the intersection will be typically lower than the sum of the two contributing

rivers. Using the lateral discharge option, the surplus water is withdrawn from the model, preserving a proper representation of flood scenarios.

- Cross-sections: these are points along the river, where its profiles are defined. The profiles were obtained from the DEM and vary in length depending on the topography. In a manner similar to that of the calculations points, they were defined approximately each 2 km of river. Due to the resolution of the DEM, flood defences are mostly not included in the profiles. The river beds are not included either. Therefore, it is assumed that the DEM represents the mean water levels in the rivers, as has been done in other pan-European studies (e.g. Alfieri et al. 2014).

As a consequence of that last point, mean discharges were subtracted from extreme discharges in the entire model. Mean discharge values were obtained from the same Bayesian Network as for extreme discharges, simply by replacing extreme rainfall/snowmelt and runoff coefficients by annual means. Also in this setup, the BN model performed well.

Once the calculation in SOBEK model was done, the data had to be post-processed to obtain the water levels at the calculation points. Therefore, water levels were linearly interpolated along the rivers to increase the density of estimates. Then, the data were loaded into GIS software and extrapolated over the DEM in the nearest neighbourhood of the respective river segments. Coastal segments were included in the nearest-neighbour calculation in order to avoid a situation where the water levels in a river are extrapolated along the coastline. From the whole area lying below water levels of the river, only those zones hydrologically connected with the rivers were included.

Table 7-2. Validation results for 100-year flood maps.

Region	Correct (%)		Fit (%)	
	JRC	RAIN	JRC	RAIN
Saxony, Germany	**57**	**60**	**36**	**29**
Chemnitz (NUTS-2)	50	48	30	30
Dresden (NUTS-2)	44	57	29	24
Leipzig (NUTS-2)	71	68	43	35
England	**51**	**78**	**40**	**44**
Severn river basin	76	82	57	49
Thames river basin	66	67	41	38
Other river basins	48	78	38	44
Lower Austria	**54**	**60**	**24**	**26**

The model results were compared with a pan-European map by the Joint Research Centre (Alfieri et al. 2014). This source was used to calibrate the model, which was done through adjustment of the roughness coefficient. Roughness was defined as a global value for each of seven sub-simulations (representing different regions of Europe) in which the SOBEK model was divided.

Both the RAIN map and the JRC map were contrasted with a number of local, high-resolution studies (see "Data sets" section). The following equations were used:

$$Correct(\%) = \frac{FA_{EM} \cap FA_{LM}}{FA_{LM}} \times 100 \qquad (2)$$

$$Fit(\%) = \frac{FA_{EM} \cap FA_{LM}}{FA_{EM} \cup FA_{LM}} \times 100 \qquad (3)$$

where FA_{EM} is the area flooded in the European map and FA_{LM} is the area flooded in the reference local map. The results of the comparison are presented in Table 7-2. In England and Lower Austria the RAIN map achieved better results than the JRC map, though for Saxony the results are slightly worse. It should be also noted that for lower return periods the accuracy drops (30-years, for England and Lower Austria), but increases for larger return periods (1000-year in England and 300-year in Lower Austria).

7.3   Present climate

River flood hazard zones in the historical scenario are presented in two variants: without flood protection (Fig. 7.5) and with flood protection estimated from the FLOPROS database (Fig. 7.6). The area of the flood zones is presented in Fig. 7.7 (by country) and Fig. 7.8 (by river basin). The total area identified within the 5 return periods considered here was almost 389,000 km^2, which is about six times more than the total for coastal flood hazard, if we do not include impact of flood defences.

A majority of the flood zones in the domain were 10-year zones, with only one-sixth belonging to other zones. More than half of the flood hazard was concentrated in only seven countries: Germany, Hungary, France, Romania, Italy, Russia (only a small part of this country is included in the domain) and Poland. Splitting the hazard zones by river basin we see also that only seven of them combine more than half of the endangered area: Danube (mainly in Austria, Hungary, Serbia and Romania), Neva (Russia), Vistula (Poland), Elbe (mainly Germany), Oder (mostly Poland and Germany), Rhine (mainly Germany) and Po (Italy).

Taking into account flood defences, the 1000-year zone is only slightly smaller (376,000 km^2). A decrease is noticeable only in Netherlands, where "dike rings" provide a high level of protection from both coastal and river floods, and Austria, where flood defences along the Danube have a high protection standard. The 10-year flood zone is mostly constrained to the Dniester river catchment (6,400 km^2), while the 30-year zone is mostly present in the Balkans and former Soviet Union (in the basins of Danube, Nemunas and Evros, among others). Hazard increases substantially when moving to a return period of 100 years, with the largest zones observed in Italy (mainly Po river basin), Russia (mostly Neva and Narva basins) and Romania (Danube). In the next increment, Germany, Hungary and Poland appear at the top of the list.

RIVER FLOOD HAZARD ZONES
1971-2000, 10- to 1000-year return period - no flood protection

Fig. 7.5. River flood hazard zones by return period, historical scenario (1971-2000), no flood protection.

Note on map usage: Coastal and river flood risk maps presented in this report, as well as data available for download as a result of the project, were made using large-scale datasets and are intended for providing a European-wide overview of present and future probability of occurrence of floods. Therefore, extreme caution should be made when drawing local-scale conclusions from the maps. Local factors can have substantial influence on the actual level of hazard, especially the presence of hydraulic structures such as dams or flood defences. In case of the latter ("with flood protection" scenario) they represent either flood protection standard defined by law or design of the structure rather than its actual failure probability or, in most cases, only a rough estimate of the level of protection.

Fig. 7.6. River flood hazard zones by return period, historical scenario (1971-2000), with flood protection.

The country with the largest hazard level proportional to its area is Hungary, as 37% of country lies within the 1000-year zone (disregarding flood defences). Other countries with substantial hazard are the Netherlands (26% without defences, but only 1% when including flood protection), Serbia (24%), Croatia (20%) and Slovakia (14%). Four out of five of the aforementioned countries are located in the Danube basin, which is only the biggest basin in the domain and the one with largest flood extent, but also has the largest hazard as a proportion of its area (15%) among large river basins. Elevated

71

No flood protection scenario   With (estimated) flood protection scenario
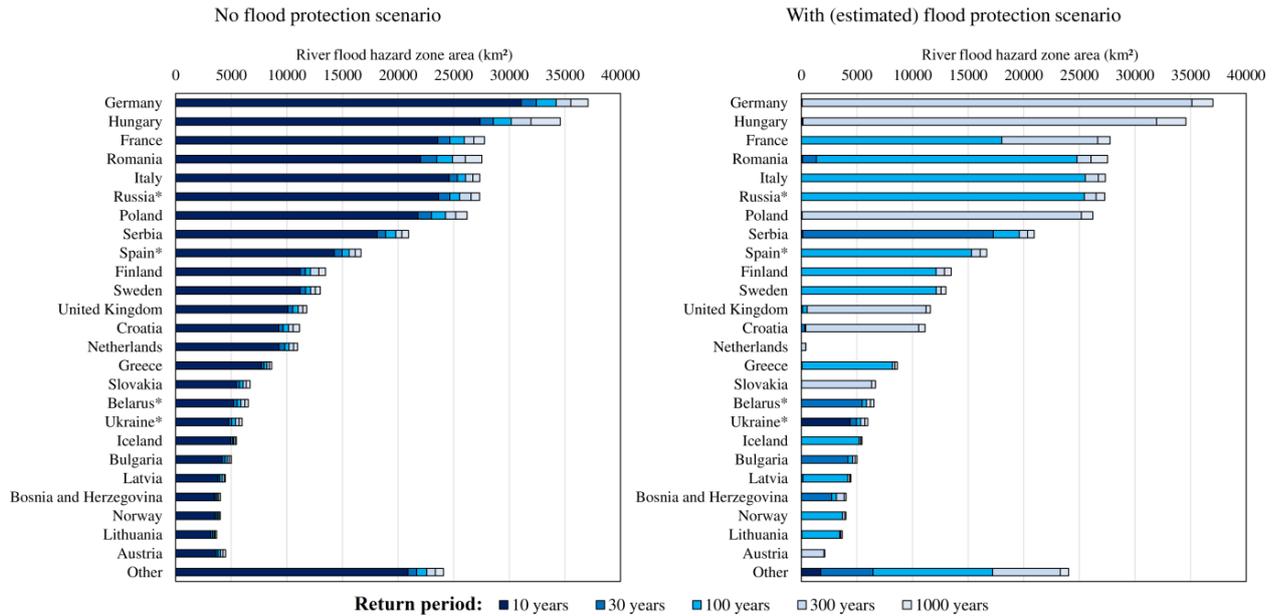
Fig. 7.7. Size of river flood hazard zones by country, without (left) and with (right) flood protection. Countries only partially located within the simulation domain are marked with an asterix (*).

No flood protection scenario   With (estimated) flood protection scenario
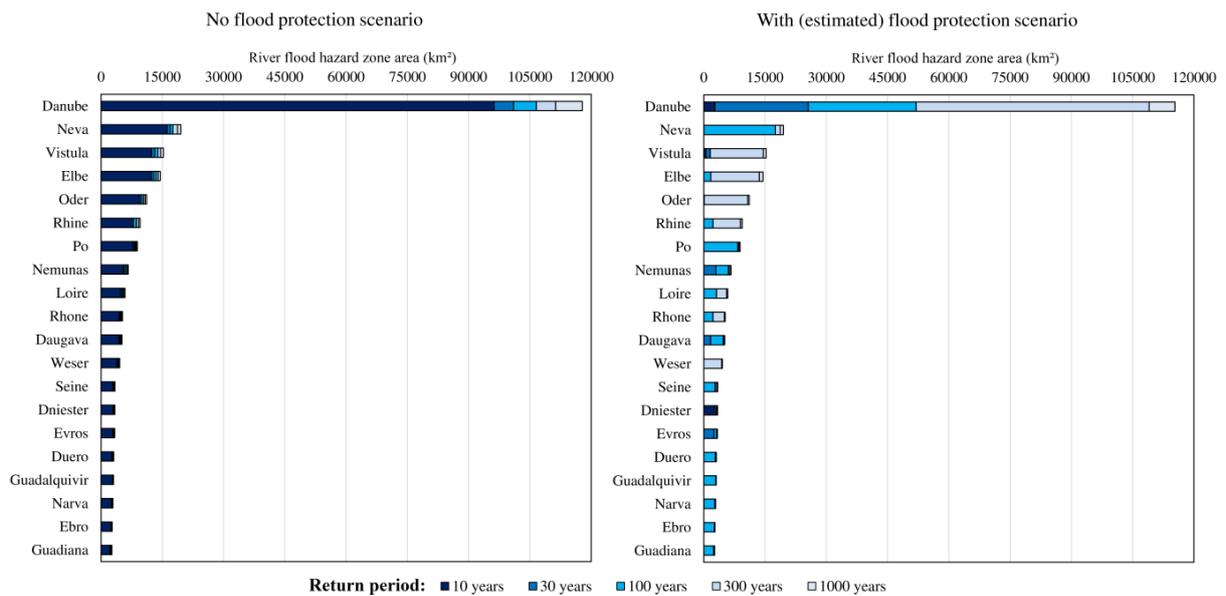
Fig. 7.8. Size of flood hazard zones in 20 river basins with the largest flood hazard, without (left) and with (right) flood protection.

hazard is also present in Po river basin (12%), Weser (10%) and Oder (9%). On the other end, Nordic countries have low levels of hazard; only 1% of Norway is within the 1000-year zone, together with 3% of Sweden and Denmark and 4% of Finland. Only 3% of the territory is in the hazard zones in Ireland, Portugal, Spain and Switzerland. In France, United Kingdom and Austria the figure is 5%, in Poland 8% and Germany 10%. Out of the 20 highlighted river basin, the lowest hazard is observed in the Iberian rivers of Ebro and Duero (3%). In general, mountainous river basins and countries tend to have less flood hazard as a proportion of their territory, since the flood is constrained to narrow

valleys, in contrast to large flood zones in the plains of Hungary or northern Europe. It should be noted, however, that the analysis encompasses only rivers that have catchments no smaller than 100 km^2, whereas numerous smaller rivers are prone to flash floods in hilly and mountainous areas.

7.4   Climate predictions

7.4.1   General remarks

Future river flood hazard depends on largely changes in river discharge. These were considered as a result of future trends in precipitation, snowmelt and runoff coefficient (i.e. maximum annual total runoff derived from climate model divided by maximum annual precipitation and snowmelt). Effects of changes in land cover (lakes, marshes, build-up areas) on discharge were not considered here.

The hazard was analysed in five increments – 10-, 30-, 100-, 300- and 1000-year return periods. We also consider the change in flood hazard in context of existing (estimated) flood protection standards. For the purpose of this analysis, the dikes are assumed to be as high as the water level for a given return period in the historical scenario (1971–2000). The return period was taken from the protection standards database FLOPROS (Scussolini et al. 2015). Therefore, if the water level with the same return period equalling the protection standard is higher in the future scenario compared to the historical scenario, the area currently protected by this theoretical dike is considered flooded.
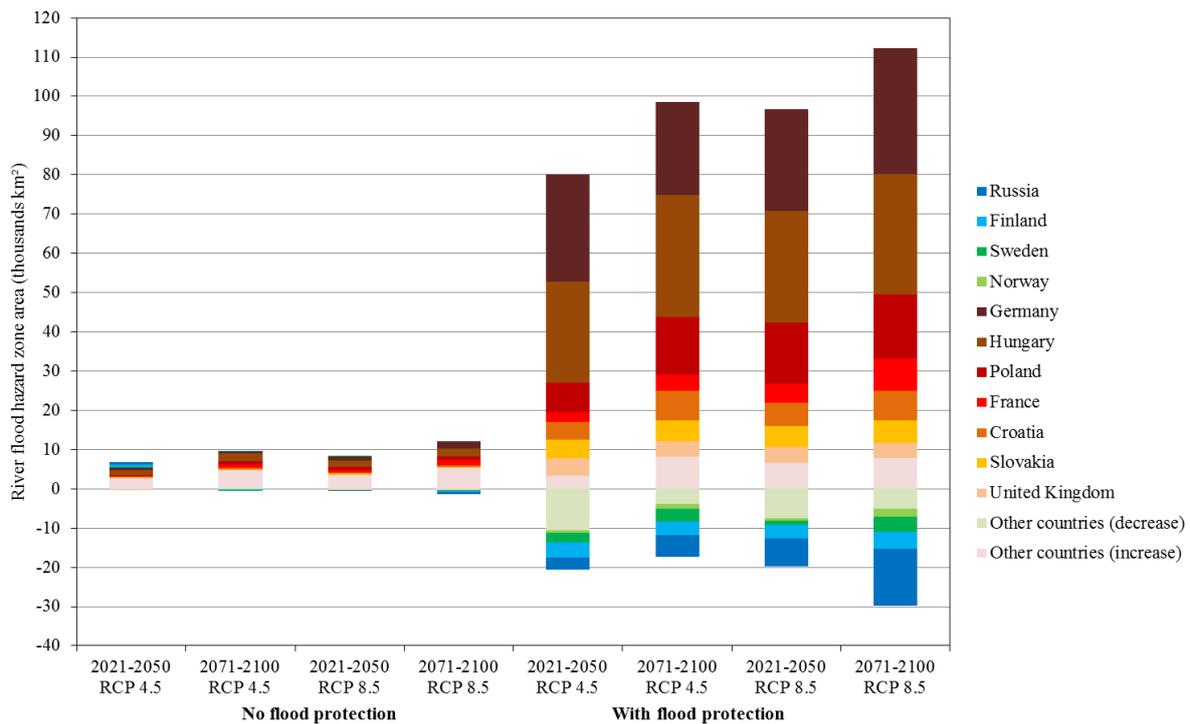
Fig. 7.9. Contributions of selected countries to overall changes in 100-year flood zone area in Europe by scenario.

Flood hazard zones cover only up to 7.2% of the domain, therefore, for the sake of clarity, the graphical representation in the maps (Fig. 7.10, Fig. 7.11) was changed compared to that of the previous section (Fig. 7.5, Fig. 7.6). I.e. we calculate the area covered by flood hazard zones per

50x50 km cells, and the change in that area in the future. We only present the 100-year flood scenario in those graphs, but the presented trends are mostly representative for the other time periods as well, even though in the "with flood protection" flooding may occur or not at all in a given region at different return periods. Those aspects are discussed in the next section.

7.4.2   Trends in flood hazard

Similar to the results of the coastal flood hazard analysis, the overall size of the river flood hazard zones increased for all four future scenarios. Still, there is a small change in their area when we do not consider flood defences. By mid-century (2021–2050), RCP 4.5 scenario adds 6,500 km^2 (1.7%) to the 1000-year zone, while RCP 8.5 increases the flood overlay by 8,000 km^2 (2.1%) compared to 1971–2000. For 2071–2100, these figures are 17,100 km^2 and 9,800 km^2, respectively (Fig. 7.12, top left), which constitutes 2.5–4.4% of the 1971–2000 flood zone. This modest increase can be attributed to the modest, on average, increase in river discharge in Europe as whole. For 1000-year discharge it is about 5% by mid-century in RCP 4.5 and around 7% by the end of the century. For RCP 8.5, the increase is about 8% in both time periods. Naturally, the same relative change in discharge has very different effects depending on the size of the river and characteristics of the floodplain. The aforementioned percentages are also simple averages of all rivers sections drained by catchments with an area of 100 km^2 and more in Europe, though very similar figures are obtained when averaging discharge at river mouths.

Taking into consideration flood protection standards, the differences between scenarios are more visible. All the increments of flood zones increase in all scenarios, except the 300-year zone, which decreases slightly in all scenarios. The 10-year zone, estimated at 6,400 km^2 in 1971–2000, is projected to reach 28,000–50,000 km^2. The largest expansion in absolute terms was calculated for the 30-year zone, from 43,200 km^2 in the end of the 20th century to 130,000–183,000 km^2 by 2071–2100. The 100-year will be larger by around a third (from 215,000 to 275,000-297,000 km^2). Smaller changes are expected in flood hazard with lower probability of occurrence: the 300-year zone is projected decrease by 1,700–15,700 km^2, while the 1000-year zone could add 6,700–18,600 km^2.

Nevertheless, trends in river flood hazard are very diversified across Europe. Changes in flood extents presented in (Fig. 7.10, Fig. 7.11) were aggregated to a 50x50 km grid. Fig. 7.12 shows the size of the flood zones for selected countries which have one of the largest flood zones, and which between themselves contain around 40% of all flood hazard in Europe, while Fig. 7.13 presents the same for river basins, where almost half of the flood zones in Europe occur. With or without flood defences, the largest increases in the hazard can be observed in central Europe, particularly in Germany, Hungary and Poland, as can be seen in Fig. 7.9. Increased hazard could be observed also in France and the UK. Meanwhile, decreases are mostly observed in northern Europe, particularly in Scandinavia, mainly due to the projected decline in total snowfall over the winter season and, consequently, snowmelt. To a lesser extent, a decrease of flood hazard is projected in many locations around the Mediterranean Sea.

River floods

Area of hazard zones at risk from a 100-year flood, assuming <u>no flood protection</u>.
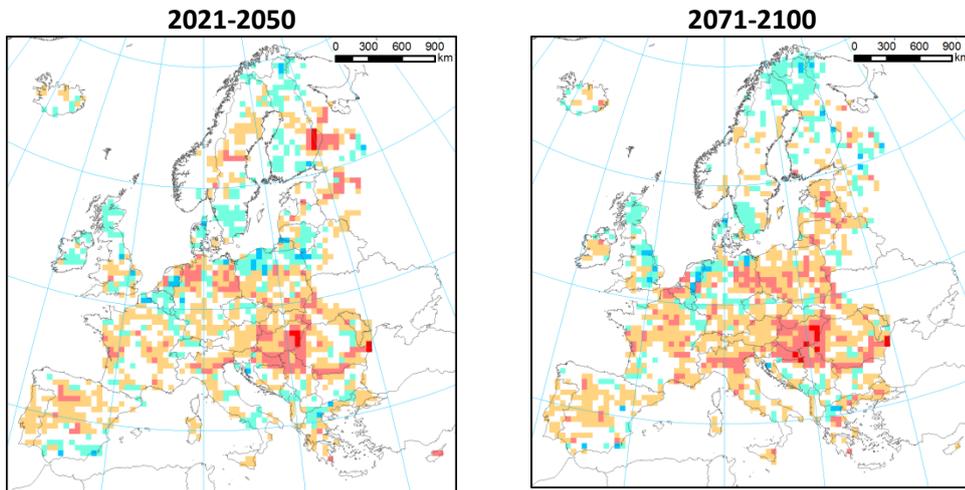
Reference Period:

1971-2000:

Predicted Changes

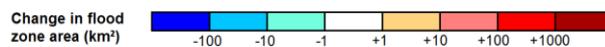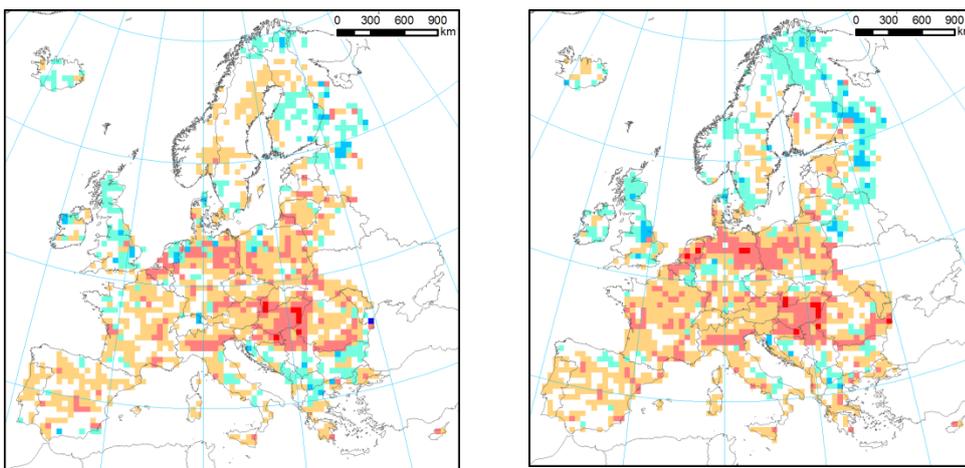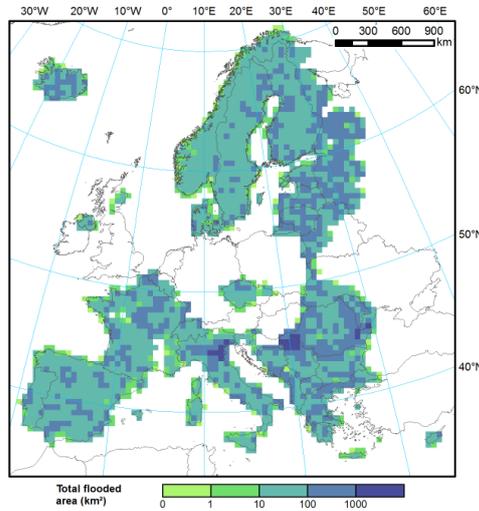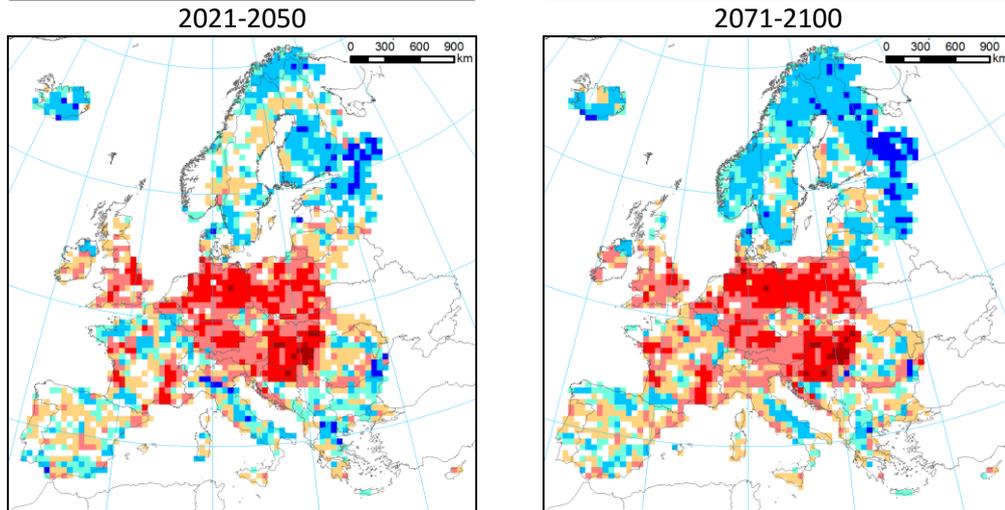|	2021-2050	2071-2100
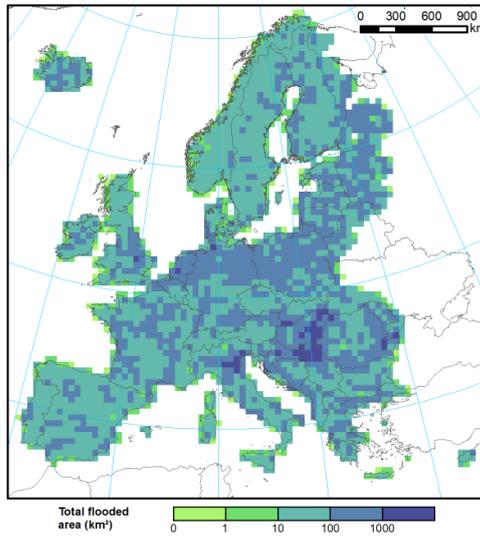
RCP 4.5:

RCP 8.5:

Fig. 7.10. Total area of 100-year river flood hazard zones (no flood protection), aggregated to 50x50 km grid, and changes under climate scenarios.

River floods

Area of hazard zones at risk from a 100-year flood, assuming <u>current flood protection</u>.

Present

1971-2000:

Predicted Changes

2021-2050   2071-2100

RCP 4.5:

2021-2050   2071-2100
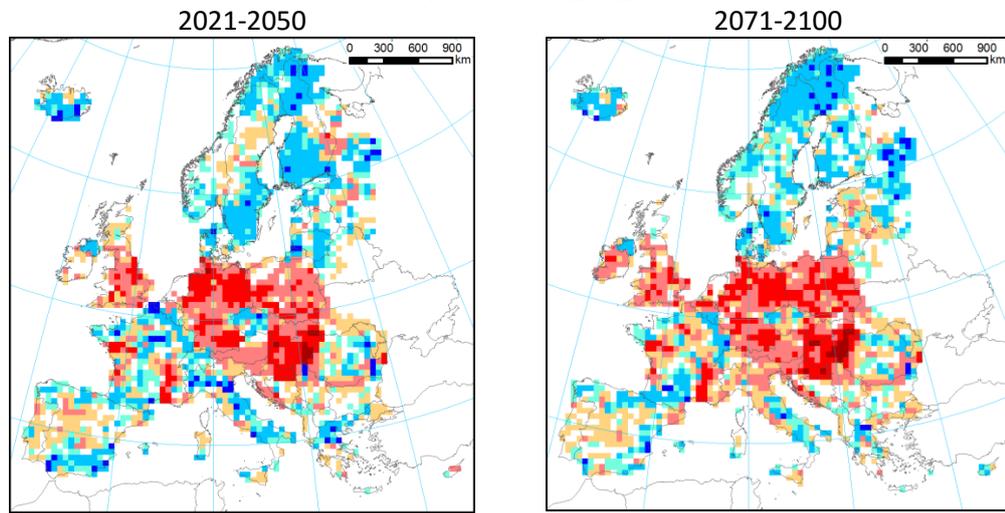
RCP 8.5:

Fig. 7.11. Total area of 100-year river flood hazard zones (with estimated current flood protection), aggregated to 50x50 km grid, and changes under climate scenarios.

Germany

The country with the biggest (absolute) flood hazard is Germany. It is reckoned (in the FLOPROS database) that the country-wide protection standard is 100 years. The majority of the defence will not maintain that standard. A quarter of the present flood hazard zone is projected to be endangered by only 30-year floods, and almost half in the 2071–2100 RCP 8.5 scenario. 63–82% of the hazard zone will have a return period of no more than 100 years. Germany is the largest contributor to European flood hazard in scenarios "with flood protection" 2021–2050 RCP 4.5 and 2071–2100 RCP 8.5. Within Germany, the largest increase is observed in the north-east part, mainly in the Elbe river basin. Smaller increases, and even some decreases could be found in the central part of the country, with relatively modest changes in hazard in the Rhine river basin.

Hungary

Hungary has the largest contribution to an increase in flood hazard in Europe except for the two scenarios, where expansion of flood zones is higher in Germany (2021–2050 RCP 4.5 and 2071–2100 RCP 8.5). Hungary is completely contained with the Danube river basin, including one of its biggest tributaries, Tisza river. Without flood protection, the increase is the largest in the 2021–2050 RCP 4.5 scenario, which stands out from other scenarios. Flood protection standard are anticipated at 100 years, but the 30-year zone is projected to cover a third of the entire area at risk by mid-century, and half by end of the century. Virtually all flood defence could become below their current standard of protection by 2071–2100. Very similar pattern could be observed in Romania, which is also entirely in the Danube basin, except for the coastal region. The flood protection is considered to be of lower standard (50 years) throughout the country, and already by 2021–2050 may become insufficient to cope with a 30-year flood, which will replace two-thirds of the 100-year zone. In many locations, even a 10-year flood will be above the current protection standard. However, the 100-year zone itself will be slightly smaller (except for 2021–50 RCP 4.5 scenario) due to a decrease in extreme discharge in some of the smaller tributaries of Danube.

France

France, which includes several large rivers, a general increase in flood hazard is project in each subsequent scenario. It is estimated that flood protection standard in the country is around 50 years, with 100 years or more in some regions. The largest fraction of the flood hazard is contained in the Loire river basin, though the largest increase in hazard is projected in the Rhone basin in southern France. All five increments of flood zones are projected to expand in all scenarios. Half of the 100-year zone will become a 30-year zone by mid-century in RCP 4.5 scenario and almost all of it by 2071–2100 (RCP 8.5). Some decrease of hazard can be only observed in some scenarios in the mountainous south-western part of the country (Pyrenees and Massif Central).

Italy

In Italy more contrasting trends could be observed. With flood protection standard estimated mostly at about 50–70 years, most of the 100-year flood zone is projected to become a 30-year zone. However, in the 2021–2050 scenarios there is a decrease of the 100-year and 300-year zones, due to a decrease in hazard in the Apennines. However, large increases are projected in the Po river basin, which contains a third of all river flood hazard zones in Italy. Similarly, in Spain the 30-year zone is

projected to increase (mainly due to trends in the central part of the country), but the 100-year will decrease thanks to lower extreme discharges in the coastal regions.

Nordic countries

Diversified, but on the whole contrasting with the rest of Europe, trends are projected in northern Europe. In Fig. 7.12 an aggregate for Finland and Sweden is presented, while in Fig. 7.13 data for Neva river basin, mostly located in north-western Russia, are shown. Throughout the region, the flood protection standards are estimated at 40–50 years. In most of the area, a decrease in discharges due to reduced snowmelt is expected, which is the main contributor to extreme floods. In some parts, however, a slight increase is projected, therefore a 30-year zone will replace part of the area currently at risk from a 100-year flood event. In Sweden and Finland, the latter will shrink by about one-fourth in all scenarios, together with a slight decrease in the extent of the 300-year zone. The 1000-year zone will be larger in 2021–2050 than in 1971–2000, but will become smaller in 2071–2100. In the Neva basin, the 100-year zone will become significantly smaller. In the 2071–2100 RCP 8.5 scenario this zone has only a third of the area in the historical scenario, while the 300-year zone is smaller by half, and 1000-year zone by a quarter. The flood hazard in Norway and Iceland is projected to decline as well.

Other countries

Other countries worth mentioning are Poland, the United Kingdom and the Netherlands. Poland, comprised mostly of two large river basins (Vistula and Oder) is expected to experience a decline in hazard for 300-year and 1000-year floods in 2021–2050 RCP 4.5 scenario. In other scenarios, flood extents will increase, with the 100-year zone replacing about two-thirds of the 300-year zone. It should be noted, however, that flood protection standards for Poland are grossly overestimated in FLOPROS, which assigned the highest design standard in use (200 years) to the entire territory. That said, it does not change the conclusion that a significant increase in hazard is projected.

Trends in the river flood hazard in the United Kingdom show stark contrasts (flood protection included): 30-year, and particularly 100-year zones will expand from almost none to half of all zones, while 300-year and 1000-year zones will become smaller. This is caused by a projected decline in extreme river discharge in Northern Ireland and Scotland, and increase in England and Wales.

Finally, in the Netherlands flood protection standards are lower than 1000 years only in the Meuse river basin. However, due to the increase in extreme river discharges, the 1000-year zone is expected to expand from barely 400 km^2 to about 2400 km^2 by mid-century and 3100 (RCP 4.5) or 8500 km^2 (RCP 8.5) by end-century. More than half of the aforementioned area of 8500 km^2 is already contained in the 300-year zone.

7.4.3 Uncertainties

The analysis includes several sources of uncertainties, on many levels, similarly to coastal flood analysis. The first is related to input data. River discharge scenarios were calculated using a statistical model, and though it has good quality compared to alternative approaches, it is not as accurate as scenario derived from gauging stations for local flood studies. The results do not include changes in land use (build-up areas, lakes, marshes), both in historical or future scenarios. Also, the river flow
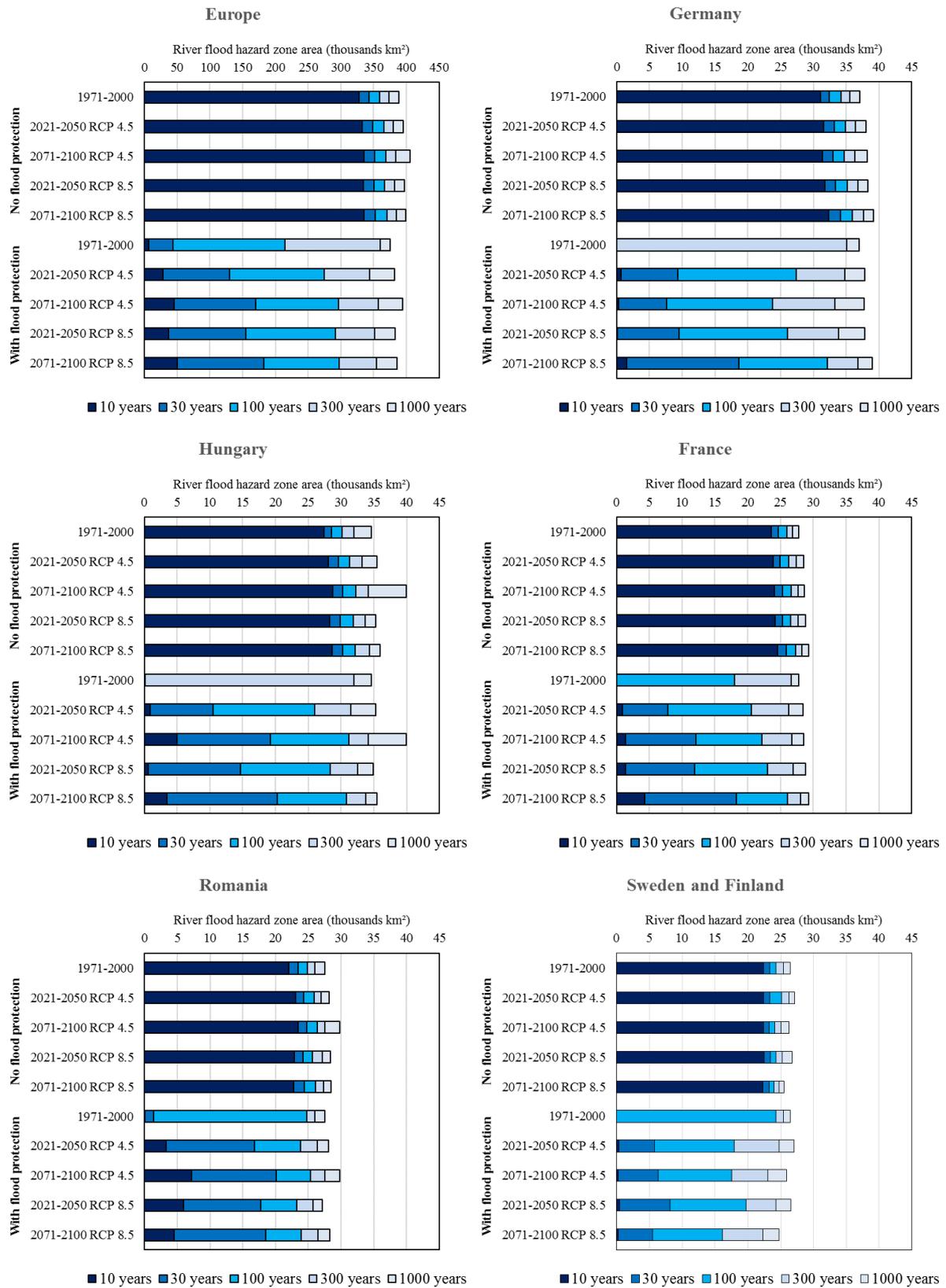
Fig. 7.12. Impact of climate change on river flood hazard zone area, with and without flood protection, for selected countries and Europe within the domain (note different scale for the graph for Europe).
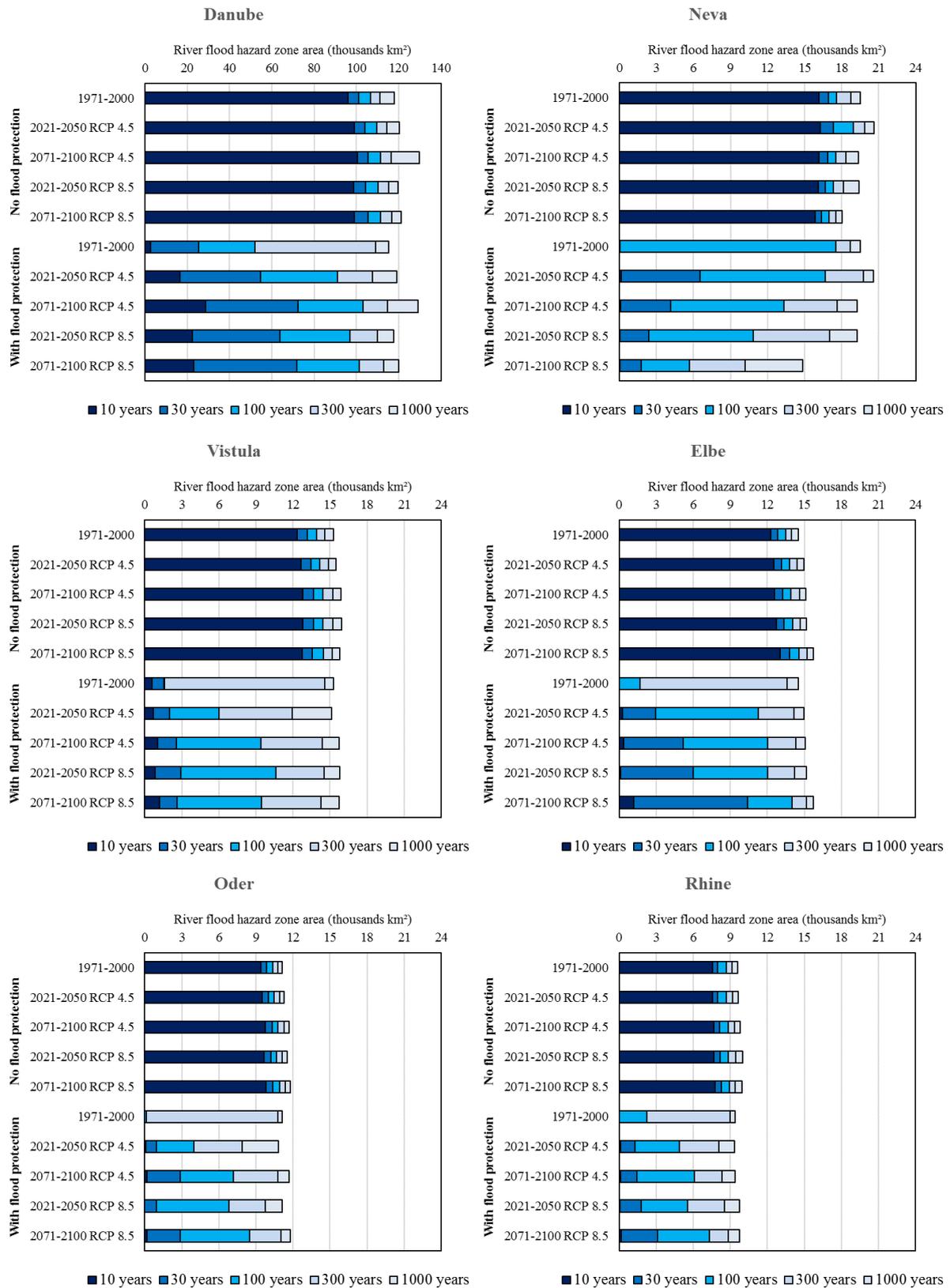
Fig. 7.13. Impact of climate change on river flood hazard zone area, with and without flood protection, for selected river basins with largest flood zones (note different scale for the graph for Danube).

was obtained from the hydrodynamic model utilizing one-dimensional "steady state" simulation and GIS mapping, which is not as accurate as a full two-dimensional simulation. The maps were validated in three regions, showing tendency to overestimate hazard.

Another source of uncertainty is the type of events analysed. Only rivers with catchments that have an area of at least 100 km^2 were included in the calculation. This omits very small rivers where dangerous flash floods can occur, especially in hilly or mountainous terrain. Flash floods also happen without any river at all; insufficient drainage in an area is enough to cause a flood. Moreover, we estimate the extreme river discharge based on two main factors causing flood – rainfall and snowmelt, while floods in northern Europe are also caused by ice and frazil blocking the river flow. We also do not include the reduction of the flood wave through reservoirs or bypass channels but rather consider the flow under 'natural' conditions.

Some uncertainty is related with delimitation of flood hazard zones. Vertical accuracy of the pan-European DEM, could influence the results to some degree, as vegetation and urban areas were only filtered out to some extent. Most crucially, however, the elevation model does not include the bed or embankments of rivers. It is assumed that the surface of DEM represents roughly the mean water level in the river, though some other studies used 'bankfull' discharge. Also, bed geometry can change in the future, modifying the transformation of river discharges into water levels. Existence of flood defences, when close to the river, can substantially alter the flow during an extreme event. Here, we only consider the defences after the flood zones were delimitated. Additionally, the flood protection standards used here are only the nominal values that do not take into account the failure probability of the flood defence structure itself. Large parts of those standards are anyway only estimates, and all are considered to be same for all rivers in a given administrative unit, which is very unrealistic. Different rivers have wildly different protection standards based on estimated or anticipated flood risk. Furthermore, the calculation of climate change impact on flood defences is based on two assumptions. One, that the protection levels equal the water levels from the historical scenario, whereas they are locally defined using various techniques, time periods and safety margins added on top of the "design" water levels. Second, that the flood defence structure remain unchanged in the future, even though they can deteriorate over time, or they could be modernised.

Last but not least, there is uncertainty related with future climate projections. As can be noticed from Fig. 7.9, Fig. 7.11 and the text, difference between RCP 4.5 and RCP 8.5 scenarios is sometimes very large. This alone illustrates the significant uncertainty related with climate change and the climate models, as the latter are known to have limited accuracy for precipitation, let alone extreme rainfall. Also, the results of only one climate model were analysed.

7.5   Summary

In this chapter we analysed river flood hazard in a domain covering most of the European continent. Extreme river discharges and their probability of occurrence were calculated using a newly-developed statistical model based on Bayesian Networks. In this model, data from EURO-CORDEX climate simulations were utilized to make projections of future river discharges. The model's results were successfully validated and used as boundary conditions for a hydrodynamic simulation of water levels. The resulting flood maps, covering catchments with an area of 100 km^2 and more, have also

shown relatively good accuracy. They were obtained for five different return periods in a historical scenario and two climate change scenarios (RCP 4.5 and 8.5) in two time periods.

The results show that river flood hazard is more evenly distributed across Europe than coastal floods. The Danube basin stands out in both total area at risk and flood hazard area relative to the size of the basin, while Germany was found to contain the largest flood-prone area of all analysed territories. When flood protection is not included, the increase in hazard zones is modest; results show, however, that some of the existing flood defences will need to be enhanced to cope with increased water levels. Throughout Europe, 10-year, 30-year and 100-year floods will expand greatly. Germany, Hungary, Poland and France are expected to have the largest absolute increases in flood hazard zone area. On the other hand, northern Europe (Scandinavia, Scotland, north-western Russia) will encounter a decrease. This contrasting trend is caused by a projected decline in total snowfall over the winter season, which in turn will result a decrease in snowmelt, which is the prime factor behind floods in that region. In the rest of Europe, more extreme rainfall will cause larger floods.

8. Assessment of impact indicators for winter phenomena

Andrea Vajda, Ilari Lehtonen, Matti Kämäräinen, Ari Venäläinen (FMI)

In order to assess the impact of severe winter weather events, such as heavy snowfall, blizzard, heavy snow load and freezing rain on the critical infrastructure (CI) we have defined a set of impact indicators for each phenomenon, taking into account the exposure of CI to the events.

The definition of impact threshold process was based on:

- a literature review on the subject, covering more than 100 research papers published in national and international journals and books, reports of research projects and research councils from Europe, Canada and the USA;
- media reports, including a large number of identified severe winter events and their impacts on CI over Europe during 2000-2014;
- surveys conducted with CI operators (29) covering different sectors, such as transportation, energy sector, telecommunication, rescue services, and surveys conducted with weather services (18);
- warning practices of the European Weather Services gathered into a common database for use at the Meteoalarm website (www.meteoalarm.eu);
- cases studies of past events.

A classification defined by two threshold levels was developed for the studied winter phenomena; the qualitative descriptions of the thresholds are:

- *1st threshold:* Some adverse impacts are expected, their severity depends on the resilience of the system, transportation is mainly affected.
- *2nd threshold*: The weather phenomena are so severe that is likely that adverse impact will occur, CI system is seriously impacted.

The threshold values were defined for different weather parameters derived from daily data series, based on the severity of the identified impacts and consequences. The impacts and consequences related to exceeding a particular threshold vary across Europe and depend on the resilience of the system, especially the transport infrastructure. The thresholds defined and the impacts and consequences of each winter phenomena are presented in the following tables.

These defined impact indicators allow the estimation of probabilities of winter extremes in the present and future climate.

Table 8-1. Snowfall (Rs (snowfall rate)/24h , 1 mm precipitation=1 cm of snow)

Threshold	Impacts	Consequences
Rs ≥ 6 cm	Reduced friction and slipperiness on roads, when combined with low temperature and wind, rail points may get stuck.	Increased accident rate in road traffic, reduced road capacity, road closures, possible delays and cancellations.
Rs ≥ 25 cm	Slippery roads, accumulated snow banks. Poor visibility. Accumulated snow on power lines, structures and trees.	Disturbed traffic, high accident rate, closed roads, delays and cancellations of trains. Broken tree limbs or fallen trees on power lines, damaged or broken power lines, power outages. Limited access to repair equipment. Collapsed roofs.

Table 8-2. Blizzard (Rs (snowfall rate), Wg (wind gust) and T (temperature))

Threshold	Impacts	Consequences
Rs ≥ 10 cm, Wg ≥ 17 m/s, T ≤ 0 °C	Fallen trees on roads, rails and electricity lines; snow banks, slippery roads, poor visibility, rail points may get stuck. Accumulated snow on structures and power lines.	Increased rate of injuries and accidents in road traffic (2-4 times more accidents compared to the mean), delays, and cancellations in all transportation modes. Wild power failure, damaged buildings: detached roofs and falling scaffoldings.

Table 8-3. Freezing rain (RR (rain rate)/24 h)

Threshold	Impacts	Consequences
RR ≥ 5 mm	Accumulation of ice on roads, vehicles, trees, power lines and structures, slippery roads and bridges, hazardous driving conditions. The accumulated ice may cause forest damage, possible canopy and stem breakage.	Increased rate of accidents and injuries; disruptions of normal transportation (road, rail, aviation). Broken trees might damage the power lines, lost in power transmission efficiency or even power outages.

| RR ≥ 25 mm | Substantial damage to trees, e.g. excessive tree breakage, damaging ice thickness on electricity lines, pole-mounted communication system, cellular towers and other structures. Ice accumulation snaps the power cables or even failure of transmission towers.

Roads and vehicles covered by thick ice. | Distribution and transmission line failure, power outages, severe disruption of transportation, collapses of communication towers and infrastructure that delays the emergency responses. Prolonged and widespread interruptions, outages may last for 5-10 days.

Serious disruption in transportation, road closures, villages and cities might be cut off for several days. |

Table 8-4. Crown snow load (SL (snow load))

Threshold	Impacts	Consequences
SL ≥ 20 kg m^{-2}	Wet snow accreting on trees causes damage to forest: canopies and stems may break or lean and birches start to bend. If the soil is unfrozen, some trees may be also uprooted. Sliding snow on building's roofs	Fallen trees may disturb transportation, resulting in reduced road capacity and inaccessible roads. Damaged trees leaned and bended over power lines interrupt the power transmission resulting in power outages. Snow falling from high structure may cause property damage, injuries or even fatalities.
SL ≥ 60 kg m^{-2}	Heavy wet snow or snow load combined with ice accretion causes serious forest damage. Even power poles may collapse and high voltage power transmission towers may crash. Ice accretion on wind turbines reduces aerodynamic performance of the blades, cause instrument error. Snow load on building structure.	Power transmission lines and communication wires will break due to heavy snow load and damaged trees fallen over the lines leading possibly to total failure in power grid system. Roofs at defectively constructed buildings may collapse. Power losses for wind turbine, reduced wind energy production. Damages in building's roofs, structural failure and possible collapse.

9. Heavy snowfall

Matti Kämäräinen and Andrea Vajda (FMI)

9.1 Introduction

Snowfall is typically connected to wintertime weather conditions and cold air masses. Heavy snowfalls covering large areas are typically related to low pressure systems, quite often moving in the west – east (or southwest – northeast) direction in Europe. The densest snowfall is often observed in the cold air mass, on the northern side of the low pressure center or just in front of the approaching warm frontal zone. Rising upward air motion due to topography (hills, mountains) can strengthen the precipitation. In some cases, snowfall is a result from convection in cold air masses, but then the event typically has a more local character. In the coastal areas dense snow showers can form over the open sea water (sea-effect snow).

Severe winter storms, heavy snowfall and extreme cold sometimes disrupt several sectors or even the entire transport system, such as the snowstorm over the UK during 2-9 February 2009, over Western Europe in December 2010 or over the whole continent in February 2012, when the usability of many airports and roads was disrupted. Road maintenance and operating costs, although variable from year to year, are considerable; for example, in the USA nearly 39% of annual road operating costs can be attributed to winter maintenance (Pisano et al. 2002). Safety during winter conditions is also negatively affected. Snow, sleet or ice on road surface decreases road surface friction, increasing slipperiness, resulting in a sharp increase in accident rates (Andreescu and Frost 1998, Andersson 2010), while blowing snow reduces visibility. In addition, in order to maintain road usability, snow removal logistics need to be considered, snow removal tools (snow ploughs, snow pushers) may also lead to damages in road surfaces. Heavy snowfall impacts other critical infrastructure as well, for example by causing failure in power transmission and disturbing the flow of emergency and rescues services. The magnitude of the influence and corresponding damage depends not only on the intensity of the weather extreme, but also on the preparedness of society for different extreme weather conditions.

9.2 Method

The occurrence of heavy snowfall events was estimated using the E-OBS dataset. Since the dataset does not distinguish between the liquid and solid states of precipitation, we have calculated the occurrence of snowfall using the daily precipitation amounts that accumulate when the daily mean temperature is below 0°C. The spatial interpolation methodology has smoothed the magnitudes of the extremes in the variation of the variables, thus we have applied correction factor of 0.66 for precipitation as indicated by the cross-validation with station observations (Haylock et al. 2008). The exceedance of impact thresholds, i.e. Rs ≥ 6 cm and Rs ≥ 25 cm (as described in Chapter 8) was analyzed for each grid cell and the frequency (which described the spatial variation of events better than the annual probability) of heavy snowfall events over Europe were calculated for the present climate (1981-2010).

In order to assess the changes in the probability and magnitude of severe winter events in the future climate, we have used a set of six RCMs at 50 km spatial resolution and 6-hour time resolution produced in EURO-CORDEX. For details, please refer to Section 3.3. The six models used were SMHI-RCA4-CanESM2, SMHI-RCA4-NorESM1, SMHI-RCA4-IPSL-CM5A-MR, KNMI-RACMO22E-EC-EARTH, KNMI- RACMO22E-HadGEM2-ES and MPI-CSC-REMO2009-MPI-ESM-LR.

All of these models used the RCP 4.5 and RCP 8.5 emission scenarios. The time horizon studied was 2021-2050 and 2071-2100. Based on the calculation of annual probabilities using the six RCMs, the multi-model mean of the change compared to the control period (1971-2000) was defined and presented for each threshold of the studied phenomena. The multi-model mean is the average change indicated by the six models giving each model equal weight.

The identification of snowfall events in RCMs output was performed in 6-hourly time resolution of the models. Prior to the analysis of the corresponding probabilities for the critical impact thresholds, the daily amounts of snowfall were calculated from the 6-hourly data, by identifying the snowfall based on the 2-meter temperature, which was required to be below 0°C.

Definition of snowfall between E-OBS and climate models differs, as the criterion in E-OBS is stricter (below 0°C daily mean temperature). This possibly leads to underestimation of snowfall in E-OBS compared to station observations, as snowfall may occur during the day if below-zero temperatures exist occasionally. On the other hand, the climate model precipitation data would have needed similar correction factor treatment as the E-OBS dataset to be comparable to station observations: it is likely that regional climate model precipitation output is smoothed and thus is also underestimated compared to station observations.

The statistical significance of the projected changes in the probabilities was assessed applying the non-parametric Wilcoxon signed-rank test (Wilks, 2011). Note that according to this test, the projected change is statistically significant in the case of six models at the 95% level only if all the models indicate either positive or negative change.

9.3   Present climate

Snow events impacts the entire continent, dense snowfalls (≥ 6 cm/day) occur every year over the northern parts and in the mountainous areas (not shown), with mean annual frequencies up to maximum 5 days/year in western and Southern Europe (Fig. 9.1). Only southern parts of Portugal and Spain do not encounter 6 cm snowfall events at all. The occurrence of dense snowfall events increases towards the eastern and northern part of the continent, where the average number of days with snowfall ≥ 6 cm varies between 10 and 20. The highest frequencies, over 20 days/year, are observed in the Alps, Pyrenees, Scandinavian Mountains and in Iceland.

Heavy snowfall events (≥ 25 cm/day) are the most frequent over the western coast of Norway, Iceland, the Alps and Pyrenees, in average with at least 4 days/year (Fig. 9.2). The Scandinavian countries and some parts of the Balkan Peninsula might be affected by 1 heavy snowfall case/year, the western coast of the Balkan Peninsula by 3 cases/year, while in the rest of the continent these cases occur only sporadically.
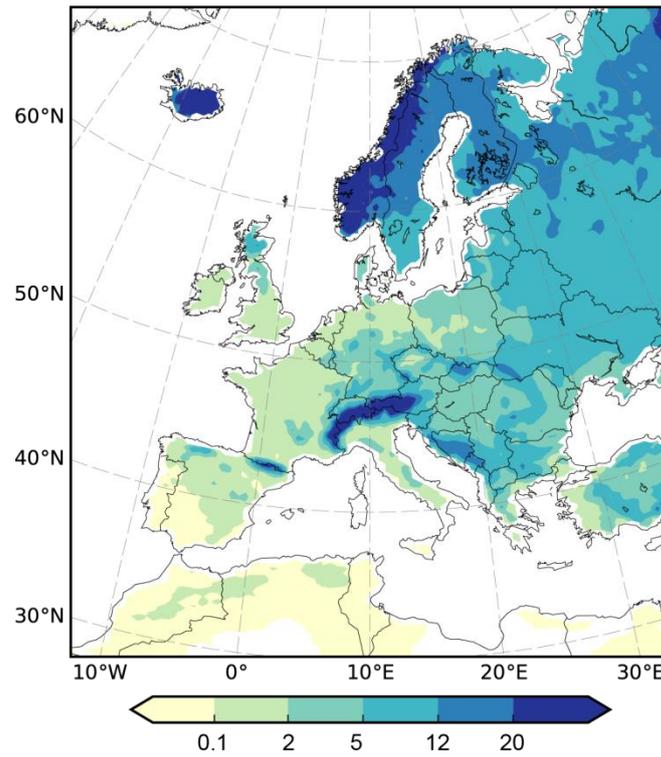
Fig. 9.1. Mean annual number of days with snowfall exceeding 6 cm during 1981-2010, based on E-OBS data.
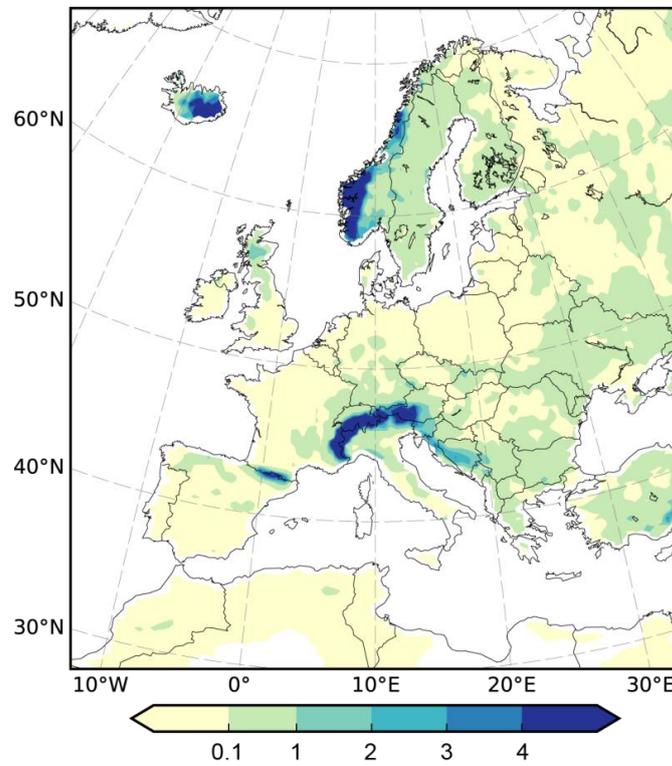

Fig. 9.2. Mean annual number of days with snowfall exceeding 25 cm during 1981-2010, based on E-OBS data.

9.4 Climate predictions

The multi-model mean geographical pattern of dense and heavy snowfall in the present day climate (1971-2000, as defined in the Method section) resembles the climatology described by the E-OBS data, even though the probabilities indicated by the latter were occasionally higher, especially in the northern and eastern parts of the domain (Fig. 9.3 and Fig. 9.4). The three SMHI-RCA4 runs produce the smallest probabilities of snowfall of the six climate models that were used, for both thresholds (not shown).

The climate change signal in 6 cm/day events (Fig. 9.3) is clear, statistically significant and strong in both analyzed future periods and in both emission scenarios. According to the multi-model mean, large areas in central, eastern and south-eastern part of Europe, the Pyrenees, the Baltic Sea and the Norwegian Sea will already encounter a significant decrease (10 – 25 percentage points, pp) of annual probabilities during 2021-2050 under both emission scenarios. The decrease of annual probabilities for dense snowfall (6 cm/day) is projected to be more robust by 2071-2100, especially under RCP 8.5. According to this scenario, a decrease of 25 – 50 pp is expected over most of central, south-eastern and eastern part of Europe. No significant increase is projected for the Alpine region and Fennoscandia, with the exception of southern Sweden, where the decreasing trend is common with the neighboring areas, e.g. the Baltic Sea.

Even though the annual probabilities are not expected to change in northern countries and Alpine region the overall annual number of snowfall events actually decreases everywhere in Europe (not shown), with strong decreasing signal found over the coasts of Norway, Iceland and the Alpine region. This signal is statistically significant, covers even larger areas than the change signal in annual probabilities, and can be seen already in the 2021-2050 period.

The 25 cm/day events are already so rare in the present-day climate that significant decreasing trends can be found only over Norway, Iceland and the Alps (25 – 50 pp) by 2100 (Fig. 9.4). In other areas the signal is insignificant, inconsistent and either slightly positive or negative. Vajda et al. (2011) reported a weak decrease in the frequency of heavy snowfall over Northern Europe, but this result was not reproduced by the six climate models used in this study.

Heavy Snowfall

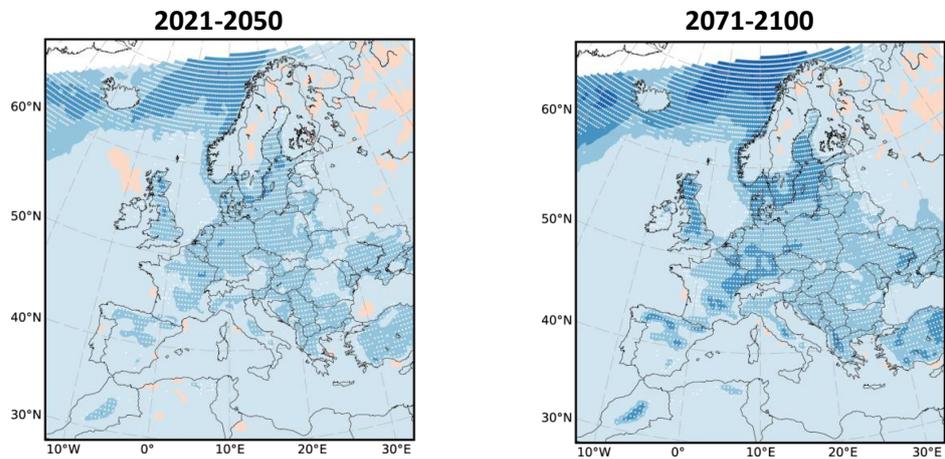**Annual probability of snowfall exceeding 6 cm / 24h (%)**

**Reference
Period**
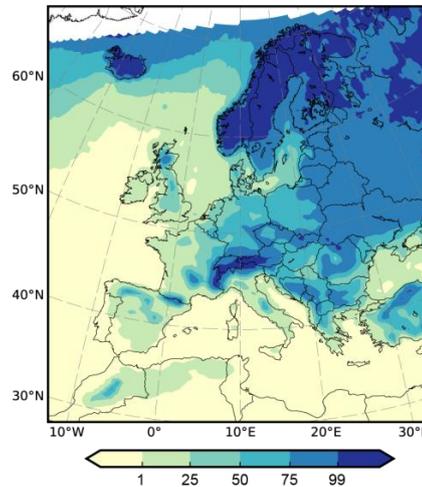
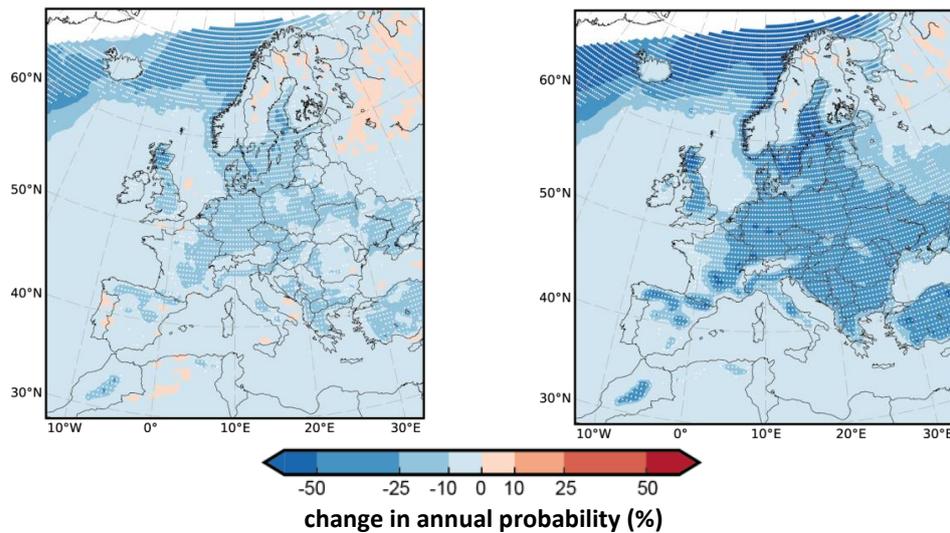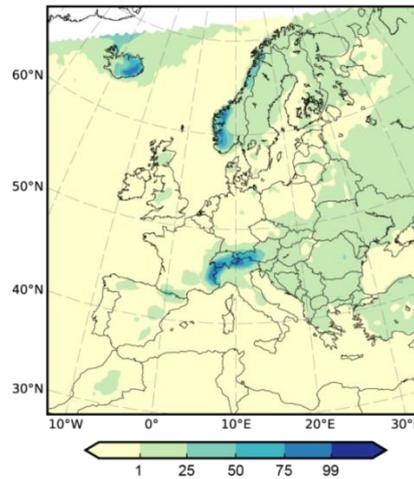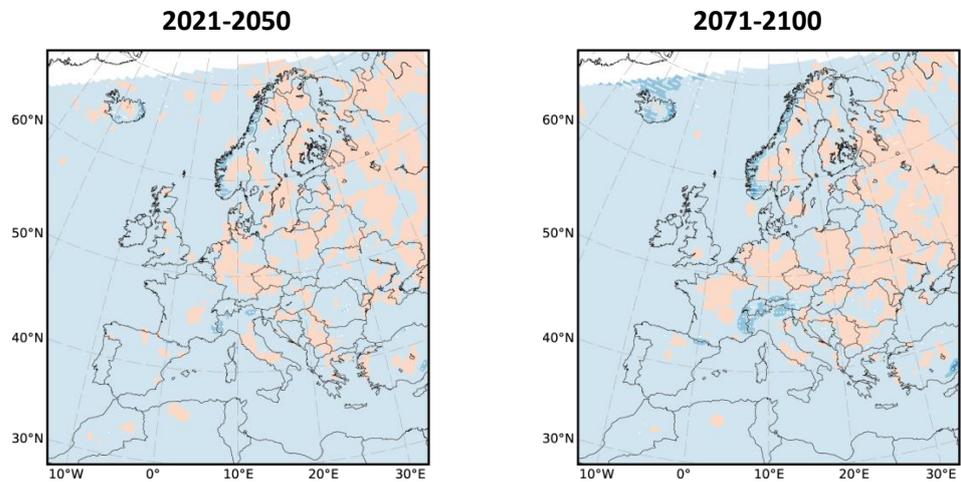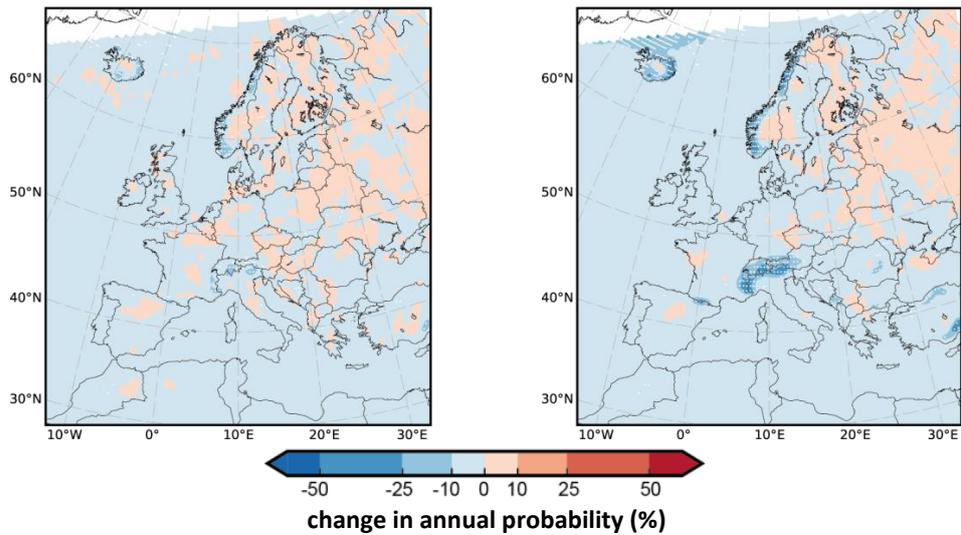1971-2000:

**Predicted
changes**

RCP 4.5:

RCP 8.5:

Fig. 9.3. (top) Multi-model mean annual probability (%) of snow fall exceeding 6 cm/24 h during 1971–2000. Multi-model mean change in annual probability of snow fall exceeding 6 cm/24 h (in percentage points) under the RCP 4.5 scenario (middle) and the RCP 8.5 scenario (bottom). White dots denote significant change at the 95% level.

Heavy Snowfall

Annual probability of snowfall exceeding 25 cm / 24h (%)

**Reference
Period**

1971-2000:

**Predicted
Changes:**

RCP 4.5:

RCP 8.5:

2021-2050 · 2071-2100

change in annual probability (%)

Fig. 9.4. (top) Multi-model mean annual probability (%) of snow fall exceeding 25 cm/24 h during 1971–2000. Multi-model mean change in annual probability of snow fall exceeding 25 cm/24 h (in percentage points) under the RCP 4.5 scenario (middle) and the RCP 8.5 scenario (bottom). White dots denote significant change at the 95% level.

10. Blizzards (snow storms)

Ilari Lehtonen and Andrea Vajda (FMI)

10.1 Introduction

A blizzard is a severe storm condition defined by low temperature, sustained wind or frequent wind gust and considerable precipitating or blowing snow, which can cause damage to structures and failures in transport control systems, as well as reduced road friction and visibility. A blizzard can have large negative impacts on society, affecting e.g. all transport means, electricity supply, and possibly causing also damage to buildings. Blizzard conditions may generate delays and cancellations in all transport modes and increase the rate of accidents, e.g during the blizzard on 23 November 2008 in Finland, described in details in RAIN D2.2 Report-List of Past Cases and by Rauhala and Juga (2010).

10.2 Method

In the evaluation of probabilities of blizzard events over Europe we have used the 6-hour forecast of 10 m wind gust and precipitation sum and the 6-hour reanalysed 2-m mean temperature from the ERA-Interim dataset. The days with blizzard conditions, i.e. Rs ≥ 10 cm, Wg ≥ 17 m/s, T ≤ 0 °C, (as described in Chapter 8 and identical to the definition used in the FP7 project EWENT) for each grid point were identified and the annual exceedance probabilities were calculated for the studied period (1981-2010).

In addition, we studied the connection of blizzards to large-scale circulation by comparing the risk between winters with positive and negative North Atlantic Oscillation (NAO) index during 1981–2010. This was motivated by the fact that it has been recently demonstrated that NAO is highly predictable months ahead and this predictability has high value for planning and adaptation to extreme winter conditions (Scaife et al., 2014). We compared the average annual frequency of blizzards between the 15 winters with positive December–February seasonal mean NAO with those 15 winters with negative seasonal mean NAO. In assessing the statistical significance of the difference in the frequency we applied the Student's t test. The NAO indices were obtained from the website of Climate Prediction Center of National Center for Environmental Prediction at http://www.cpc.ncep.noaa.gov/. The NAO basically describes fluctuations in the difference of atmospheric pressure at sea level between Iceland and the Azores and the NAO has been frequently used to illustrate the effect of large-scale circulation anomalies on winter weather in Europe. Strong positive (negative) phases of NAO tend to be associated with wet and mild (dry and cold) conditions in Northern Europe and dry (wet) conditions in Southern Europe (e.g. Hurrell 1995).

In order to assess the changes in the probability and magnitude of severe winter events in the future climate we have used a set of six RCMs at 50 km spatial resolution and 6-hour time resolution produced in EURO-CORDEX (see Section 3.3 for details). The six models used were SMHI-RCA4-CanESM2, SMHI-RCA4-NorESM1, SMHI-RCA4-IPSL-CM5A-MR, KNMI-RACMO22E-EC-EARTH, KNMI-RACMO22E-HadGEM2-ES and MPI-CSC-REMO2009-MPI-ESM-LR. All of these models used the RCP

4.5 and RCP 8.5 emission scenarios. The time horizons studied were 2021-2050 and 2071-2100, and 1971-2000 as a control period.

Because wind gust data were not available from the MPI-M-LR-MPI-CSC-REMO2009 model, we instead used the mean wind speed data with a threshold of daily maximum value of 7 m/s. Based on the calculation of annual probabilities using the six RCMs, the multi-model mean of the change compared to the control period (1971-2000) was defined and presented for each threshold of the studied phenomena. The multi-model mean is the average change indicated by the six models giving each model equal weight. The statistical significance of the projected changes in the probabilities was assessed applying the non-parametric Wilcoxon signed-rank test (Wilks, 2011). Note that, according to this test, the projected change is only statistically significant in the case of six models at the 95% level if all the models indicate either a positive or a negative change.

10.3   Present climate

In the present climate, blizzards occur most commonly in Norway and Iceland, with annual probabilities up to 75% according to the ERA-Interim reanalysis data (Fig. 10.1).
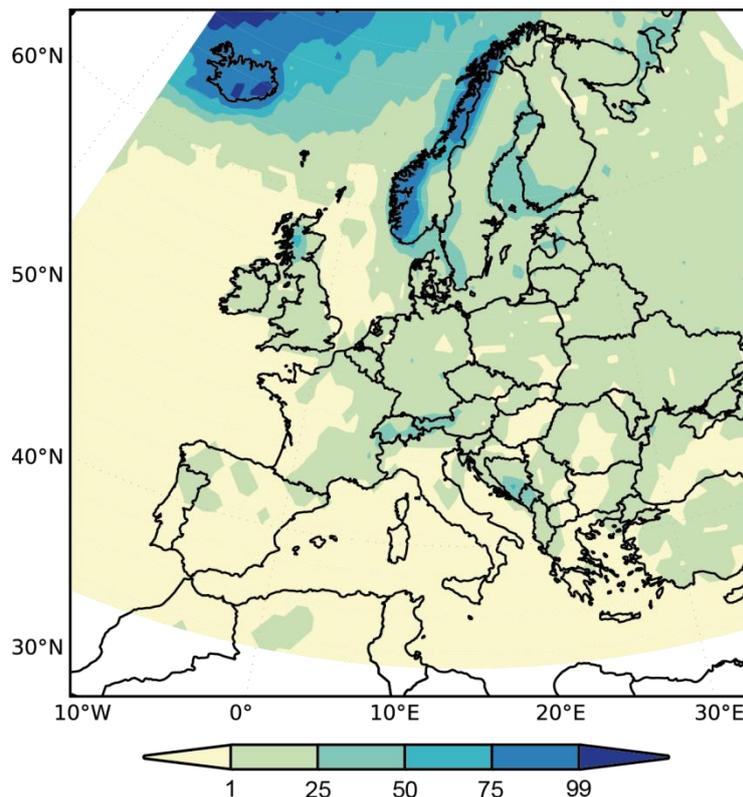
Fig. 10.1. Annual probability (%) of blizzard during the period 1981-2010 based on ERA-Interim data.

Blizzards generally become less frequent towards southern and eastern part of the continent, their annual probability ranging between 1 and 25 %. In Scandinavia, they are usually more frequent on coastal areas (50% probability) than inland because of higher wind gust speeds near the coast. In Central and Southern Europe, the annual probability of blizzards exceeds 50% over the Alps. In the

Mediterranean region blizzards largely do not occur. However, due to the relatively coarse resolution of ERA-Interim data and the difficulties in wind gust prediction the frequency of blizzard events might be underestimated.
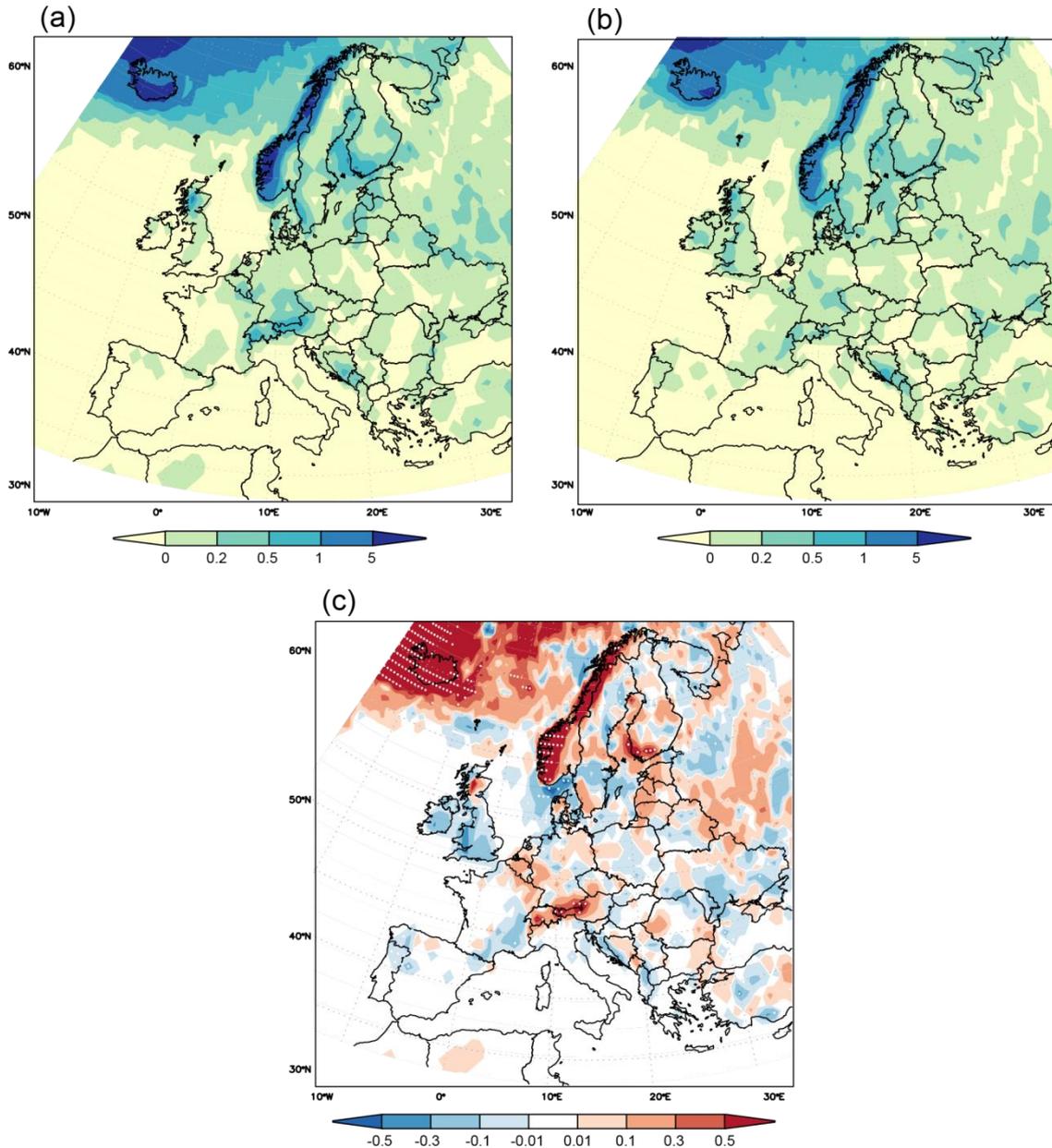
Fig. 10.2. (a) Average annual frequency of blizzards during the NAO positive winters in 1981–2010 as derived from the ERA-Interim reanalysis. (b) As in (a) but for NAO negative winters. (c) The difference in average annual frequency of blizzards between the NAO positive and NAO negative winters during 1981–2010 as derived from the ERA-Interim reanalysis.

In Fig. 10.2 we show the average annual frequency of blizzards separately for winters characterized by positive and negative NAO. The gross features of the spatial risk patterns are very similar during both kind of winters but there are some visible differences (c). Blizzards tend to occur more commonly during the positive NAO phase around Iceland and in Norway and perhaps also over the

Alps and at the south-western coast of Finland. Elsewhere no significant differences could be found. However, it seems that, for example, in England and Ireland blizzards occur mostly during negative phase of NAO but the small sample size of the events does not allow making any strong conclusions.

10.4 Climate predictions

Fig. 10.3 shows the multi-model mean annual probability of a blizzard during 1971–2000 and the projected change in the probability for the future periods 2021–2050 and 2071–2100 under the RCP 4.5 and RCP 8.5 scenarios. Similar to the reanalysis, the regional climate models indicate that blizzards occur most frequently) over the mountainous regions, with 99% annual probability locally over the Scandes and the northernmost sea areas near Iceland; probabilities up to 75% occur in the Alps and over the Eurasian Steppe in Ukraine and Russia. The higher modelled probability of blizzards over the steppe compared to the surrounding areas is most likely because of enhanced wind speed due to lesser surface friction. Although this pattern was not clearly visible in the reanalysis data, it was present in all of the included model simulations.

In the future, blizzards are projected to occur less frequently over many areas. Under the RCP 8.5 scenario, the projected decrease is the most pronounced, locally by 25% for the far-future 2071–2100 period, but the spatial pattern of changes is similar for other periods as well. In general, the probability of blizzards will decrease by 10 percentage points (pp) over most of the continent and by 25 pp over the Baltic Sea by 2050. This change is more pronounced by 2100. However, for most of the continent no significant change is anticipated in the future climate. Locally in some northern inland areas, such as over the Scandes and northern Russia, the probability of blizzards is projected to increase slightly, however these changes are mainly not statistically significant. Over maritime and coastal areas, blizzards are projected to become clearly less frequent, by 10-25 pp also in the north by 2100. In Central and Southern Europe, the probability of blizzards is projected to decrease by 25 pp mainly over the mountainous areas by 2100, as they rarely occur elsewhere already during the reference period. In addition, there is expected a decrease by 25 pp in the probability of blizzards over the Eurasia Steppe in the future (2071-2100).

The projected decrease in the probability of blizzards is evidently due to the projected decrease in storminess over most of the Atlantic regions (Vajda et al. 2011) and the increase in temperature, which is more pronounced in the RCP 8.5 than in the RCP 4.5 scenario (e.g., Collins et al. 2013). This will lead to shortened winters and thus the season when blizzards are possible will be shorter than nowadays. On the other hand, wintertime precipitation is projected to increase in Northern Europe and hence blizzards may become more frequent over those northern areas, where winters are still cold enough that most of precipitation falls as snow for several months. It has been noted already in previous studies that snowfall may increase in the coldest climate zones (e.g. Vajda et al. 2011, de Vries et al., 2014; Räisänen 2016).

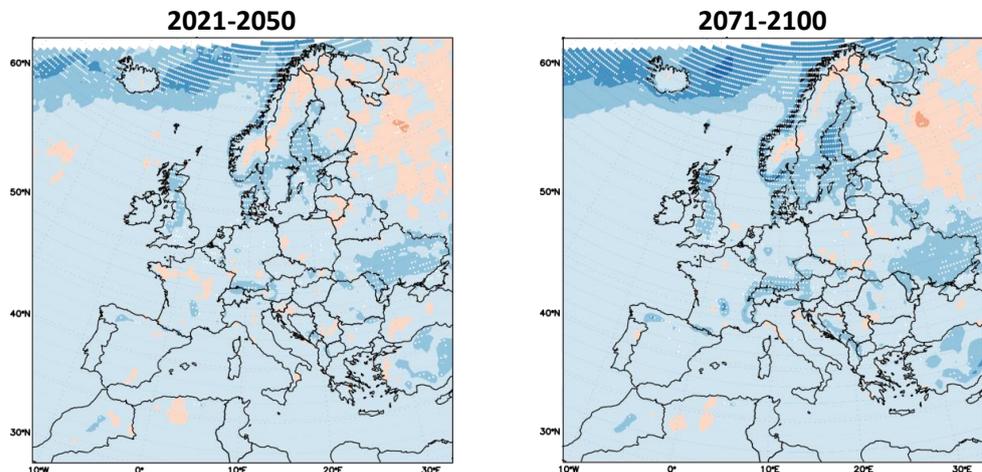# Blizzards (snow storms)

Annual probability of blizzards (%)

**Reference
Period**

1971-2000

**Predicted
Changes**
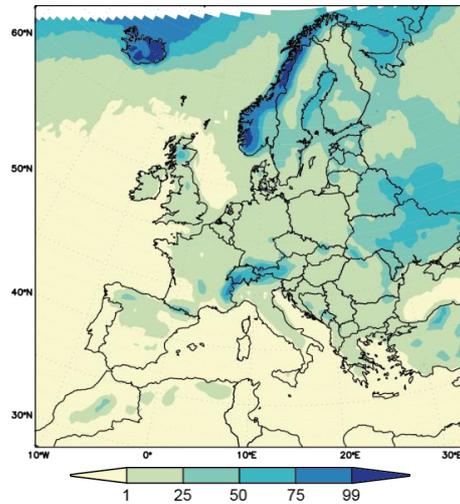
RCP 4.5:

RCP 8.5:

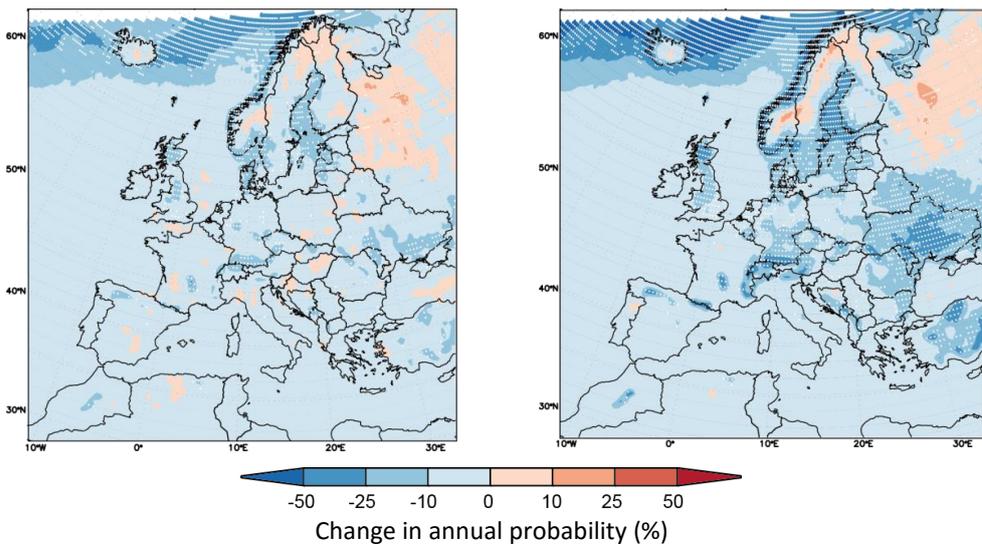Change in annual probability (%)

Fig. 10.3. (top) Multi-model mean annual probability (%) of blizzards during 1971–2000. Multi-model mean change in annual probability of blizzards (in percentage points) under the RCP 4.5 scenario (middle) and the RCP 8.5 scenario (bottom). White dots denote significant change at the 95% level.

11. Crown snow load

Ilari Lehtonen and Andrea Vajda (FMI)

11.1 Introduction

Crown snow load is snow and rime that tightly attaches to tree crowns and other structures in freezing temperatures. The accumulation of snow on tree branches and other structures is dependent on several meteorological factors. The accumulation of snow is most efficient when the temperature at the time of precipitation is close to the freezing point, preferably approximately between 0 and 0.5 °C. Slightly wet snow is the heaviest and if the temperature falls below 0 °C after the snowfall, then snow attaches tightly to the branches as it freezes. In addition, wind speed affects the snow accumulation. Increasing wind speed enhances the accretion of snow, since snow then falls more horizontally. On the other hand, if the wind speed is too high, snow is blown away from the tree branches. Thus heavy wet snowfall with moderate wind speed poses the greatest risk for heavy snow accumulation on trees. Furthermore, heavy crown snow loads increase the risk for wind damages as heavily snow-loaded tree crowns are susceptible to break down under high wind speeds (Valinger and Lundqvist 1992). Damaged trees may further inflict disturbances in power transmission by bending or falling over power transmission lines. Moreover, snow, rime and ice accumulation on power lines themselves causes problems in power transmission. The most severe snow-load events with ice accretion may even seriously damage power transmission line towers and lead to great economic losses (e.g. Lahti et al. 1997; Zhou et al. 2012). For instance, over 20,000 damaged trees fell over power lines due to a single blizzard (the Pyry storm) in Finland in 2001 (Hoppula 2005). This event and its impacts on CI were described in details in D2.1 Report-List of past cases.

11.2 Method

The snow load amounts were estimated by applying a snow load model developed at the Finnish Meteorological Institute (FMI) for predicting heavy snow loads on tree crowns. This model estimates the amount of snow load on tree crowns assuming an exemplar tree that has a cone-shaped crown with a projected catchment area of one square meter from above and from the side in the direction of the wind (Fig. 11.1). The model uses as input variables 2-m air temperature, 2-m relative humidity, 10-m wind speed, precipitation, cloudiness and global radiation. Based on these variables, the model estimates the amount of rime, dry snow, wet snow and frozen snow on tree crowns. Riming efficiency in the model is furthermore affected by elevation. The total snow load is the sum of these four components. The snow load is increased due to snow and rime accumulation and it is decreased due to melting and wind removal. Also high solar radiation decreases the snow load, because radiation may warm tree branches above 0 °C in freezing temperatures. Freezing and melting, moreover, affect the snow type. The model has a time step of one hour. A detailed description of the model is presented by Lehtonen et al. (2014).
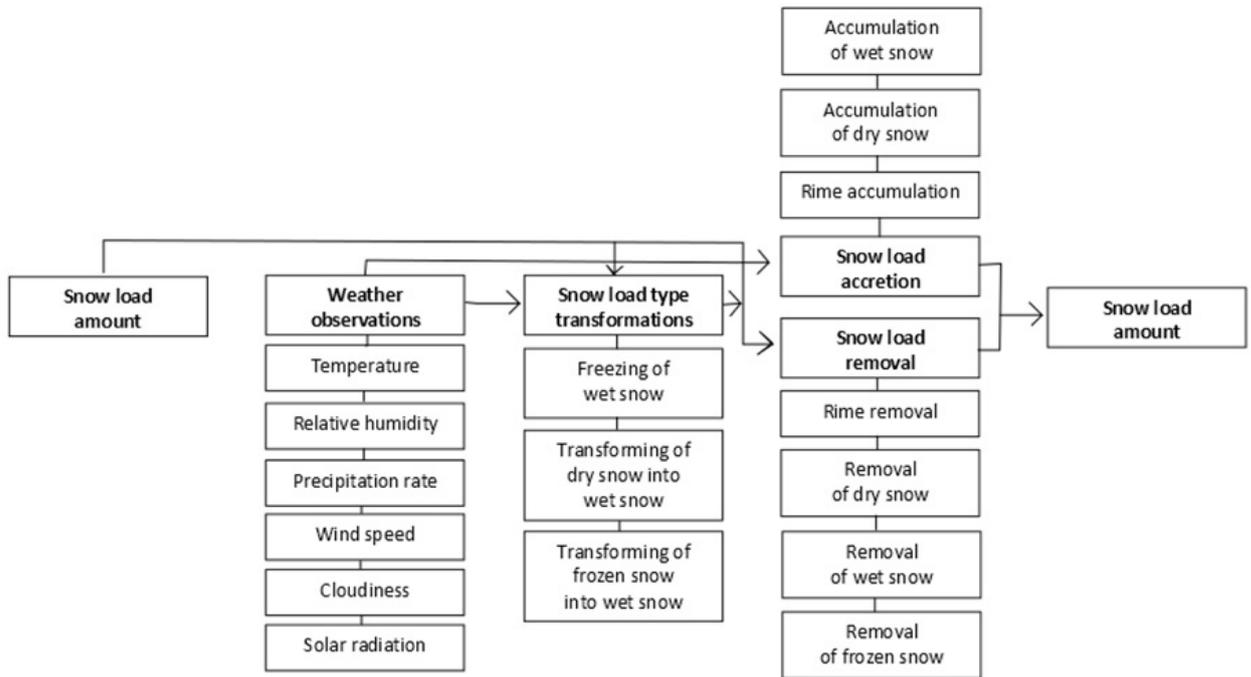
Fig. 11.1. A schematic structure of FMI snow load model.

To determine the probabilities for heavy snow loads over the period 1981–2010, we used the following parameters from the ERA-Interim reanalysis dataset with 0.75° spatial resolution as input for the snow load model: 6-hour reanalyzed air temperature, wind speed and cloudiness values, as well as 2-m dew point temperatures which were converted to relative humidity. For cloudiness, we used only low cloud cover data because the idea of cloudiness in the model is to assure that rime accretion occurs only during cloudy situations and only low-level cloudiness is in that case relevant. Precipitation and global radiation were available as forecasted fields initialized at 00 and 12 UTC each day. For these variables, we used 12-hour forecasts, which were provided with 3-hour time spans. We moreover used high-resolution elevation data downloaded from www.worldclim.org website and produced by the National Aeronautics and Space Administration. The elevation data was interpolated onto the same 0.75° × 0.75° grid as that of the weather variables by using the box-averaging method.

Finally, we calculated the probabilities that the modelled total snow load exceeded the selected thresholds, i.e. 20 and 60 kg m^{-2} (as described in Chapter 8) and determined the annual probabilities that these thresholds were surpassed on at least one day per year. Note that, as the accumulation of snow is a cumulative process, the thresholds are often exceeded on several consecutive days during a single event.

In order to assess the changes in the probability and magnitude of severe winter events in the future climate we have used a set of six RCMs at 50 km spatial resolution and 6-hour time resolution produced in EURO-CORDEX (See Section 3.3 for details). The six models used were: SMHI-RCA4-

CanESM2, SMHI-RCA4-NorESM1, SMHI-RCA4-IPSL-CM5A-MR, KNMI-RACMO22E-EC-EARTH, KNMI-RACMO22E-HadGEM2-ES and MPI-CSC-REMO2009-MPI-ESM-LR. All of these models used the RCP 4.5 and RCP 8.5 emission scenarios. The time horizons studied were 2021-2050 and 2071-2100, and 1971-2000 as a control period.

The snow loads were calculated basically similarly than from the reanalysis data. First, all the model data, which was depending on the model available with a 3-hour or 6-hour temporal resolution, were interpolated onto a regular 0.5° × 0.5° latitude–longitude grid. The topography data was interpolated onto the same grid. From the MPI-M-LR-MPI-CSC-REMO2009 model cloudiness and radiation data were not available and we thus neglected the effect of solar radiation on the snow loads and assumed the cloudiness to be 80% all the time. The effect of solar radiation on the modeled snow load is in most circumstances negligible, but mainly in spring it can reduce the modeled snow loads substantially (Lehtonen et al., 2014). Cloudiness only affects the riming efficiency in the model and the assumption was based on the fact that the situations otherwise favorable for riming (temperature slightly below the freezing point, high relatively humidity and moderate wind speed) are usually rather cloudy. Based on the calculation of annual probabilities using the six RCMs, the multi-model mean of the change compared to the control period (1971-2000) was defined and presented for each threshold of the studied phenomena. The multi-model mean is the average change indicated by the six models giving each model equal weight.

The statistical significance of the projected changes in the probabilities was assessed applying the non-parametric Wilcoxon signed-rank test (Wilks, 2011). Note that, according to this test, the projected change is statistically significant in the case of six models at the 95% level only if all the models indicate either positive or negative change.

11.3 Present climate

Based on the ERA-Interim reanalysis data, heavy snow loads occur in Europe clearly most often over the Scandes and the Alps (Fig. 11.2). Over these areas the lower threshold (20 kg m^{-2}) is exceeded in most of the years, the annual probability varying between 50-75% in these areas, sporadically reaching 99%. In the rest of Scandinavia, the annual probability of snow load over 20 kg m^{-2} is more reduced, varying between 1 and 25%. Similar probabilities are shown over some areas in SE Europe, especially the Balkan Peninsula, but there are large areas in Southern and Central Europe where even the lower threshold was surpassed not even once during 1981–2010. Snow loads over 60 kg m^{-2} were never reached elsewhere, except over small regions in the Alps and Scandes (Fig. 11.3) during the studied period.

Finally, we also studied the connection of heavy snow loads to large-scale circulation similarly as for the blizzards, but due to the relatively small number of events over most of Europe, no meaningful relationship could be detected over any area.
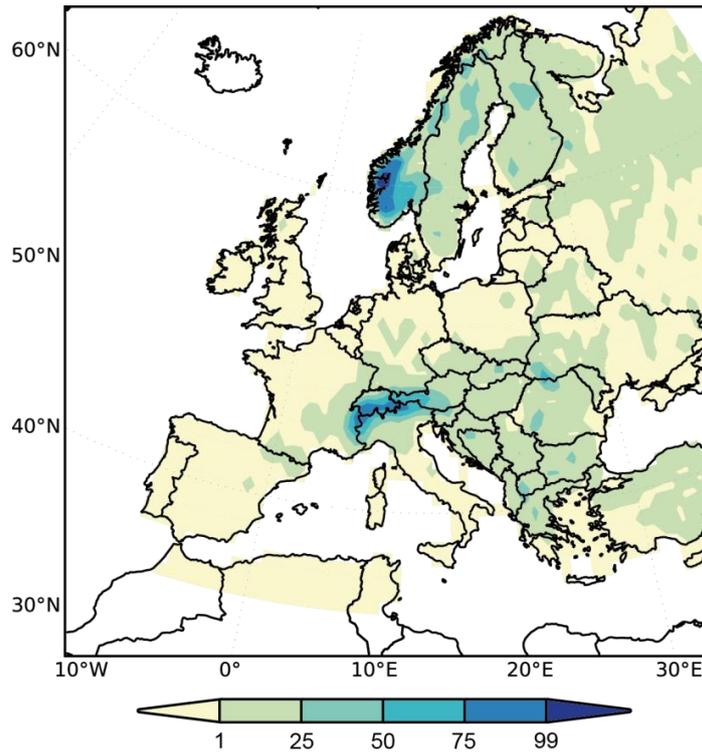
Fig. 11.2. Annual probability of crown snow load exceeding 20 kg m⁻² during the period 1981-2010 based on ERA-Interim data.

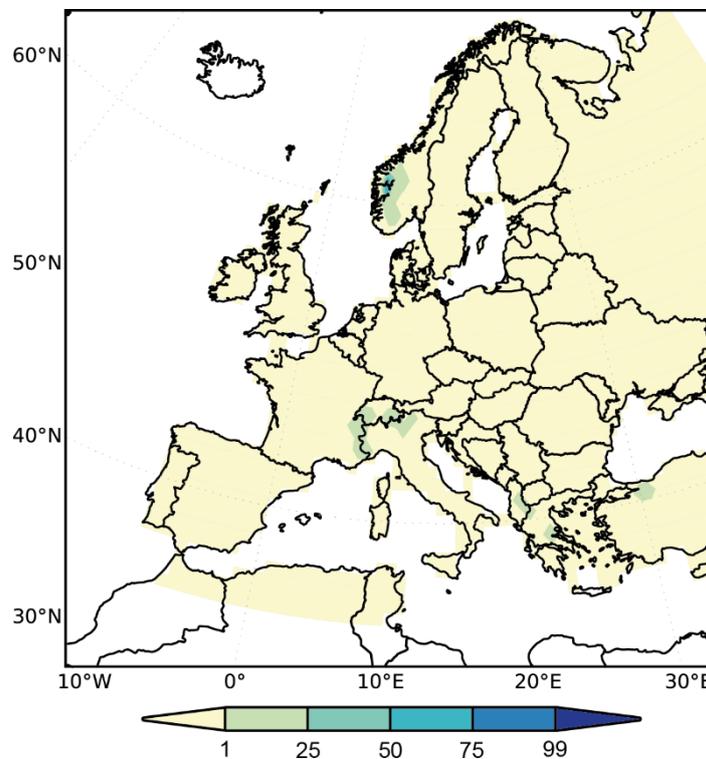**Fig. 11.3. Annual probability of crown snow load exceeding 60 kg m⁻² during the period 1981-2010 based on ERA-Interim data.**

11.4   Climate predictions

The multi-model mean geographical pattern of heavy snow loads in the present climate resembles the pattern derived from the ERA-Interim data (Fig. 11.4 and Fig. 11.5). The Alps clearly stick out with high annual probabilities (up to 99%) as well as other mountain areas in Southern and Central Europe, e.g. the Pyrenees and the Carpathian Mountains (50-75%). The probability of heavy snow load events over these mountain ranges is more evident in the model data, which is probably due to a higher spatial resolution of the data compared to the reanalysis. There are also more model years contributing into the multi-model mean than in the reanalysis, which is the main reason for having smaller areas with no events compared to the ERA-Interim results. In Northern Europe, the maximum probability of heavy snow load events with amount over 20 kg m^{-2} is located rather on the eastern side of the Scandes than along the mountain ridge. This is mainly caused by the three global models downscaled by the SMHI-RCA4 model. When comparing the probability maps of individual models (not shown), it is moreover evident that the global models which were downscaled with the same regional model produced very similar probability patterns. Clearly, the highest probabilities were modeled by the MPI-M-LR-MPI-CSC-REMO2009 model, which was probably partly because of the lacking data and the assumptions we made, although this model also had quite an apparent wet bias. In this model, also the higher threshold (60 kg m-2) was occasionally exceeded outside of the mountain areas. In that sense, the global models downscaled by the SMHI-RCA4 regional model most resembled the reanalysis, as in these models the higher threshold was very rarely exceeded anywhere.

The future projections indicate decrease of risk over most of Europe for both threshold values (20 and 60 kg m^{-2}), including the southern part of Scandinavia; for snow load above 20 kg m^{-2}, the degree of the decrease is low (0-10 pp), reaching larger values (10-25 pp) only in the mountainous regions by 2050. The change is more evident for the far future (2071-2100), when a significant decrease is expected for these areas, even by 50 pp according to the RCP 8.5 scenario. In northernmost Europe, the risk is mainly projected to increase by 10-25 pp, this change being more pronounced by the end of century. However, models do not unanimously agree on the increase of the risk in the north, unlike the agreement on a decrease over many areas. The changes in the probability of heavy snowfall events with amounts over 60 kg m^{-2} are similar but are smaller, as these events are already very rare even in the present climate. The projected change pattern of snow load is rather similar to that of the blizzards because of the same reasons. Higher temperatures shorten the snow season, but in the north, where it is still cold enough, this is overridden by increased precipitation.

Crown Snow Load
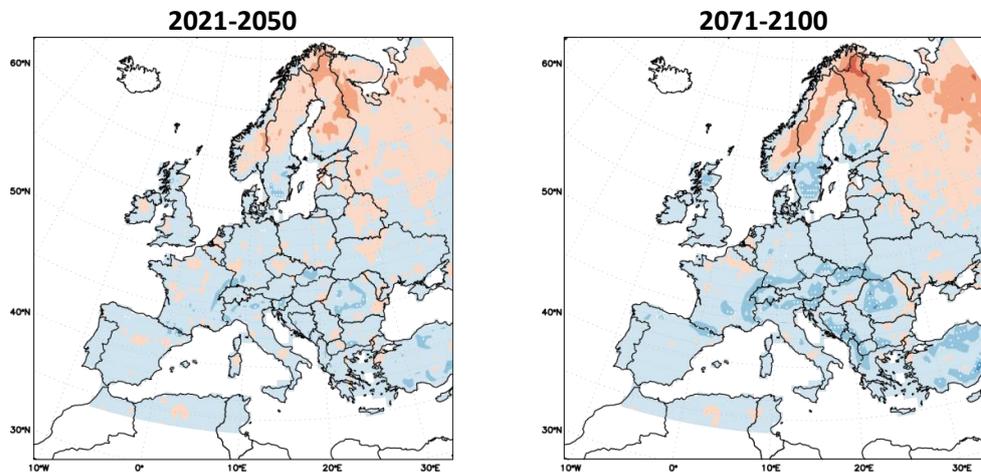
Annual probability of exceeding 20 kg m² (%)

Reference Period

1971-2000:

Predicted Changes

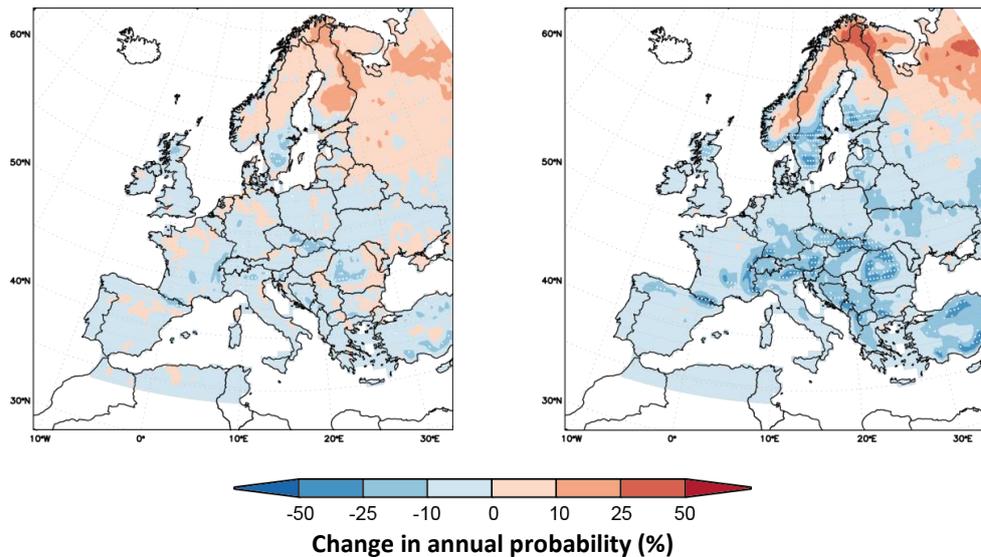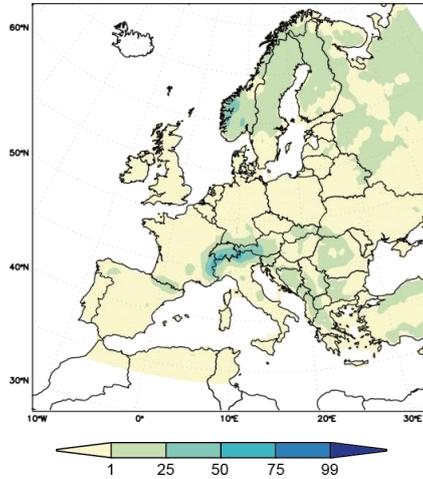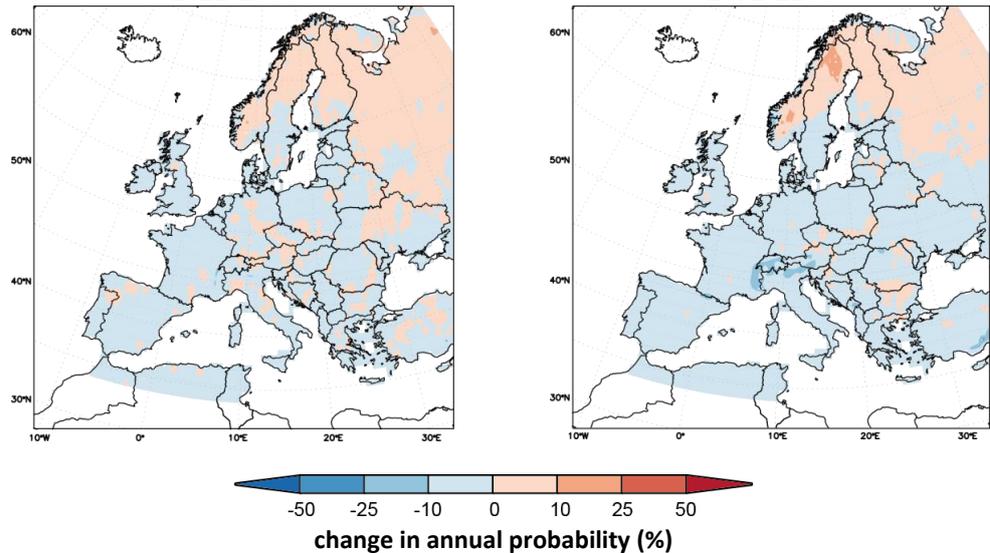RCP 4.5:

RCP 8.5:

2021-2050

2071-2100
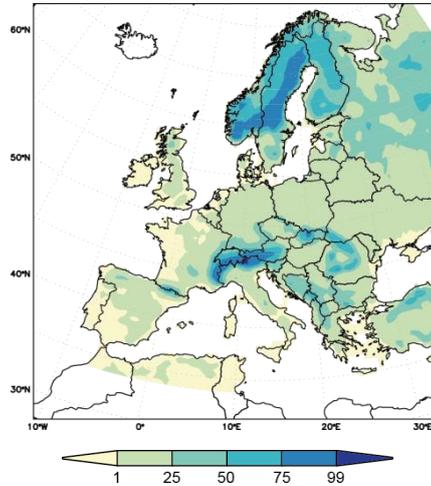
Fig. 11.4 (top) Multi-model mean annual probability (%) of snow load exceeding 20 kg m^{-2} during 1971–2000. Multi-model mean change in annual probability of snow load exceeding 20 kg m^{-2} (in percentage points) under the RCP 4.5 scenario (middle) and the RCP 8.5 scenario (bottom). White dots denote significant change at the 95% level.

Crown Snow Load

Annual probability of exceeding 60 kg m² (%)

Reference Period

1971-2000:

Predicted Changes

RCP 4.5:

2021-2050   2071-2100

RCP 8.5:

2021-2050   2071-2100

change in annual probability (%)
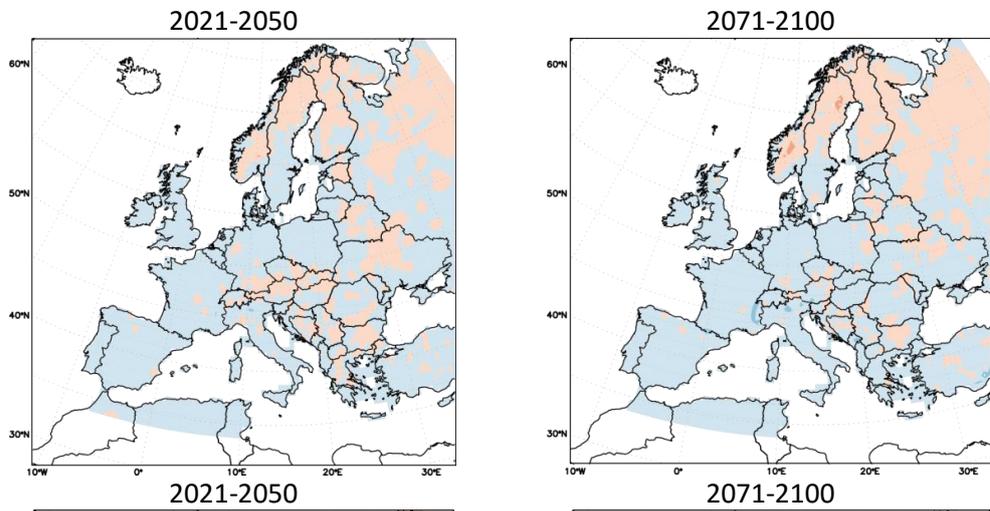
Fig. 11.5 (top) Multi-model mean annual probability (%) of snow load exceeding 60 kg m⁻² during 1971–2000. Multi-model mean change in annual probability of snow load exceeding 60 kg m⁻² (in percentage points) under the RCP 4.5 scenario (middle) and the RCP 8.5 scenario (bottom). White dots denote significant change at the 95% level.

12. Freezing rain

Matti Kämäräinen, Andrea Vajda and Hilppa Gregow (FMI)

12.1 Introduction

Freezing rain causes an accumulation of ice on the surface and infrastructure. The raindrops are required to be supercooled which causes them freeze upon impact, and for this reason it can occur also with above-freezing near-surface temperatures. Freezing rain is a relatively rare but high-impact wintertime weather phenomenon affecting central, eastern and northern Europe. Although major events resulting in heavy ice accretion are not as common as lighter, short-lived cases, the damages they cause to critical infrastructure (transportation, communication and energy), agriculture and forestry are substantial. For example, the ice coat formed on trees and power lines causes them to fail, leading to severe power outages, transportation disruption, delays in emergency responses, and severe economic losses (Call 2010, Lambert 2011). Short-lived cases are also harmful because of the reduced friction on road surfaces that results in increased rates of accidents and difficulties in transportation. Although less severe, due to their more common occurrence, the economic losses generated by the short-lived cases are significant for society. More intense freezing rain may lead to multiple failures of infrastructure, such as the cases registered for example in UK on 23—24 January, in Moscow on 25 December 2010, or in Slovenia from 31 January to 4 February 2014, described in details in D2.1 Report – List of past cases.

12.2 Method

For calculating the probabilities of freezing rain, a precipitation detection algorithm, originally used in numerical weather prediction at the Finnish Meteorological Institute, was adopted for climatological analyses of this study. The original algorithm was simplified by excluding the identification of other precipitation types, which made it computationally more efficient and suitable for large climatological datasets.

To find the near-surface cold layer and the above-surface melting layer structures essential to formation of freezing rain, the algorithm uses temperature and humidity information from 925, 850 and 700 hPa levels and temperature information from the near-surface level. Surface pressure is used to locate the surface relative to these pressure levels in order to avoid analysing below-surface data.

The principle of the algorithm is presented in Fig. 12.1. First, the precipitation and temperature from the near-surface level and the presence of an above-surface melting layer are checked. If they indicate the possibility of freezing rain, then the surface pressure is used to measure the height of the near-surface cold layer. If high enough near-surface cold layer (h > h_cold; h in hPa, T < T_cold; T in °C) and moist (RH > RH_melt; RH in %) and warm (T > T_melt) enough above layer(s) are found, freezing rain is predicted. Selected values of the adjustable parameters can be seen in Table 12-1, and they are the values that have been used in numerical weather prediction, except for the precipitation (Pr > Pr_lim; Pr in mm/6h), which was selected so that the mean occurrence bias,

calculated over all the validation stations, became zero. This ensures that no over- or underprediction of freezing rain happened in the domain.

The method is not suitable for an analysis of high elevation terrain (over 2500 m) due to scarcity of the pressure layers used. This adds uncertainty to the results in highest tops of Norway and in the Alpine regions.

Table 12-1: Threshold values selected for identification of freezing rain. See text and Fig. 12.1 for definitions of parameters.

h_cold (hPa) >	RH_melt (%) >	T_melt (°C) >	T_cold (°C) <	Pr_lim (mm/6h) >
15	90	0	0	0.0393
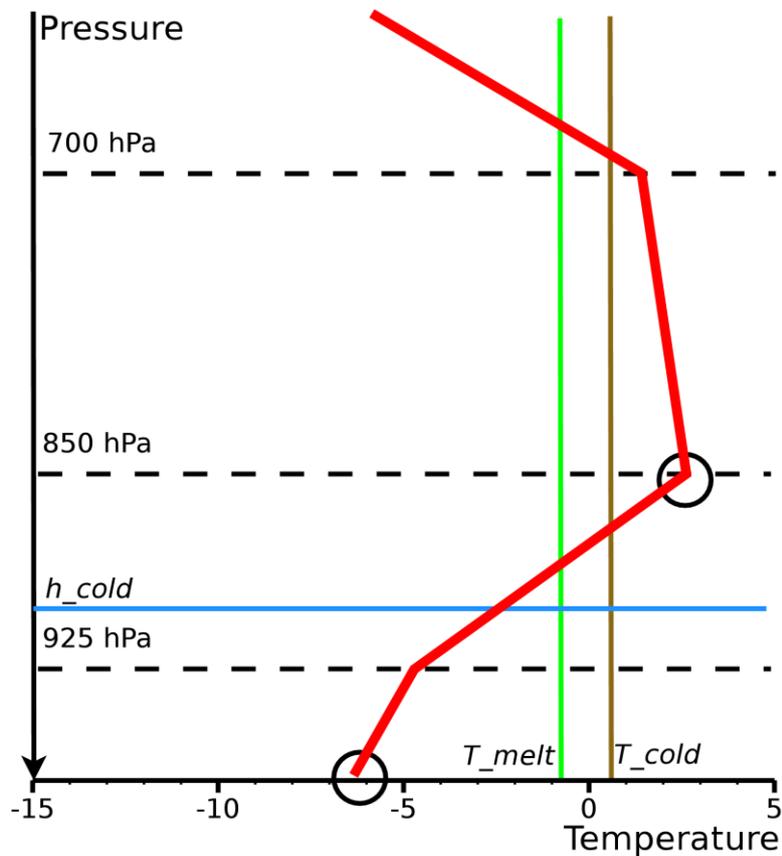
Fig. 12.1. An example of a freezing rain event identified by the method. Thick and cold near-surface cold layer and above-surface melting layer are present: their temperatures are evaluated at levels marked with circles. Different adjustable threshold parameters are shown in blue, green and brown colours. See text for details.

The method was validated using the 6-hourly SYNOP observations from 200 manually operated weather stations over Europe (predicted data) and the ERA-Interim reanalysis (predictor data) in station locations. For this purpose, the 6-hourly ERA-Interim data from different pressure levels was interpolated to station locations. In the validation the categorical verification measures Heidke Skill Score (HSS; Heidke, 1926), the Critical Success Index (CSI), and the Symmetric Extremal Dependence

Index (SEDI; Jolliffe, 2012) were evaluated during the 1979-2014 period. Additionally, the yearly number of predicted freezing rain events per station was evaluated and compared to the observed number of freezing rain events of the whole domain separately. Validation results are presented in Table 12-2.

Table 12-2. Validation results of the freezing rain identification method. Predicted annual number of freezing rain events in validation stations ("Individual stations") is compared to observed number: similarly, the predicted annual mean number of freezing rain events ("Mean over stations") is compared to observed mean number. Correlation coefficient, mean value (units: number of 6-hourly freezing rain events in 1979-2014), predicted and observed standard deviation, Heidke Skill Score, Critical Success Index, and Symmetric Extremal Dependence Index are shown.

	Correlation	Mean value (PRED and OBS)	Standard deviation (PRED)	Standard deviation (OBS)	HSS	CSI	SEDI
Individual stations	0.54	0.42	1.13	1.06	0.19	0.10	0.63
Mean over stations	0.90	0.42	0.22	0.16	--	--	--

When mean yearly variability of events is calculated, good overall agreement between predicted and observed freezing rain events is achieved (R=0.90).

To determine the occurrence of freezing rain in the present-day climate, the ERA-Interim reanalysis dataset in the original 0.75° spatial resolution was used. The identification of freezing rain was performed in the provided 6-hourly time resolution of the reanalysis and the climate models. The daily amounts of freezing rain were calculated from the 6-hourly data. The occurrence of freezing rain with 5 mm/24 h and 25 mm/24 h threshold values (as described in Chapter 8) were estimated and transformed to annual probabilities that these thresholds were surpassed at least on one day during a year. As the freezing rain events are known to be short-lasting in many cases with a duration of less or much less than 6 hours (Cortinas, 2000), it is likely that due to the available temporal resolution of the data our results slightly overestimate the duration and precipitation rates of this phenomenon.

In order to assess the changes in the probability and magnitude of severe winter events in the future climate we have used a set of six RCMs at 50 km spatial resolution and 6-hour time resolution produced in EURO-CORDEX (see Section 3.3 for details). The six models used were: SMHI-RCA4-CanESM2, SMHI-RCA4-NorESM1, SMHI-RCA4-IPSL-CM5A-MR, KNMI-RACMO22E-EC-EARTH, KNMI-RACMO22E-HadGEM2-ES and MPI-CSC-REMO2009-MPI-ESM-LR. All of these models used the RCP 4.5 and RCP 8.5 emission scenarios. The time horizons studied were 2021-2050 and 2071-2100, and 1971-2000 as a control period.

Based on the calculation of annual probabilities using the six RCMs, the multi-model mean of the change compared to the control period (1971-2000) has been defined and presented for each threshold of the studied phenomena. The multi-model mean is the average change indicated by the six models, giving each model equal weight. The statistical significance of the projected changes in

the probabilities was assessed applying the non-parametric Wilcoxon signed-rank test (Wilks, 2011). Note that, according to this test, the projected change is statistically significant in the case of six models at the 95% level only if all the models indicate either positive or negative change.

12.3   Present climate

Annual probabilities of freezing rain, based on ERA-Interim 1981-2010, find their maximums in Eastern Europe (Fig. 12.2 and Fig. 12.3). Both threshold values, 5 mm/day and 25 mm/day, are most frequently exceeded in Ukraine and over the Balkan Peninsula. Locally over 40% of the years encounter 5 mm freezing rain events, where locally over 4% of the cases exceed 25 mm/day partially in the same areas. The southern coast of Norway is also frequently threatened by 5 and 25 mm/day events. Virtually all European countries suffer from 5 mm/day events at least occasionally. The 25 mm/day events are much more infrequent, and the few individual grid cells showing >1% probabilities outside the locations mentioned previously cannot be used to derive climatological conclusions due to scarcity of the data.
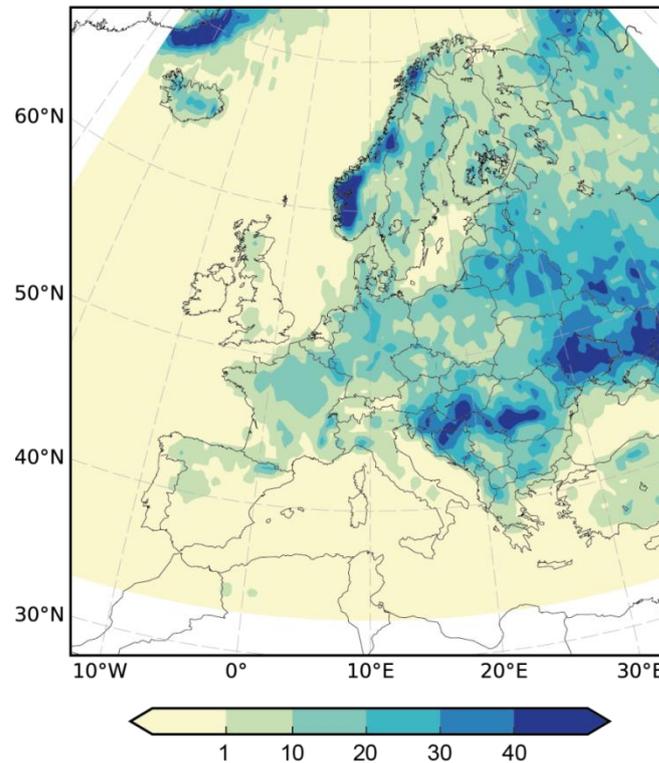
Fig. 12.2. Annual probability of freezing rain exceeding 5 mm/24 h during the period 1981-2010 based on ERA-Interim data.
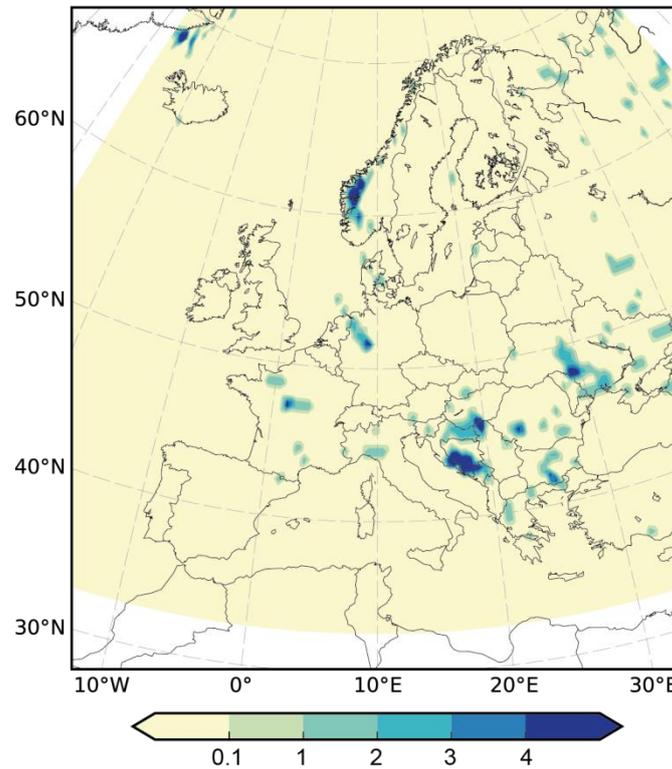
Fig. 12.3. Annual probability of freezing rain exceeding 25 mm/24 h during the period 1981-2010 based on ERA-Interim data.

12.4 Climate predictions

The ERA-Interim-based present-day climatology of freezing rain was completed using the mean of the historical 1971-2000 (as defined in Method section) simulations from the six regional climate models (Fig. 12.4Fig. 12.5). All models generated the spatial patterns of the freezing rain qualitatively well with few or no events in southern Europe and over the warm sea areas, which in many cases prevent the formation of the near-surface cold layer required to supercool the raindrops. However, compared to ERA-Interim, all three SMHI-RCA4 solutions underestimate the occurrence of the phenomenon, especially in Eastern Europe. The EC-EARTH driven KNMI-RACMO model output resembles ERA-Interim the most, while the HadGEM2-ES driven KNMI-RACMO run as well as the MPI-M-LR driven MPI-CSC-REMO model overestimate the occurrence of 5 mm/day events. The 25 mm/day events lack in the SMHI-RCA4 model solutions, and compared to ERA-Interim, the Alpine region shows extreme events more frequently in other models.

Together these six models produce a probability distribution which is smoother than ERA-Interim, but resembles it more than any of the individual models alone: underestimation of occurrence by three models is compensated by the overestimation of two models.

A climate change signal can be seen in change of the probability of the 5 mm/day events in the near-future 2021-2050 period (Fig. 12.4).

Freezing Rain

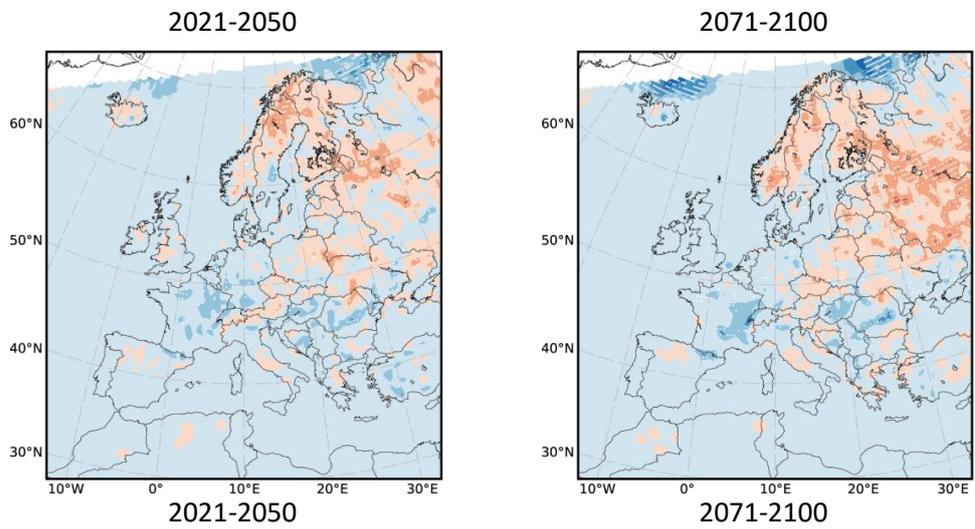**Annual probability (%) of freezing rain exceeding 5 mm/24 h**

Reference Period
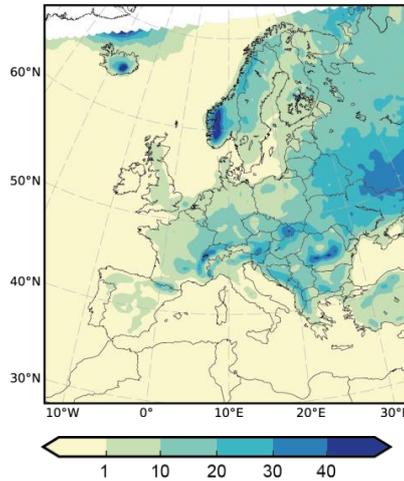
1971-2000:

Predicted Changes
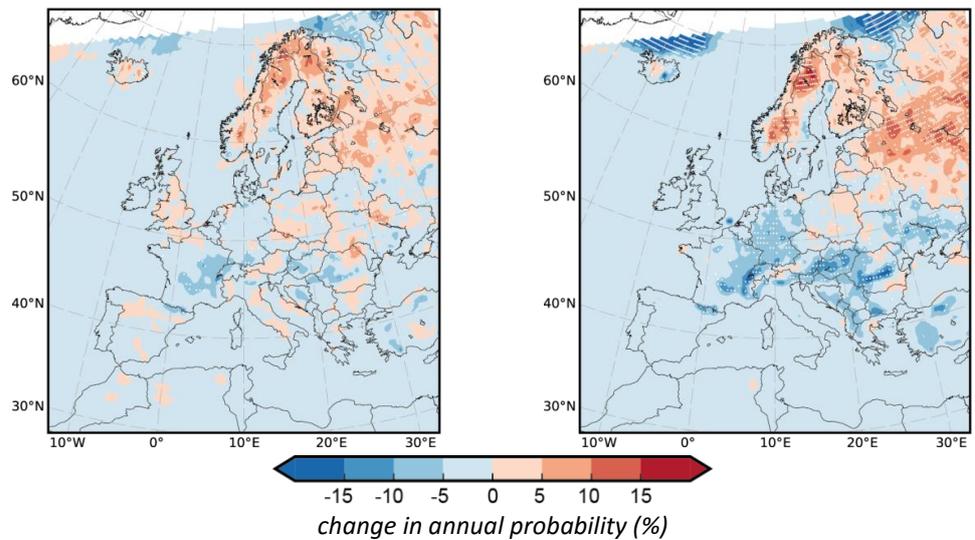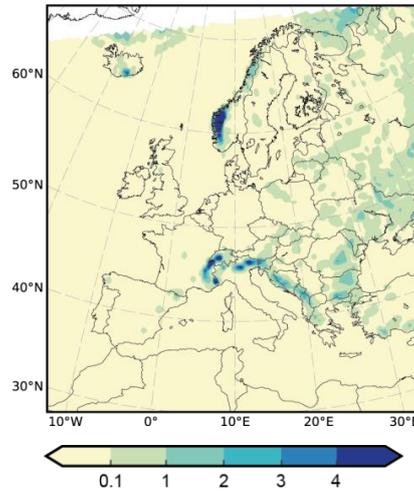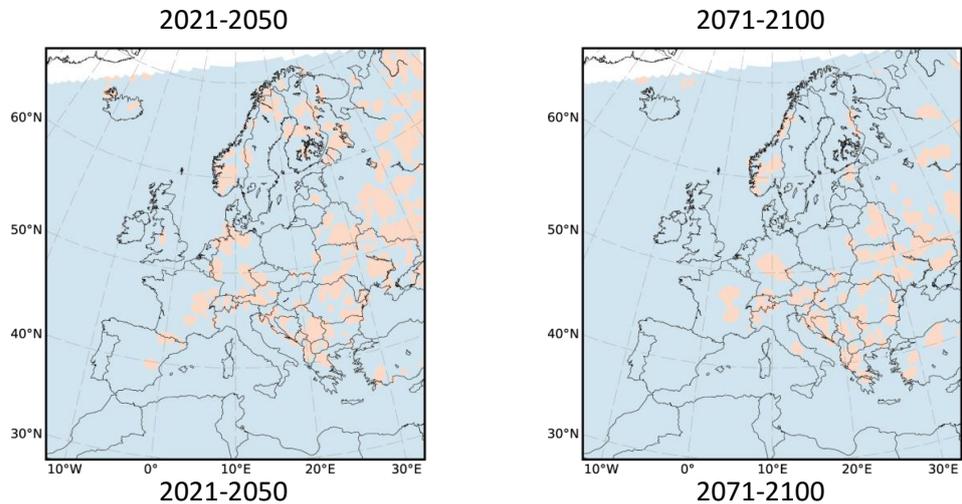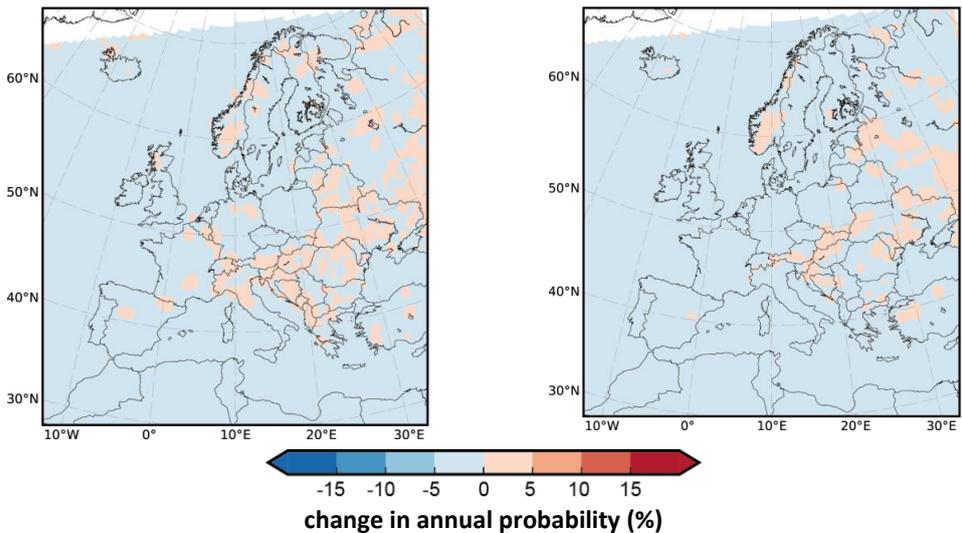
RCP 4.5:

RCP 8.5:

Fig. 12.4 (top) Multi-model mean annual probability (%) of freezing rain exceeding 5 mm/24 h during 1971–2000. Multi-model mean change in annual probability of freezing rain exceeding 5mm/24 h (in percentage points) under the RCP 4.5 scenario (middle) and the RCP 8.5 scenario (bottom). White dots denote significant change at the 95% level.

Freezing Rain

Annual probability (%) of freezing rain exceeding 25 mm/24 h

**Reference
Period**

1971-2000:

**Predicted
Changes**

RCP 4.5:

| 2021-2050 | 2071-2100 |

RCP 8.5:

| 2021-2050 | 2071-2100 |

change in annual probability (%)

Fig. 12.5 (top) Multi-model mean annual probability (%) of freezing rain exceeding 25 mm/24 h during 1971–2000. Multi-model mean change in annual probability of freezing rain exceeding 25 mm/24 h (in percentage points) under the RCP 4.5 scenario (middle) and the RCP 8.5 scenario (bottom). White dots denote significant change at the 95% level.

Regardless of the emission scenario, climate models predict a northward shift in the occurrence of events, so that annual probabilities decrease by 0 to 5 percentage points in central Europe, and increase by 0 to 10 percentage points in Fennoscandia and in northern Russia. The signal is marginally stronger with RCP 8.5 compared to RCP 4.5. Areas with a coherent coverage of statistically significant grid cells can be found in northern Sweden and northern Norway as well as in France and southern Germany. Towards the end of century, the northward shift in the occurrence becomes stronger and the areas with significant grid cells wider and more coherent. The difference between the emission scenarios becomes stronger as well: for example, in northern Sweden the probability of 5 mm/day freezing rain events increases from the present-day value of 10 -20% to 15% - 25% under RCP 4.5, and to 20% - 30% under the RCP 8.5 scenario. Freezing rain events of 25 mm/day are so rare (Fig. 12.5), also in the future climate, that no signals of any kind can be seen in the annual probabilities.

Individual climate models show different climate change signals in freezing rain. The SMHI-RCA4 model outputs, which simulate the least 5 mm/day freezing rain events in the present-day simulations, shows the weakest climate change signal. Strong climate change is simulated by the HadGEM2-ES -driven KNMI-RACMO and the MPI-M-LR -driven MPI-CSC-REMO regional models.

The apparent reason for the decrease of the occurrence of freezing rain in the future is the warming of the near-surface air in central Europe. Warmer winters mean less near-surface cold layer situations. The increase of freezing rain in northern countries is not so easily explained. It is possible that the winters are so cold in the present climate and the transition from warm summer to cold winter and vice versa is so fast, that the occurrence of a melting layer is rarer than in central Europe. In the future climate on the other hand, the winters become warmer and the simultaneous occurrence of a melting layer and a near-surface cold layer could become more common. However, further research is needed to assess how the conditions related to the development of freezing rain will be changing under the projected climate change.

13. Wildfires

Ilari Lehtonen, Ari Venäläinen and Andrea Vajda (FMI)

13.1 Introduction

Uncontrolled forest fires impact both natural and built-up environments as well as humans. The occurrence of a forest fire requires the same basic elements as any fire: heat, oxygen and fuel. Preceding and prevailing weather conditions are crucial for setting conditions susceptible to fire in a forest. Drought, high temperatures and pronounced evaporation dry off organic material in forests, i.e. the fuel. Strong wind during/after ignition substantially intensifies spreading of the fire and raises the likelihood of the surface fire transition to a crown fire (Rothermel 1991). A crown fire is a fire carried through the crowns of living trees. It typically leads to more severe impacts and is harder to extinguish than surface fire alone. The majority of fires are caused by human activities. For example, Ganteume et al. (2013) estimated that only about 7% of the fires (whose cause was known) in North Europe, 0.5% in Central Europe and 5% in South Europe were caused by natural sources. Similarly, a review by Bowman et al. (2009) showed that the variation in the occurrence of fires cannot be predicted by climate forcing alone, but that other aspects such including human behavior have to be taken into account, too. Weather and climate are not the only forcing mechanisms of forest fires, but they determine the conditions for fires to occur and spread, once an ignition occurs, and this way remain as the key factors for explaining the spatial and temporal variability of fires.

Climate change will indisputably increase forests' fire sensitivity in areas where increases in summertime temperatures are accompanied by notable decreases in precipitation, such as in the Mediterranean area (Mouillot et al. 2002; Bedia et al. 2014). In more northern regions, estimates of the summertime precipitation amounts are inconclusive (Jylhä et al. 2009; Ylhäisi et al. 2010) making the effect of future climate on fire sensitivity not self-evident.

13.2 Method

Fire danger indices are used to assess forest fire danger. These indices combine several relevant climatic/weather variables like temperature, precipitation, wind speed and air humidity into suitable format that depicts fire ignition and fire spread risk. The Canadian Fire Weather Index, FWI, based on the Canadian Forest Fire Danger Rating System (Van Wagner, 1987) is one of the most widely-used indices, being used in countries across North and South America, Europe and Asia (De Groot et al., 2006).

FWI is composed of six components that describe the moisture content of organic layers at different depths and predict the rate of fire spread and the frontal fire intensity (Fig. 13.1). The calculation of FWI requires daily measurements of dry-bulb temperature, relative humidity, wind speed and accumulated precipitation.
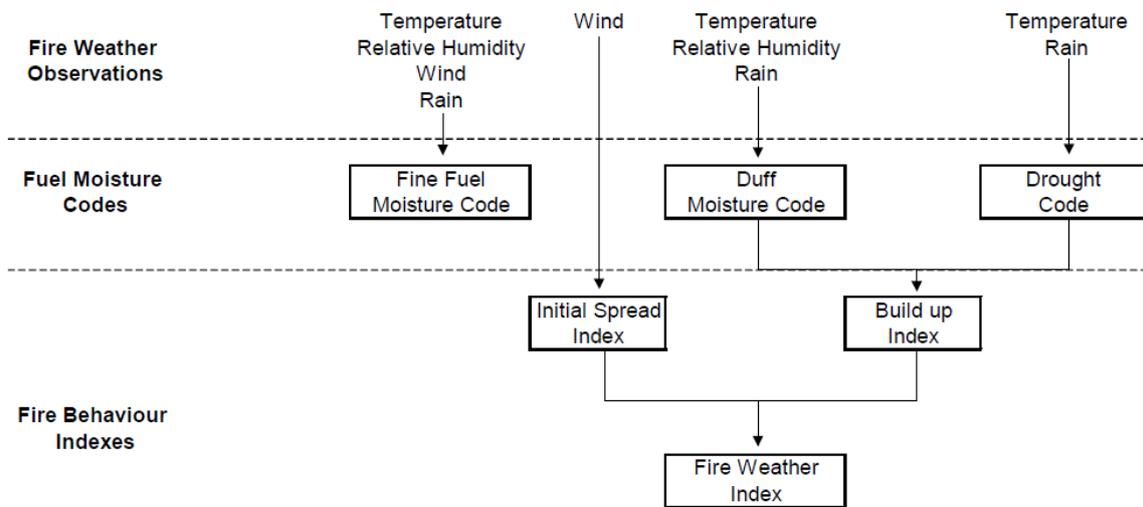
Fig. 13.1. A schematic structure of the Fire Weather Index. Figure adopted from Camia and Bovio (2000).

The FWI represents the likely intensity of a fire and was originally divided in six classes. However, because the FWI was built up to represent fire behavior in a generalized standard fuel type, the FWI System has different meanings in different forest or fuel types. That is why the FWI class scale should always be fitted to the regional pattern of fire weather.

To assess the probability of forest fire danger over Europe, we considered two thresholds: **FWI >20** and **FWI >45**. Moriondo et al. (2006) used a FWI threshold value of 45 for extreme risk for the Mediterranean region in their study on the impact of climate change on fire danger. Lehtonen et al. (2013) selected limits based on a study by Tanskanen et al. (2005): the limits were FWI>32 (extreme risk), 17-32 (high risk), 16-31) medium risk) and <8 low risk. The threshold of 20 used in this study can be regarded as applicable in cool climate regions. In Southern Europe, FWI values larger than 45 are relatively common, whereas they occur only very occasionally in the rest of Europe.

The ERA-Interim dataset with 1.5° spatial resolution was used in the calculation of FWI. The probability was calculated for the whole year. In Northern Europe, the season usually starts in May at the earliest after snow has melted, whereas in Southern Europe the season is centered in the summer months, although in some areas out-of summer fires are also common.

The results for the exceedance of threshold were presented as probabilities in percent (%):

$$Probability = 100*(no.\ of\ cases) / (no.\ of\ days)$$
Eq. 13-1

The input parameters required for deriving the FWI are the mid-day temperature, relative humidity and wind speed, together with the precipitation sum of the previous 24 hours. In the study, the 12 UTC values were used.

In order to assess the changes in the probability and magnitude of forest fire events in the future climate, we have used a set of six RCMs at 50 km spatial resolution and 6-hour time resolution produced in EURO-CORDEX (see Section 3.3 for details). The six models used were: SMHI-RCA4-CanESM2, SMHI-RCA4-NorESM1, SMHI-RCA4-IPSL-CM5A-MR, KNMI-RACMO22E-EC-EARTH, KNMI-

RACMO22E-HadGEM2-ES and MPI-CSC-REMO2009-MPI-ESM-LR. All of these models used the RCP 4.5 and RCP 8.5 emission scenarios. The time horizons studied were 2021-2050 and 2071-2100, and 1971-2000 as a control period. From the model data, we calculated the FWI index similarly as from the reanalysis data. Based on the calculation of annual probabilities using the six RCMs, the multi-model mean of the change compared to the control period (1971-2000) has been defined and presented for each threshold of the studied phenomena. The multi-model mean is the average change indicated by the six models giving each model equal weight.

The statistical significance of the projected changes in the probabilities was assessed applying the non-parametric Wilcoxon signed-rank test (Wilks, 2011). Note that according to this test, the projected change is statistically significant in the case of six models at the 95% level only if all the models indicate either positive or negative change.

13.3   Present climate
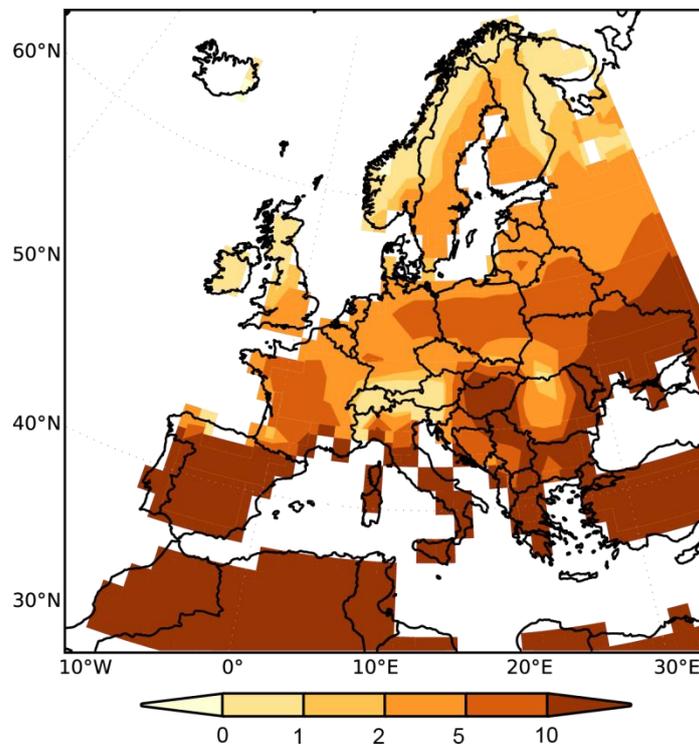
Fig. 13.2. Probability (%) of forest fires, FWI > 20 during the period 1981-2010 based on ERA-Interim data.

Due to its dependence on hot and dry weather, the daily probability of fire risk described by FWI>20 (Fig. 13.2) is the highest - with values above 10% - over Southern Europe, including the Iberian Peninsula, the Mediterranean, the Balkan Peninsula, and SE Europe. The probability decreases gradually towards Northern Europe, reaching the lowest values, below 1% in the northern part of the British Isles and Norway and up to 5% in the rest of Fennoscandia, where the frequency of dry spells during the fire season is more increased.

The probability of extreme fire risk, defined by FWI > 45 is reduced in most of Europe, with values below 1% (Fig. 13.3). Exception is the Mediterranean region, where fires are quite common, especially during summer months, the probability of high fire risk varying between 2-10 %.
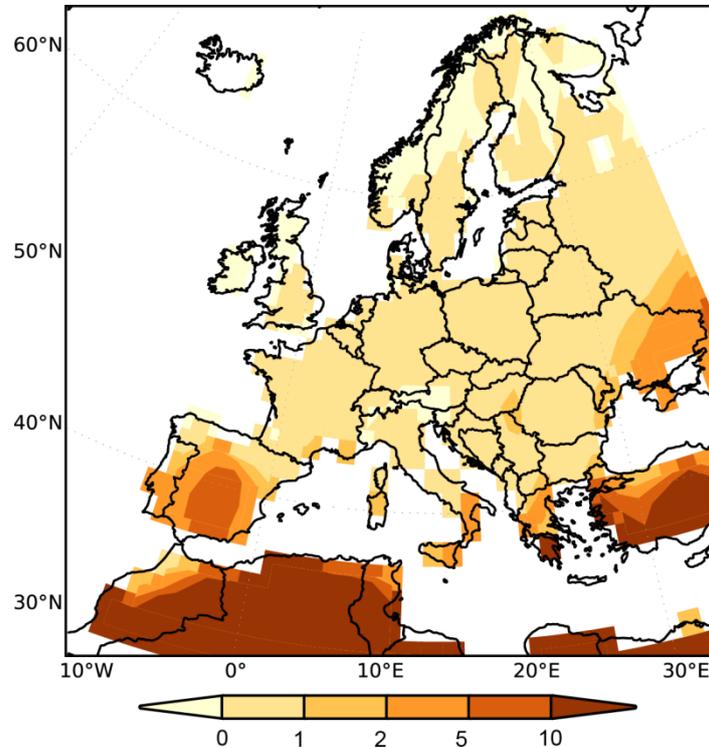

Fig. 13.3. Probability (%) of forest fires, FWI > 45, during the period 1981-2010 based on ERA-Interim data.

13.4 Climate predictions

The modeled forest fire risk in Europe using the EURO-CORDEX data increases towards the south (Fig. 13.4 and Fig. 13.5) similarly to that derived from the reanalysis data (Fig. 13.2 and Fig. 13.3). The higher threshold is only rarely exceeded in Northern Europe (1%) and there are areas where it is never modeled to be achieved (Fig. 13.5).

In the future, the risk for wildfires is mainly projected to increase. However, in the north, the multi-model mean change is small or even negative over many areas, although this decreasing risk was nowhere indicated by all the models. This is interesting, as in many studies the forest-fire risk in the boreal zone has been found to increase as a response to global warming (e.g. Flannigan et al., 2009; Sherstyukov and Sherstyukov, 2014). However, as Lehtonen et al. (2016) pointed out, the scatter among the future model projections for high forest-fire danger is large in Northern Europe. Hence, the multi-model mean, that consists only of models downscaled with three different regional climate models, may not be representative enough. Moreover, it is biased towards the SMHI-RCA4 model that was used for downscaling three of the six models used here. The increase in the meteorological

Fire Weather

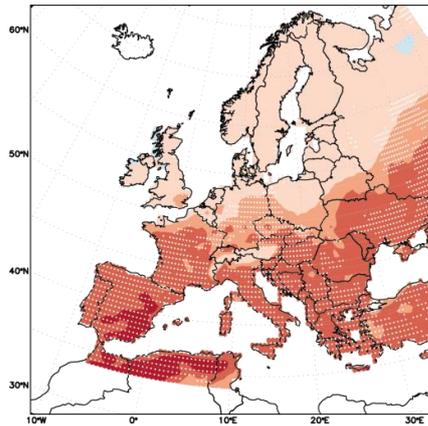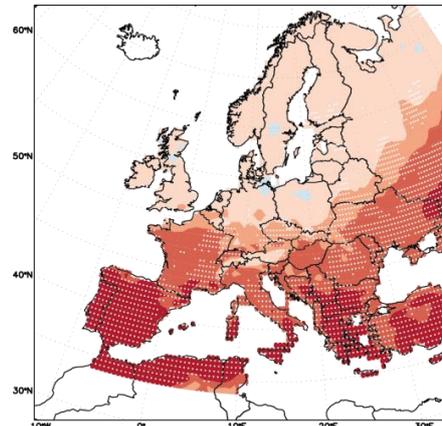**Daily probability of Fire Weather Index > 20**

**Reference
Period**
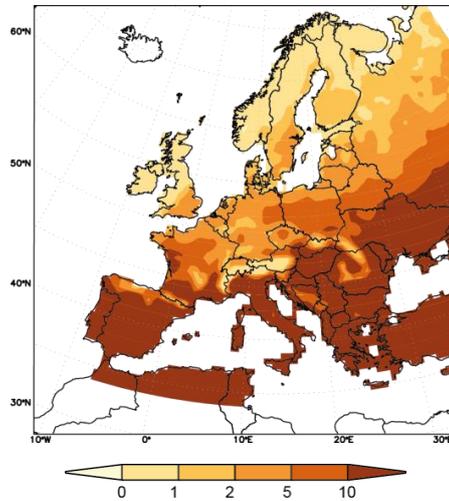
1971-2000:

**Predicted
Changes**

RCP 4.5:

RCP 8.5:
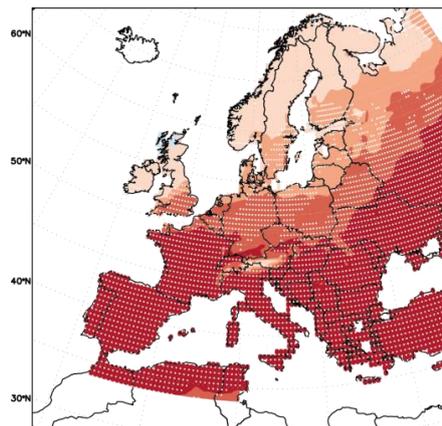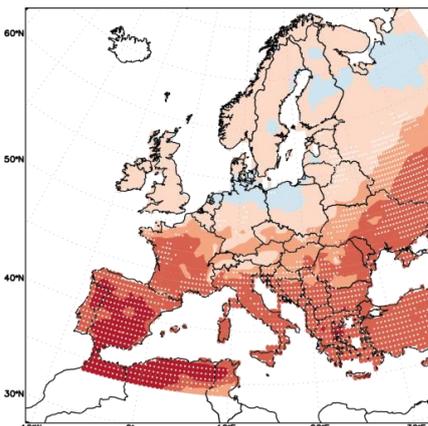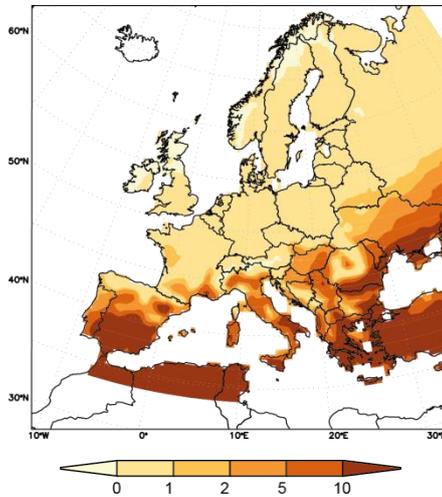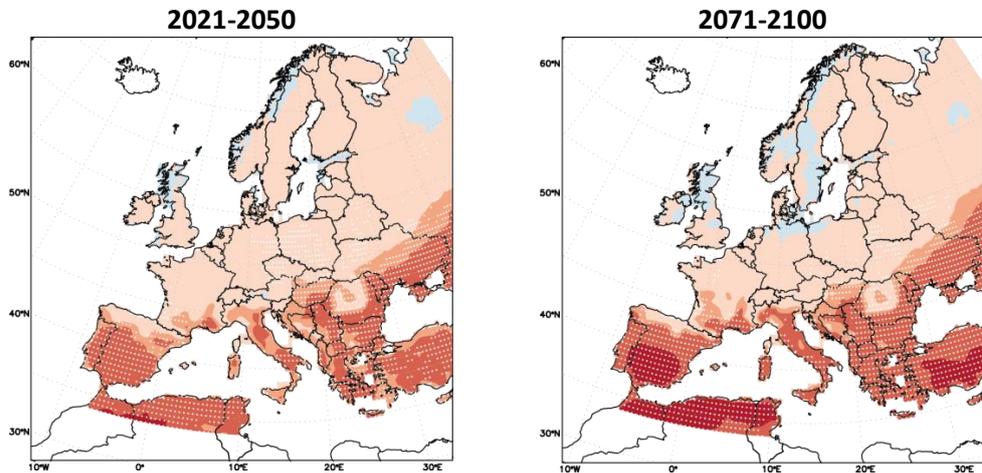

change in daily probability (%)

Fig. 13.4. (top) Multi-model mean probability (%) of forest fire risk (FWI>20) during 1971–2000. Multi-model mean change in probability (in percentage points) of forest fire risk (FWI>20) under the RCP 4.5 scenario (middle) and the RCP 8.5 scenario (bottom). White dots denote significant change at the 95% level.

116

Fire Weather

Daily probability of Fire Weather Index > 45
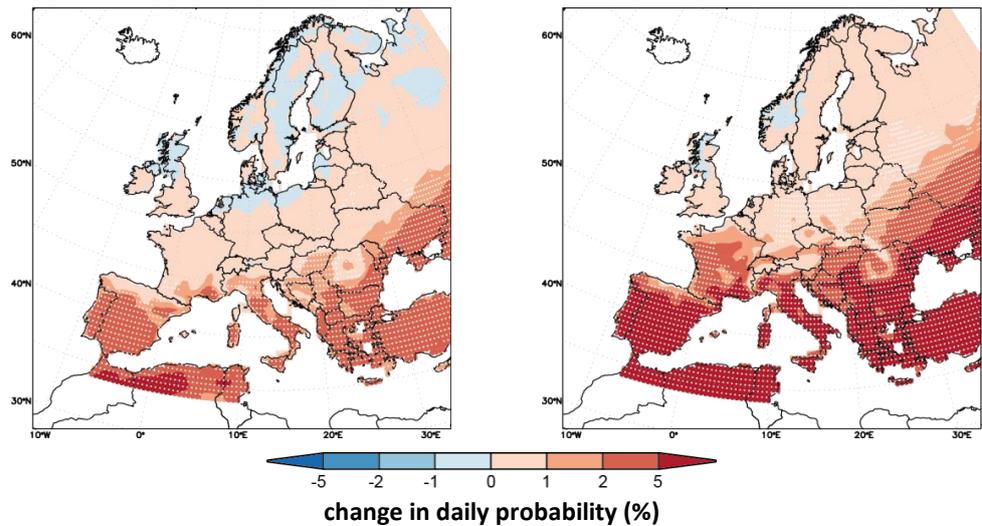
**Reference
Period**

1971-2000:

**Predicted
Changes**

RCP 4.5:

RCP 8.5:

2021-2050   **2071-2100**

change in daily probability (%)

**Fig. 13.5. (top) Multi-model mean probability (%) of forest fire risk (FWI>45) during 1971–2000. Multi-model mean
change in probability (in percentage points) of forest fire risk (FWI>45) under the RCP 4.5 scenario (middle) and the RCP
8.5 scenario (bottom). White dots denote significant change at the 95% level.**

fire risk is more evident in Southern and Central Europe, where models unanimously project an increase in daily probability of fire risk (FWI>20) by 2-5 pp and locally >5 pp by 2050 and predominantly by >5% by 2100 in most of Southern Europe. The change is more robust under the RCP 8.5 scenario. Similar changes are expected for the very high forest fire risk (FWI>45), although the degree of change is somehow lower. This increase is both due to increasing temperatures and to decreasing summer precipitation. Although in the north the temperature is projected to increase as well, some models also indicate an increase of precipitation, which would have an opposite effect on the fire risk; a slight decrease (1 pp) in the daily probability of very high fire risk is projected by the multi-model mean for some areas of Scandinavia. However, this change was not significant among the models. Nevertheless, the fire activity in Southern Europe is expected to increase less than the meteorological fire risk alone because reduction in productivity is expected to reduce the total availability of fuel to burn and thus restrict the actual fire activity (Migliavacca et al., 2013)

14. Large hail

Tomáš Púčik and Pieter Groenemeijer, European Severe Storms Laboratory

14.1 Introduction

Thunderstorms are sometimes accompanied by hailfall. The size of the hailstones most frequently reaches between 5 – 10 mm (Berthet et al. 2011). Large hail, which is commonly defined as a hail with stone diameters exceeding 20 mm and very large hail, defined as a hail with diameter over 50 mm, are much rarer occurrences. Whenever such large hail occurs, it is potentially very destructive and can cause enormous monetary losses reaching several billions of Euros. The extent of the damage depends strongly on whether the hailstorm passes over a populated area. Large hail can cause damage to cars, windows, greenhouses, roofs, and infrastructure components such as railway and traffic signalling systems and related components. Accumulations of large amounts of hail can bring traffic to a standstill and block drainage systems, thereby causing or exacerbating flash flooding.

Fig. 14.1. The largest hailstone recorded to date in Europe that fell on 6 August 2013 in Undingen, Germany. Hailstone measured 14.1 cm across and weighed 360 grams. Photo (and measurement) courtesy of Marco Kaschuba.

14.2 Method

Observational records of phenomena such as large hail or tornadoes are very inhomogeneous, and strongly depend on national efforts in individual countries (Antonescu and Kühne, 2015). As these phenomena are very local, they are often missed by weather station networks operated by national weather services. Therefore, reports from the media or amateur weather observers are used as well. In Europe, a European Severe Weather Database (see Section 3.1.2) makes an effort to collect such records. Even though reporting rates increased remarkably over the past years, Groenemeijer and Kühne (2014) state that the database cannot be used to build a reliable climatology of thunderstorm related phenomena. The data can, however, be used to develop *proxies* for severe weather, an effort that was pioneered by Brooks et al. (2003). Such proxies are quantities computed by an atmospheric model that exhibit a high covariance with the occurrence of the hazard.

The components of a proxy for convective hazards are based on the physical ingredients required for the formation of storms. These are:

1. The presence of **convective** (or latent) **instability.** Thunderstorms are a manifestation of deep, moist convection occurring in the atmosphere. Convection requires that atmosphere is unstable, a rapid decreases of temperature with height. When the vertical temperature gradient is large, rising bubbles of air that contain high amounts of humidity – which condense during this ascent – may become warmer than their environment, which reinforces their upward motion.

   As a measure for instability, the *Lifted Index* (LI) was used (Galway, 1956). LI is a measure of the temperature difference between the environment at 500 hPa level (which translates to the height of approximately 5.5 km) and a parcel ascending to this level from below. In case that the ascending parcel is warmer (thus unstable), LI will attain negative values. In our case, we calculated LI using parcels ascending from 925, 850 and 700 hPa (levels below the model surface were eliminated) and took the minimum value of LI.

2. **The presence of strong vertical wind shear.** Vertical wind shear is a change of the wind vector with height. Thunderstorms tend to be better organised and longer lived as the vertical wind shear increases (e.g., Weisman and Klemp 1982). In case that vertical wind shear is very strong, the updraft of a thunderstorm may attain rotation, which enhances it (e.g. Klemp, 1987). This type of thunderstorm is called supercell and is almost always accompanied by severe weather (Smith et al. 2012). Virtually all very large hail and violent tornado events are caused by this type of thunderstorm. Other forms of organized convection, such a bow-echoes are also typically associated with strong deep-layer shear (Doswell and Evans, 2001).

   As a measure for vertical wind shear, we calculated the magnitude of the vector difference between the 500 hPa and the wind 10 m above the surface. We call this deep-layer shear (DLS).

The combination of instability and vertical wind shear as a proxy for conditions that sustain severe thunderstorms has been used in several recent studies using both reanalysis and climate data (Brooks 2013, Diffenbaugh et al. 2013, Gensini and Mote 2015).
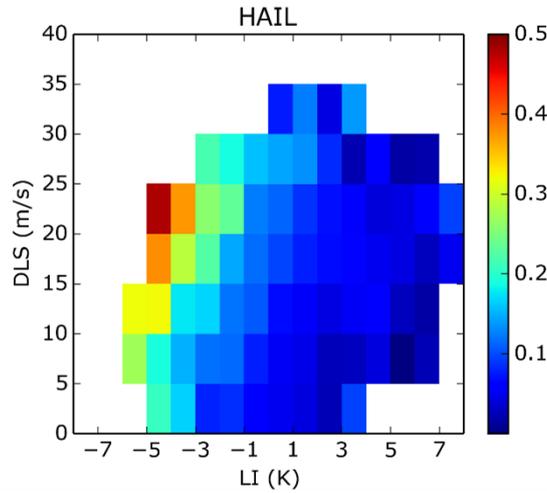

Fig. 14.2: Probability of large hail as a function of LI and DLS given that a thunderstorm occurs. From Púčik et al. (2015).

We here use a probabilistic instead of a deterministic approach, by assigning a probability of hazard occurrence to each combination of the predictor parameters DLS and LI, using results from Púčik et al. (2015). Fig. 14.2 shows the probability of large hail, given that a thunderstorm occurs. The probability is highest for unstable situations (left of the figure) and, given sufficient instability, increase with increasing shear (towards the top of the diagrams). We subsequently applied a Gaussian filter on the probability matrix to smooth out sampling artefacts and extrapolated the values into those where no values were observed.
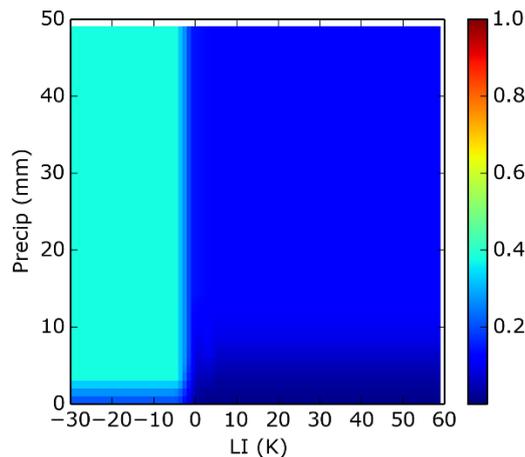

Fig. 14.3. Probability of thunderstorm initiation as a function of LI and simulated 6 hourly accumulated precipitation.

The procedure up to this point only gives the probability of severe weather given that a thunderstorm has formed. It is equally important to know what is the probability is that thunderstorm will form. Even when the atmosphere is very unstable and strong wind shear is present, thunderstorms may not form if no process to release the instability is present. We modelled

121

the probability of thunderstorm occurrence as a function of instability (LI) and 6-hourly precipitation sum simulated by the model (Fig. 14.3). Data from the probability matrix are based on the work of Westermayer (2016). The final probability of a hazard (large hail in this case) consists of the product of two probabilities:

$$P(large\ hail) = P(thunderstorm) * P(large\ hail\ given\ thunderstorm) \qquad \text{Eq. 14-1}$$

The probabilities were calculated for all time periods of the model output and were summed over the time period and averaged in order to obtain an average yearly number of events in every model grid box.

The calculated probabilities that were used are, strictly speaking, valid for the occurrence of an event within 150 kilometre of a point within 3 hours (Pučik et al, 2016) and the probability that a local observer will encounter this hazard is typically much smaller. In order to calibrate the simulated probabilities to the local probabilities we introduced a calibration factor. To do so, we used data from a large network of hailpads across southern and central France by ANELFA (Berthet et al. 2011). The average probability with which a hailpad across this network is hit is 0.029 (Berthet, personal communication). We calculated the ratio of the observed frequency to the umber simulated events for this particular area and applied this ratio as a calibration factor to the whole domain and was calculated separately for each model run. Obviously, it is possible that relatively large errors were made by calibrating only using a number of hail networks.

We computed the proxy parameters in 15 different EURO-CORDEX model runs (see Section 3.3) and computed ensemble means of these model runs. We evalutated simulations for the future periods 2021-2050 and 2071-2100 according to the climate scenarios RCP 4.5 and RCP 8.5, which were contrasted to an historical run 1971 – 2010.

14.3 Present climate

In the reference period of 1971-2000, the highest risk of large hail (diameter ≥ 2 cm) is simulated for parts of northern Africa (north of the Atlas Mountains), eastern Spain and Italy (Fig. 14.4). A local minimum is located over the Alps, where dry air in the highlands prevent development of a very unstable airmass.

The average frequency of large hail in Central Europe is 1 event in 50 to 1 event in 25 years at any given location. Parts of Iberia, Italy and the eastern Adriatic Sea coastline have a higher frequency, ranging from 1 event in 25 to 1 event in 10 years. This may not seem very high, but hail often falls in a rather narrow path (e.g. on average of 1.3 km according to Changnon, 1992). Thus, an observer that finds himself in an area on a day with large-scale conditions very conducive to large hail will still most likely be missed by the hail swath. Even in a rather hail-prone area such as S France, an average annual frequency of large hail affecting one hailpad is around 0.03, corresponding to a return period of more than 30 years.

The annual probability of very large hail (diameter ≥ 5 cm) is approximately a factor of 10 lower than that of large hail (Fig. 14.5). Very large hail is a rare phenomenon that occurs exclusively with supercell thunderstorms
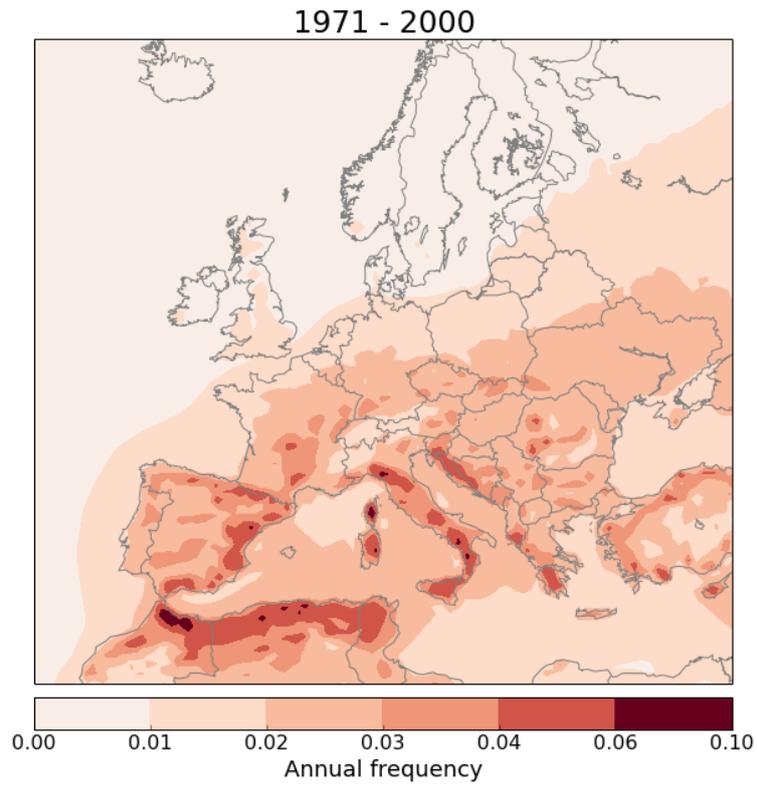
1971 - 2000

Fig. 14.4. Annual probability of large hail (diameter ≥ 2 cm) based on the ensemble of historical runs.

1971 - 2000

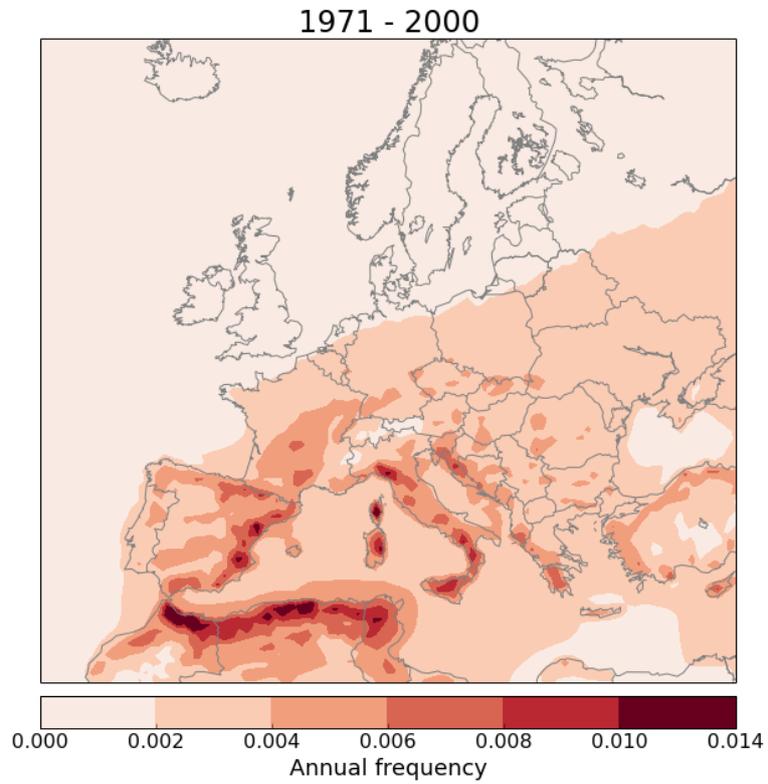**Fig. 14.5. as in Fig. 14.4, but for very large hail (diameter ≥ 5 cm).**

According to the model output, such large hail occurs over central Europe at any given location on average of once in 500 to once in 125 years. In regions like northern Africa, eastern Spain, Sardinia, Corsica, north-western and southern Italy and, probability is higher with an average local return period of very large hail being about 100 years.

The main uncertainty concerning our present and future climatology of (very) large hail events results from the fact that it is not directly based on the observations of real events, but model simulated environments. Due to the lack of homogeneous data across the whole Europe it is not possible to perform a pan-European validation of the model. It is likely that small-scale minima and maxima are in reality not located where they would normally occur. Results from (Punge et al, 2014), who used the occurrence of overshooting tops, a characteristic of hail-bearing storm clouds, as a proxy for hail occurrence, arrived at a spatial distribution with different small-scale features, but very similar large-scale patterns, wchich lends confidence to the accuracy of the approach taken here. It is likely that the grid spacing of 0.44°, or about 50 km, is not sufficient to accurately resolve the effects of most mountain ranges on the environmental characteristics that modulate large hail occurrence.

14.4   Climate predictions

Even though the used method may not depict small-scale minima and maxima very accurately, it can be used to study the effects of climate change. Fig. 14.6. shows both the present frequency of large hail occurrence and the changes simulated for the RCP 4.5 and RCP 8.5 scenarios for the periods of 2021-2050 and 2071-2100. Changes larger than twice the sample standard deviation of the ensemble, back dots are shown. We consider this a relatively strict criterion for the significance of the changes.

In case of the RCP 4.5 scenario, the changes are small for both periods. For 2021-2050, we find only a very few gridpoints with a significant change. For 2071-2100, increase is only larger than twice the ensemble standard deviation near the Alps and over Russia. The model ensemble simulates an increase of about 1 event in 200 to 100 years near the Alpine region, compared to the current state of 1 event in 50 to 25 years, i.e. relative increase of approximately 25%.

More robust increases are simulated for the RCP 8.5 scenario. For the period of 2021-2050, a significant increase is forecast over the coastal areas of the Mediterranean such as eastern Spain, northern Italy, and the eastern Adriatic Sea coastline with an average increase of 1 event in 200 to 100 years. A slight decrease in the number of events is forecast over the Atlantic Ocean just south of Iceland, but this decrease is not larger than twice the ensemble standard deviation. The period of 2071-2100 yields significant increases over much of Europe and the central Mediterranean. A slight, insignificant decrease is forecast over Morocco. Over much of Central Europe, the pre-Alpine areas, eastern Spain, Italy and extreme northern Africa, the frequency of large hail events should increase by approximately one additional event every 100 years. Certain spots, however, such as north-western Italy, have a projected increase of 1 event in 40 years. In a relative sense, the frequency increases by 30 - 60% over large areas of central and south-central Europe.

Large hail

Annual probability of occurrence of hail with diameter ≥ 2 cm
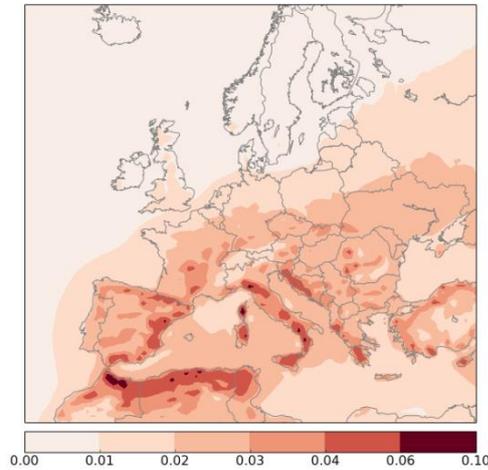
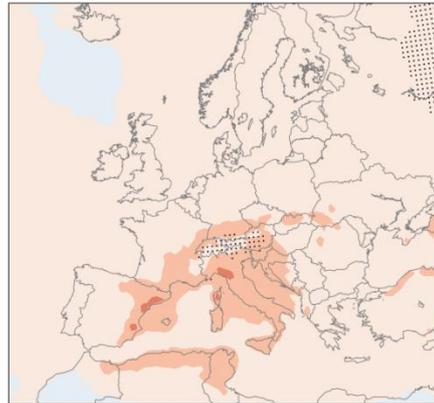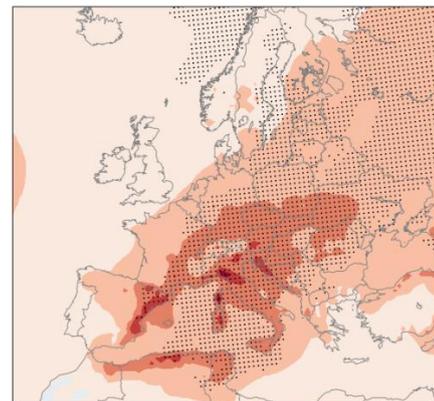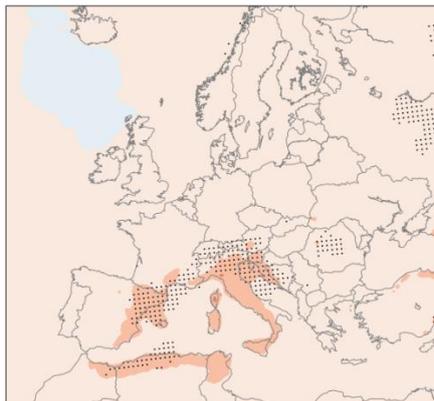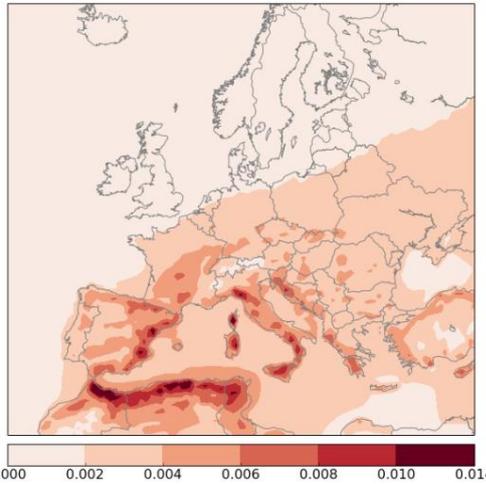**Fig. 14.6. Graphic showing the present frequency of large hail over Europe (top row) and the projected changes in the RCP 4.5 and RCP 8.5 scenarios (bottom two rows). Black dots denote ensemble mean changes exceeding twice the standard deviation of the ensemble.**

Large hail

Annual probability of occurrence of hail with diameter ≥ 5 cm
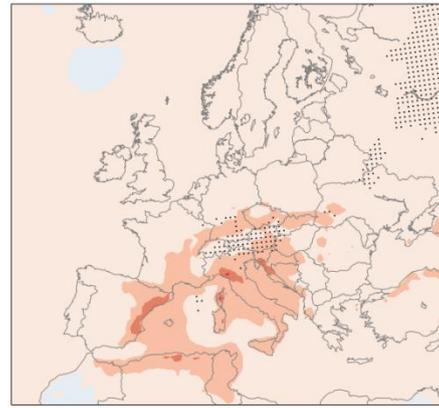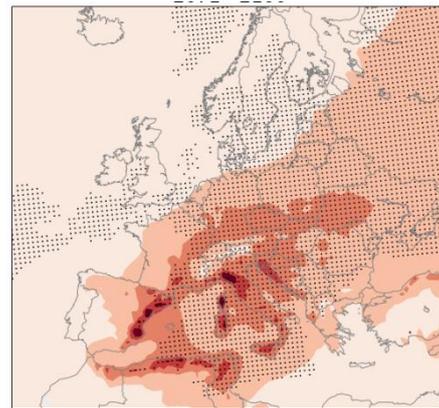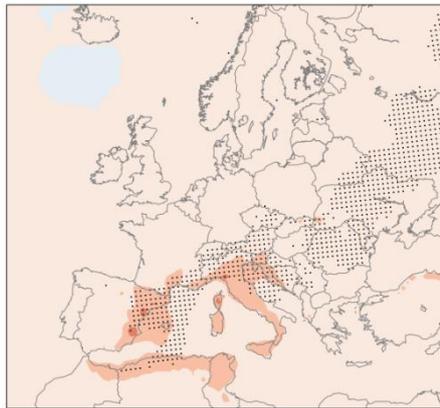
**Reference
Period**

1971-2000:

**Predicted
Changes**

RCP 4.5:

RCP 8.5:

change of annual probability

Fig. 14.7: As in Fig. 14.6, but for very large hail.

The results show that global warming will lead to an increase in the frequency of large hail events. There are no areas for which the ensemble mean shows a decrease in the frequency larger than twice the ensemble standard deviation. In the RCP 8.5 scenario significant increases over a large portion of Europe are expected for the late 21st century. The patterns in the occurrence of very large hail (Fig. 14.1) are qualitatively very similar to that of large hail, but quantitatively different.

14.4.1 Origins of changes

To better understand the trends in the probability of thunderstorm hazards in the future, we have investigated the trends in the parameters (LI, DLS) used to infer the hazard probability. Trends in the conditions favourable for thunderstorm initiation will be covered in the chapter dedicated to the thunderstorms and lightning (number 15). For the sake of brevity we illustrate these changes by only considering the RCP 8.5 2071 – 2100 scenarios, which features the largest changes.

The distribution of the 1st percentile of Lifted Index is a value corresponding to the 1% most unstable situations that occur at a location. This parameter in the historical scenario (1971-2000) and its changes across Europe as predicted by the EURO-CORDEX RCP 8.5 simulations are depicted in Fig. 14.8. The 1st percentile of the Lifted Index shows that regions with the highest instability are located near the Mediterranean Sea, which is an important source of low-level moisture. They are also located near the arid, hot regions such as Sahara or Iberian Peninsula, which are the source of steep vertical temperature gradient.
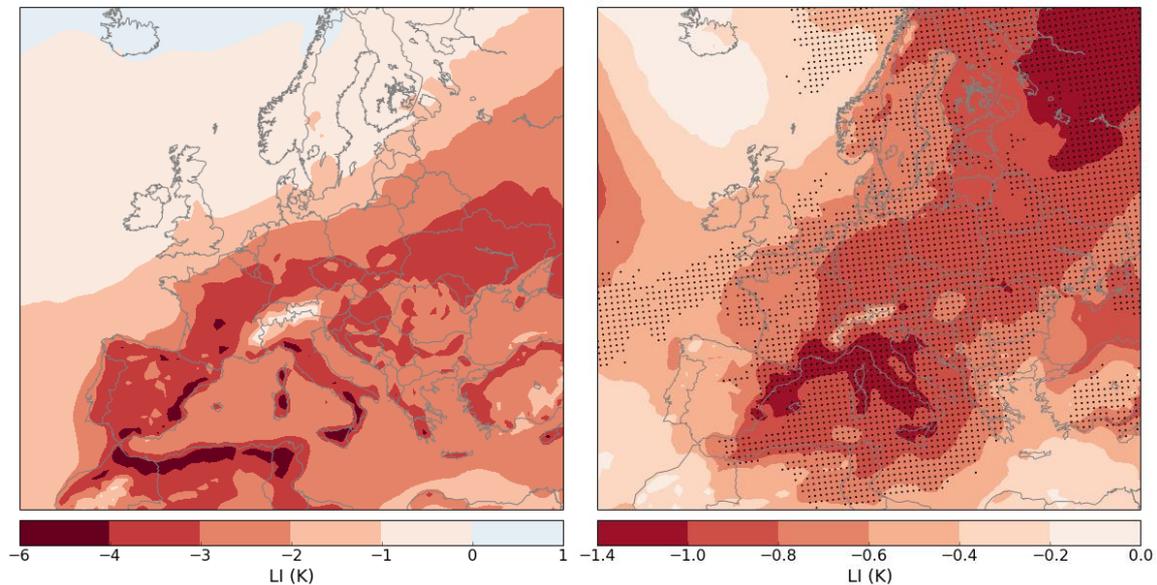
Fig. 14.8. Left: Ensemble mean of 1st percentile LI from historical simulations. Right: Change in the ensemble mean of 1st percentile LI between the RCP 8.5 2071-2100 and the historical 1971-2000 simulations. Black dots represent that the ensemble mean change exceeds two times the standard deviation of the differences in LI between individual simulations.

A significant change in LI is forecast according to the RCP 8.5 scenarios for the 2071-2100 period. The biggest decrease in LI (thus the greatest destabilisation) is simulated over the northern Mediterranean and over Russia. Most of the grid points over Europe show that simulated change is significant. Small, insignificant change in LI is forecast over the Atlantic south of Iceland, over north-

western Africa and over the south-eastern Mediterranean. A decrease in LI across much of the domain is caused by the increase in low-level moisture (not shown) as temperatures increase in the future. Reason is that maximum possible content of water vapour in the airmass increases exponentially with the increasing temperature.

15. Convective windstorms

Tomáš Púčik and Pieter Groenemeijer, European Severe Storms Laboratory

15.1 Introduction

Convective windstorms are smaller in area than windstorms that occur in conjunction with low pressure areas and are more difficult to predict. Nevertheless, they can be equally damaging and measured wind gusts have exceeded 50 m/s in extreme cases. For the purpose of this study, we have used two wind speed thresholds: 25 m/s and 32 m/s, which will be referred to as *severe winds* and *extremely severe winds*, respectively. The prevalence of convective windstorms during the vegetation period exacerbates their damaging potential: uprooted or snapped trees strongly affect critical infrastructure as they can damage power lines or completely block major traffic routes. The strongest wind gusts can even topple high tension masts or damage infrastructure along highways or railways.

Convective windstorms generally come in two forms. The first very local form is when severe gusts result from downbursts, which are pockets of rain-cooled air plunging rapidly from the base of the thunderstorm towards the ground. The second form of convective windstorms produce long wind damage swath resulting from fast traveling, well organised convective systems. Such widespread convective windstorms are called derechoes (Johns and Hirt, 1987).

Fig. 15.1. Convective windstorm impacting NW Germany on 9 June 2014. This windstorm uprooted thousands of trees and brought the rail traffic in the region to a virtual standstill for several days. Photo courtesy of Arjan van Beelen.

15.2   Method

For convective windstorms, the same methodology was used as for large hail. For the details, we refer to Section 14.2. Regarding the environments of convective windstorms, the probability matrix of the two predictors Lifted Index (LI) and Deep-Layer Shear (DLS) suggest a strong dependence on both. In contrast to large hail, enhanced probability can also be found in more conditions, but very strong wind shear (DLS above 30 m/s). This regime reflects the convective systems forced by strong cold fronts during the cool half of the year.
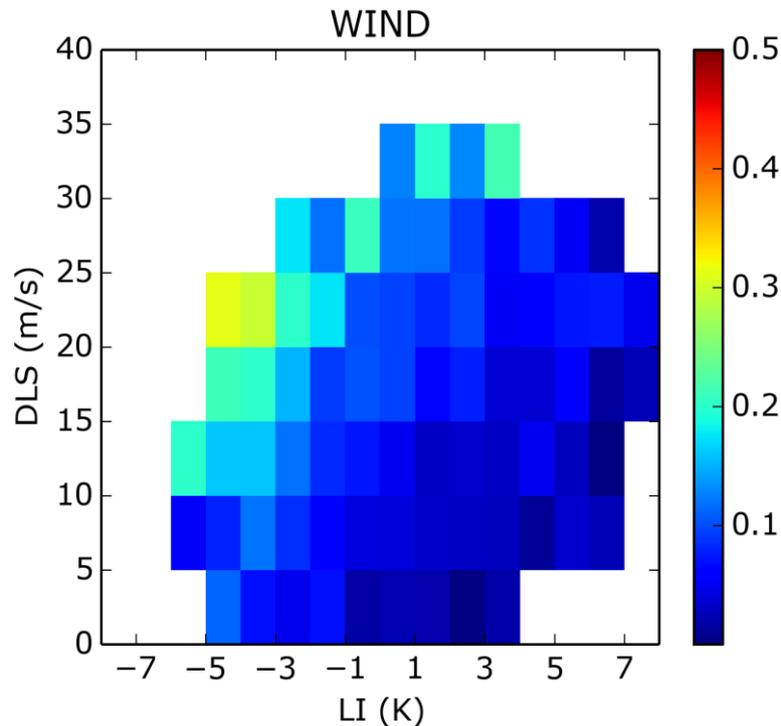

Fig. 15.2. Probability of severe convective wind gusts (i.e. wind speed ≥ 32 m/s), as a function of Lifted Index (LI) and Deep-layer shear (DLS).

Convective windstorms can occur as local downbursts and as derechoes, which typically form in somewhat different environments. Derechoes occur usually in a very unstable environment and in the presence of strong vertical wind shear (Coniglio et al. 2010). Downbursts, on the other hand, can form in more quiescent conditions, with only little instability and weak vertical wind shear. Microphysical processes within the storm and the dryness of the air underneath the base of the thunderstorm play crucial role in the development of downbursts (Wakimoto 1985). Because these factors are not taken into consideration in the LI – DLS probability matrix, our approach is better suited for the detection of environments favourable for derechoes than downbursts. Compared to the probability of large hail (Fig. 14.2), the probability of severe wind gusts is somewhat more favoured in situations with modest instability and very strong DLS than large hail, which in turn is more likely in conditions of moderate DLS and very strong instability (i.e. very negative LI).
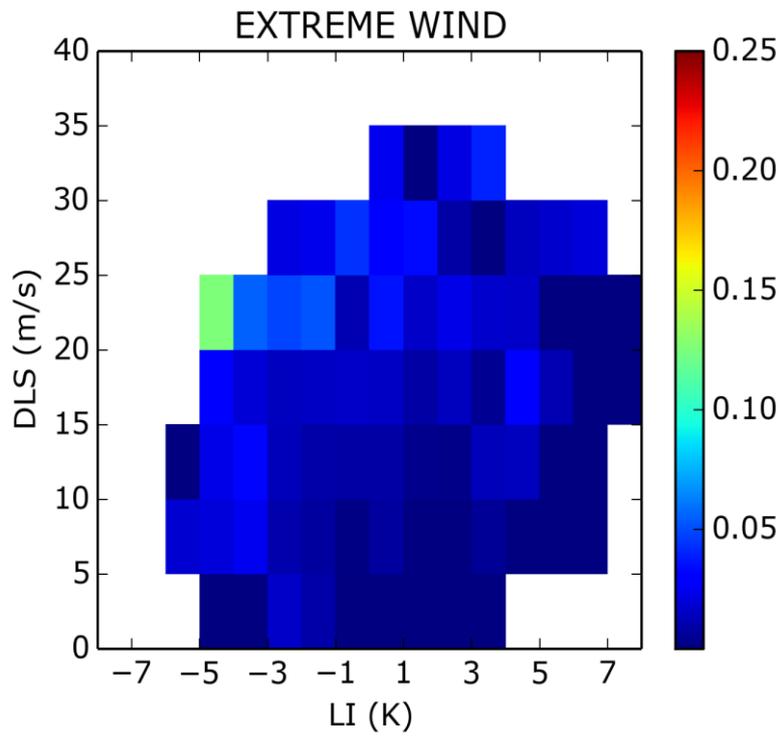
Fig. 15.3. As in Fig. 15.2, but for extremely severe convective wind gusts (i.e. wind speed ≥ 32 m/s).
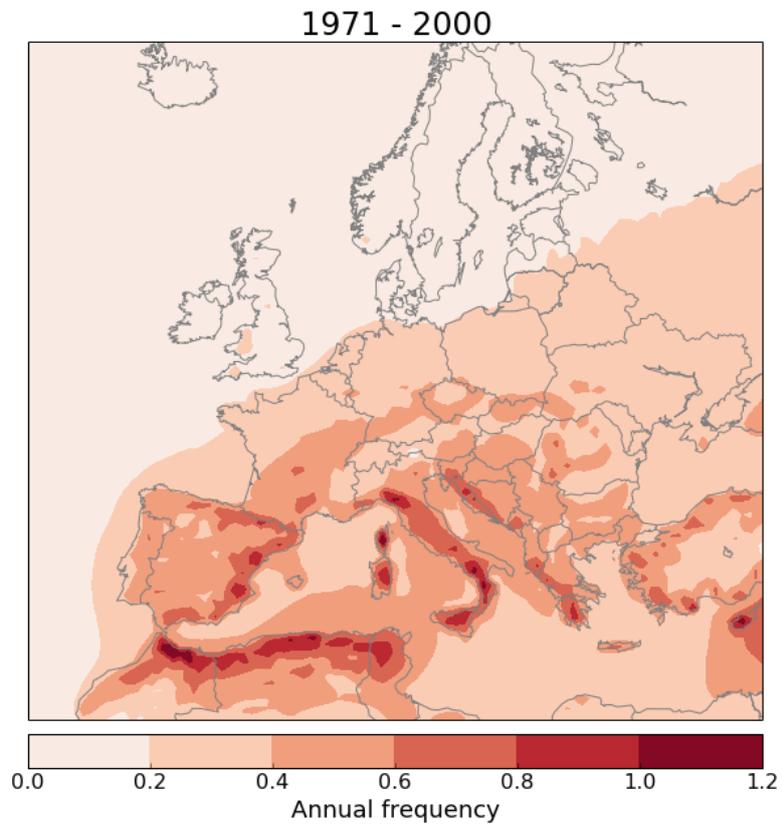

Fig. 15.4. Annual probability of severe convective wind gusts based on the ensemble of historical runs.

The local probability of severe wind gusts is calculated as follows:

P(severe wind gust) = P(thunderstorm) * P(severe wind gust given thunderstorm) **Eq. 15-1**

We want to estimate the local hazard probability instead of the probability that the hazard occurs somewhere within a model grid cell. For this purpose, we calibrated the modelled probabilities using the observations of wind gusts at the weather stations over southern Germany during the warm half of the year (April to September). We assumed that severe wind gusts during this period are almost exclusively caused by thunderstorms. Using these data, we arrived at a local annual probability of 0.206, i.e. approximately translates to 1 event in 5 years. For each historical model run a calibration ratio was calculated between the local observed probability and model simulated probability.

15.3   Present climate

The spatial patterns in the local maxima of hail and wind gust events (compare Fig. 14.4 and Fig. 15.4) are qualitatively almost identical, even though severe wind is slightly more favoured by strong DLS and hail more by strong instability. Local maxima are located over the northern Africa, eastern Spain, Italy and the eastern Adriatic Sea coastline. Even though spatial patterns are quite similar, local probabilities are very different. For example, consider the coastline area of the Gulf of Genoa – both hail and wind gust events have a strong maximum here. But while the maximum frequency of large hail is almost 1 event in 10 years, maximum frequency of severe convective wind gusts exceeds 1 event in 1 year. That means wind gusts are by one order of magnitude more frequent than the hail events. Central Europe has an average frequency of convective windstorms of 1 event in 5 years to 1 event in 2 years, compared to the frequency of 1 event in 50 to 1 event in 25 years for large hail.

The difference between the maximum hail and maximum wind gust probabilities in favourable environment is too small to explain such a difference in annual frequency. Actually, maximum probability of large hail was higher than of severe wind gusts. That means an environment of high instability and strong wind shear is more likely to result in a large hail than severe wind gust event. From this perspective, one would expect the hail events to occur more frequently than wind gusts. The answer to this paradox lies in the spatial coverage of these hazards. While hail swaths are often very narrow (as mentioned above), severe wind gusts typically cover wider areas, especially when associated with large convective systems. In such systems, damage swath can be tens of kilometers wide while hailstreaks are typically only a few kilometres wide. Therefore, the local probability of severe convective wind gusts is higher than of large hail.

Annual probability of extremely severe convective wind gusts is about 5 times lower than the probability of severe convective wind gusts. Over much of central Europe, average frequency of extreme gusts is 1 event in 25 to 1 event in 10 years, compared to the 1 event in 5 to 2 years for severe gusts. Maximum frequencies of around 1 event in 6 years are simulated over the parts of Italy and northern Africa.

15.4   Climate predictions

Fig. 15.6 shows the present frequency of severe convective wind gusts occurrence along with the changes simulated for the RCP 4.5 and RCP 8.5 scenarios for the periods of 2021-2050 and 2071-2100. For the RCP 4.5 scenario, the period of 2021-2050 shows almost no changes that, compared to the historical run, exceed twice the ensemble sample standard deviation (the chosen significance threshold). The only grid points for which this is the case are located over the Alps and have increases in frequency of less than 1 event in 20 years (compared to the current frequency of 1 event in 5 to 1 event in 2 years).
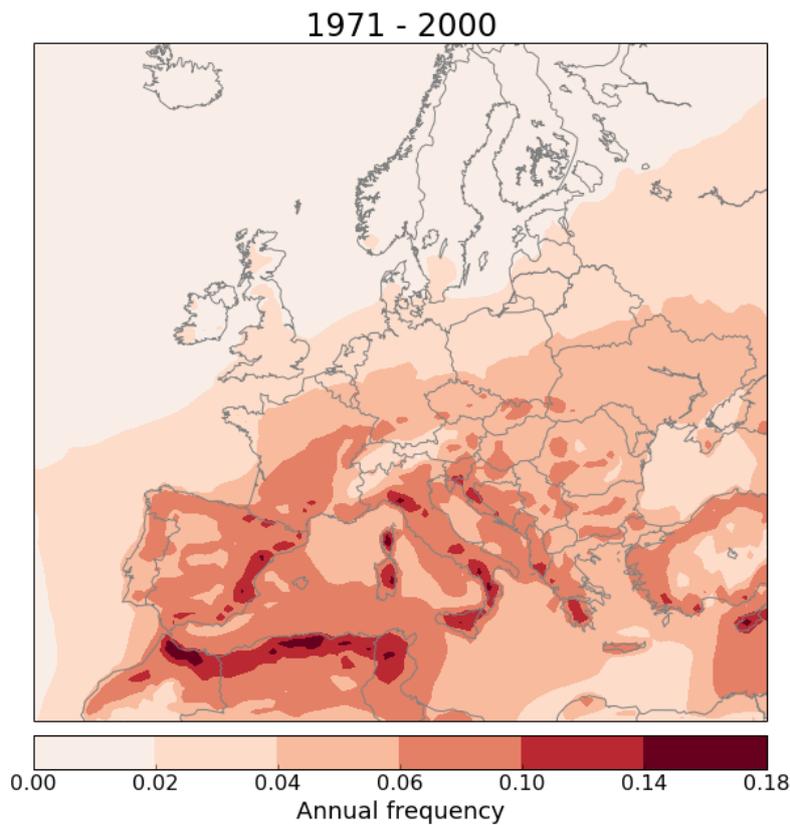

Fig. 15.5. As Fig. 15.4, but for extremely severe convective wind gusts.

The simulations for 2071-2100 exhibit stronger increases in expected event frequency of up to 1 event in 10 years in the Alps. Parts of Spain, Italy and the eastern Adriatic Sea coastline show increases of 1 event in 10 to 5 years. The changes do not meet the relatively strict significance threshold of being larger than twice the ensemble sample standard deviation, except over the Alps and parts of northern Russia.

Convective windstorms

Annual probability of severe convective wind gust over 25 m/s
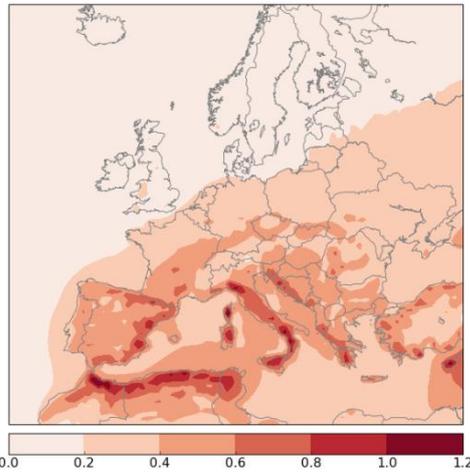
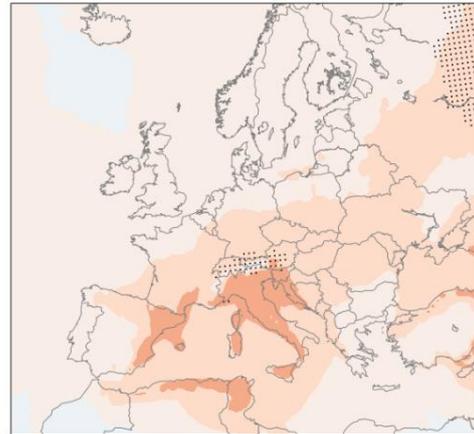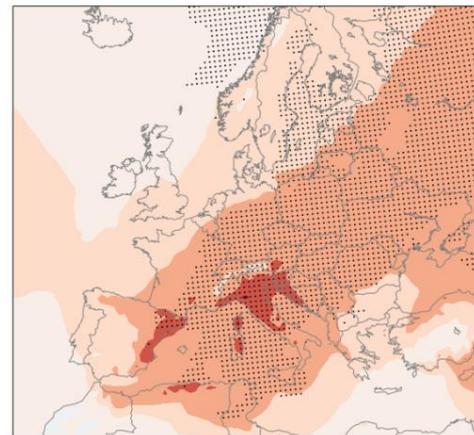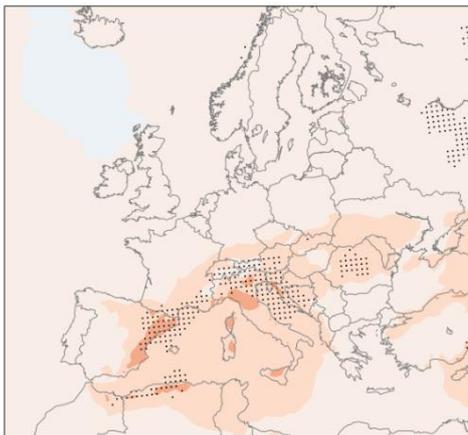**Fig. 15.6. Present annual frequency of severe convective wind gusts over Europe (top row) and the projected changes in the RCP 4.5 and RCP 8.5 scenarios (bottom two rows). Dots in the grid points denote statistically significant change - mean relative change in the ensemble exceeds twice the standard deviation of the changes in the individual ensemble members.**

Convective windstorms

Annual probability of severe convective wind gust over 32 m/s
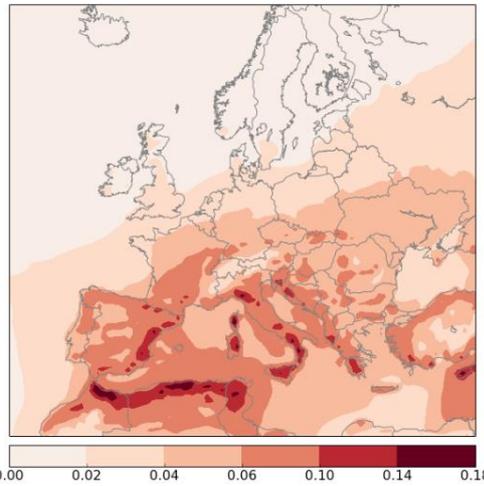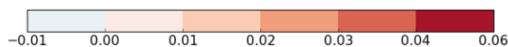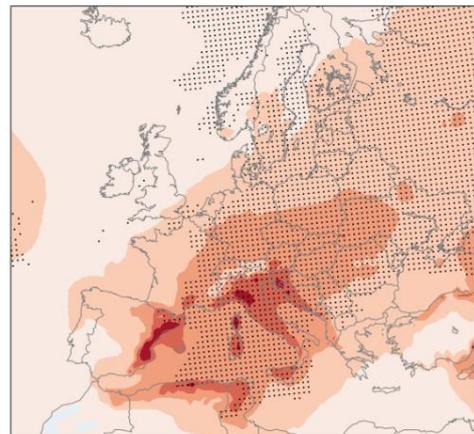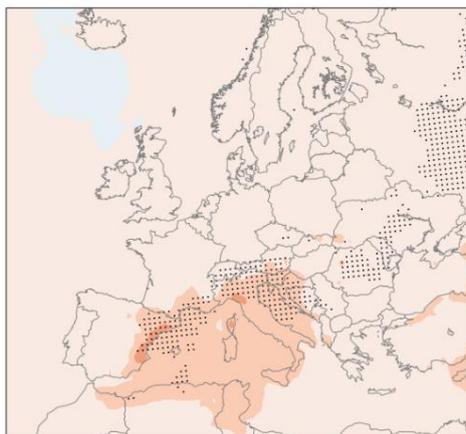
Fig. 15.7 as in Fig. 15.6, but for extremely severe convective wind gusts (i.e. wind speeds ≥32 m/s). Please note the difference in the color scale with respect to Fig. 15.6.

The RCP 8.5 scenario shows more significant changes than the RCP 4.5. Even the 2021-2050 period shows more gridpoints with significant increases than the 2071-2100 period of RCP 4.5. For the 2021-2050 period, significant changes are projected for the north-eastern Spain, northern I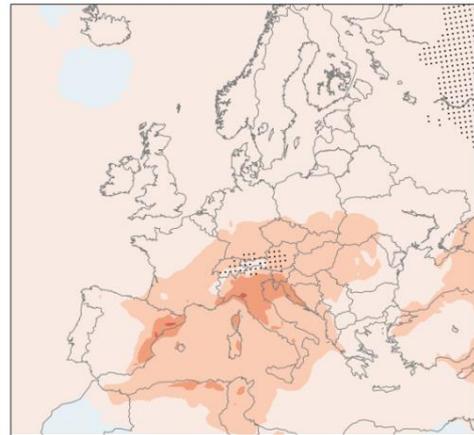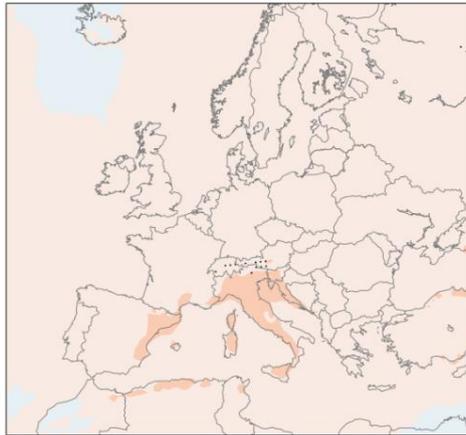taly, the Adriatic Sea coastline area, south-western Austria and parts of Romania. The frequency is forecast to increase by one 1 event in 20 to 1 event in 5 years. For the 2071-2100 period even more robust changes are predicted, which are significant for a wide swath from north-eastern Spain through the central Mediterranean into central and eastern Europe. In this area, the frequency is forecast to increase by an additional 1 event in 10 to 1 event in 3 years, corresponding to relative increases of probability of 30 – 60% (not shown).

Over eastern Spain, there are fewer gridpoints with significant change in the 2071 - 2100 period than in the 2021-2050 period, even though the increases are larger. The reason for this is the spread of the model solutions for the 2071-2100 increased when compared to the 2021 - 2050 period, so that changes are not statistically significant. Some models forecast a strong drying of southwest Europe and hence less (severe) thunderstorm activity.

The changes in the patterns of extremely severe convective wind gusts are qualitatively similar to the severe gust (Fig. 15.7). Relatively speaking, the changes are similar in magnitude. In conclusion, important increases in the frequency of convective windstorms are projected for most of Europe in the RCP 8.5 scenario for the late 21st century. The RCP 4.5 scenario simulations show modest increases changes over Europe. The biggest uncertainty regarding the future development is observed over south-western and south-eastern Europe.

16. Tornadoes

Tomáš Púčik and Pieter Groenemeijer, European Severe Storms Laboratory

16.1 Introduction

Tornadoes are arguably the most violent thunderstorm related phenomena. Once considered to be very rare in Europe, recent research actually shows that there are hundreds of tornadoes reported each year in Europe (Groenemeijer and Kuhne 2014; Antonescu et al. 2016). Some tornadoes are capable of producing enormous damage as instantaneous windspeeds in them can exceed 100 m/s. Because wind measurements inside tornadoes are extremely rare, tornadoes are rated according to the damage they cause using the so-called Fujita scale (with tornado ratings F0 - F5). Most tornadoes are weak (F0 - F1), causing similar damage to ordinary convective windstorms, such as damage to trees or powerlines. However, strong (F2 - F3) and especially violent (F4 - F5) tornadoes may inflict very significant damage also to more sturdy components of infrastructure, for example buildings of power plants. In this study, we use one threshold levels for a tornado – one that encompasses all tornadoes regardless of their intensity, i.e. F0 – F5 on the Fujita scale.

Fig. 16.1. An F4 tornado on the outskirts of Venice on 8 July 2015. Venice and the surrounding area are one of the most tornado prone region in Europe according to the reports. Photo by Valentina Abinanti.

16.2   Method

For tornadoes the same method as for large hail and convective windstorms was employed. For more details, refer to Section 14.2.

Similar to large hail and convective windstorms, the probability of tornadoes is highest in environments of high instability and strong vertical wind shear (Fig. 16.2). Tornadoes, like convective windstorms, form in two regimes. Most of the strong and virtually all violent tornadoes are associated with supercell thunderstorms. These tornadoes are associated with the presence of strong vertical wind shear (Thompson et al. 2003). However, weak tornadoes can also form in more inconspicuous conditions, arising from the small scale circulations along the convergence lines under growing cumuliform clouds.
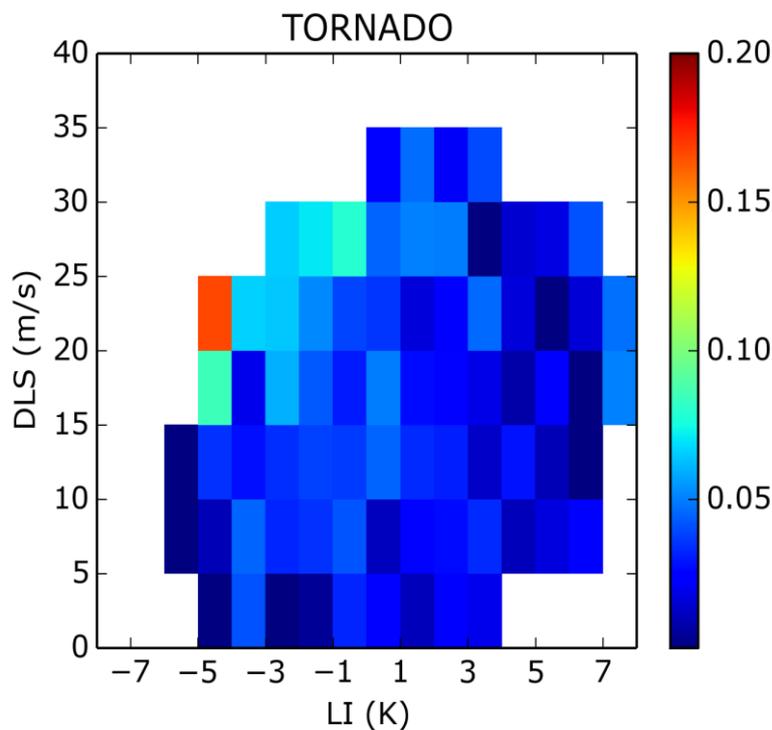
Fig. 16.2. Probability of tornado as a function of Lifted Index (LI) and Deep-Layer Shear (DLS).

The absolute probability values indicate that tornadoes are less likely to occur than the other two thunderstorm-related phenomena analysed (large hail, convective windstorms). For example, for a LI below -4 K and DLS above 20 m/s, the probability of large hail is almost 50%, the probability of severe convective wind gusts is 35% and the probability of a tornado is only 18%, and this particular point is likely an outlier within the sample noise.

The probability of tornado is calculated as a product of two probabilities (See Section 14.2):

   P(tornado) = P(thunderstorm) * P(tornado given thunderstorm)   **Eq. 16-1**

In order to compute the local probability of tornadoes, the modelled probabilities in the reference period were normalized to an estimate of the actual local probability of tornadoes. We used data from Germany, a country with the most consistent reporting of tornadoes over the past 10 years. During the period 2006-2015, Germany was affected by 173 F0, 97 F1, 44 F2 and 9 F3 tornadoes. Using the average track width and length for different tornado intensities (based on Groenemeijer and Kuhne 2014), a total area affected by tornadoes was calculated. Using this information, we arrived at the local annual probability of occurrence 0.000050. That means that the average frequency of tornado hitting any particular location in Germany is 1 event in 20 000 years. This may be a slight underestimation, because not all tornadoes that actually occurred have been reported, and because the ten-year sample did not contain any violent F4 or F5 tornadoes, which are known to have occurred in Germany (and elsewhere in Europe) longer ago.

16.3   Present climate

The spatial patterns of the local maxima of tornadoes (Fig. 16.3) are quite similar to those of large hail and severe wind gusts (Fig. 14.4 and Fig. 15.4**Error! Reference source not found.**). It is possible that a potential inclusion of further predictors (such as vertical wind shear in the lower troposphere or cloud base height will slightly change the distribution, but this is a longer research endeavour than could be completed within the present study. Local maxima are located over the northern Africa, parts of eastern Spain, Italy and the north-eastern Adriatic Sea coastline.
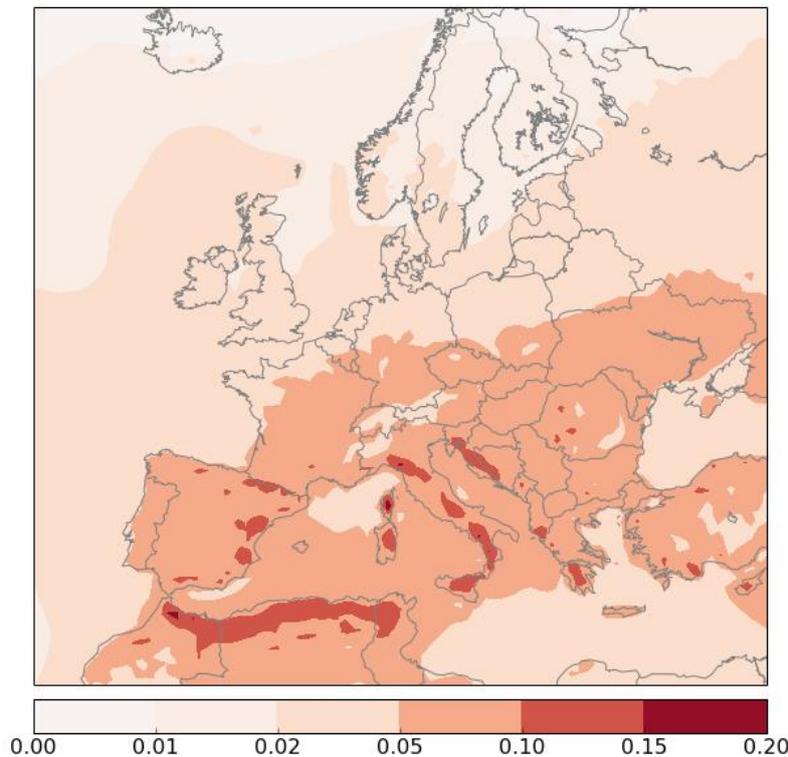
Fig. 16.3. Annual probability of a location being affected by a tornado during the period 1971-2000, based on the ensemble of historical runs, multiplied by a factor of 1000.

As suggested above, there are big differences between the frequencies (probabilities) of tornadoes and the other two phenomena. Again, consider the coastline area of the Gulf of Genoa. A local person (structure) would be hit by tornado on average once per 10 000 to once per 5000 years. To put this into perspective of the other thunderstorm related phenomena, this person would experience severe convective wind gust on average of once a year and large hail on average of once per 10 years. The majority of people in Europe will in fact, never experience tornado in their lifetime.

16.4 Climate predictions

Fig. 16.4 shows the present annual frequency of tornadoes occurrence along with the changes simulated for the RCP 4.5 and RCP 8.5 scenarios for the periods of 2021-2050 and 2071-2100.

For the RCP 4.5 scenario, the period of 2021-2050 shows small changes compared to the historical period. Only a few grid points over the Alps actually show a small change that is bigger than twice the intermodel standard deviation (the chosen significance threshold). Towards the late 21st century (2071-2100), still only a few gridpoints over the Alps and over Russia show an increase that is significant according to this strict criterion. In a relative sense, the highest increases are on the order of 20-25 % over south-central Europe.

In the RCP 8.5 scenario there are larger areas of significant changes within the ensemble than in the RCP 4.5. Towards the first half of the 21st century (2021-2050), simulations show that significant increases in frequency should occur over the north-eastern Spain, parts of the Balearic Sea and the Adriatic Sea and their coasts. The tornado frequency should increase by approximately 1 event in 100 000 years (0.01 x 10^{-3} per annum, p.a. hereafter) to 1 event in 50 000 years (0.02 x 10^{-3} p.a.). In a relative sense, this corresponds to increases of around 20%. Further north, there are increases as well, but they are more modest and not larger than twice the intermodel standard deviation.

Even more statistically significant changes are projected by the end of the 21st century (2071-2100). Much of Europe is then expected to undergo a significant increase in the frequency of tornadoes. The highest increase is simulated over the parts of north-western and north-eastern Italy, as well as for parts of Slovenia and south-western Austria. For these regions, the increase of frequency will be on the order of 1 event in 25 000 years (0.04 x 10^{-3} p.a.), which is an increase of about 50%. The surrounding areas should see an increase of around 1 event in 100 000 years (0.01 x 10^{-3} p.a.) to 1 event in 33 000 years (0.03 x 10^{-3} p.a.), which amount to relative increases typically between 20 and 50%.

Certain areas show statistically not significant changes even for the RCP 8.5 scenario, despite the fact that ensemble mean hints at an increase. For example, consider the eastern Spain area where ensemble mean shows the same value of annual frequency change as for northern Italy. However, projected change was marked as not significant. As we have already mentioned in the previous sections concerning large hail and convective windstorms, development over much of western and particularly south-western Europe is questionable with a large spread between the model solutions. Some models predict a significant drying and fewer convective situations to occur in Iberia and the Maghreb.

Tornadoes

Annual probability of a location being affected by a tornado (x 1000)
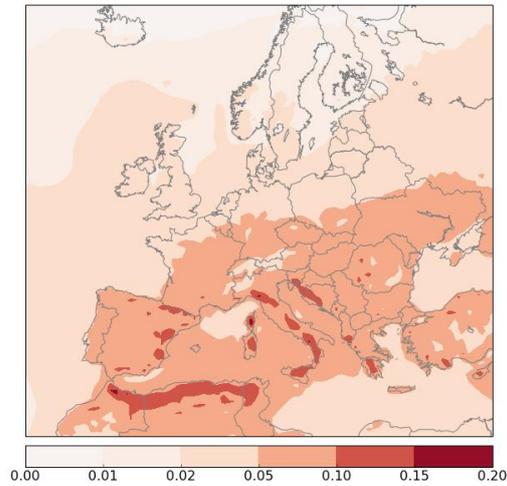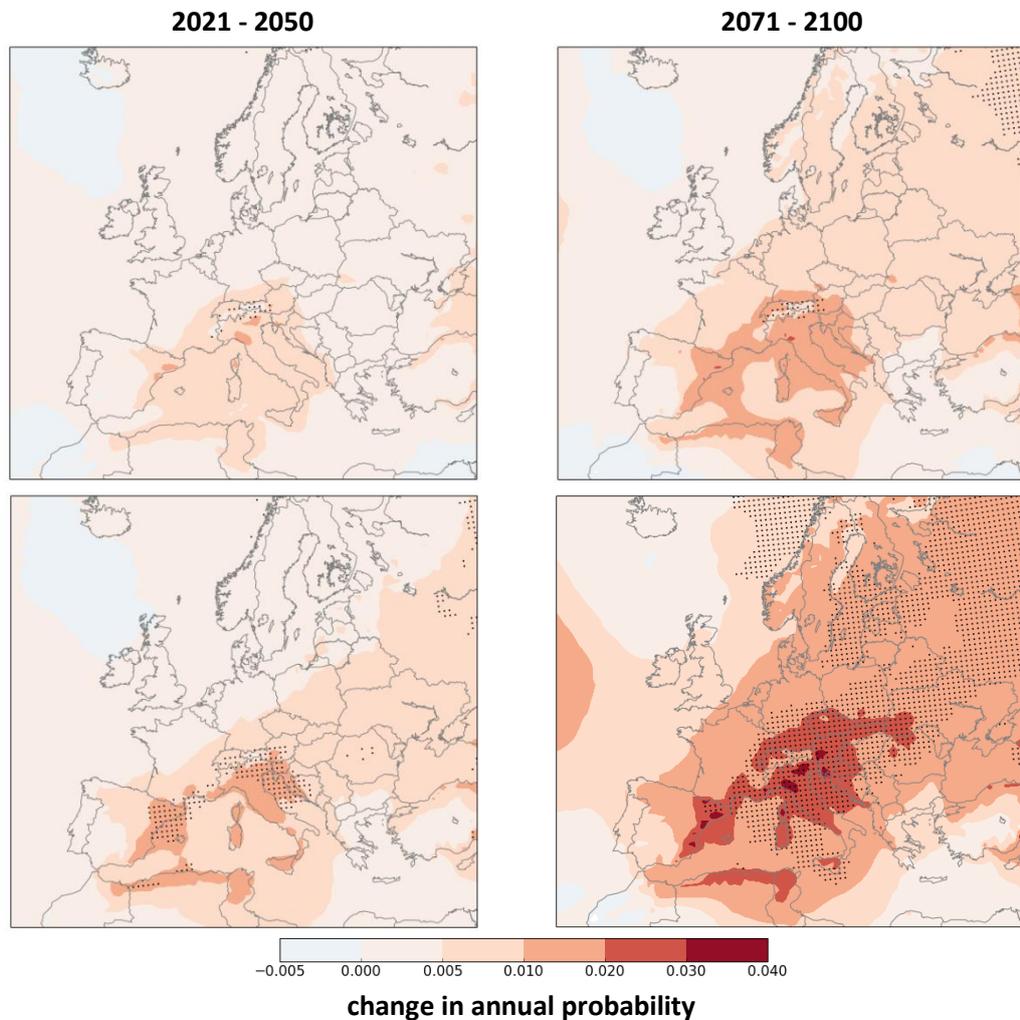
Fig. 16.4. Annual probability of a location being affected by a tornado (top row) and projected changes in the RCP 4.5 and RCP 8.5 scenarios (bottom two rows) * 1000. Dots in the grid points denote change exceeds twice the standard deviation of the individual ensemble member changes.

17. Lightning (thunderstorms)

Tomáš Púčik and Pieter Groenemeijer, European Severe Storms Laboratory

17.1 Introduction

The occurrence of lightning is the very definition of a thunderstorm, regardless of the other phenomena that occur with it. Even though the other accompanying phenomena are responsible for most of the monetary damage inflicted by thunderstorms, lightning can be very damaging as well. From the perspective of critical infrastructure, lightning poses risk especially to the electrical components. A single lightning strike suffices to incapacitate a power transmission network or a railroad signalling system.

Fig. 17.1: Lightning striking the local airfield on 2 August 2014 in Slaný, Czech Republic. Lightning originated in the upper part of thunderstorm, striking many kilometres away from its core. Such strikes can be unexpected and are often very powerful. Photo by Jan Drahokoupil.

17.2   Method

A good estimate for the distribution of lightning activity over Europe can be obtained by counting lightning strikes that have been detected by lightning detection systems over a relatively long period of time (spanning several years of detection). There are several such systems in place that are ground-based or satellite-based and detect the location of lightning with differing spatial accuracy. Some of these networks have an open data policy, whereas others are private.

Recent publications (Anderson and Klugmann, 2014; Poelman et al. 2016) describe and show the lightning density as detected by such networks. All lightning detected by the Met Office's Arrival Time Difference system between 2006 and 2012, described in the former publication, are shown in Fig. 17.2. Although this is a relatively short period of data availability, the spatial accuracy of the system can give an impression of the magnitude of relatively localized variations. Most prominently, it displays the strong relation between orography and lightning occurrence. Many of Europe's moderately high mountain chains are important foci for thunderstorms.

In order to study changes of the lightning climate in the future, we again use the method of defining a proxy. The following proxy was used and computed from model data every two hours, namely where the following criteria were simultaneously met:

1.   Lifted Index (LI) < 0 K,

2.   Precipitation sum > 1 mm.

These conditions reflect two factors necessary for thunderstorm formation. The first is a presence of instability in the atmosphere and the second is an initiation of the convection. An average annual sum of the favourable situations for thunderstorm formation was calculated for each of the model runs and time periods.

Unlike for the other thunderstorm hazards (large hail, convective windstorms and tornadoes), it is impossible to compute the local probability of lightning hitting a certain object. Therefore, the factor of local probability has not been assessed in this case. The model results thus do show a number of situations favourable for thunderstorm formation over a large area, instead of the real probability of lightning hitting an object.

17.3   Present climate

In the present climate, the highest frequency of situations favourable for thunderstorms is obtained over the mountainous areas in Europe, such as the Pyrenees, the Apennines or the Carpathians (Fig. 17.3). This is a result also found in the observations (Fig. 17.2). Many other local minima and maxima are also successfully reproduced using the proxy model.
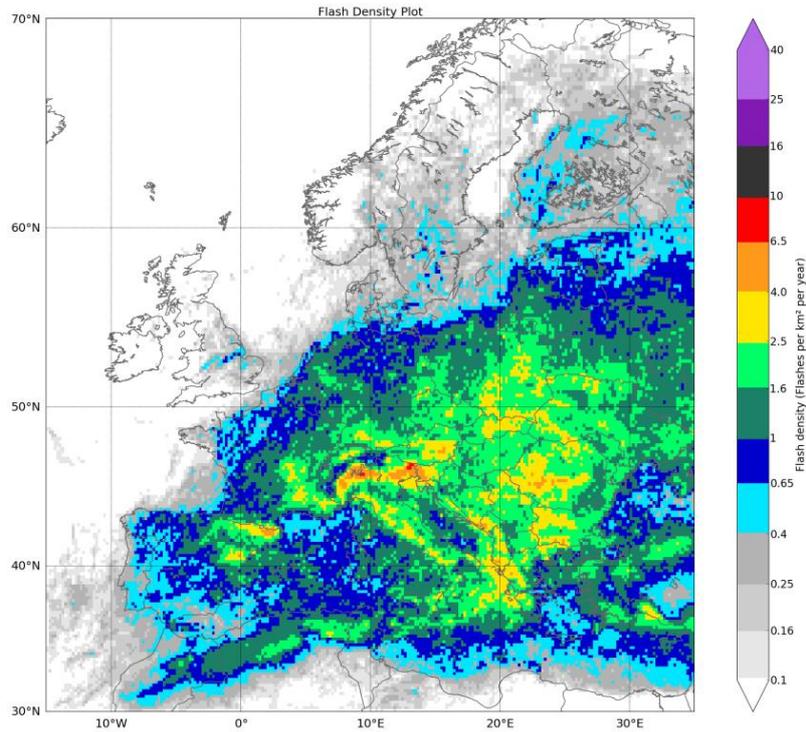
Fig. 17.2. Lightning density as detected by the Met. Office Arrival Time Difference system between 2006 and 2012. From: Anderson and Klugmann, 2014.
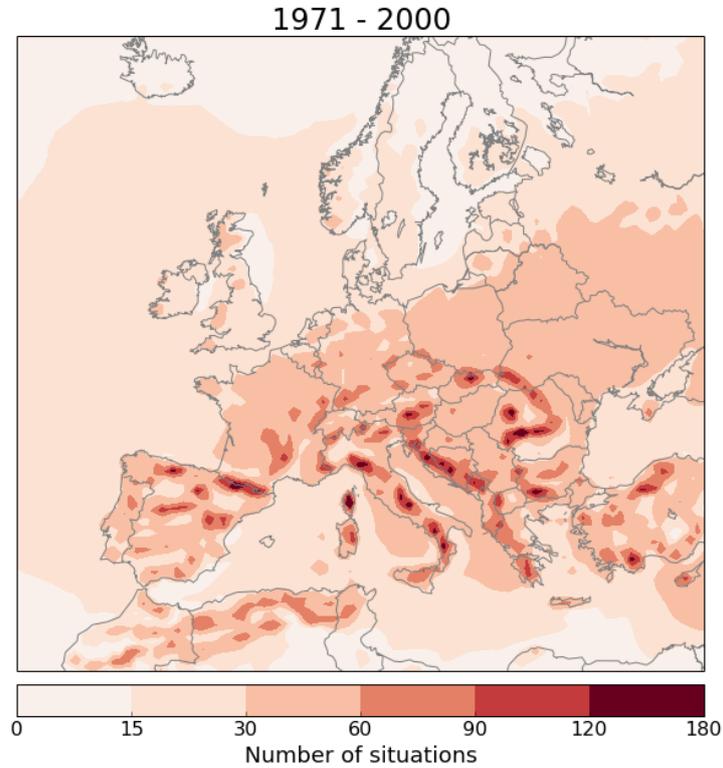
Fig. 17.3. Annual number of 6-hourly situations conducive to thunderstorm formation based on the ensemble of historical runs.

Lightning (thunderstorms)

Number of 6-hourly period favourable for thunderstorm formation
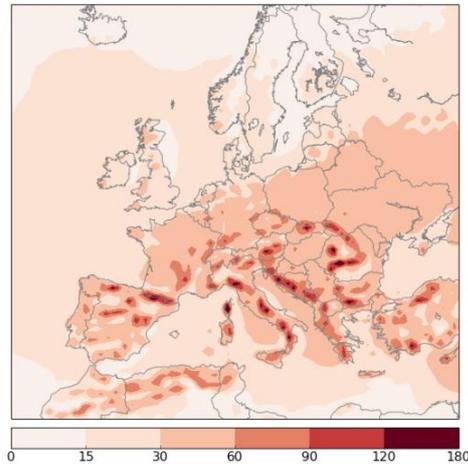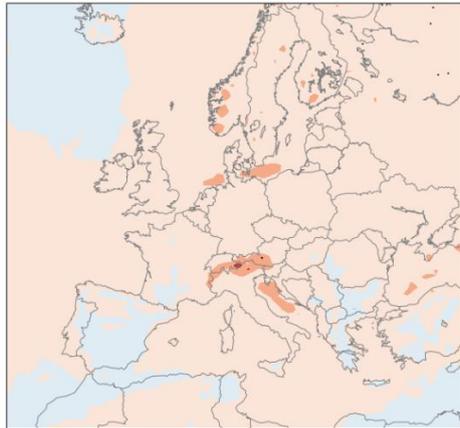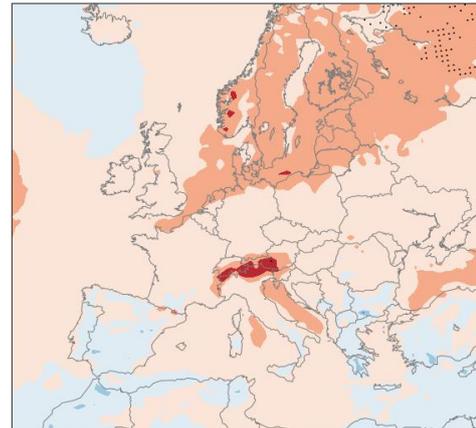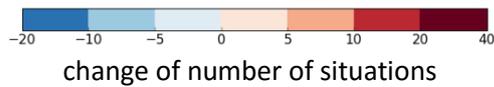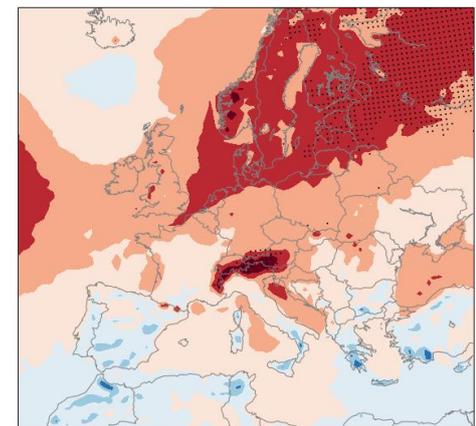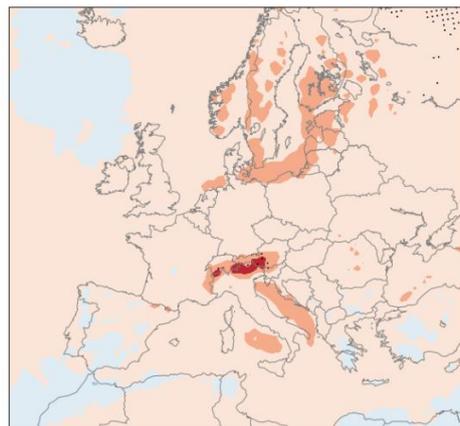
Fig. 17.4. Present frequency of situations favourable for thunderstorm formation over Europe (top row) and the projected changes in the RCP 4.5 and RCP 8.5 scenarios (bottom two rows). Dots in the grid points denote that the mean change in the ensemble exceeds twice the standard deviation of the changes in the individual ensemble members.

However, both lightning observation datasets exhibit the maximum frequency ("lightning hotspot" of Europe) over far north-eastern Italy, which is not reflected in our model. Furthermore, they also show a very steep decline in the lightning activity from the pre Alpine areas towards the central Alps with local minimum there. This is also not reproduced by the models. One of the reasons for these inconsistencies is that the model resolution is too coarse to be able to accurately represent the complex orography of this region.

17.4 Climate predictions

Fig. 17.4 shows the present annual number of situations favourable for thunderstorm formation along with the changes simulated for RCP 4.5 and RCP 8.5 scenarios for the periods of 2021-2050 and 2071-2100.

Concerning the RCP 4.5 scenario and 2021 – 2050 period, only statistically not significant are forecast for basically the whole Europe. There are only a few gridpoints with the significant change. Not significant increase is forecast for much of Europe, while a decrease is simulated over the parts of southern Europe, namely Spain, Greece and Bulgaria. Predictions are very similar also for the 2071 – 2100 time frame. Mostly statistically not significant increase is simulated over most of Europe with an exception of several gridpoints with significant increase over Russia. In terms of values, ensemble mean shows an average increase by up to 10 situations while an insignificant decrease of similar degree is simulated for Spain, southern Italy and the southern Balkans area.

RCP 8.5 scenario shows more significant changes than the RCP 4.5 scenario, but only for the 2071 – 2100 period. For 2021 – 2050, results are very similar to the RCP 4.5 scenario. By 2071 – 2100, ensemble mean predicts significant increase over two regions in Europe: Alpine range and north-eastern Europe. Rest of the continent should experience not significant increase while a decrease was again simulated for much of Iberian Peninsula, southern Italy and the southern Balkans.

The EURO-CORDEX models predict a significant increase in instability over much of Europe so that the expectation would be that also the number of situations favourable for thunderstorm formation would significantly increase. However, as discussed above, this is not the case. Presence of atmospheric instability is essential for thunderstorm formation, but not sufficient by itself and an initiating factor must be present as well. While atmosphere should indeed get more unstable, it seems that the frequency of situations in which atmosphere is unstable but thunderstorms do not initiate may increase. This is the most likely explanation of the discrepancy between the future changes in the instability and in the favourable thunderstorm situations.

Our findings consider only the situations favourable for thunderstorm formation, regardless of the lightning frequency (and thus lightning risk) in thunderstorms. Fuchs et al. (2015) have investigated the relation of lightning frequency in thunderstorm to the environmental factors. They found that significant lightning flash rates are (among other factors) associated with the large atmospheric instability. Romps et al. (2014) made a similar finding and predicted an increase in the lightning frequency in the future for the United States, owing to the increase in the atmospheric instability. As atmospheric instability should increase also over much of Europe towards the late 21st century, it can

be inferred that while the number of thunderstorm situations will not change significantly, future thunderstorms will be capable of producing more frequent lightning.

18. Summary

The report has evaluated the occurrence of a large number of (hydro-)meteorological hazards in the present climate and presented an outlook for changes in the occurrence frequency that can be expected during the 21st century in response to climate change. For the assessments, newly developed thresholds and methods were used and applied for the first time to an ensemble of regional climate models across Europe with the aim to provide input for a risk analysis framework. This framework will allow recommendations for adaptation strategies. In addition, the information can be used directly by critical infrastructure managers and public safety authorities in risk analyses independent of the RAIN project. To that aim, the data have been made publicly available. Please refer to Appendix B for more information.

The obtained spatial distributions and trends differ strongly between the various phenomena. Table 18-1 summarizes the results per hazard.

Hazard	Present spatial distribution of risk	Trends	Effects of climate change mitigation (RCP 4.5 vs. 8.5)
Windstorm	• highest risk in northwest Europe • moderate risk elsewhere	• possibly, an increase over Central Europe, particularly in RCP 8.5 scenario • the uncertainty of the projections is relatively high • a slight decrease over Mediterranean Sea and North Atlantic is more certain	• mitigation yields an important reduction of trends
Heavy precipitation	• highest risk along mountain ranges, particularly along Mediterranean coasts • moderate risk elsewhere	• increase across all of Europe, most pronounced in NW Europe, particularly Fennoscandia and the British Isles • especially strong and significant increases in the RCP 8.5 scenario by the end of the century • increase stronger for sub-daily high-intensity events than for long duration events	• mitigation will help to avoid the particularly strong increases in RCP 8.5 scenario
Coastal floods	• hazard strongly correlated to flood protection • low risk in the Netherlands, higher in other West-European countries and Poland	• widespread increase in risk, primarily because of rising sea level • areas with particularly high risk: French coasts, central and southern UK, Germany, Italy (Adriatic), northern Poland, Danube delta	• mitigation only marginally reduces risk. Significant sea level rise occurs even in the RCP 4.5 scenario

River floods	- hazard strongly correlated to flood protection - potential for large flooding in areas such as Italy (Po), Hungary, Serbia, Romania (Danube)	- increase over central Europe and UK - slight decrease over northern and north-eastern Europe	mitigation moderately reduces risk
Heavy snowfall	- highest risk across northern and eastern Europe and in mountains, moderate in central Europe - very heavy snowfall affecting only the highest mountains	reductions everywhere except central and northern Fennoscandia, and some parts of Russia	mitigation results in less risk reduction in the RCP 4.5 scenario
Blizzards (snow storms)	highest risk in Norway, coastal part of Scandinavia and in the Alps	reduction across Europe, with the exception of Scandinavian mountains and northwest Russia	mitigation results in less risk reduction in the RCP 4.5 scenario
Crown snow load	- highest over the Scandes and the Alps - moderate in Scandinavia and southeast Europe	- risk reductions over most of Europe - increase in risk in Northern and northeast Europe	mitigation causes a reduction of the predicted regional increases and decreases
Freezing rain	- highest risk in Eastern and South-Eastern Europe and southern coast of Norway - modest risk elsewhere	- increases in risk in northern and north-eastern Europe - reduction of risk in Central and southeast Europe	mitigation causes a modest reduction of the predicted regional increases and decreases
Wildfires	- highest risk in southern Europe - lower risk at higher latitudes	- large increases in risk in southern and central Europe - reduced increase in northern Europe	mitigation can strongly reduce the risk increases
Lightning	- highest risk in central and southern Europe, particularly near mountain ranges - moderate risk elsewhere	- increases across most of Europe, particularly north of 50° N and across the Alps - strongest relative increases around 100% across far northern Europe in RCP 8.5 at the end of the century	mitigation results in lesser increase in thunderstorm activity over far northern Europe
Hail, Tornadoes, Convective Windstorms	- highest risk in Mediterranean countries - moderate risk in west, central and eastern Europe - low risk in northern Europe	- increases of risk, strongest increases in south-central Europe - trend in southwest Europe uncertain	mitigation will reduce half of the simulated increase of 10 – 30% across much of Europe and 30 – 60% in south-central Europe

Table 18-1. Summary of the main results of the present and future hazard probability distributions across Europe.

Windstorms

Across the European continent, the modelled 50-year return levels in the present day climate are highest in north-western Europe, in particular in coastal areas. The probability that the present day 50-year return levels are exceeded in the future increases in large parts of the European land area. The strongest increase is found in the late period of RCP8.5. In Southern Germany and across the Balkans the change reaches almost 0.02, which is a doubling of the probability. However, the uncertainties among the different ensemble members are relatively large and the ensemble mean changes almost never exceed the ensemble standard deviation in the land areas. Only above the Mediterranean and North Atlantic, where the probability of return level exceedance decreases in the future, the mean projected changes are larger than the ensemble standard deviation.

Heavy precipitation

An increase in the number of relevant precipitation events is predicted all over Europe for both scenarios, which becomes statistically significant over large areas at the end of the 21st century. The strength of the increase is dependent on the greenhouse gas levels, as the strongest increase is predicted for the aggressive RCP 8.5 emission scenario. The increase is most pronounced in North-Western Europe, especially over Scandinavia and across the British Isles. The numbers of sub-daily, high-intensity events are predicted to increase at a higher rate than the number of long-duration events characterised by high accumulated rain amounts.

Coastal floods

For coastal floods, a distinction was made between the case in which flood protection was ignored and the case in which the current level of flood protection was assumed. Without protection, the majority of the area of coastal flood hazard zones can be found mostly in low-lying river deltas and estuaries and in countries along the North Sea. Future trends of hazard were found to differ strongly between regions and scenarios. Sweden, Finland and Estonia, lying in area with significant ground uplift rate with encounter a decrease in their flood hazard zones in all scenarios. Although some regions see decreases in hazard probability, it is projected to increase in subsequent decades across most of Europe. The trend is driven more by sea level rise than by changes in storminess. When assuming current levels of flood protection, differences between regions remain very large. In many areas, 100-year and 300-year flood zones, which constitute the majority of total hazard, will mostly become 10-year and 30-year zones by 2071–2100. Many flood defences, therefore, will no longer fulfil their designed or intended protection standards. Climate change mitigation has a minor effect on the reduction of the risk, as sea level rise will already be strong in the more conservative RCP 4.5 scenario.

River floods

The river flood hazard is more evenly distributed across Europe than coastal floods. The Danube basin stands out from other river basins in both absolute and relative (relative to the total size of basin) area at flood risk, while Germany was found to contain the largest flood-prone area of all analysed territories. When flood protection is not included, the increase in hazard zones is modest; results show, however, that some of the existing flood defences will need to be enhanced to cope

with increased water levels. Throughout Europe, 10-year, 30-year and 100-year floods will expand greatly. Germany, Hungary, Poland and France are expected to have the largest absolute increases in flood hazard zone area. On the other hand, northern Europe (Scandinavia, Scotland, north-western Russia) will encounter a decrease. This contrasting trend is caused by a projected decline in snowfall, which in turn will result in a decrease in snowmelt, which is the prime factor behind floods in that region. In the rest of Europe, more extreme rainfall will cause larger floods.

Winter weather

European CI is regularly affected by a variety of severe winter weather phenomena. Presently, **snow** events, such as heavy snowfall, blizzards and crown snow load events have the highest probability in northern Europe and the Alpine region. Although very heavy snow fall events (> 25 cm) occur in general only over the higher European mountains, large areas from Northern and SE Europe might be also impacted. Events with heavy snow load (60 kg m^{-2}) have not occurred elsewhere than in the Alps and Scandes during the studied period.

The connection of **blizzards** to large-scale circulation was also studied, but strong conclusions could not be drawn due to the small sample size.

The multi-model mean of six RCMs indicated a general decrease in the **heavy snowfall** and **blizzard** events disruptive for CI, however for the heavy snowfall events this trend was uncertain, involving a slight increase in the frequency of the events over the eastern and northern part of the continent. **Crown snow load** events are projected to become less frequent over most of Europe except Northern and NE part of Europe, where an increase of 10-25 pp is expected by 2100.

The spatial and temporal variation of **freezing rain** over Europe has been defined applying a new freezing rain typing algorithm developed in FMI. The present climatology of freezing rain is characterized by high annual probabilities (>30%) in Eastern and SE Europe and the southern coast of Norway, but all the European countries suffer of freezing rain events with >5mm/24 h at least occasionally. Very severe freezing rain events are rare. Climate models predict a northward shift in the occurrence of freezing rain events, with slight decrease in probability in central Europe but intensification in Fennoscandia and Northern Russia.

Wildfires

Wildfire risk is currently highest over southern Europe decreasing gradually northwards. Extreme fire risk is rarely expected in most of the continent, except on the Mediterranean shores. In the future the meteorological forest fires risk is projected to increase strongly in Central and especially in Southern Europe, for Northern Europe the trend was smaller. CI will be affected by the wildfire hazard, most often in the hot summers in Central and Southern Europe. Climate change mitigation (cutting down emissions from RCP8.5 to RCP4.5 scenario) strongly reduces these increases.

Thunderstorm-related hazards

The probability of **tornadoes**, **large hail** and **severe wind gusts** related to severe thunderstorms is distributed very similarly across Europe, according to the model used. Maxima were located near

medium-high mountain ranges and along the flanks of high mountains like the Alps, as well as along the coasts of the Mediterranean countries. Away from these areas a somewhat lower but non-negligible risk of these hazards still exists as observations show. Projections for the 21st century indicate that these hazards are likely to become more common, especially towards the end of the century. Although these increases are not limited to any particular area, they are the highest in south-central Europe and amount to 30-60% in the RCP 8.5 scenario in the period 2071-2100. In the RCP 4.5 scenario, the changes are approximately half as large.

Regarding the probability of **lightning**, the zones at highest risk are concentrated near mountain ranges in Central and, especially, Southern Europe. The risk is relatively low in Northern Europe in the reference period. The projections for the 21st century indicate that increases are to be expected especially across Northern Europe and across the Alps. Across these areas the relative increases amount to 100% across some areas in the RCP8.5 scenario. In other regions, increases are smaller. The difference between the two RCP scenarios is substantial, with the RCP 4.5 indicating changes that are roughly half as large as RCP 8.5.

References

Alfieri, L., Salamon, P., Bianchi, A., Neal, J., Bates, P., Feyen, L., 2014. Advances in pan-European flood hazard mapping. *Hydrological Processes* **28**, pp. 4067–4077. doi:10.1002/hyp.9947

Anderson, G., D. Klugmann, 2014: A European lightning density analysis using 5 years of ATDnet data. *Natural Hazards and Earth System Sciences*, **14**,pp. 815-829.

Andersson A., 2010. Winter road conditions and traffic accidents in Sweden and UK: present and future climate scenarios. Dissertation A131, *University of Gothenburg*, Sweden, 113 p.

Andreescu M.P. and Frost D.B., 1998: Weather and traffic accidents in Montreal, Canada. *Climate Research* **9**, pp. 225–230.

Antonescu, B., D. M. Schultz, F. Lomas, and T. Kühne, 2016. Tornadoes in Europe. Synthesis of the observational datasets. *Monthly Weather Review*, in press.

Aviso, 2015. Combined mean dynamic topography,http://www.aviso.altimetry.fr/en/data/products/auxiliary-products/mdt.html, last accessed 15 January 2016.

Barredo, J. I., 2007. Major flood disasters in Europe: 1950–2005. *Natural Hazards*, **42**, pp. 125–148. doi:10.1007/s11069-006-9065-2

Batstone, C., Lawless, M., Tawn, J., Horsburgh, K., Blackman, D., McMillan, A., Worth, D., Laeger, S., Hunt, T., 2013. A UK best-practice approach for extreme sea-level analysis along complex topographic coastlines. *Ocean Engineering* **71**, pp. 28–39. doi:10.1016/j.oceaneng.2013.02.003

BBC, 2013: http://www.bbc.com/news/world-europe-24996292. Website accessed February 23rd 2016.

Bedia J., Herrera S., Camia A., Moreno J.M., Gutiérrez J.M. (2014). Forest fire danger projections in the Mediterranean using ENSEMBLES regional climate change scenarios. *Climatic Change,* **122**, pp. 185–199.

Beniston, M., Stephenson, D.B., Christensen, O.B., Ferro, C.A., Frei, C., Goyette, S., and J. Palutikof, 2007. Future extreme events in European climate: an exploration of regional climate model projections. *Climatic Change*, **81**, pp. 71–95.

Berrisford, P., Dee, D., Fielding, K., Fuentes, M., Kallberg, P., Kobayashi, S. and Uppala, S., 2009: The ERA-Interim archive (Technical Report). European Centre for Medium-range Weather Forecasting, Reading.

Berthet, C., J. Dessens, J. L.Sanchez, 2011: Regional and yearly variations of hail frequency and intensity in France. *Atmospheric Research.*, **100**, pp. 391–400.

BODC , 2015. International sea level, https://www.bodc.ac.uk/data/online_delivery/international_sea_level/, accessed 18 January 2016

Bowman, D., Balch, K., Artaxo, P., Bond, W., Carlson, J., Cochrane, M., D'Antonio, C., DeFries, R., Doyle, J., Harrison, S., Johnston F., Keeley, J., Krawchuk, M., Kull, C., Marston, J., Moritz, M., Prentice, C., Roos, C., Scott, A., Swetnam, T., Der Werf, G. and Pyne, S., 2009. Fire in the Earth System. *Science*, **324**, pp. 481–484.

Brooks, H. E., 2013. Severe thunderstorms and climate change. *Atmospheric Research*, **123**, pp. 129–138.

Call, J., 2010: Changes in ice storm impacts over time: 1886-2000. *Weather, Climate and Society*, DOI: 10.1175/2009WCAS1013.1

Carson, M., Koehl, A., Stammer, D., Slangen, A. B. A., Katsman, C. A., van de Wal, R. S. W., Church, J., White, N., 2016. Coastal Sea Level Changes, Observed and Projected during the 20th and 21st Century. *Climatic Change*, **134**, pp. 269–281. doi:10.1007/s10584-015-1520-1

Centro de Estudios Hidrográfico, 2012. Anuario de aforos 2011-2012, http://ceh-flumen64.cedex.es/anuarioaforos/default.asp. Accessed 14 January 2016.

Changnon, S. A., 1992. Temporal and spatial relationships between hail and lightning. *Journal of Applied Meteorology*, **31**, pp. 587–604.

Coles, S., Bawa, J., Trenner, L., and P. Dorazio, 2001: An introduction to statistical modeling of extreme values. London. Springer.

Collins, M., R. Knutti, J. Arblaster, J.-L. Dufresne, T. Fichefet, P. Friedlingstein, X. Gao, W.J. Gutowski, T. Johns, G. Krinner, M. Shongwe, C. Tebaldi, A.J. Weaver and M. Wehner, 2013. *Long-term Climate Change: Projections, Commitments and Irreversibility*. In: *Climate Change* The Physical Science Basis. Contribution of Working Group I to the Fifth Assessment Report of the Intergovernmental Panel on Climate Change [Stocker, T.F., D. Qin, G.-K. Plattner, M. Tignor, S.K. Allen, J. Boschung, A. Nauels, Y. Xia, V. Bex and P.M. Midgley (eds.)]. Cambridge University Press, Cambridge, United Kingdom and New York, NY, USA.

Coniglio, M. C., J. Y. Hwang, and D. J. Stensrud, 2010. Environmental factors in the upscale growth and longevity of MCSs derived from rapid update cycle analyses. *Monthly Weather Review*, **138**, pp. 3514–3539.

De Jager, A. L., Vogt, J. V., 2010. Development and demonstration of a structured hydrological feature coding system for Europe. *Hydrological Sciences Journal* **55**, pp. 661–675. doi:10.1080/02626667.2010.490786

De Vries, H., G. Lenderink and E. Meijgaard, 2014: Future snowfall in western and central Europe projected with a high-resolution regional climate model ensemble. *Geophysical Research Letters*, **41**, 4294–4299.

Dee, D.P. et al. (35 co-authors), 2011. The ERA-Interim reanalysis: configuration and performance of the data assimilation system. Quart J R Meteorol Soc **137**, pp.553–597.

Deltares, 2014a. Delft3D-FLOW User Manual.
http://oss.deltares.nl/documents/183920/185723/Delft3D-FLOW_User_Manual.pdf

Deltares, 2014b. DelftDashboard. https://publicwiki.deltares.nl/display/OET/DelftDashboard, accessed 24 March 2016.

Deltares, 2015. SOBEK User Manual.
http://content.oss.deltares.nl/delft3d/manuals/SOBEK_User_Manual.pdf

DHI GRAS, 2014. EU-DEM Statistical Validation Report. European Environment Agency, Copenhagen. http://ec.europa.eu/eurostat/documents/4311134/4350046/Report-EU-DEM-statistical-validation-August2014.pdf

Diffenbaugh, N. S., M. Scherer, and R. J. Trapp, 2013. Robust increases in severe thunderstorm environments in response to greenhouse forcing. *Proceedings of the National Academy of Sciences, USA,* **110**, pp. 361–366.

Dotzek, N., P. Groenemeijer, B. Feuerstein, and A. M. Holzer, 2009. Overview of ESSL's severe convective storms research using the European Severe Weather Database ESWD. *Atmos. Res.*, **93**, pp. 575–586.

Ebita, A., Kobayashi, S., Ota, Y., Moriya, M., Kumabe, R., Onogi, K., ... & Kamahori, H, 2011. The Japanese 55-year Reanalysis" JRA-55": an interim report. Sola, **7**, pp. 149-152.

Egbert, G. D., Bennett, A. F., Foreman, M. G. G., 1994. Topex/Poseidon tides estimated using a global inverse model. *Journal of Geophysical Research,* **99**, pp. 24821–24852. doi:10.1029/94JC01894

Egbert, G. D., Erofeeva, S.Y. (2014). TPXO8-atlas. http://volkov.oce.orst.edu/tides/tpxo8_atlas.html. Accessed 16 January 2016.

Egbert, G. D., Erofeeva, S.Y., 2002. Efficient inverse modeling of barotropic ocean tides. *Journal of Atmospheric and Oceanic Technology* **19**, pp. 183–204.

EMODnet, 2016. Portal for Bathymetry, http://portal.emodnet-bathymetry.eu/. Accessed 18 January 2016.

Environment Agency, 2015. Data Download, http://www.geostore.com/environment-agency/WebStore?xml=environment-agency/xml/ogcDataDownload.xml. Accessed 14 January 2016.

European Environment Agency, 2007. CLC2006 technical guidelines. *EEA Technical report No 17/2007*, European Environment Agency, Copenhagen.

European Environment Agency, 2014. Corine Land Cover 2000 raster data. http://www.eea.europa.eu/data-and-maps/data/corine-land-cover-2000-raster-3. Accessed 12 January 2016.

Evans, J.S. and Doswell III, C.A., 2001. Examination of derecho environments using proximity soundings. *Weather and Forecasting*, **16**, pp. 329–342.

Fal, B., 2000. Przepływy charakterystyczne głównych rzek polskich w latach 1951-1995. Materiały Badawcze - Instytut Meteorologii i Gospodarki Wodnej. *Hydrologia i Oceanologia* 26, IMGW, Warsaw, 137 pp.

Farr, T. G., Rosen, P. A., Caro, E., Crippen, R., Riley, D., Alsdorf, D., 2007: The Shuttle Radar Topography Mission. *Reviews in Geophysics* **45**:RG2004. doi:10.1029/2005RG000183

Feyen, L., Dankers, R., Bódis, K., Salamon, P., Barredo, J. I., 2012. Fluvial flood risk in Europe in present and future climates. *Climatic Change,* **112** pp. 47–62. doi:10.1007/s10584-011-0339-7

Flannigan, M, B. Stocks, M. Turetsky and M. Wotton, 2009. Impacts of climate change on fire activity and fire management in the circumboreal forest. *Glob. Change Biol.*, **15**, pp. 549–560.

Fuchs, B. R., S. A. Rutledge, E. C. Bruning, J. R. Pierce, J. K. Kodros, T. J. Lang, D. R. MacGorman, P. R. Krehbiel, and W. Rison, 2015. Environmental controls on storm intensity and charge structure in multiple regions of the continental United States. *J. Geophys. Res. Atmos.*, **120**, pp. 6575–6596.

Galway, J. G., 1956: The lifted index as a predictor of latent instability. *Bull. Amer. Meteor. Soc.*, **37**, pp. 528–529.

Ganteaume, A., Camia, A., Jappiot, M., San-Miguel-Ayanz, J., Long-Fournel, M., and Lampin, C., 2013.: A review of the main driving facors of forest fire ignition over Europe. *Environmental Management*, 51, pp. 651-662.

Gensini, V. A., and T. L. Mote, 2015: Downscaled estimates of late 21st century severe weather from CCSM3. *Climatic Change*, **129**, pp. 307–321.

Global Runoff Data Centre, 2015. Homepage, http://www.bafg.de/GRDC/EN/Home/homepage_node.html. Last accessed 14 January 2016.

Göber, M., Zsótér, E. and Richardson, D.S., 2008. Could a perfect model ever satisfy a naïve forecaster? On grid box mean versus point verification, *Meteorol. Appl.*, **15**, pp. 359-365.

Groenemeijer, P. H., and A. van Delden, 2007. Sounding-derived parameters associated with large hail and tornadoes in the Netherlands. *Atmospheric Research*, **83**, pp. 473–487.

Groenemeijer, P.H., and T. Kühne, 2014: A climatology of tornadoes in Europe: Results from the European Severe Weather Database. *Monthly Weather Review*, 142, 4775–4790.

Hanea, A. M., Kurowicka, D., Cooke, R. M., 2006. Hybrid Method for Quantifying and Analyzing Bayesian Belief Nets. Quality and Reliability, *Engineering International*, **22**, pp. 709–729. doi:10.1002/qre.808

Haylock, M.R., Hofstra, N., Klein Tank, A.M.G., Klok, E.J., Jones P.D. and New, M., 2008. A European daily high-resolution gridded dataset of surface temperature and precipitation. *J. Geophys. Res (Atmospheres)*, **113**, D20119, doi:10.1029/2008JD10201

Heidke, P. 1926. Berechnung des Erfolges und der Gute der Windstarkevorhersagen im Sturmwarnungsdienst (Measures of success and goodness of wind force forecasts by the gale-warning service), *Geogr. Ann.*, **8**, pp. 301–349.

Hofstra, N., Haylock, M., New, M. and Jones, P.D., 2009. Testing E-OBS European high-resolution gridded data set of daily precipitation and surface temperature. *Journal of Geophysical Research: Atmospheres*, **114**.

Hoppula P., 2005. Tykkylumi ja otolliset säätilanteet sen aiheuttamille puustovaurioille (Crown snow-load and favourable weather conditions for forest damage caused by it). MSc thesis, University of Helsinki, Helsinki, 87 pp. [in Finnish]

Hurrell, J.W., 1995. Decadal trends in the North Atlantic Oscillation: regional temperature and precipitation. *Science*, **269**, pp. 676–679.

IPCC 2007: https://www.ipcc.ch/publications_and_data/ar4/wg1/en/ch10s10-3-6-1.html. Website last accessed February 23rd 2016.

IPCC, 2014: Climate Change 2014: Synthesis Report. Contribution of Working Groups I, II and III to the Fifth Assessment Report of the Intergovernmental Panel on Climate Change [Core Writing Team, R.K. Pachauri and L.A. Meyer (eds.)]. IPCC, Geneva, Switzerland, 151 pp.

Johns, R. H., and C. A. Doswell III, 1992. Severe local storms forecasting. *Wea. Forecasting*, **7**, pp. 588–612.

Johns, R.H. and Hirt, W.D., 1987. Derechos: Widespread convectively induced windstorms. *Weather and Forecasting,* **2**, pp. 32-49.

Joint Research Centre (2015). Global Land Cover 2000. http://forobs.jrc.ec.europa.eu/products/glc2000/glc2000.php. Last accessed 12 January 2016.

Jolliffe, I. T. and Stephenson, D. B. 2012. Forecast Verification: A Practitioner's Guide in Atmospheric Science. Wiley, Hoboken, 2 edn.

Jylhä K., Ruosteenoja K., Räisänen J., Venäläinen A., Tuomenvirta H., Ruokolainen L., Saku S., Seitola T., 2009. The changing climate in Finland: estimates for adaptation studies (in Finnish with English abstract, extended abstract and captions for figures and tables). ACCLIM project report, Report 4, Finnish Meteorological Institute, Helsinki.

Kalnay, E., Kanamitsu, M., Kistler, R., Collins, W., Deaven, D., Gandin, L., ... & Zhu, Y., 1996. The NCEP/NCAR 40-year reanalysis project. Bulletin of the American meteorological Society, **77**,pp. 437-471.

Kistler, R., Collins, W., Saha, S., White, G., Woollen, J., Kalnay, E., ... & van den Dool, H, 2001. The NCEP-NCAR 50-year reanalysis: Monthly means CD-ROM and documentation. Bulletin of the American Meteorological society, **82**, pp. 247-267.

Klawa, M., and Ulbrich, U., 2003. A model for the estimation of storm losses and the identification of severe winter storms in Germany. *Natural Hazards and Earth System Science*, **3**, pp. 725-732.

Klemp, J.B., 1987. Dynamics of tornadic thunderstorms. *Annual review of fluid mechanics*, **19**, pp. 369-402.

Klok, E.J. and Klein Tank, A.M.G. 2009. Updated and extended European dataset of daily climate observations. Int J Climatol, **29**, pp. 1182–1191

Kotlarski, S., Keuler, K., Christensen, O. B., Colette, A., Déqué, M. , …, Wulfmeyer, V., 2014. Regional climate modeling on European scales: a joint standard evaluation of the EURO-CORDEX RCM ensemble. *Geoscientific Model Development,* **7**, pp. 1297–1333. doi:10.5194/gmd-7-1297-2014

Kurowicka, D., Cooke, R., 2006. Uncertainty analysis with high dimensional dependence modelling. John Wiley and Sons Ltd., 279 pp.

Lahti K., Lahtinen M. and Nousiainen K., 1997. Transmission line corona losses under hoar frost conditions. *IEEE Transactions on Power Delivery*, **12**, pp. 928–933

Lambert S.J. and Hansen B.K., 2011: Simulated Changes in the Freezing Rain Climatology of North America under Global Warming Using a Coupled Climate Model, *Atmosphere-Ocean*, **49**, pp. 289-295, DOI: 10.1080/07055900.2011.607492

Land Niederösterreich, 2015. Download von Geodaten und Karten, http://www.noel.gv.at/Land-Zukunft/Karten-Geoinformation/Karten-Geodaten-Angebot/DownloadGeodatenKarten.html. Accessed 14 January 2016.

Leckebusch, G. C., and Ulbrich, U., 2004. On the relationship between cyclones and extreme windstorm events over Europe under climate change. *Global and planetary change*, **44**, pp. 181-193.

Leckebusch, G. C., Renggli, D., and Ulbrich, U., 2008. Development and application of an objective storm severity measure for the Northeast Atlantic region. Meteorologische Zeitschrift, **17**, pp. 575-587.

Lehtonen, I., A. Venäläinen, M. Kämäräinen, H. Peltola and H. Gregow, 2016. Risk of large-scale fires in boreal forests of Finland under changing climate. *Nat. Hazards Earth Syst. Sci.,* **16**, pp. 239–253.

Lehtonen, I., P. Hoppula, P. Pirinen and H. Gregow, 2014. Modelling crown snow loads in Finland: a comparison of two methods. Silva Fenn., 48, article id 1120, doi:10.14214/sf.1120.

Lehtonen, I., Ruosteenoja, K., Venäläinen, A. and Gregow, H., 2014. The projected 21st century forest-fire risk in Finland under different greenhouse gas scenarios. *Boreal Env. Res.* **19**, pp. 127–139.

Lumbroso, D. M., Vinet, F. (2011). A comparison of the causes, effects and aftermaths of the coastal flooding of England in 1953 and France in 2010. Natural Hazards and Earth System Sciences 11(8):2321–2333. doi:10.5194/nhess-11-2321-2011

Mastrandrea, M.D., Field, C.B. Stocker, T.F., Edenhofer, O., Ebi, K.L., Frame, D.J. , Held, H., Kriegler, E., Mach, K.J. , Matschoss, P.R. ,. Plattner, G.-K , Yohe , G.W. and Zwiers, F.W, 2010. Guidance Note for Lead Authors of the IPCC Fifth Assessment Report on Consistent Treatment of Uncertainties. Intergovernmental Panel on Climate Change (IPCC). Available at http://www.ipcc.ch.

Migliavacca, M., A. Dosio, A. Camira, R. Hobourg, T. Houston-Durrant, J.W. Kaiser, N. Khabarov, A.A. Krasovskii, B. Marcolla, J. San Miguel-Ayanz, D.S. Ward and A. Cescatti, 2013. Modeling biomass burning and related carbon emissions during the 21st century in Europe. *J. Geophys. Res.-Biogeo.*, **118**, pp. 1732–1747.

Moriasi D., Arnold J., Van Liew M., Binger R., Harmel R. and Veith T., 2007. Model evaluation guidelines for systematic quantification of accuracy in watershed simulations. *Transactions of the ASABE*, **50**, pp. 885–900.

Moriondo, M., Good, P., Durao, R., Bindi, M., Giannakopoulos, C., and Corte-Real, J., 2006. Potential impact of climate change on fire danger in the Mediterranean area. *Clim. Res.*, **31**, 85-95.

Mouillot F., Rambal S., Joffre R., 2002. Simulating climate change impacts on fire frequency and vegetation dynamics in a Mediterranean-type ecosystem. *Global Change Biology,* **8**, pp. 423-437.

Muis S., Verlaan M., Winsemius H., Aerts J. C. J. H. and Ward P. J., 2015. The first global-scale hindcast of extreme sea levels. *E-proceedings of the 36th IAHR World Congress*, The Hague, the Netherlands.

Munich Re, 2002. Winter storms in Europe (II). Munich.

Mutua, F. M., 1994. The use of the Akaike Information Criterion in the identification of an optimum flood frequency model. *Hydrological Sciences Journal*, **39**, pp. 235–244.

Norwegian Water Resources and Energy Directorate, 2015. Historiske vannføringsdata til produksjonsplanlegging, https://www.nve.no/hydrologi/hydrologiske-data/historiske-data/historiske-vannfoeringsdata-til-produksjonsplanlegging/. Accessed 14 January 2016.

Paprotny, D., Morales-Nápoles, O., 2015. A Bayesian Network for extreme river discharges in Europe. *Safety and Reliability of Complex Engineered Systems*, CRC Press/Balkema, pp. 4303–4311.

Peltier, W. R., Argus, D. F., Drummond, R., 2015. Space geodesy constrains ice-age terminal deglaciation: The global ICE-6G_C (VM5a) model. *Journal of Geophysical Research: Solid Earth*, **120,** pp. 450–487. doi:10.1002/2014JB011176

Pisano P., Goodwin L. and Stern A., 2002. Surface transportation safety and operations: the impacts of weather within the context of climate change. *In: Proceedings of the U.S. Department of Transportation Research Workshop: Potential Impacts of Climate Change on Transportation*, *Washington* DC, Oct. 1-2, pp. 165-184

Poelman, D. R., W. Schulz, G. Diendofer, M. Bernardi, 2016. The European lightning location system EUCLID – Part 2: Observations. *Nat. Hazards Earth Sys. Sci*, **16**, pp. 607-616.

Poulter, B., Halpin, P. N., 2008. Raster modelling of coastal flooding from sea-level rise. *International Journal of Geographical Information Science*, **22**, pp. 167–182.

Púčik, T., P. Groenemeijer, D. Rýva, and M. Kolář, 2015. Proximity soundings of severe and nonsevere thunderstorms in central Europe. *Monthly Weather Review*, **143**, pp. 4805-4821.

Punge, H.J., Bedka, K.M., Kunz, M. and Werner, A., 2014. A new physically based stochastic event catalog for hail in Europe. *Natural Hazards*, **73**, pp. 1625-1645.

Räisänen, J., 2016. Twenty-first century changes in snowfall climate in Northern Euripe in ENSEMBLES regional climate models. *Clim. Dyn.*, **46**, pp. 339–353.

Rasmussen, E. N., and D. O. Blanchard, 1998. A baseline climatology of sounding-derived supercell and tornado forecast parameters. *Wea. Forecasting*, **13**, 1148–1164.

Rauhala J. and Juga I, 2010. Wind and snow storm impacts on society. In *Proceedings of SIRWEC 15th International Road Weather Conference*, Quebec City, Canada, 5-7 February 2010

Rijkswaterstaat, 2016. Waterbase, http://live.waterbase.nl/, last accessed 18 January 2016.

Rio, M.-H., Mulet, S., Picot, N., 2014. Beyond GOCE for the ocean circulation estimate: Synergetic use of altimetry, gravimetry, and in situ data provides new insight into geostrophic and Ekman currents. *Geophysical Research Letters*, **41**, pp. :8918–8925. doi:10.1002/2014GL061773

Rockel, B., and Woth, K., 2007. Extremes of near-surface wind speed over Europe and their future changes as estimated from an ensemble of RCM simulations. *Climatic Change*, **81**, pp. 267-280.

Rojas, R., Feyen, L., Bianchi, A., Dosio, A., 2012. Assessment of future flood hazard in Europe using a large ensemble of bias-corrected regional climate simulations. *Journal of Geophysical Research* **117**:D17109. doi:10.1029/2012JD017461

Romps, D. M., J. T. Seeley, D. Vollaro, J. Molinari, 2014: Projected increase in lightning strikes in the United States due to global warming. *Science*, **346**, pp. 851–854.

Rothermel R.C., 1991. Predicting behaviour and size of crown fires in the Northern Rocky Mountains. Research Paper INT-438. United States Department of Agriculture, Forest Service. Intermountain Research Station, Ogden, Utah.

Sächsisches Landesamt für Umwelt, Landwirtschaft und Geologie, 2015. Geodatendownload des Fachbereichs Wasser, http://www.umwelt.sachsen.de/umwelt/wasser/10002.htm?data=ueg. Last accessed 14 January 2016.

Sampson, C. C., Smith, A. M., Bates, P. D., Neal, J. C., Alfieri, L., Freer, J. E., 2015. A high-resolution global flood hazard model. *Water Resources Research,* **51**, 7358–7381. doi:10.1002/2015WR016954

Scaife, A.A., A. Arribas, E. Blockley, A. Brookshaw, R.T. Clark, N. Dunstone, R. Eade, D. Fereday, C.K. Folland, M. Gordon, L. Hermanson, J.R. Knight, D.J. Lea, C. MacLachlan, A. Maidens, M. Martin, A.K. Peterson, D. Smith, M. Vellinga, E. Wallace, J. Waters, and A. Williams, 2014. Skillful long-range

prediction of European and North American winters, *Geophysical Research Letters*, **41**, 2514–2519, doi:10.1002/2014GL059637

Scussolini, P., Aerts, J. C. J. H., Jonkman, B., Bouwer, L. M., Winsemius, H. C., de Moel, H., Ward, P. J. , 2015. FLOPROS: an evolving global database of flood protection standards. *Natural Hazards and Earth System Sciences Discussions*, **3**, 7275–7309.

Sherstyukov, B.G. and A.B. Sherstyukov, 2014. Assessment of increase in forest fire risk in Russia till the late 21st century based on scenario experiments with fifth-generation climate models. *Russ. Meteorol. Hydrol.*, **39**, pp. 292–301.

Simmons, A., Uppala, S., Dee, D. and Kobayashi, S., 2006. ERA-Interim: New ECMWF reanalysis products from 1989 onwards. ECMWF Newsletter **110**, pp. 26–35.

Slangen, A. B. A., Carson, M., Katsman, C. A., van de Wal, R. S. W., Koehl ,A., Vermeersen, L. L. A., Stammer, D., 2014. Projecting twenty-first century regional sea-level changes. *Climatic Change*, **124**, 317–332. doi:10.1007/s10584-014-1080-9

SMHI, 2016. SMHI Öppna data, http://opendata-catalog.smhi.se/explore/. Accessed 18 January 2016.

Smith, B. T., R. L. Thompson, J. S. Grams, C. Broyles, and H. E. Brooks, 2012. Convective modes for significant severe thunderstorms in the contiguous United States. Part I: Storm classification and climatology. *Wea. Forecasting*, **27**, pp. 1114–1135.

Swedish Meteorological and Hydrological Institute, 2015. Vattenweb Mätningar, http://vattenweb.smhi.se/station/. Last accessed 14 January 2016.

Swiss Re: Storm over Europe – An underestimated risk, Swissre Publishing, Order No. 201 00239 en,RN,9,00,3000en or http://www.swissre.com, 2000.

Tanskanen, H., Venäläinen, A., Puttonen, P. and Granström, A., 2005. Impact of stand structure on surface fire ignition potential in *Picea abies* and *Pinus sylvestris* forests in southern Finland. *Can. J. For. Res,*, **35**,pp. 410–420.

Thompson, R.L., R. Edwards, J. A. Hart, K. L. Elmore, and P. Markowski,2003. Close proximity soundings within supercell environments obtained from the rapid update cycle. *Wea. Forecasting,* **18**, pp. 1243–1261.

UHLSC, 2015. Research Quality. http://uhslc.soest.hawaii.edu/data/download/rq. Accessed 18 January 2016.

Ulbrich, U., Brücher, T., Fink, A., Leckebusch, G.C., Krüger, A. and Pinto, J.G., 2003. The central European floods of August 2002: Part 1 – Rainfall periods and flood development, *Weather*, **58**, pp. 371–377.

Vajda A., Tuomenvirta H., Jokinen P., Luomaranta A., Makkonen L., Tikanmäki M., Groenemeijer P., Saarikivi P., Papadakis M., Tymvios F., Athanasatos S., 2011: Probabilities of adverse weather affecting transport in Europe: climatology and scenarios up to the 2050s. FMI Reports 2011:9, 85 p.

Valinger E., Lundqvist L., 1992. The influence of thinning and nitrogen fertilisation on the frequency of snow and wind induced stand damage in forests. *Scottish Forestry*, **46**, pp. 311–320

Van Wagner, C., 1987. Development and structure of the Canadian Forest Fire Weather IndexSystem. Canadian Forestry Service, Ottawa, Ontario. *Forestry Technical Report*, **35**, 37 pp.

Venäläinen, A., Korhonen, N., Koutsias, N.,Xystrakis, F., Urbieta, I.R. and Moreno, J.M., 2014. Temporal variations and change in forest fire danger in Europe for 1960-2012. *Nat.Hazards Earth Syst. Sci.*, **14**, pp. 1477-1490, doi:10.5194/nhess-14-1477-2014.

Viewfinder Panoramas, 2014. Digital elevation data. http://viewfinderpanoramas.org/dem3.html. Accessed 13 January 2016.

Vogt, J.V., Soille, P., de Jager, A., Rimaviciute, E., Mehl, W., …, Bamps, C., 2007. A pan-European River and Catchment Database. EC-JRC (Report EUR 22920 EN), Luxembourg, 120 p.

Voldoire, A., Sanchez-Gomez, E., Salas y Mélia, D., Decharme, B., Cassou, C., …, Chauvin, F., 2013. The CNRM-CM5.1 global climate model: description and basic evaluation. *Climate Dynamics*, **40**, pp. 2091–2121. doi:10.1007/s00382-011-1259-y

Vousdoukas M. I., Voukouvalas E., Annunziato A., Giardino A. and Feyen L. (2016). Projections of extreme storm surge levels along Europe. *Climate Dynamics*, doi:10.1007/s00382-016-3019-5

Wakimoto, R. M., 1985. Forecasting dry microburst activity over the high plains. *Monthly Weather Review*, **113**, pp. 1131–1143.

Ward, P. J., Jongman, B., Sperna Weiland, F., Bouwman, A., van Beek, R. (2013). Assessing flood risk at the global scale: model setup, results, and sensitivity. *Environmental Research Letters* **8**(4):044019. doi:10.1088/1748-9326/8/4/044019

Weisman, M. L., and J. B. Klemp, 1982: The dependence of numerically simulated convective storms on vertical wind shear and buoyancy. *Monthly Weather Review*, **110**, pp. 504–520.

Westermayer, A.T., P. Groenemeijer, G. Pistotnik, R. Sausen, E. Faust, 2016: Identification of favorable environments for thunderstorms in reanalysis data. *Meteorologische Zeitschrift*, in press.

Weyant, J., Ch. Azar, M. Kainuma, J. Kejun, N. Nakicenovic, P.R. Shukla, E. La Rovere and G.Yohe, 2009. Report of 2.6 Versus 2.9 Watts/m2 RCPP Evaluation Panel (PDF). Geneva, Switzerland: IPCC Secretariat.

Wilks, D.S., 2011. Statistical Methods in the Atmospheric Sciences, 3rd edn, Academic Press, Oxford, Waltham, 607 p.

Winsemius, H. C., Van Beek, L. P. H., Jongman, B., Ward, P. J., Bouwman, A., 2013. A framework for global river flood risk assessments. *Hydrology and Earth System Sciences* **17**, pp. 1871–1892. doi:10.5194/hess-17-1871-2013

Wiśniewski, B., Wolski, T., 2009. Katalogi wezbrań i obniżeń sztormowych poziomów morza oraz ekstremalne poziomy wód na polskim wybrzeżu, Maritime University of Szczecin, Szczecin, 156 pp.

WMO, 2009. ´Guide to hydrological practices´, Report, WMO-No 168, vol.II.

Ylhäisi J.S., Tietäväinen H., Peltonen-Sainio P., Venäläinen A., Eklund J., Räisänen J., Jylhä K.,.2010. Growing season precipitation in Finland under recent and projected climate. *Natural Hazards and Earth System Sciences*, **10**, pp. 1563-1574.

Zhou Y., Niu S., Lü J and Zhou L., 2012. Meteorological conditions of ice accretion based on real-time observations of high voltage transmission line. *Chinese Science Bulletin*, **57**, pp. 812–818.

Zwiers, F. W., and Kharin, V. V., 1998. Changes in the extremes of the climate simulated by CCC GCM2 under CO2 doubling. *Journal of Climate*, **11**, pp. 2200-2222.

Appendix A: Abbreviations

CanRCM4_r2	Canadian Regional Climate Model, Version 4
CanESM2	Second Generation Canadian Earth System Model
CCCma	Canadian Centre for Climate Modelling and Analysis
CCLM4-8-17	COSMO model in Climate Mode, Version 4.8.17
CNRM-CM5	CNRM-GAME (Météo-France/CNRS) and CERFACS Earth System Model
CSIRO-Mk-3-6-0	Commonwealth Scientific and Industrial Research Organisation (Australia) Earth System Model
EC-EARTH	A European Earth System Model (www.ec-earth.org)
GFDL-ESM2M	Geophysical Fluid Dynamics Laboratory – Earth System Model ESM2M
HadGEM2-ES	Met Office Hadley Centre Earth System Model
HIRHAM5	HIRHAM Regional Climate Model Version 5 of the Danish Meteorological Institute
IPSL-CM5A-MR	Institute Pierre Simon Laplace – Climate Model Version 5A Medium Resolution
KNMI	Royal Netherlands Meteorological Institute
MIROC5	Model for Interdisciplinary Research on Climate of the Center for Climate System Research, The University of Tokyo, Japan
MPI-CSC	Max Planck Institute – Climate Service Centre
MPI-ESM-LR	Max Planck Institute - Earth System Model – Low Resolution
NorESM1-M	Norwegian Earth System Model 1 – Medium Resolution
NUIM	National University of Ireland Maynooth
RACMO22E	RACMO Regional Climate Model Version 2.2 of KNMI
RCA4	Rossby Centre regional Atmospheric model, Version 4
REMO2009	Regional Model of MPI-CSC, 2009 Version
SHMI	Rossby Centre, Swedish Meteorological and Hydrological Institute
WEGC	Wegener Center for Climate and Global Change, University of Graz, Austria
WRF341	Weather Research and Forecasting Model Version 3.41

Appendix B: Access to RAIN data repository

The hazard probability data generated within RAIN Work Package 2 have been made available on the internet and can be used under the condition that the authors are attributed. The data can be accessed here:

http://dx.doi.org/10.4121/collection:ab70dbf9-ac4f-40a7-9859-9552d38fdccd

The formal citation of the dataset is as follows:

European Severe Storms Laboratory; TU Delft, Faculty of Civil Engineering and Geosciences, Department of Hydraulic Engineering; Freie Universität Berlin, Institute of Meteorology; Finnish Meteorological Institute, 2016. RAIN: Pan-European gridded data sets of extreme weather probability of occurrence under present and future climate. TU Delft. Dataset.